SYNTHESIS, PHOTOPHYSICAL CHARACTERIZATION, AND APPLICATION OF ASYMMETRIC THIAZOLOTHIAZOLES AS MOLECULAR SENSORS

by

Nickolas Anthony Sayresmith

A dissertation submitted to the faculty of
The University of North Carolina at Charlotte
in partial fulfillment of the requirements
for the degree of Doctor of Philosophy in
Nanoscale Science

Charlotte

2021

Approved by:

_____
Dr. Michael G. Walter

_____
Dr. Christopher Bejger

_____
Dr. Thomas A. Schmedake

_____
Dr. Jerry Troutman

_____
Dr. Vasily Astratov

ABSTRACT

NICKOLAS ANTHONY SAYRESMITH. Synthesis, photophysical characterization, and application of asymmetric thiazolothiazoles as molecular sensors.
(Under the direction of DR. MICHAEL G. WALTER)

Small molecule fluorophores are critical for fluorescence spectroscopy, and enable the measurement of a wide array of biological processes and dynamics. For many biological sensing applications, the overall efficacy of the fluorophore is closely correlated to the strength of the fluorophore's excited state dipole. Structurally, this is achieved by designing electronically asymmetric dyes having a donor-π-acceptor (D- π -A) molecular architecture. The electron donating and accepting substituents are chosen to maximize mesomeric effect differences, thus facilitating intramolecular charge-transfer (ICT), while also balancing application-specific requirements. In biosensing for example, donor and acceptor substituents may also be chosen based on water-solubility, toxicity, and specificity considerations. Also important, is the planarity, rigidity, and stability conferred by the π-conjugated bridge. These structural features of the π-bridge ensure strong π-π overlap, inhibited rotation, and minimal degradation, thus enabling strong absorbance, large quantum yields, and enhanced photostability – key requirements for sensing applications. One such class of π-bridge moieties demonstrating structure-function characteristics ideal for fluorophores is a class of heterocycles known as thiazolo[5,4-d]thiazoles (TTz). TTzs are fused, bicyclic heteroaromatic compounds whose unique molecular structure ensures planarity, rigidity, and stability. As such, reported is a novel mixed-pot synthetic approach for accessing D-π -A TTz fluorophores in a single step. The mixed-pot synthesis is modified from the classic literature approach by incorporating additional aromatic aldehydes, resulting in a product distribution of two symmetric TTzs and one asymmetric TTz (a-TTz). A first generation of TTz fluorophores were synthesized, photophysically characterized, and assessed for their solvent,

temperature, pH, and membrane voltage (V_M) sensing capabilities. These first-generation a-TTzs showed promising V_M sensitivity, good membrane localization, negligible cytotoxicity, and excellent photostability compared to current-state-of-the art voltage sensitive dyes (VSDs). Given the promising results of the first-generation dyes, a second generation of a-TTzs VSDs were designed specifically to increase voltage sensitivity, water-solubility, and specificity. Additionally reported, are a series of computational and analytical studies designed to probe mechanistic and thermochemical understandings of the novel mixed-pot TTz reaction. These studies provide compelling evidence for a new mechanism previously unconsidered within the literature. Furthermore, kinetic and thermodynamic differences between products and probable intermediates are elucidated in a detailed reaction coordinate (RC) diagram. Combined with reaction studies under both aerobic and anaerobic conditions, the RC diagram provides insight into how thermodynamic control can be achieved so that the mixed-pot product distribution trends more favorably towards high a-TTz yields.

ACKNOWLEDGEMENTS

First, I would like to think my advisor, Dr. Michael G. Walter, for all of his kindness, insight, and encouragement. And a big thank you to my committee, as well, for all of their support, mentoring, and enlightening conversations. I'm also very grateful for all the members of the Walter Research Group for their company and assistance throughout the years. And I thank the Chemistry department as a whole for their help with instrumentation (special shout out to Dr. Adam Fessler and Dr. Carlin), their engaging lectures, and many interesting conversations.

Finally, I would like to thank my family and friends. My Mom and Dad have been extremely supportive, loving, and encouraging. My brothers, Kris and Jack, are always great company and ready to help with anything. My Aunt Mushi and Uncle Tom are great and welcoming people who are always there for me too. And my Grandma who has helped me so much and provides so much love. I couldn't have done it without any of them.

Table Of Contents

LIST OF TABLES

LIST OF FIGURES

LIST OF ABBREVIATIONS

A	acceptor
a	Onsager cavity radius
A_2-TTz	diacceptor thiazolothiazole
A-ArCHO	acceptor aromatic aldehyde
Abs	absorption
a-TTz	asymmetric thiazolothiazole
Bu_2N-PhCHO	4-(dibutylamino)benzaldehyde
Bu_2N-TTz-Py	2-(N,N-Dibutyl-4-aminophenyl)-5-(4-pyridyl)thiazolo[5,4-d]thiazole
c	speed of light
D	donor
D_2-TTz	didonor thiazolothiazole
D-ArCHO	donor aromatic aldehyde
DCM	dichloromethane
ddq	2,3-dichloro-5,6-dicyano-1,4-benzoquinone
DFT	density functional theory
DMF	dimethylformamide
Eem	energy of max emission
Eex	energy of max excitation
Em	emission
ext coeff	extinction coefficient
FBS	fetal bovine serum
FLIM	fluorescence lifetime imaging
GC-MS	gas chromatography-mass spectrometry
h	hour
h	Planck's constant
HEK	human embryonic kidney
HOMO	highest occupied molecular orbital
ICT	intramolecular charge transfer
I_{im}	Intensity value at intracellular membrane
I_{pm}	Intenisty value at plasma membrane
k_{nr}	nonradiative rate
k_r	radiative rate
LE	locally excited state
LED	light emitting diode
LUMO	lowest unoccupied molecular orbital
Me_2N-PhCHO	4-(dimethylamino)benzaldehyde

Me_2N-TTz-Py	2-(N,N-Dimethyl-4-aminophenyl)-5-(4-pyridyl)thiazolo[5,4-d]thiazole
MeTHF	2-methyltetrahydrofuran
NMR	nuclear magnetic resonance
OPV	organic photovoltaic
PBS	phosphate-buffer saline
Ph_2N-PhCHO	4-(diphenylamino)benzaldehyde
Ph_2N-TTz-CHO	2-(N,N-Diphenyl-4-aminophenyl)-5-(4-formylphenyl)thiazolo[5,4-d]thiazol
Ph_2N-TTz-COOH	2-(N,N-Diphenyl-4-aminophenyl)-5-(4-carboxyphenyl)thiazolo[5,4-d]thiazole
Ph_2N-TTz-Py	2-(N,N-Diphenyl-4-aminophenyl)-5-(4-pyridyl)thiazolo[5,4-d]thiazole
PL	photoluminescence
PPV	p-phenylenevinylene
PyCHO	4-pyridinecarboxaldehyde
QY	quantum yield
RA	rubeanic acid (AKA dithiooxamide)
ROI	regions of interest
RT	room temperature
SS	Stokes shift
Std.	standard
TCSPC	time-correlated single photon counting
THF	tetrahydrofuran
TLC	thin layer chromatography
TTz	thiazolo[5,4-d]thiazole
VSD	voltage sensitive dye
Δf	polarizability factor
$\Delta F/F$	fractional change in fluorescence
$\Delta\mu$	change in dipole moment
ε	molar extinction coefficient
ε_0	vacuum permittivity
η	refractive index
λ_{max}	wavelength of max absorbance
μ	ground state dipole
μ^*	excited state dipole
ν_a	wavenumber of absorbance
ν_f	wavenumber of emission
τ_F	fluorescence lifetime

Φ_F	fluorescence quantum yield

CHAPTER 1: Introduction

1.1 Thiazolo[5,4-d]thiazoles (TTzs)

Thiazolo[5,4-d]thiazoles (TTzs) are planar, bicyclic heteroaromatic compounds whose unique molecular structure afford them a suite of highly desirable photophysical and electronic properties.[1-3] For example, the conjugated, highly rigid molecular structure of TTzs well supports large fluorescence quantum yields,[4] efficient electronic communication,[5] and fast hole mobilities.[6] Furthermore, TTzs (and thiazoles too) demonstrate not only high thermal stability, but also high oxidative stability as well - a key advantage over thienothiophenes.[7-9] Consequently, TTz research has increased dramatically since their first accurate and complete characterization by Johnson and Ketcham in the early 1960's (see Ephraim 1891 for first ever reported synthesis - inaccurately characterized).[10] Since that time, TTzs have been widely used in various sensing applications (e.g. metal sensing[11] and biological sensing[12]), as the anolyte in redox flow batteries,[13] and, most prevalently, in semiconductor applications (e.g. organic photovoltaics[14-16] and field effect transistors[17, 18]). Additionally, their ease of tunability make them well suited for directly and/or post-synthetically forming conjugated bridges within various structural motifs including both symmetric[19] and asymmetric[20] small molecules, polymer backbones,[21] and as the struts of metal organic frameworks (MOFs)[22, 23] and covalent organic frameworks (COFs)[24].

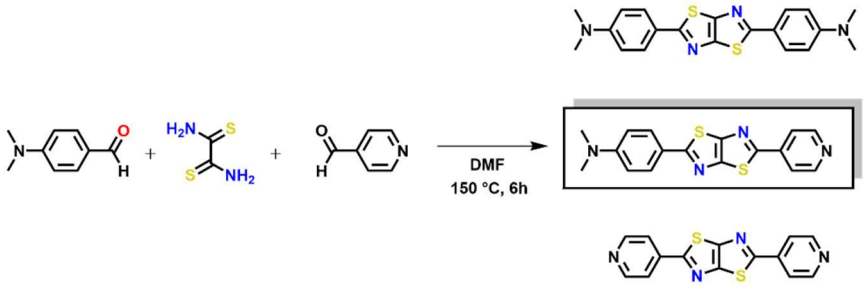

Figure 1.1. Example of a mixed-pot TTz reaction with donor-acceptor functionality.

With respect to its synthesis, TTzs have been accessed through various synthetic routes, albeit most of the diversity comes from relatively old patents.[25-31] Within academic literature, however, TTzs have been synthesized almost exclusively via a double condensation and subsequent oxidation reaction between an aromatic aldehyde and dithiooxamide in DMF at reflux for 4+ hours.[16] High temperatures and long reaction times are required due to the poor nucleophilicity of thioamides and the poor electrophilicity of most aromatic aldehydes, thus resulting in only moderate yields a majority of the time. And because isolation of an aminomercaptothiazole intermediate is unfeasible, asymmetric TTzs are most commonly made from the post-modification of an initially symmetric TTz[32] (e.g. monohalogenation/monodeprotection followed by Stille,[33] Sonogashira,[34] or Suzuki[35-38] coupling). However, not only do these post-synthetic coupling routes require multiple purification steps, but they are also nonselective and give low overall yields.

An alternative method to post-synthetic modification of a symmetric TTZ is the direct synthesis of an asymmetric TTz.[39] This strategy is accomplished via a mixed-pot synthesis of 2 or more aromatic aldehydes. The benefit of this method is that the asymmetric TTz is accessed immediately after a single reaction and purification step, whereas a post-synthetic modification strategy introduces more complexity. Although direct synthesis of an asymmetric TTz is a feasible route, only one such example exists within the literature, and its treatment in the study is little more than cursory and warrants further study. Examples of directly synthesized, asymmetric TTzs most likely remain scant within the literature due to issues involving a distribution of major products, thus leading to low yields. However, post-synthetic methods already demonstrate low overall yields, and so, the synthesis of simple asymmetric TTzs via a mixed-pot condensation/oxidation reaction can be a preferred way to access asymmetric TTzs, especially if yields reach parity.

1.2 Fluorophores, environmental effects, and asymmetry

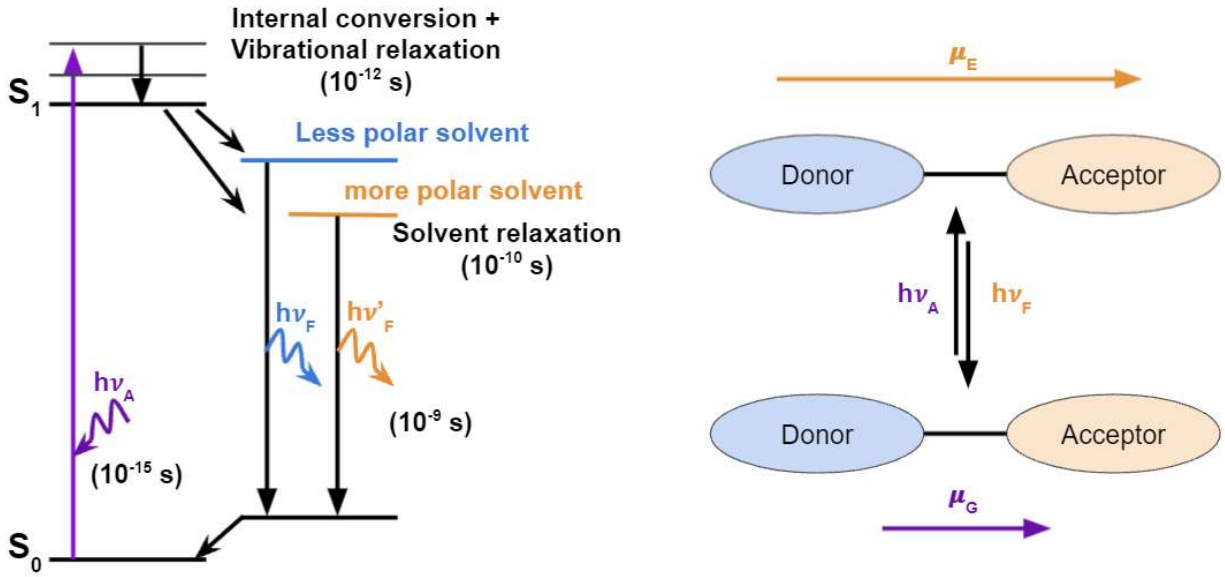

Figure 1.2. Jablonski diagram (left) and figure demonstrating how highly polar compounds with electron donating and accepting moieties can have much larger dipoles in their excited state (μ_E) than in their ground state (μ_G).

The design and optimization of small molecule fluorophores is critically important for fluorescence spectroscopy, and enables a wide array of chemical and biological sensing applications.[40] Examples include highly sensitive detection of ions[41-44] or toxins[45] and the measurement of various cellular processes (e.g. protein folding, biomolecular diffusion, polarization events). In regard to fluorescent sensors, one commonly exploited photophysical phenomenon is the environmental dependence of emission wavelengths. The Stokes shift, quantum yields, and fluorescence lifetimes of a fluorophore can be highly sensitive to the surrounding environment, which includes solvent polarity, aggregation, and/or binding interactions. This is because the fluorescence lifetime of a molecule is typically longer than external nuclear rearrangement (e.g. solvent relaxation), and so the excited state can interact with and be stabilized by the dipoles of surrounding molecules (**Figure 1.2**). And the more polar the solvent, the stronger the stabilizing effect. Likewise, the more polar the excited state of the fluorophore, the more

strongly it interacts with surrounding molecules. And a fluorophore's dipole moment is typically increased upon excitation. In other words, a fluorophore's environmental sensitivity is strongly correlated to the magnitude of its excited state dipole. As such, many fluorophores are designed with a high degree of electronic asymmetry. This is typically accomplished by situating a π-conjugated aromatic bridge between chemical functionalities with highly different mesomeric effects (electron donating vs withdrawing). The structural motif of these donor-π-acceptor (D-π-A) fluorophores facilitates intramolecular charge-transfer (ICT) properties in the excited state, thus enhancing their overall environmental sensitivity and sensing efficacy.[46-48] Shown in **Figure 1.3**, is one such D-π-A (Bu_2N-TTz-Py) demonstrating strong solvatofluorochromism (**Chapter 1**).

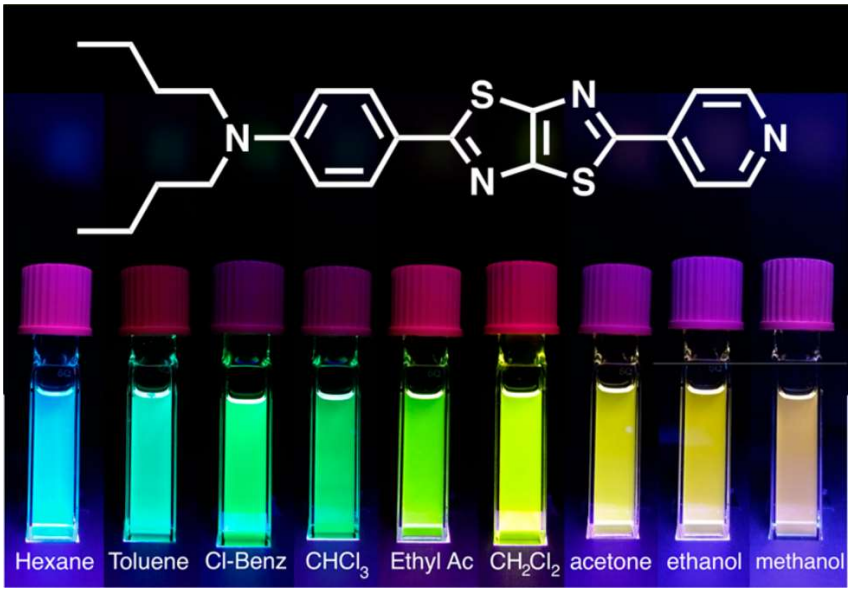

Figure 1.3. D-π-A fluorophore, Bu_2N-TTz-Py, demonstrating positive solvatofluorochromism.

1.3 Transmembrane voltage and voltage sensitive dyes

Cells experience rapidly changing electrical fields across their membranes (both extra- and intra- cellular) due to intentionally manufactured ion gradients.[49] This transmembrane voltage corresponds to cellular communication and homeostasis, thus belying many key cellular events including differentiation, apoptosis, and gene expression. As a result, the development of methods

capable of measuring the transmembrane voltage has received significant attention in the fields of medicine and neurobiology. Traditionally, the transmembrane voltage (V_M) has been measured electrophysiologically which requires the insertion of invasive electrodes and pipets.[50] As a consequence, electrophysiological measurements involving multiple cells and/or subcellular regions are time consuming, if not impossible. Although difficult to perform on multiple cells simultaneously, electrophysiological measurements benefit from high sensitivity and temporal resolution.[51]

It has been shown that optical imaging can also be used to measure V_M, thus allowing measurements that are less invasive and more easily capable of tracking multicellular dynamics.[52] Optical imaging utilizes luminescent dyes capable of either directly or indirectly measuring V_M, and can be classified into two categories: 1.) slow response dyes, and 2.) fast response dyes. Slow response dyes typically rely on a combination of transient ion movement and Forster Resonance Energy Transfer (FRET). Consequently, slow response-dyes are highly sensitive yet only indirectly measure V_M via slow-moving ions, and thus have low temporal resolutions and high subthreshold voltages. In effect, slow-response dyes are largely incapable of probing dynamic, ensemble cellular events.[53]

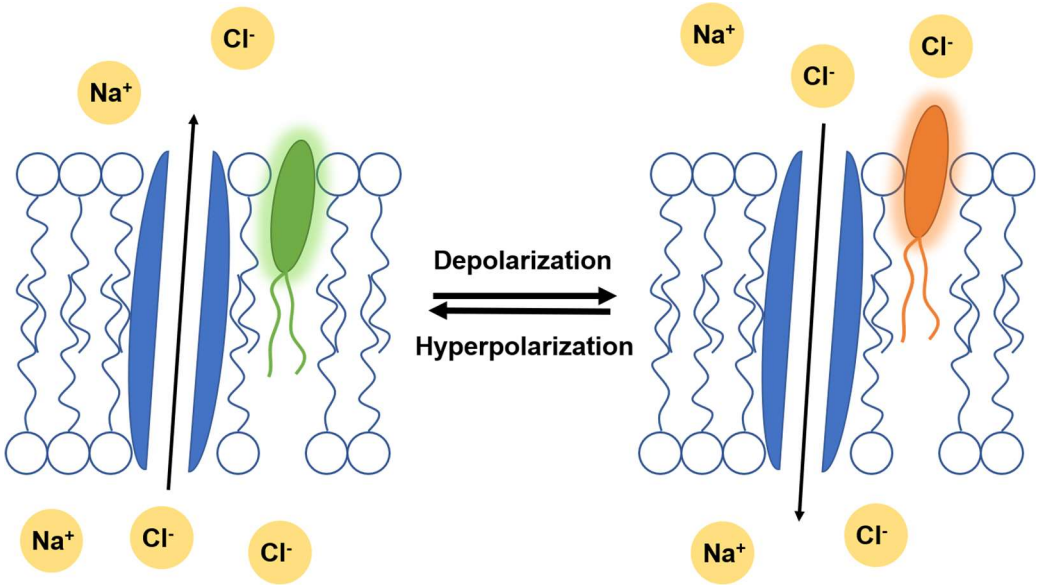

Figure 1.4. Intercalated fast-response dye changing color in response to cellular polarization events.

Fast-response dyes, on the other hand, directly probe V_M using intramolecular energy transfer mechanisms which are sensitive to electronic fields (e.g. intramolecular charge transfer (ICT) and photoelectron transfer (PeT)). Opposite to slow-response dyes, fast-response dyes have high temporal resolutions and low subthreshold voltages yet have traditionally demonstrated low voltage sensitivities. Additionally, fast-response dyes have stringent signal-to-noise (S:N) requirements as they compete with autofluorescence and tissue absorption. This requires optical dyes to have excellent membrane staining, high photostability, high brightness, and wavelengths of excitation and emission which are transparent to biological tissue. Finally, dyes must also demonstrate low cytotoxicity, especially for in-vivo applications. Therefore, although they are fundamentally capable of simultaneous, multicellular measurements, fast-response dyes still require further optimization.

1.4 Dissertation Summary

This dissertation focuses on the synthesis, photophysical characterization, and sensing applications of asymmetric thiazolothiazoles (a-TTzs). In **Chapter 2**, a facile mixed-pot TTz

reaction is reported and shown to form asymmetric TTzs in one synthetic step. Four new D-π-A compounds are reported and shown to demonstrate strong solvatofluorochromism, large transition dipole moments, and high quantum yields in nonpolar solvents. These photophysical properties are proven to be desirable in sensing applications involving temperature, pH, and membrane voltage sensitivity. As part of determining their efficacy towards voltage sensing, Bu_2N-TTz-Py is shown to have good membrane localization, negligible cytotoxicity, promising voltage sensitivities, and photostabilities 4 times higher than comparable voltage sensitive dyes (VSDs).

Chapter 3 is a compilation of mechanistic and thermochemical reaction studies based on computational modeling and LC/PDA/ESI-MS analysis with respect to the a-TTz mixed-pot reaction introduced in **Chapter 2**. The goal is that by gaining a more fundamental understanding of the TTz reaction, its mechanism and thermochemistry can be exploited for better experimental design and higher yields. Regarding its mechanism, computation predicts, and experimental mass spectra (MS) corroborate, that the mechanism most likely proceeds through S-centered nucleophilic addition (NA) to form thioether intermediates. This contrasts with the currently accepted mechanism which is said to proceed via N-centered NA and form a diazomethine intermediate. Computational studies also predict that accepting moieties have a stabilizing effect on intermediates and products as compared to effects of donating moieties. Consequently, a-TTzs are predicted to be less thermodynamically stable than acceptor symmetric TTzs (A_2-TTz), but more stable than donor symmetric TTzs (D_2-TTz). And according LC/PDA/ESI-MS analysis of the Py_2-TTz reaction under anaerobic conditions, TTz formation is reversible. This is important because it suggests that anaerobic conditions may give thermodynamic control over the reaction whereby experimental parameters (e.g. reactant ratios) can be optimized to obtain high a-TTz yields.

Chapter 4 is focused on developing a second generation of a-TTz VSDs with better voltage sensitives, water-solubility, and selectivity. Reported are the syntheses of a pyridinium a-TTz with quaternary ammonium functionality [Me_2N-TTz-Py(NPr)] and, separately, a click a-TTz with alkynyl functionality (Figure 1.5). Both syntheses were monitored via LC/PDA/ESI-MS. SN_2 alkylation of Me_2N-TTz-Py with a haloalkane to form Me_2N-TTz-Py(NPr) was attempted, but PDA and mass spectra provided no conclusive evidence that the reaction was successful. An alternative route whereby alkylation precedes TTz formation proved more successful. Regarding the click-TTz, reported is the successful synthesis of an a-TTz pentynyl ester via mixed-pot condensation.

Lastly, **Chapter 5** concludes with a summary of work done and recommendations for future research concerning the optimization of synthetic efforts and voltage sensing efficacy of a-TTz VSDs.

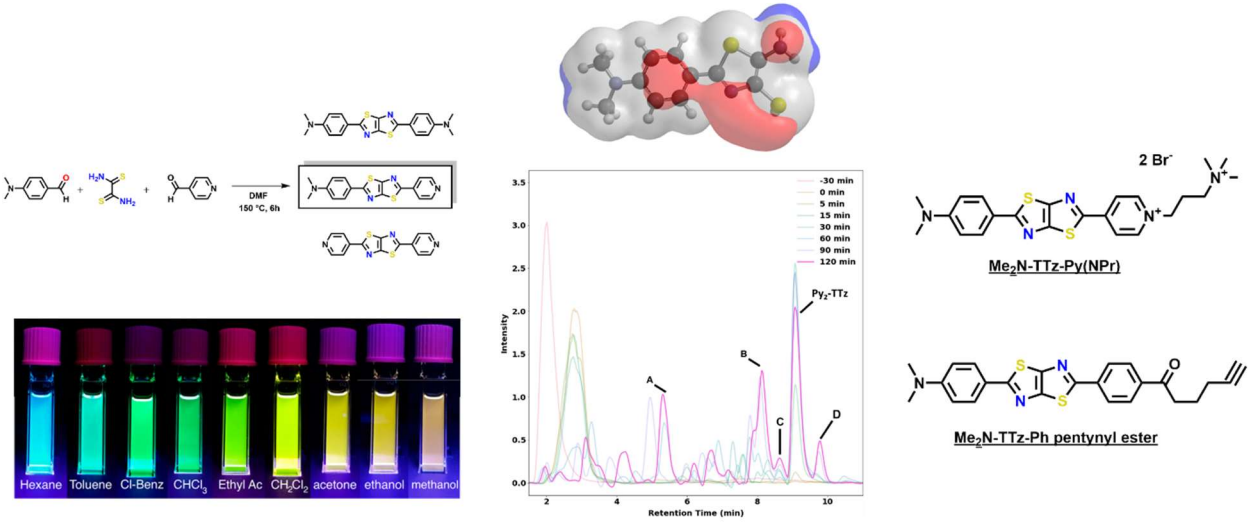

Figure 1.5. Visual chapter summary.

1.5 References

1. Johnson, J. R.; Ketcham, R., Thiazolothiazoles. I. The Reaction of Aromatic Aldehydes with Dithioöxamide1. *Journal of the American Chemical Society* **1960,** *82* (11), 2719-2724.

2. Papernaya, L. K.; Shatrova, A. A.; Sterkhova, I. V.; Levkovskaya, G. G.; Rozentsveig, I. B., Microwave-assisted synthesis of 2,5-diarylthiazolo[5,4-d]thiazoles from benzaldehydes and dithiooxamide. *Russian Journal of Organic Chemistry* **2015,** *51* (3), 373-377.

3. Reginato, G.; Calamante, M.; Dessì, A.; Mordini, A.; Peruzzini, M.; Zani, L., Cross-coupling reactions: Some applications to the synthesis of thiazolothiazole- and benzobisthiazole-based dyes for new generation solar cells (DSSC). *Journal of Organometallic Chemistry* **2014,** *771*, 117-123.

4. Woodward, A. N.; Kolesar, J. M.; Hall, S. R.; Saleh, N.-A.; Jones, D. S.; Walter, M. G., Thiazolothiazole Fluorophores Exhibiting Strong Fluorescence and Viologen-Like Reversible Electrochromism. *J. Am. Chem. Soc.* **2017,** *139* (25), 8467-8473.

5. Shi, Q. Q.; Fan, H. J.; Liu, Y.; Hu, W. P.; Li, Y. F.; Zhan, X. W., Synthesis of Copolymers Based on Thiazolothiazole and Their Applications in Polymer Solar Cells. *The Journal of Physical Chemistry C* **2010,** *114* (39), 16843-16848-16848.

6. Umeyama, T.; Hirose, K.; Noda, K.; Matsushige, K.; Shishido, T.; Saarenpaa, H.; Tkachenko, N. V.; Lemmetyinen, H.; Ono, N.; Imahori, H., Donor-Acceptor Alternating Copolymer Based on Thermally Converted Isothianaphthene Dimer and Thiazolothiazole Subunits. *The Journal of Physical Chemistry C* **2012,** *116* (33), 17414-17423-17423.

7. Johnson, J. R.; Rotenberg, D. H.; Ketcham, R., Thiazolothiazoles. II. Parent heterocycle and its carboxylic and amino derivatives. *J. Am. Chem. Soc.* **1970,** *92* (13), 4046-4050.

8. Osaka, I.; Zhang, R.; Liu, J.; Smilgies, D.-M.; Kowalewski, T.; McCullough, R. D., Highly Stable Semiconducting Polymers Based on Thiazolothiazole. *Chem. Mater.* **2010,** *22* (14), 4191-4196.

9. Saito, M.; Osaka, I.; Suzuki, Y.; Takimiya, K.; Okabe, T.; Ikeda, S.; Asano, T., Highly Efficient and Stable Solar Cells Based on Thiazolothiazole and Naphthobisthiadiazole Copolymers. *Sci. Rep.* **2015,** *5*, 14202.

10. Ephraim, J., Ueber die Einwirkung von Aldehyden auf Thioamide I. *Berichte der deutschen chemischen Gesellschaft* **1891,** *24* (1), 1026-1031-1031.

11. Jung, J. Y.; Kang, M.; Chun, J.; Lee, J.; Kim, J.; Kim, Y.; Kim, S. J.; Lee, C.; Yoon, J., A thiazolothiazole based Cu2+ selective colorimetric and fluorescent sensor via unique radical formation. *Chemical Communications* **2001,** *49* (2), 176-178-178.

12. Roy, I.; Bobbala, S.; Zhou, J.; Nguyen, M. T.; Nalluri, S. K. M.; Wu, Y.; Ferris, D. P.; Scott, E. A.; Wasielewski, M. R.; Stoddart, J. F., ExTzBox: A Glowing Cyclophane for Live-Cell Imaging. *Journal of the American Chemical Society* **2018,** *140* (23), 7206-7212-7212.

13. Luo, J.; Hu, B.; Debruler, C.; Liu, T. L., A π-Conjugation Extended Viologen as a Two-Electron Storage Anolyte for Total Organic Aqueous Redox Flow Batteries. *Angewandte Chemie International Edition* **2018,** *57* (1), 231-235.

14. Earmme, T.; Hwang, Y.-J.; Murari, N. M.; Subramaniyan, S.; Jenekhe, S. A., All-Polymer Solar Cells with 3.3% Efficiency Based on Naphthalene Diimide-Selenophene Copolymer Acceptor. *Journal of the American Chemical Society* **2013,** *135* (40), 14960-14963.

15. Li, Y., Molecular Design of Photovoltaic Materials for Polymer Solar Cells: Toward Suitable Electronic Energy Levels and Broad Absorption. *Accounts of Chemical Research* **2012,** *45* (5), 723-733.

16. Reginato, G.; Mordini, A.; Zani, L.; Calamante, M.; Dessì, A., Photoactive Compounds Based on the Thiazolo[5,4-d]thiazole Core and Their Application in Organic and Hybrid Photovoltaics. *European Journal of Organic Chemistry* **2016,** *2016* (2), 233-251.

17. Lim, D. H.; Jang, S. Y.; Kang, M.; Lee, S.; Kim, Y. A.; Heo, Y. J.; Lee, M. H.; Kim, D. Y., A systematic study on molecular planarity and D-A conformation in thiazolothiazole- and thienylenevinylene-based copolymers for organic field-effect transistors. *Journal of Materials Chemistry C* **2017,** *5* (39), 10126-10132-10132.

18. Osaka, I.; Sauve, G.; Zhang, R.; Kowalewski, T.; McCullough, R. D., Novel thiophene-thiazolothiazole copolymers for organic field-effect transistors. *Advanced Materials* **2007,** *19* (23), 4160-+-+.

19. Dutta, P.; Park, H.; Lee, W.-H.; Kang, I.-N.; Lee, S.-H., A crystalline D-π-A organic small molecule with naphtho[1,2-b:5,6-b′]dithiophene-core for solution processed organic solar cells. *Organic Electronics* **2012,** *13* (12), 3183-3194.

20. Zani, L.; Reginato, G.; Mordini, A.; Calamante, M.; Peruzzini, M.; Taddei, M.; Sinicropi, A.; Parisi, M. L.; Biani, F. F. d.; Basosi, R.; Cavallaro, A.; Bruzzi, M., An unusual thiazolo[5,4-d]thiazole sensitizer for dye-sensitized solar cells. *Tetrahedron Letters* **2013,** *54* (30), 3944-3948.

21. Zhang, M. J.; Sun, Y. P.; Guo, X.; Cui, C. H.; He, Y. J.; Li, Y. F., Synthesis and Characterization of Dioctyloxybenzo 1,2-b:4,3-b ' -dithiophene-Containing Copolymers for Polymer Solar Cells. *Macromolecules* **2011,** *44* (19), 7625-7631-7631.

22. Rizzuto, F. J.; Faust, T. B.; Chan, B.; Hua, C.; D'Alessandro, D. M.; Kepert, C. J., Experimental and Computational Studies of a Multi-Electron Donor–Acceptor Ligand Containing the Thiazolo[5,4-d]thiazole Core and its Incorporation into a Metal–Organic Framework. *Chemistry - A European Journal* **2014,** *20* (52), 17597-17605.

23. Khatun, A.; Panda, D.; Sayresmith, N.; Walter, M.; Saha, S., Thiazolothiazole-Based Luminescent Metal–Organic Frameworks with Ligand-to-Ligand Energy Transfer and Hg2+ Sensing Capabilities. *Inorganic Chemistry* **2019**.

24. Biswal, B. P.; Vignolo-González, H. A.; Banerjee, T.; Grunenberg, L.; Savasci, G.; Gottschling, K.; Nuss, J.; Ochsenfeld, C.; Lotsch, B. V., Sustained Solar H2 Evolution from a Thiazolo[5,4-d]thiazole-Bridged Covalent Organic Framework and Nickel-Thiolate Cluster in Water. *Journal of the American Chemical Society* **2019,** *141* (28), 11082-11092-11092.

25. Beck, G.; Heitzer, H.; Holtschmidt, H. dichlorothiazolothiazole from dichloro iminie. 1976.

26. Beck, G.; Holtschmidt, H. dichlorothiazolothiazole from chloroisocyanide. 1974.

27. Roethling, T.; Polanek, M.; Hansen, P.; Kibbel, H.; Naumann, K.; Thust, U. thiazolothiazole from imine. DD216241, 1984.

28. Roethling, T.; Schroeder, A.; Kibbel, H.; Kochmann, W.; Naumann, K. Thiazolothiazole. DD208354, 1984.

29. Roethling, T.; Schroeder, A.; Kibbel, H.; Kochmann, W.; Naumann, K. arylalkyl-thiazolothiazole. DD210457, 1984.

30. Roethling, T.; Schroeder, A.; Kibbel, H.; Kochmann, W.; Naumann, K. Thiazole thioester. DD210454, 1984.

31. Seybold, G.; Heinz, E., Bicyclen der Thiazol- und Isothiazolreihe. *LIEBIGS ANNALEN DER CHEMIE* **1979,** *1979* (9), 1271-1446.

32. Benin, V.; Yeates, A. T.; Dudis, D., Preparation of halogenated derivatives of thiazolo[5,4-d]thiazole via direct electrophilic aromatic substitution. *Journal of Heterocyclic Chemistry* **2008,** *45* (3), 811-819.

33. Van Mierloo, S.; Vasseur, K.; Van den Brande, N.; Boyukbayram, A. E.; Ruttens, B.; Rodriguez, S. D.; Botek, E.; Liégeois, V.; D'Haen, J.; Adriaensens, P. J.; Heremans, P.; Champagne, B.; Van Assche, G.; Lutsen, L.; Vanderzande, D. J.; Maes, W., Functionalized Dithienylthiazolo[5,4-d]thiazoles For Solution-Processable Organic Field-Effect Transistors. *ChemPlusChem* **2012,** *77* (10), 923-930-930.

34. Ziessel, R.; Nano, A.; Heyer, E.; Bura, T.; Retailleau, P., Rational Design of New Thiazolo□Thiazole Dyes as Input Energy Units in Molecular Dyads. *Chemistry - A European Journal* **2013,** *19* (8), 2582-2588.

35. Dessi, A.; Consiglio, G. B.; Calamante, M.; Reginato, G.; Mordini, A.; Peruzzini, M.; Taddei, M.; Sinicropi, A.; Parisi, M. L.; Biani, F. F. d.; Basosi, R.; Mori, R.; Spatola, M.; Bruzzi, M.; Zani, L., Organic Chromophores Based on a Fused Bis-Thiazole Core and Their Application in Dye-Sensitized Solar Cells. *European Journal of Organic Chemistry* **2013,** *2013* (10), 1916-1928-1928.

36. Nazim, M.; Ameen, S.; Akhtar, M. S.; Seo, H. K.; Shin, H. S., Novel liquid crystalline oligomer with thiazolothiazole-acceptor for efficient BHJ small molecule organic solar cells. *Synthetic Metals* **2014,** *187*, 178-184-184.

37. Zani, L.; Reginato, G.; Mordini, A.; Calamante, M.; Peruzzini, M.; Taddei, M.; Sinicropi, A.; Parisi, M. L.; Biani, F. F. d.; Basosi, R.; Cavallaro, A.; Bruzzi, M., An unusual thiazolo 5,4-d thiazole sensitizer for dye-sensitized solar cells. *Tetrahedron Letters* **2013,** *54* (30), 3944-3948-3948.

38. Zhang, W.; Feng, Q.; Wang, Z.-S.; Zhou, G., Novel Thiazolo[5,4-d]thiazole-Based Organic Dyes for Quasi-Solid-State Dye-Sensitized Solar Cells. *Chemistry – An Asian Journal* **2013,** *8* (5), 939-946-946.

39. Knighton, R. C.; Hallett, A. J.; Kariuki, B. M.; Pope, S. J. A., A one-step synthesis towards new ligands based on aryl-functionalised thiazolo[5,4-d]thiazole chromophores. *Tetrahedron Letters* **2010,** *51* (41), 5419-5422.

40. Lakowicz, J. R., *Principles of Fluorescence Spectroscopy*. Springer: Baltimore, 2006.

41. Kumar, M.; Kumar, A.; Singh, M. K.; Sahu, S. K.; John, R. P., A novel benzidine based Schiff base "turn-on" fluorescent chemosensor for selective recognition of Zn2+. *Sensor Actuat B-Chem* **2017,** *241*, 1218-1223.

42. Liu, Z.; He, W.; Guo, Z., Metal coordination in photoluminescent sensing. *Chem. Soc. Rev.* **2013,** *42* (4), 1568-1600.

43. Yang, Y.-S.; Ma, C.-M.; Zhang, Y.-P.; Xue, Q.-H.; Ru, J.-X.; Liu, X.-Y.; Guo, H.-C., A highly selective "turn-on" fluorescent sensor for zinc ion based on a cinnamyl pyrazoline derivative and its imaging in live cells. *Anal. Methods* **2018,** *10* (16), 1833-1841.

44. Narayanaswamy, N.; Chakraborty, K.; Saminathan, A.; Zeichner, E.; Leung, K.; Devany, J.; Krishnan, Y., A pH-correctable, DNA-based fluorescent reporter for organellar calcium. *Nature Methods* **2019,** *16* (1), 95-102.

45. Yang, X.; He, L.; Xu, K.; Yang, Y.; Lin, W., The development of an ICT-based formaldehyde-responsive fluorescence turn-on probe with a high signal-to-noise ratio. *New J. Chem.* **2018,** *42* (15), 12361-12364.

46. Zhu, L.; Younes, A. H.; Yuan, Z.; Clark, R. J., 5-Arylvinylene-2,2′-bipyridyls: Bright "push–pull" dyes as components in fluorescent indicators for zinc ions. *J. Photoche. Photobiol., A: Chem.* **2015,** *311*, 1-15.

47. Kucherak, O. A.; Didier, P.; Mély, Y.; Klymchenko, A. S., Fluorene Analogues of Prodan with Superior Fluorescence Brightness and Solvatochromism. *J. Phys. Chem. Lett.* **2010,** *1* (3), 616-620.

48. Niko, Y.; Kawauchi, S.; Konishi, G.-i., Solvatochromic Pyrene Analogues of Prodan Exhibiting Extremely High Fluorescence Quantum Yields in Apolar and Polar Solvents. *Chem. Eur. J.* **2013,** *19* (30), 9760-9765.

49. Membrane Potential Imaging in the Nervous System, Methods and Applications. 2010.

50. Woodford, C. R.; Frady, P. E.; Smith, R. S.; Morey, B.; Canzi, G.; Palida, S. F.; Araneda, R. C.; Kristan, W. B.; Kubiak, C. P.; Miller, E. W.; Tsien, R. Y., Improved PeT Molecules for Optically Sensing Voltage in Neurons. *Journal of the American Chemical Society* **2015,** *137* (5), 1817-24.

51. Kulkarni, R. U.; Miller, E. W., Voltage Imaging: Pitfalls and Potential. *Biochemistry* **2017,** *56* (39), 5171-5177.

52. Kuhn, B.; Fromherz, P., Anellated Hemicyanine Dyes in a Neuron Membrane: Molecular Stark Effect and Optical Voltage Recording. *The Journal of Physical Chemistry B* **2003,** *107* (31), 7903-7913.

53. Miller, E. W.; Lin, J. Y.; Frady, P. E.; Steinbach, P. A.; Kristan, W. B.; Tsien, R. Y., Optically monitoring voltage in neurons by photo-induced electron transfer through molecular wires. *Proceedings of the National Academy of Sciences* **2012,** *109* (6), 2114-2119.

CHAPTER 2: Synthesis, photophysical characterization, and sensing applications of first generation asymmetric thiazolothiazoles

2.1 ABSTRACT

A family of asymmetric thiazolo[5,4-d]thiazole (TTz) fluorescent dye sensors have been developed and their photophysical sensing properties are reported. The π-conjugated, TTz-bridged compounds are synthesized via a single-step, double condensation/oxidation of dithiooxamide and two different aromatic aldehydes: one with strong electron donating characteristics and one with strong electron accepting characteristics. The four reported dyes include electron donating moieties (N,N dibutylaniline and N,N diphenylaniline) matched with three different electron accepting moieties (pyridine, benzoic acid, and carboxaldehyde). The asymmetric TTz derivatives exhibit strong solvatofluorochromism with Stokes shifts between 2270 and 6050 cm^{-1} and transition dipole moments ($\Delta\mu$ = 13 – 18 D) that are among the highest reported for push-pull dyes. Fluorescence quantum yields are as high as 0.93 in nonpolar solvents and the fluorescence lifetimes (τ_F) vary from 1.50 to 3.01 ns depending on the solvent polarity. In addition, thermofluorochromic studies and spectrophotometric acid titrations were performed and indicate the possibility of using these dyes as temperature and/or acid sensors. In vitro cell studies indicate good cell membrane localization, insignificant cytotoxicity, promising voltage sensitivities, and photostabilities that are 4 times higher than comparable dyes. Their ease of synthesis and purification, remarkable photophysical properties, and chemically sensitive TTz π-bridge make these asymmetric dye derivatives attractive for environmental and biological sensing or similar molecular optoelectronic applications.

2.2 INTRODUCTION

Small molecule fluorophores are attractive molecular tools for environmental sensing applications and biosensing/bioimaging techniques due to their high microenvironmental sensitivity, selectivity, and temporal resolution.[1] Fluorescent molecules can either turn on/off their fluorescence or chromically shift their emission through the binding or interaction of various metal ions,[2-5] reactive oxygen species,[6] organic toxins,[7] or cell organelles/membranes;[8, 9] and can greatly enhance cell fluorescence microscopic imaging.[10] Molecular sensors with large fluorescence Stokes shifts are advantageous for these applications due to a low overlap between excitation and emission.[8]

A large majority of these molecular derivatives are designed with push-pull (electron withdrawing and donating) functional groups positioned at either ends of a π-conjugated aromatic core, which facilitates intramolecular charge-transfer (ICT) properties in the excited state.[11-13] Such push-pull dyes typically exhibit strong solvatofluorochromism and high environmental sensitivity as a result of the spatially separated and strengthened excited-state dipole.[14, 15] New push-pull fluorophore discoveries in this field are driven by efforts to enhance ICT character, and therefore, increase their efficacy for monitoring molecular interactions, processes, and other events which require high specificity and environmental sensitivity.

Highly fluorescent, thiazolo[5,4-d]thiazole (TTz) chromophores have recently emerged as an important class of multifunctional heterocyclic compounds.[16-19] Molecular materials containing the fused, bicyclic thiazole backbone have exhibited strong fluorescence and electrofluorochromism,[16] and have been used in a variety of applications such as light-harvesting dyes in photovoltaics,[20-25] redox flow batteries,[17] and molecular sensors.[19, 26] Additionally, polymers incorporating the TTz moiety exhibit efficient electronic communication for organic

field-effect transistors with high free charge carrier mobility and good optoelectronic tunability.[27-30] The rigidity of the TTz structure is especially attractive for molecular optoelectronics due to their high thermo-oxidative and photochemical stability.[25, 30] Surprisingly, there have been very few reports of asymmetric TTz materials even though there exists a high demand for tunable, push-pull, small molecular systems that can be incorporated into a conjugated polymer backbone, or also for use in molecular sensing applications. This is especially relevant for asymmetric dyes that have shown promising photophysical properties as light harvesting dyes in small molecule solar cells.[23, 31-35] One challenge to the synthesis of asymmetric TTzs is the fact that the typical reaction pathway for forming the bicyclic heterocycle requires two, immediately sequential condensation steps, such that the isolation of the singly condensed intermediate is unfeasible. As a consequence, the introduction of asymmetry in most previously reported asymmetric TTzs have required the derivatization of an initially symmetric TTz using post-synthetic, low selectivity, mono-halogenation/mono-deprotection and Pd cross-coupling reactions.[23, 32, 34, 36-38] To emphasize, such routes towards asymmetric TTzs use multiple synthetic steps, require a similar number of purification procedures, and often result in low overall yields.

To address some of these issues, we have developed a new family of highly fluorescent, solvatofluorochromic, push-pull TTz compounds that can be accessed using a simple, single-step reaction (**Figure 2.1a**).

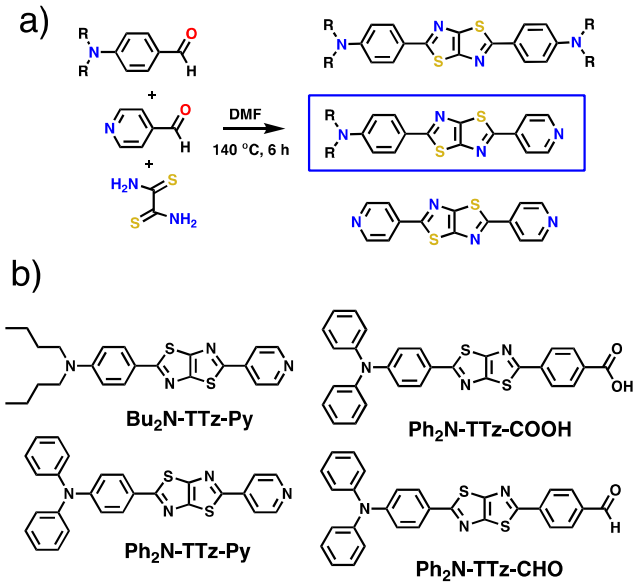

Figure 2.1. (a) Single step, synthetic reaction to form asymmetric TTz fluorophores and (b) the four asymmetric TTz compounds explored in this work

The synthetic strategy begins by heating two different, readily available aromatic aldehyde precursors with dithiooxamide resulting in one asymmetric and two symmetric TTz chromophores. Judicious selection of the aromatic aldehyde precursors yields in an amphiphilic asymmetric TTz whose fluorescence on a column is uniquely distinguishable and whose column retention is intermediate that of its symmetric counterparts. In this way, silica gel chromatography gives an easily identifiable asymmetric TTz band (yellow fluorescence) in the middle of two spatially distant symmetric TTz bands (both with blue fluorescence). Four push-pull asymmetric TTz compounds were obtained in this manner (Bu_2N-TTz-Py, Ph_2N-TTz-Py, Ph_2N-TTz-COOH, and Ph_2N-TTz-CHO – **Figure 2.1b**) containing various electron-donating groups (dibutylamino, diphenylamino) and electron-withdrawing groups (pyridine, benzoic acid, and carboxaldehyde). The unique structural features of these chromophores compared to similar push-pull compounds composed of hydrocarbons is the highly fluorescent, electron deficient, heterocyclic TTz bridge connecting the two asymmetric functional groups, whereby the lack of hydrogens in the TTz bridge allows for enhanced planarity by minimizing any steric effects typical of hydrocarbons.[9, 11-13] The

rigid, fused-thiazole, bicyclic aromatic structure provides thermo-oxidative stability and the increased planarity further enhances the electronic interactions across the dye.[16] This means that compared to typical hydrocarbon-based, fluorescent biological dyes, the TTz dyes presented herein demonstrate much larger Stokes shifts, enhanced absorption coefficients, and red-shifted absorption and emission.[39] In addition, the thiazolothiazole bicyclic ring system provides further chemical functionality in a compact, π-conjugated bridge. All these properties make asymmetric TTzs a synthetically simple, photochemically attractive, and novel class of dyes suitable for environmental and biological sensing.

2.3 EXPERIMENTAL METHODS

Materials and Instrumentation. 4-pyridine carboxaldehyde, 4-(dibutylamino)benzaldehyde, 4-(diphenylamino)benzaldehyde, terephthalaldehyde, dithiooxamide, and all solvents used for spectroscopic measurements were purchased from Sigma-Aldrich and used without further purification. ^{1}H and ^{13}C NMR measurements were obtained with either a JEOL 300 MHz NMR or a JEOL 500 MHz NMR. High resolution mass spectra were obtained using a ThermoFisher Scientific MSQ Plus Single Quadrupole Mass Spectrometer. Solution-state UV-Vis spectra were collected on a Cary 300 UV-Vis spectrophotometer. Time-resolved measurements were taken on a Jobin Yvon-Spex Fluorolog equipped with a 389 nm diode laser for time-resolved PL decay measurements. Igor Pro 6.3 software was used to fit PL(t) decay data to single/multiple exponential decays. Quantum yields were calculated using 9,10-diphenylanthracene as a reference (quantum yield [Φ_F] in cyclohexane = 0.97).[40, 41] Density functional theory (DFT) calculations were performed with Spartan computational software using B3LYP[42, 43] density functional and 6-31G*[44] basis set. Temperature studies were conducted using a 10 μM Bu_2N-TTz-Py MeTHF solution placed inside of a Norrell 502 NMR tube and sequentially

submerged in the following liquid N_2 baths: octanol (-16 ºC), acetonitrile (-41 ºC), acetone (-94 ºC), pentane (-131 ºC), MeTHF (-136 ºC), and liquid N_2 itself (-196 ºC). The phosphorescence spectrum of Bu_2N-TTz-Py (see S2) was collected similarly at -196 °C by pumping with 389 nm light while inside a liquid nitrogen bath and then probing the emission within 2 sec of removing from the bath. A single crystal suitable for analysis was mounted on an Agilent Gemini Ultra diffractometer and kept at 100(1) K during data collection. The structure was solved with the SHElXS structure solution program using direct methods and refined with the SHELX OLEX2 refinement packages.[45, 46] Human embryonic kidney cells (HEK 293T) were a kind gift from Prof. Bryan Dickinson, and Mouse macrophage J774A.1 cells were a kind gift from Prof. Deborah Nelson at the University of Chicago. Cells were cultured in Dulbecco's Modified Eagle's Medium (Invitrogen Corporation, USA) containing 10% heat inactivated Fetal Bovine Serum (FBS) (Invitrogen Corporation, USA), 100 U/mL penicillin, and 100 µg/mL streptomycin. Cells were maintained at 37 ºC under 5% CO_2.

Spectrophotometric acid titrations. Spectrophotometric acid titrations were measured on a 10 µM Bu_2N-TTz-Py $CHCl_3$ solution. The concentration of TTz was held constant by serially titrating with individually prepared stock solutions of 10 µM Bu_2N-TTz-Py in $CHCl_3$ containing increasing amounts of TFA at the following molar ratios of TFA to TTz (χ): 10:1, 10^3:1, and 10^6:1. The stock solution was made by simultaneous dilution using TFA volumes calculated as follows:

$$V_{TFA} = \chi * \left(\frac{[TTz]_0}{[TFA]_0} * V_{TTz}\right)$$

where V_{TFA} and V_{TTz} are the volumes and $[TFA]_0$ and $[TTz]_0$ are the concentrations of TFA and TTz, respectively. Care was taken to ensure that the desired χ and the chosen

concentrations and TTz volume result in a diluted TTz concentration ($[TTz]_1$) which was greater than or equal to the TTz concentration of the initial solution:

$$[TTz]_1 = \frac{[TTz]_0 * V_{TTz}}{(V_{TTz} + V_{TFA})} \geq 10\ \mu M$$

The volume of stock solution (V_S) required to prepare the i^{th}+1 titration was calculated using the following equation:

$$V_S = -V_i \left(\frac{c_{i+1} - c_i}{c_{i+1} - [TFA]_1} \right)$$

where $[TFA]_1$ is the concentration of TFA in the stock solution and V and c are the volume and concentration after the i^{th} titration.

Cell labeled spectral measurements. Excitation and emission spectra were collected by labeling the alveolar macrophage cell line J774.A1 (~ 0.5 x 10^5 cells) with 1 μM Bu_2N-TTz-Py in phosphate buffered saline (PBS) buffer and 0.1% TritonX-100. Cells were incubated with dye for 10 min at RT, washed thrice with PBS, and dispersed in a cuvette for fluorescent spectral measurements (Fluoromax-4, Horiba Scientific, Edison, NJ, USA). Excitation spectra were collected at 520 nm emission. Emission spectra were collected by exciting at 440 nm.

Electrophysiology. Whole cell voltage clamping measurements of 500 nM Bu_2N-TTz-Py labeled HEK 293T cells were performed with Axopatch 200A amplifier (Molecular Devices), digitized using an NI-6251 DAQ (National Instruments), and controlled using WinWCP software (Strathclyde Electrophysiology Software). Patch pipettes were pulled using a Sutter P-97 Micropipette puller. Patch pipettes with resistances between 5 - 10 MOhm were used in voltage clamping experiments. The patch pipette was positioned using an MP325 motorized manipulator (Sutter). Metamorph premier Ver. 7.8.12.0 was linked to an NI-6501 DAQ to enable voltage triggered image acquisition. Extracellular solution composition was 145 mM NaCl, 20 mM

glucose, 10 mM HEPES, pH 7.4, 3 mM KCl, 2 mM $CaCl_2$, 1 mM $MgCl_2$ (310 mOsm); and the intracellular solution composition was 115 mM potassium gluconate, 10 mM EGTA tetrapotassium salt, 10 mM HEPES, pH 7.2, 5 mM NaCl, 10 mM KCl, 2 mM ATP disodium salt (290 mOsm).

Microscopy. Imaging was carried out on an IX83 inverted microscope (Olympus Corporation of the Americas, Center Valley, PA, USA) using 100X, 1.4 NA, DIC oil immersion objective (PLAPON, Olympus) and an Evolve Delta 512 EMCCD camera (Photometrics, USA). Filter wheel, shutter, and CCD camera were controlled using Metamorph premier Ver 7.8.12.0 (Molecular Devices, LLC, USA). For photostability studies, HEK 293T cells were labeled with 500 nM Bu_2N-TTz-Py and illuminated continuously with ~5 W/cm^2 power light source, periodically acquiring images at 1 min interval. Bu_2N-TTz-Py channel images were obtained using 480/20 bandpass excitation filter, 575/40 bandpass emission filter and 89016 dichroic. VF2.1.Cl channel images were obtained using 500/20 bandpass excitation filter, 535/40 bandpass emission filter and 69002 dichroic. For CellMaskTM red, images were obtained using the 640/30 bandpass excitation filter, 705/72 bandpass emission filter and 89016 dichroic.

Cellular localization: Time-lapse imaging was performed to probe the membrane localization of Bu_2N-TTz-Py at longer time scale. HEK 293T cells were labelled with 500 nM Bu_2N-TTz-Py and a plasma membrane marker (IX CellMask^{TM} Red, Thermofisher) for 10 mins in 1X HBSS (Hank's balanced salt solution, Thermofisher). Excess unbound dyes were washed with 1X PBS and imaged after 30 mins incubation in 1X HBSS. The membrane localized Bu_2N-TTz-Py and CellMask^{TM} Red were sequentially imaged every 20 mins. Intensity values at plasma membrane (I_{PM}) were calculated by drawing regions of interest (ROI) around the whole cell and subtracting intracellular intensity (I_{IM}, ROI drawn within the cell) for Bu_2N-TTz-Py and CellMask

images, respectively. The normalized intensity ratio of Bu_2N-TTz-Py to CellMask™ Red, at plasma membrane (I_{PM} ratio) and intracellular membrane (I_{IM} ratio), were plotted w.r.t. time.

Cytotoxicity: Cellular toxicity of voltage sensitive dyes was characterized using Annexin V-Cy5 (BioVision) staining of phosphatidylserine that are exposed to outer leaflet of plasma membrane during apoptosis. HEK 293T cells were labelled with 500 nM of indicated dyes for 15 mins, followed by incubation with Annexin V-Cy5 for 20 mins in dark and washed, fixed with 4% paraformaldehyde before imaging. As a positive control, unlabeled HEK cells were incubated at 65°C for 10 mins to induce apoptosis and stained with Annexin V-Cy5 as above. Cytotoxicity percentage is calculated as number of Annexin V-Cy5 positive cells to total number of nuclear stained cells. Number of cells quantification were performed using Analyze particle function of ImageJ program.

2-(N,N-dibutyl-4-aminophenyl)-5-(4-pyridyl) thiazolo[5,4-d]thiazole (Bu_2N-TTz-Py): 4-Pyridinecarboxaldehyde (1.3401 g, 12.511 mmol), dithiooxamide (1.0007 g, 8.3253 mmol), and 4-(dibutylamino)benzaldehyde (2.9108 g, 12.474 mmol) were mixed in 40 mL anhydrous DMF for 6 h at 120 °C. After refrigerating overnight, a brownish-yellow powder precipitate was collected via vacuum filtration and rinsed with DMSO and water (1.374 g). Using a 1:1 hexanes:chloroform mixture, 31.4 mg of the crude product was purified by silica gel column chromatography (Silica Flash M60). The eluent was removed under vacuum, thereby yielding a yellow solid (2.3 mg, 2.9%). **^{1}H NMR** (500 MHz, CD_3CN, δ): 8.67 (d, J = 5.05 Hz, 2H), 7.84 (d, J = 6.20 Hz, 2H), 7.79 (d, J = 9.15 Hz, 2H), 6.74 (d, J = 9.90 Hz, 2H). **^{13}C NMR** (126 MHz, DCM, protonated): 202.19, 197.48, 152.01, 142.06, 142.03. 141.96, 141.94, 129.87, 128.65, 121.66. **UV-Vis λ_{max} ($CHCl_3$, $M^{-1}cm^{-1}$):** 424 nm (ε = 17,700). **ESI-MS**: calcd for $C_{23}H_{27}N_4S_2^+$, 423.1677; found, 423.1659**.**

2-(N,N-diphenyl-4-aminophenyl)-5-(4-pyridyl) thiazolo[5,4-d]thiazole (Ph_2N-TTz-Py): 4-Pyridinecarboxaldehyde (0.2577 g, 2.406 mmol), dithiooxamide (0.2519 g, 2.0957 mmol), and 4-(diphenylamino)benzaldehyde (0.8634 g, 3.159 mmol) were mixed in 10 mL anhydrous DMF for 6 h at 120 °C. After sitting overnight, a brownish-yellow precipitate was collected via vacuum filtration and rinsed with water (0.3201 g). Using chloroform, 20.0 mg of the crude product was purified by silica gel column chromatography (Silica Flash M60). The eluent was removed under vacuum, thereby yielding a yellow solid (15.6 mg, 25.8%). **^{1}H NMR** (500 MHz, d-DMSO, δ): 8.72 (d, *J* = 5.48 Hz, 2H), 7.93 (d, *J* = 6.40 Hz, 2H), 7.89 (d, *J* = 8.70 Hz, 2H), 7.36 (m, 4H), 7.13 (m, 6H), 6.95 (d, *J* = 9.15 Hz, 2H). **^{13}C NMR** (126 MHz, DCM, protonated): 206.41, 152.86, 151.16, 150.83, 148.69, 148.63, 146.70, 129.61, 127.64, 126.21, 126.21, 125.76, 121.12, 120.28. **UV-Vis λ_{max} ($CHCl_3$, $M^{-1}cm^{-1}$):** 424 nm (ε = 46,400). **ESI-MS: calcd for $C_{27}H_{19}N_4S_2^+$, 463.1051; found, 463.0524.**

2-(N,N-diphenyl-4-aminophenyl)-5-(4-carboxyphenyl) thiazolo[5,4-d]thiazole (Ph_2N-TTz-COOH): 4-Formylbenzoic acid (0.3774 g, 2.514 mmol), dithiooxamide (0.2002 g, 1.666 mmol), and 4-(diphenylamino)benzaldehyde (0.6820 g, 2.495 mmol) were mixed in 16 mL anhydrous DMF for 6 h at 120 °C. The reaction mixture was cooled overnight, whereby a brownish-yellow solid precipitated out of solution. The precipitate was collected via vacuum filtration and rinsed with water (0.7044 g). Using chloroform, 21.7 mg of the precipitate was purified by silica gel column chromatography (Silica Flash M60). A yellow solid (6.3 mg, 24.3%) was collected after chromatographic separation. **^{1}H NMR** (500 MHz, d-DMSO, δ): 8.10 (d, *J* = 8.70 Hz, 2H), 8.05 (d, *J* = 8.70 Hz, 2H), 7.88 (d, *J* = 8.70 Hz, 2H), 7.37 (m, 4H), 7.14 (m, 6H), 6.96 (d, J = 8.70 Hz, 2H). **^{13}C NMR** (126 MHz, DCM): 203.15, 146.97, 146.79, 144.46, 144.02, 136.09, 132.34, 130.33, 129.59, 127.47, 126.62, 125.66, 124.34, 122.90, 12132. **UV-Vis λ_{max}**

($CHCl_3$, $M^{-1}cm^{-1}$): 424 nm (ε = 13,900). **ESI-MS: calcd for $C_{29}H_{19}N_3O_2S_2$, 505.0919; found, 505.0991.**

2-(N,N-diphenyl-4-aminophenyl)-5-(4-formylphenyl) thiazolo[5,4-d]thiazole (Ph_2N-TTz-CHO): Terephthalaldehyde (0.3343 g, 2.49 mmol), dithiooxamide (0.2007 g, 1.67 mmol), and 4-(Diphenylamino)benzaldehyde (0.6824 g, 2.50 mmol), were refluxed in 10 mL of DMF for 6 h under aerobic conditions. The reaction mixture was allowed to sit overnight, and the precipitated product was collected by gravity filtration and rinsed with water (0.5046 g). A portion of the product (0.1994 g) was then purified by column chromatography on silica gel using hexanes/dichloromethane (10:1, 4:1) as eluent yielding a yellow solid (17.0 mg, 2.1%). **^{1}H NMR** (300 MHz, DCM, δ): 10.03 (s, 1H), 8.15 (d, *J* = 8.26 Hz, 2H), 7.95 (d, *J* = 8.52 Hz, 2H) 7.82 (d, *J* = 8.79 Hz, 2H), 7.31 (t, *J* = 8.79 Hz, 4H), 7.13 (t, *J* = 7.95 Hz, 6H), 7.05 (d, *J* = 8.79 Hz, 2H). **^{13}C NMR** (126 MHz, DCM): 191.29, 165.94, 152.09, 150.87, 150.56, 146.80, 141.11, 129.13, 137.36, 130.31, 129.59, 127.47, 126.61, 125.66, 124.3304, 121.33. **UV-vis λ_{max} (DCM, ε = M^{-1} cm^{-1}): 434 nm (ε = 35,100) ESI-MS: calcd for $C_{29}H_{20}N_3OS_2^+$: 490.1048; found, 490.1456.**

2.4 RESULTS AND DISCUSSION

The asymmetric, push-pull TTzs were accessed via one-pot syntheses which include, in each instance, a donor aromatic aldehyde (D-BzCHO), an acceptor aromatic aldehyde (A-BzCHO), and dithiooxamide. Initial asymmetric TTz reactions relied on modifying the literature procedure to accommodate a mixed-aldehyde approach, i.e. using an equivalent molar excess of the aromatic aldehydes compared to dithiooxamide (3:2:3). Although accessed simply, the overall yields (2 - 26%) of the asymmetric TTzs (a-TTzs) were limited by the simultaneous formation of their symmetric counterparts (generalized within as D_2-TTz and A_2-TTz). The yields of Bu_2N-

TTz-Py and Ph_2N-TTz-CHO were significantly lower than Ph_2N-TTz-Py and Ph_2N-TTz-COOH. In the case of Ph_2N-TTz-CHO, further reaction and polymerization of the carboxaldehyde functionality likely hinders the overall yield. To better understand Bu_2N-TTz-Py synthesis, NMR studies were performed (see **Figure S29**) and show that the rates of reactivity of dibutylaminobenzaldehyde (Bu_2NBzCHO, A-BzCHO) and pyridinecarboxaldehyde (PyBzCHO, D-BzCHO) differ such that the formation of Py2-TTz (A_2-TTz) is favored over the a-TTz and D_2-TTz formation. It should be noted that the higher rate of reactivity of the D-BzCHO is congruent with analogous condensation reactions within the literature.[47] Another consequence of preferential D_2-TTz formation is that D-BzCHO may become the limiting reagent for the a-TTz reaction, thus leading to A_2-TTz becoming the secondary product. With these considerations in mind, the synthesis of Bu_2N-TTz-Py was studied by using an excess of the Bu_2NBzCHO (1.25 to 1 to 5 mol ratio - PyBzCHO, dithiooxamide, Bu_2NBzCHO). NMR of the crude product shows a TTz ratio of 3:1:1 [Py_2-TTz, Bu_2N-TTz-Py, $(Bu_2N)_2$-TTz] and significant amounts unreacted Bu_2NBzCHO starting material and impurities/side products. To inhibit the formation of side products, promote complete oxidation,[48] and encourage better final yields; the reaction was modified by reacting under N_2, adding dithiooxamide after heating to 120 °C, and oxidizing with DDQ after 4h of reaction time. According to an NMR of the crude product (**Figure S30)** the reaction proceeds more cleanly and results in a product ratio of 1.14 to 1 to 0.44 [Py_2-TTz, Bu_2N-TTz-Py, $(Bu_2N)_2$-TTz].

The absorption, emission, and fluorescence lifetime characteristics of all four TTz dyes were recorded in a variety of organic solvents (**Figure 2.2,** Table 2.1). Additionally, HOMO/LUMO levels of the TTz dyes were determined computationally in Spartan 16 using B3LYP/6-31g* (**Figure 2.2c, Appendix**). Molar absorptivities of all the TTz dyes ranged from 13,000 to 86,000 $cm^{-1}M^{-1}$. In comparison, the molar absorptivities of dipyridyl-TTz (in pyridine)

and its alkylated derivatives (in H_2O) range from 32,000 to 46,000 $cm^{-1}M^{-1}$.[16] Interestingly, the peak molar absorptivities of Ph_2N-TTz-Py were two or more times greater than the peak molar absorptivities of both Bu_2N-TTz-Py and Ph_2N-TTz-COOH, while those of Ph_2N-TTz-CHO were over four-fold greater than Bu_2N-TTz-Py and Ph_2N-TTz-COOH in some solvents. TTz dyes containing the diphenyl substituted donor amine exhibited an increased molar absorptivity compared to the dibutyl substituted donor amine. However, the peak absorbance of Bu_2N-TTz-Py in DCM was slightly red-shifted as compared to that of Ph_2N-TTz-Py ($\lambda_{max,\ abs}$ = 429 nm vs $\lambda_{max,\ abs}$ = 422 nm in DCM), which is attributed to the diphenylamine moiety having weaker donor characteristics. The pyridyl and formylbenzyl acceptor moieties enhance the molar absorptivities of the TTz dyes relative to the benzoic acid TTz derivative Additionally, Ph_2N-TTz-CHO demonstrated the most red-shifted peak absorbance ($\lambda_{max,\ abs}$ = 434 nm in DCM), which is attributed to the 4-formylbenzyl moiety having stronger acceptor characteristics. Due to the low estimated ground state dipole moments of the TTz dyes (μ = 6 – 8 D), their wavelengths of absorbance remained relatively solvent independent (st. dev. = ±11 nm).[49]

The TTz dyes exhibit high quantum yields (QYs) in nonpolar solvents; however, as the polarity of the solvent increases, the emission intensities and, correspondingly, the QYs decrease (e.g. for Bu_2N-TTz-Py: Φ_{hex} = 0.93, Φ_{MeOH} = 0.04). The decrease in the QY is common for dyes with strong excited-state ICT character.[12, 50, 51] In spite of having low QYs in polar solvents, the TTz dyes could be expected to perform well in applications where they are localized to nonpolar environments (e.g. cell membranes); whereby their fluorescence would increase upon localization and any unlocalized dyes would contribute little background noise.[49]

TCSPC measurements of the TTz dyes show a general upward trend for fluorescent lifetimes as the polarity increases in aprotic solvents – from 1.50 – 1.89 ns in nonpolar solvents to

~3.00 ns in polar aprotic solvents (Table 2.1). The fluorescence lifetimes in protic solvents have the opposite trend; that is, a decrease in the fluorescence lifetime as the polarity increases (e.g. for Ph_2N-TTz-COOH: $\tau_{f,\ iPrOH}$ = 2.40 ns, $\tau_{f,\ MeOH}$ = 1.80 ns). The trend reversal in the fluorescence lifetime can most likely be attributed to the presence of hydrogen bonding in protic solvents. Due mostly to large changes in the QYs, but also to increasing fluorescent lifetimes in more polar aprotic solvents, the radiative rates (k_r) decrease relatively significantly with increasing solvent polarity. At the same time, the non-radiative rates of each TTz generally increases as solvent polarity increases. As with the asymmetric TTz dyes, it has been shown that neutral red (NR), another ICT dye, shows a similar trend.[52] Regardless, the fact that the fluorescence lifetimes are solvent dependent opens up the possibility of using these TTz dyes for measuring micelle formation and viscosity in living cells using fluorescence lifetime imaging (FLIM).[1, 53]

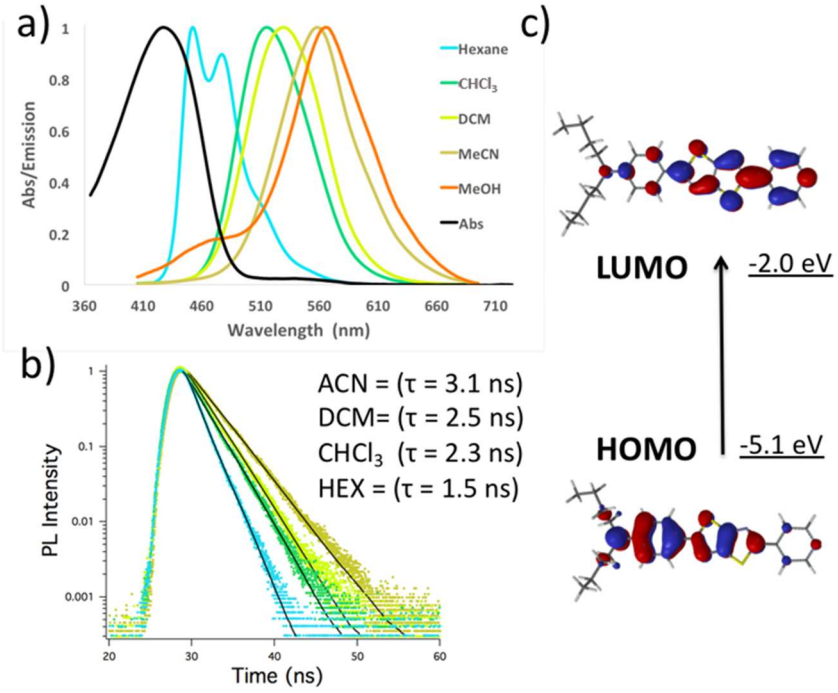

Figure 2.2. (a) Normalized UV-vis absorbance and solvent-dependent fluorescence, (b) solvent-dependent time-resolved fluorescence lifetimes, and (c) HOMO/LUMO molecular orbital configurations for Bu_2N-TTz-Py.

The presence of dual fluorescence and its dependence on solvent polarity is a well-documented phenomenon in many singly bonded D-A molecules with excited states that have highly dipolar quinoidal structures.[54] The higher frequency peak in nonpolar solvents can mostly be attributed to the locally excited (LE) state, whereas the lower frequency peak can mostly be attributed to the ICT state.[55] As is typically seen in similar D-A systems, it is suspected that the ICT state in the asymmetric TTz dye system is stabilized by the solvating effect of the polar solvent, thus causing the emission intensities of the dyes to broaden, diminish, and shift bathochromically with increasing solvent polarity. Another consequence of having electronically separated LE and ICT states is that the fluorescence lifetimes can increase in high-polar solvents even though the QYs are decreasing likewise; whereas, in typical non-ICT systems the fluorescence lifetimes and QYs are directly related.[49, 52]

Table 2.1. Optical Properties of TTz Dyes in Various Solvents

dye	solvent	Polarizability Factor Δf*	Abs (nm) λ_{max}	Abs (eV) E_{ex}	Ext. coeff. $(M \cdot cm)^{-1}$ ε	Em (nm) λ_{max}	Em (eV) E_{em}	Stokes Shift SS (eV)	Φ_F	Fluorescence Lifetime (ns) τ_F	Radiative rate (sec^{-1}) k_r	Non-radiative rate (sec^{-1}) k_{nr}
	Hex	-0.00170	410	3.02	22000	450	2.76	0.27	0.93	1.50	6.2E+08	4.4E+07
Bu_2N	$CHCl_3$	0.148	429	2.89	13000	515	2.41	0.48	0.45	2.26	2.0E+08	2.4E+08
-TTz-	DCM	0.217	430	2.88	18000	532	2.33	0.55	0.35	2.47	1.4E+08	2.6E+08
Py	MeCN	0.305	425	2.92	20000	557	2.23	0.69	0.17	3.06	5.4E+07	2.7E+08
	MeOH	0.309	424	2.93	21000	565	2.20	0.73	0.04	1.23	3.1E+07	7.8E+08
	Tol	0.0132	419	2.96	36000	482	2.57	0.39	0.93	1.80	5.2E+08	3.9E+07
Ph_2N	$CHCl_3$	0.148	422	2.94	34000	536	2.31	0.63	0.54	2.60	2.1E+08	1.8E+08
-TTz-	EtOAc	0.199	415	2.99	48000	518	2.39	0.59	0.55	2.80	2.0E+08	1.6E+08
Py	DCM	0.217	424	2.93	46000	518	2.39	0.53	0.37	3.16	1.2E+08	2.0E+08
	Acetone	0.284	415	2.99	35000	554	2.24	0.75	0.17	2.70	6.3E+07	3.1E+08
	Tol	0.0132	424	2.93	22000	487	2.55	0.38	0.78	1.70	4.6E+08	1.3E+08
Ph_2N	$CHCl_3$	0.148	424	2.93	21000	523	2.37	0.55	0.55	2.20	2.5E+08	2.0E+08
-TTz-	DCM	0.217	425	2.92	14000	548	2.26	0.66	0.33	2.90	1.1E+08	2.3E+08
COOH	iPrOH	0.272	417	2.97	16000	522	2.38	0.60	0.37	2.40	1.5E+08	2.6E+08
	MeOH	0.309	414	3.00	17000	535	2.32	0.68	0.11	1.80	6.1E+07	4.9E+08
	Tol	0.0133	425	2.92	80230	501	2.48	0.44	0.72	1.89	3.8E+08	1.5E+08
Ph_2N	ClBz	0.143	436	2.84	18024	552	2.37	0.55	0.33	2.54	1.3E+08	2.6E+08
-TTz-	Cl_2Bz	0.186	440	2.82	37000	556	2.26	0.66	0.18	2.84	6.3E+07	2.9E+08
CHO	EtOAc	0.200	428	2.90	86081	548	2.26	0.63	0.36	3.09	4.2E+07	7.5E+07
	DCM	0.217	434	2.86	35100	560	2.21	0.64	0.13	2.40	1.5E+08	1.0E+09

*Solvents were chosen to span a wide range of polarizability factors ($\Delta f, see\ Eq. 1$). For direct comparisons, similar solvents were used when possible; however, solubility differences between the compounds prohibited complete standardization in this regard. To compensate, alternative solvents were selected based on solubility and Δf proximity. E.g. the diphenylamino TTzs were not soluble in hexanes ($\Delta f = -0.0017$), so toluene ($\Delta f = 0.013$) was chosen instead.

As shown in **Figure 2.2** and listed in Table 2.1, the TTz dyes exhibit strong solvatofluorochromism – of which Bu_2N-TTz-Py shows the largest Stokes shift of the four TTz dyes (0.73 eV). The calculated HOMO/LUMO levels indicate that the strong solvatofluorochromism arises from an ICT mechanism, whereby the ground state has significant electron localization on the donor side of the molecule whereas the electron density shifts to the

acceptor moiety in the excited state. To more directly quantify the strong ICT character of the TTz dyes, the excited-state dipole moments were calculated using the Lippert-Mataga equation (**Eq 1**):

$$\nu_a - \nu_f = \frac{(\mu^* - \mu)^2}{4\pi\epsilon_0 hca^3}\Delta f + const. \quad ; \quad \Delta f = \left(\frac{\epsilon - 1}{2\varepsilon + 1} - \frac{\eta^2 - 1}{2\eta^2 + 1}\right)$$

where ν_a and ν_f are the wavenumbers of the absorption and emission peaks in cm^{-1}, respectively; μ^* and μ are the excited state and ground state dipoles, respectively; ϵ_0 is the vacuum permittivity, h is Planck's constant, c is the speed of light, a is the Onsager cavity radius, Δf is the orientation polarizability, ϵ is the relative permittivity, and η is the refractive index. The dipoles were calculated using Spartan 2016 software, and the Onsager cavity radius was calculated using Gaussian '09 software.

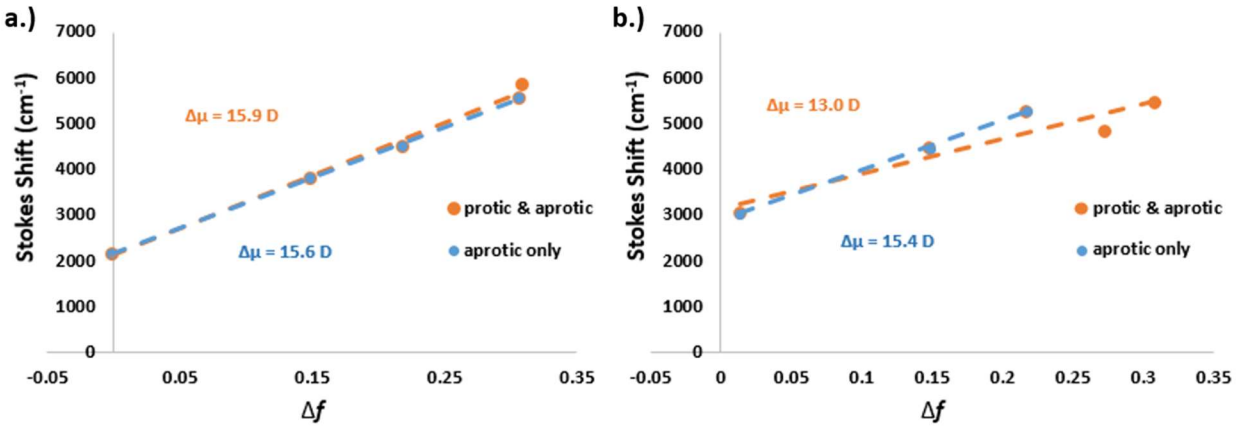

Figure 2.3. (a) Lippert-Mataga plots of Bu_2N-TTz-Py and (b) Ph_2N-TTz-COOH.

Figure 2.3 shows the Stokes shift of Bu_2N-TTz-Py and Ph_2N-TTz-COOH versus Δf. From the slopes of the Lippert-Mataga plots, the change between the dipole moments of the ground and excited states can be determined. Even though the Lippert-Mataga equation assumes no specific solvent-solute interactions (e.g. hydrogen bonding) and ignores solute polarizability, high degrees of linearity are apparent; and therefore, the estimations of the excited state dipoles are regarded as reliable. Bu_2N-TTz-Py, in particular, shows a near unity correlation with Lippert-Mataga theory,

thus suggesting minimal specific solvent-solute interactions and/or relatively rapid vibrational relaxation as compared to solvent relaxation.[11, 56, 57] Perhaps owing to the minimal solvent interactions and rapid vibrational relaxation, the estimated changes in dipole moments ($\Delta\mu$) are remarkably large (**Table 2**). Bu_2N-TTz-Py, for example, has a calculated $\Delta\mu = 15.9$ D and a $\mu^* = 24.3$ D. Compared to similar small-molecule, push-pull dyes, the asymmetric TTz dyes have some of the largest ever reported $\Delta\mu$s – twice that of Prodan and comparable to FR0 and 7AHC.[12, 58] Therefore, it is expected that these asymmetric TTzs dyes would be well suited to give high sensitivity in sensing applications whereby small changes in the polarity of the environment can lead to large differences in the wavelengths of fluorescence.

Table 2. Ground and Excited State Dipole Moments

Compound	Onsager Cavity Radius a (Å)[a]	Ground State Dipole μ (D)[a]	Excited State Dipole μ^* (D)[b]	Change in Dipole $\Delta\mu$ (D)[b]
Bu_2N-TTz-Py	6.17	8.34	24.3	15.9
Ph_2N-TTz-Py	6.11	6.06	20.8	14.6
Ph_2N-TTz-COOH	6.16	8.36	21.3	13.0
Ph_2N-TTz-CHO	6.22	6.89	24.9	18.0

[a] Calculated using DFT B3LYP/6-31G(d) with tight SCF, finegrid integral, and volume keyword
[b] Semi-empirically calculated using the Lippert-Mataga Equation

In an extension of sensing the surrounding polarity, the dependence of the wavelength of emission as a function of temperature and pH were also explored. For these efforts, Bu_2N-TTz-Py was chosen as a focal representative for the family of asymmetric TTzs since it had the highest Stokes shift and otherwise similar photophysical characteristics. For the temperature studies, a 10 μM MeTHF solution of Bu_2N-TTz-Py was created and the emission of the solution was monitored from -196 – 60 °C (see **Appendix** for phosphorescence). MeTHF was chosen for its wide liquid temperature window and ability to form a glass upon freezing; most other solvents crystallize upon solidification and inhibit fluorescence. The low temperature studies were achieved using various liquid N_2 cooling baths (see Experimental). Due to the condensation of atmospheric moisture

during low-temperature testing, only the normalized emission intensities are reported. As seen in **Figure 2.4**, Bu_2N-TTz-Py exhibits thermofluorochromism, whereby the wavelength of emission shifts bathochromically as temperature decreases (from 519 nm at 60 °C to 559 nm at -131 °C). At temperatures near the freezing point of MeTHF and below, however, the wavelength of emission rapidly blue-shifts from 559 to 544 to 503 nm at -131, -136, and -196 °C, respectively. Because the solvent polarity is dependent on the temperature of the solvent, the presence of thermofluorochromism could be fully expected, i.e. it is a direct analogue of solvatofluorochromism.[59] As a corollary, any solvent which also dissolves Bu_2N-TTz-Py will show a similar temperature affect; however, it is expected that the operable temperature range, sensitivity, and linearity would change correspondingly. Whereas as most dye systems demonstrate a hypsochromic shift upon temperature reduction, Bu_2N-TTz-Py demonstrates the opposite trend. General intuition might infer that the direct relationship between viscosity and temperature would likewise lead to faster solvation relaxation at higher temperatures and consequently red-shift the emission spectra. Higher temperatures, however, can also prevent the alignment of solvent dipoles, thus leading to a blue shift in the emission spectra as temperature increases – such as is seen for Bu_2N-TTz-Py and, previously, for Laurdan.[49, 60] Furthermore, the hypsochromic shift of the emission that was observed upon freezing is a well-known phenomenon, and can best be attributed to the complete inhibition of solvent relaxation effects upon freezing.[49] Nevertheless, to visualize the temperature dependence of the emission wavelength, a temperature-wavelength correlation profile for Bu_2N-TTz-Py in MeTHF was created (**Figure 2.4**). It was observed that the wavelength of emission shows a strong linear correlation with the solution temperature while inside the temperature range in which MeTHF is liquid. Additionally, the

TTz/MeTHF solution showed relatively high temperature sensitivity (-0.21 nm $°C^{-1}$), thus making it suitable for temperature sensing applications.[61-64]

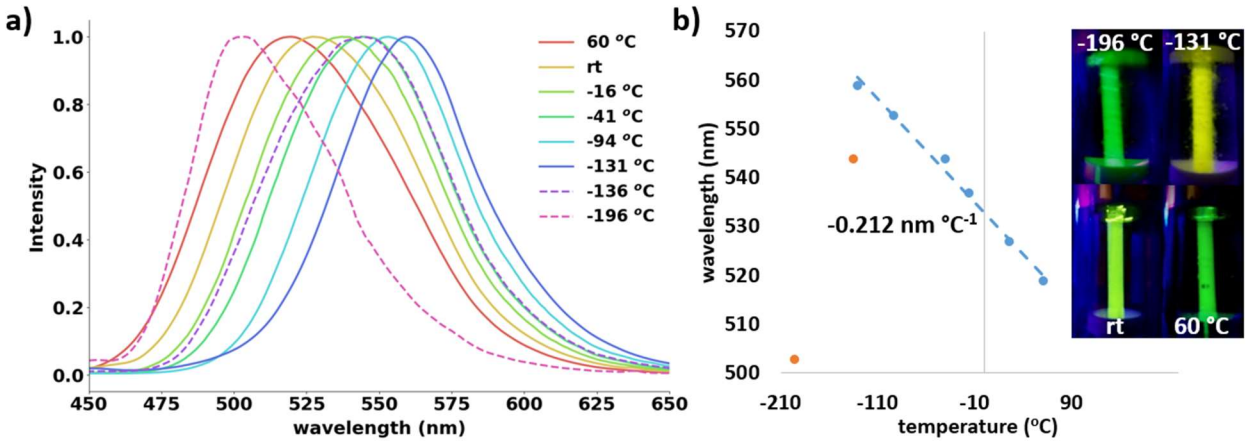

Figure 2.4. (a) Normalized emission intensity spectra of Bu_2N-TTz-Py and (b) temperature-wavelength correlation profile of Bu_2N-TTz-Py in MeTHF when T > -136 °C (blue) and T ≤ -136 °C (orange).

In order to understand the acid/base behavior of Bu_2N-TTz-Py, a series of computational, NMR, and spectroscopic studies were carried out. Based on computational calculations and NMR studies Bu_2N-TTz-Py has four basic sites which were determined to protonate as follows: 1.) the pyridyl nitrogen, 2/3.) the two core nitgrogens, and 4.) the amine (**Figure 2.5**). This was expected since aromatic amines are well known to decrease basicity due to mesomeric effects.

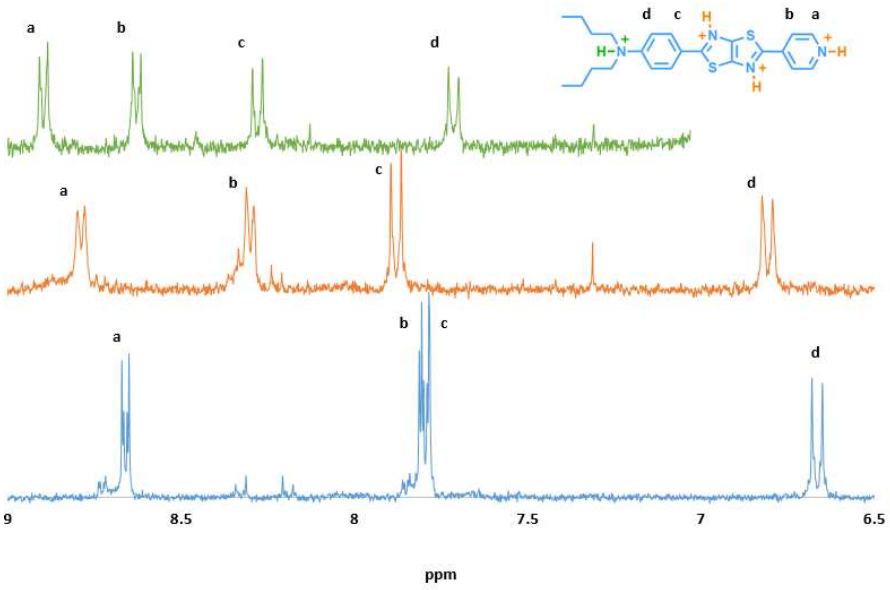

Figure 2.5. NMRs of Bu_2N-TTz-Py (blue), Bu_2N-TTz-PyH_3^{3+} (orange), and Bu_2N-TTz-Py_4^{4+} (green) in d6-DCM / d3-TFA.

For the spectroscopic studies, stock solutions of 10 μM Bu_2N-TTz-Py in $CHCl_3$ containing increasing amounts of TFA at the following molar ratios of TFA to TTz (χ): 10:1, 10^3:1, and 10^6:1. A solution of 10 μM Bu_2N-TTz-Py in $CHCl_3$ was then titrated with the TFA:TTz stock solutions and their wavelengths of absorption and emission measured. The absorbance spectra (**Figure 2.6 a/b**) shows that the protonation of the pyridyl nitrogen ($TTzH^+$) red shifts and diminishes the 425 nm absorbance peak to 461 nm. At larger TFA concentrations, the bridge TTz nitrogens appear to protonate ($TTzH_3^{3+}$) indistinguishably from one another and an absorbance peak starting at 501 nm red shifts to 516 nm while strengthening in intensity. At TFA:TTz concentrations over 1000:1, the 516 nm peak slightly red shits to 522 nm and weakens dramatically as the butylaniline group is protonated ($TTzH_4^{4+}$). At the same time, an absorbance peak from the UV increases in intensity and red shifts from 360 nm to 395 nm. As for the emission (**Figure 2.6 c/d**) behavior, protonation of the pyridyl and core nitrogens gradually diminishes the intensity of the 517 nm emission peak. At TFA:TTz concentrations greater than 1000:1, a new, blue emission peak at 461 nm appears.

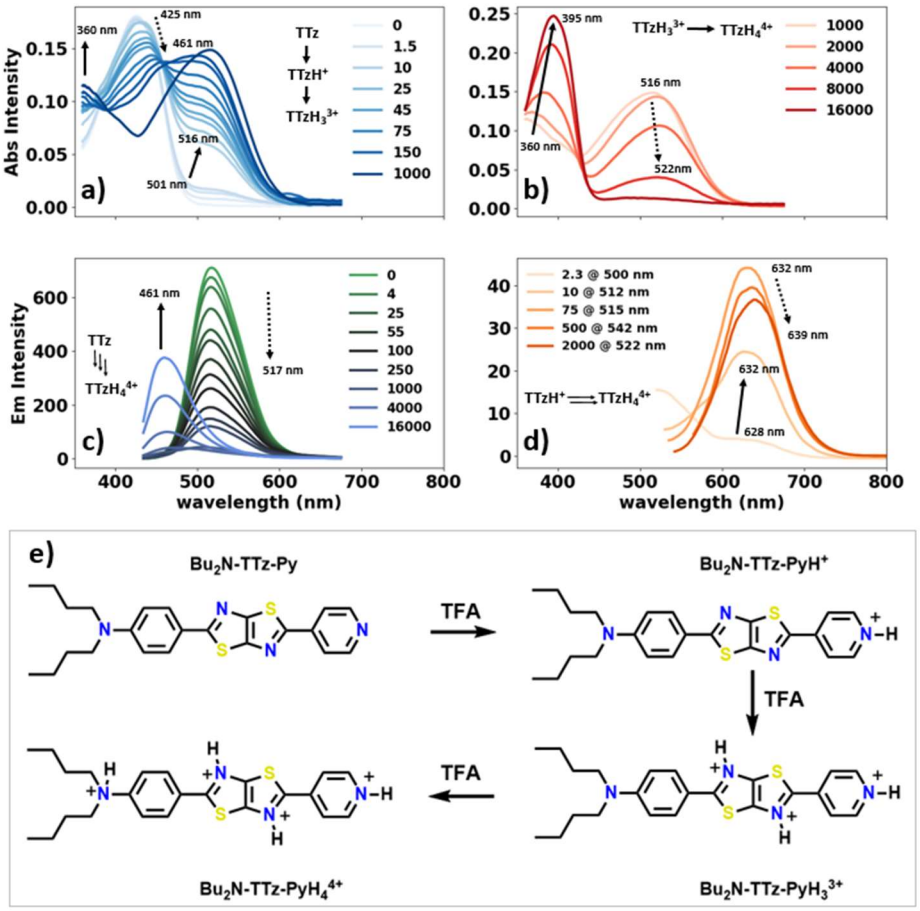

Figure 2.6. Absorption spectra (a,b) and emission spectra (c,d) of the spectrophotometric acid titrations of 10 μM Bu_2N-TTz-Py in $CHCl_3$. The legends report the molar ratios of TFA:TTz, and the wavelength of excitation is 420 nm unless otherwise noted. Proposed sequence of protonation for Bu_2N-TTz-Py (e).

A semi-log plot of the peak emission intensity vs [TFA]:[TTz] shows at least three definitive slopes, corresponding to the protonation sequence **Figure 2.7**. To elaborate, the initial quenching of the green emission occurs relatively slowly, which is attributed to the formation of $TTzH^+$. From TFA:TTz molar ratios between 7.5:1 and 1000:1, the green emission decays more rapidly which corresponds to the formation of $TTzH_3^{3+}$. And finally, at TFA:TTz molar ratios above 1000:1, $TTzH_4^{4+}$ is formed and a new, blue emission peak increases. The reduction in emissivity following triple protonation is most likely due to significant self-quenching, whereby the primary absorbance peak has red shifted enough (516 nm) to strongly overlap with the 517 nm emission peak. Additionally, DFT calculations indicate that protonation of the TTz core causes an

increased dihedral angle between the TTz bridge and pyridyl constituent, thus disrupting optimal π-π overlap.

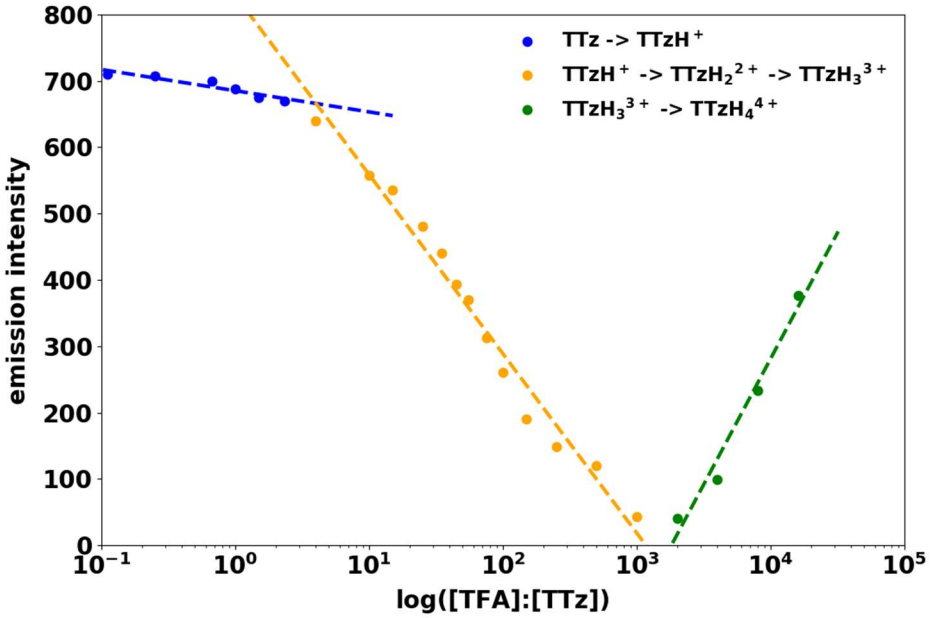

Figure 2.7. Semi-log plot of the peak emission intensity of Bu_2N-TTz-Py vs TFA:TTz mole ratio.

Having characterized the sensing capabilities of the asymmetric TTz dyes in solution, their efficacy as biologically relevant sensors was then explored via in vitro cell studies. Bu_2N-TTz-Py was selectively chosen based on its expected favorability toward membrane localization given its molecular structure (hydrophilic pyridyl head, hydrophobic dibutylamino tail). As shown in **Figure 2.8a/b,** when Bu_2N-TTz-Py is applied to HEK 293T cells, the dye localizes to cell membranes, displaying peak excitation/emission wavelengths at 423 and 483 nm, respectively (**Figure 2.8c**). Also noteworthy, the wavelength of peak emission for Bu_2N-TTz-Py in a solution of PBS with 0.1% Triton-X100 (518 nm) blue-shifts by 34 nm upon localizing to a cell membrane. A 34 nm blue shift is equivalent to the solvent polarity differential between DCM and toluene, thus further indicating that Bu_2N-TTz-Py intercalates between the phospholipid bilayer. Additionally, Bu_2N-TTz-Py has both poor solubility and low QY in aqueous environments

resulting in low background fluorescence, which is visually apparent by the high amount of contrast between the cell membrane and its surrounding environment (**Figure 2.8b**). More conclusively, **Figure 2.8d/e** show the time lapse imaging and quantification of localization of Bu_2N-TTz-Py in HEK 293T cells (6 independent experiments). Normalized against the fluorescence intensity of CellMask^{TM} red, a plasma membrane marker, the fluorescence intensities of the plasma membranes stained with Bu_2N-TTz-Py shows a 2.5% decrease after 50 min (26% decrease after 110 min). Given the brevity of the acquisition time (6 acquisitions per cell, 200 ms exposure per acquisition), the overall decrease of the plasma membrane fluorescence intensities of Bu_2N-TTz-Py is most likely not caused by photodegradation. Furthermore, the decrease of fluorescence intensities is not caused by dye internalization in any significant capacity since the normalized intensities of intracellular membranes stained with Bu_2N-TTz-Py indicate negligible TTz internalization (< 1% over 50 min, 5% over 130 min). It is therefore concluded that the majority of the fluorescence reduction after 50 min is caused by extracellular leaching.

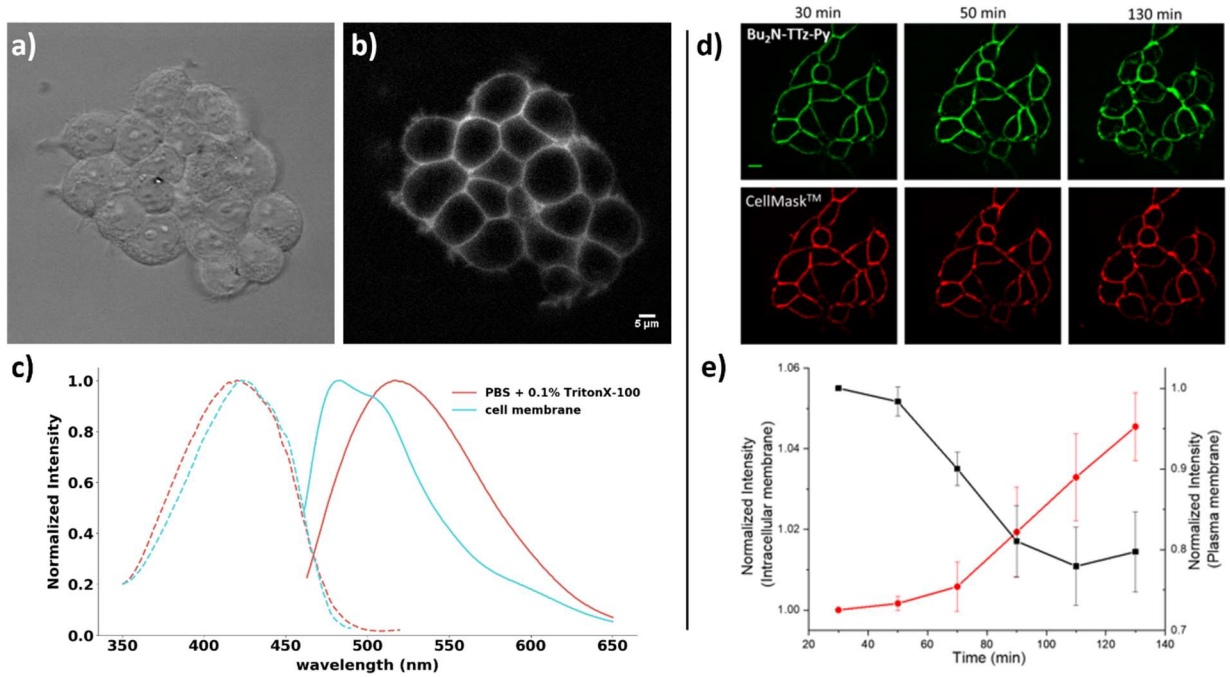

Figure 2.8. In vitro cellular characterization of Bu_2N-TTz-Py. (a, b) DIC and fluorescent images of HEK 293T cells labelled with 500 nM Bu_2N-TTz-Py in PBS buffer containing 0.01% Pluronic F127. (c) Normalized excitation/emission spectra of 1 µM Bu_2N-TTz-Py in PBS buffer with 0.1% TritonX-100 before and after loading into ~0.5 x 10^5 J774.A1 cells. Exctitation spectra (- -) were collected at 520 nm and emission spectra (-) were collected with 440 nm exctiation. (d) Time lapse imaging of HEK 293T cells show partial internalization of Bu_2N-TTz-Py, but no internalization of CellMask stain after 130 min. (e) Quantification of intracellular membrane (red trace, circles) and plasma membrane (black trace, squares) localization of Bu_2N-TTz-Py over time. Error bars represent S.E.M. of 6 independent experiments. Scale bar = 10 µm.

Having established its environmental sensitivity and proclivity for membrane localization, it was hypothesized that Bu_2N-TTz-Py could orient itself favorably within cell membranes and sense voltage differentials across the membrane. To test the membrane voltage sensitivity of Bu_2N-TTz-Py, whole-cell patch clamp electrophysiology was performed on HEK 293T cells labeled with 500 nM Bu_2N-TTz-Py. As seen in **Figure 2.9a**, cells were held at -60 mV and stepped through 10 mV increments whereby depolarizing or hyperpolarizing voltage potentials resulted in either a florescence increase or decrease, respectively. Tests concluded that Bu_2N-TTz-Py has a voltage sensitivity of approximately 10% $\Delta F/F$ per 100 mV. For context, early generation VSDs, such as RH-421, ANNINE-6, and VF2.1.Cl, display maximum voltage sensitivities of 10% – 25% $\Delta F/F$ per 100 mV.[65, 66] In other words, Bu_2N-TTz-Py shows a comparatively modest voltage sensitivity relative to comparable VSDs in the literature. It should also be noted that the voltage sensitivities, signal-to-noise, and linearity of VSDs with ICT character (e.g. Bu_2N-TTz-Py) can vary significantly depending on both the wavelength of excitation and probed emission.[67]

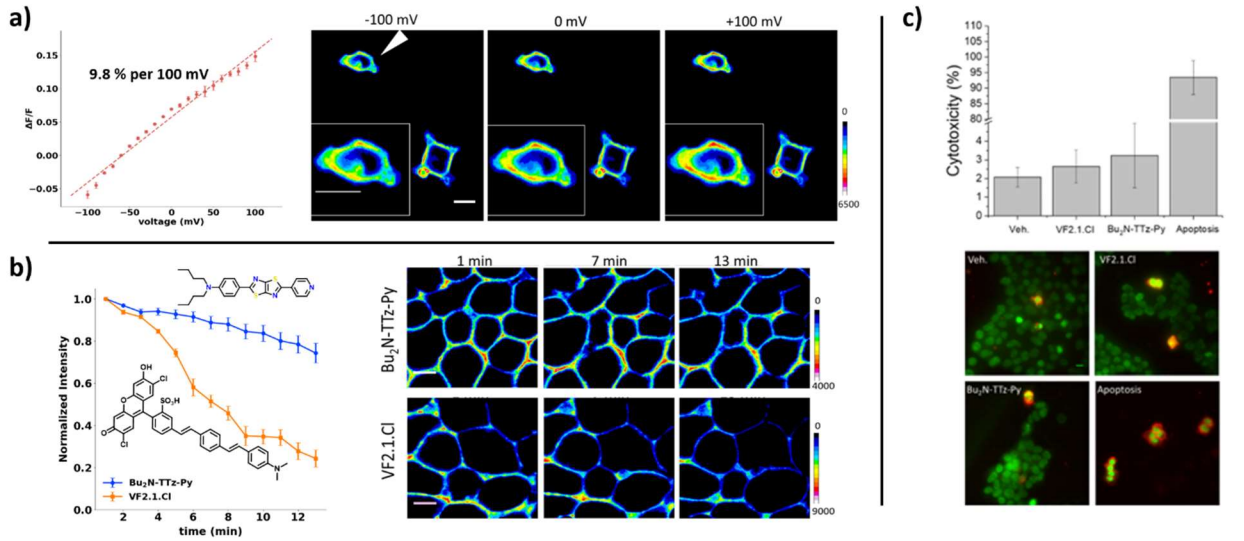

Figure 2.9. (a) Plot of fractional change in fluorescence (ΔF/F) vs clamped membrane potential of HEK 293T cells labelled with 500 nM Bu_2N-Py-TTz and representative pseudo-color images clamped at -100, 0, and +100 mV (shown by white arrow). Inset: Voltage clamped cell. (b) Photostability of Bu_2N-TTz-Py and VF2.1.Cl in HEK 293T cells (illuminated using λ = 440 nm at 5 W cm^{-2}) and their representative pseudo-color images under continuous illumination at wavelength of maximum excitation. Error bars a/b represent the standard error of mean (S.E.M.) for 3 independent experiments, n = 12 total cells. Scale bar = 10 µm. (c) Annexin V-cy5 staining of HEK 293T cells incubated with DMSO (Veh.), VF2.1.Cl, and Bu_2N-TTz-Py. Apoptosis for control (incubated cells 65 °C, 10 min). Percentages of cytotoxicity were calculated as number of 100 X Cy5 positive cells per number of nuclei stained. Error bars represent S.E.M. of three independent experiments, n = 250 cells. Scale bars = 10 µm.

Encouraged by the promising voltage sensitivity data, the photostability of Bu_2N-TTz-Py was also tested and found to be much improved over the photostability of VF2.1.Cl (**Figure 2.9b**). Whereas VF2.1.Cl had a bleaching half-life of approximately 7.5 minutes under intense illumination (I = 5 W cm^{-2}, ε = 22,300 cm^{-1} M^{-1} @ 440 nm LED[10]), the fluorescence intensity of Bu_2N-TTz-Py decayed by less than 10% in the same amount of time under identical conditions (ε = 15,000 – 20,000 cm^{-1} M^{-1} @ 440 nm LED). The improved photostability of Bu_2N-TTz-Py over that of VF2.1.Cl can best be attributed to the structural differences between both their head groups and bridging units. It is well known that fluorescein has low photostability and, in the case of VF2.1.Cl, it has been shown that derivatization of its fluorescein head group can drastically improve the photostability.[68, 69] Additionally, p-phenylenevinylene (PPV), i.e. the bridging unit in VF2.1.Cl, has been shown to have photostability issues as well. [62-64] TTz, on the other hand, has

excellent thermo-oxidative and photochemical stability. [25, 29] Furthermore, TTz has the added advantage of requiring only a single condensation step, whereas most other VSDs (including VF2.1.Cl) require multiple synthetic steps. However, the overall yields of the asymmetric TTz dyes and other VSDs remain similar.

Lastly, the cellular toxicities of Bu_2N-TTz-Py and VF2.1.Cl were characterized using Annexin V-Cy5 staining of phosphatidylserine. HEK 293T cells were labelled with Bu_2N-TTz-Py or VF2.1.Cl for 15 min, incubated with Annexin V-Cy5 for 20 min in the dark, washed, and fixed with 4% paraformaldehyde before imaging. As a positive control, apoptosis was induced via high-temperature incubation (65 °C, 10 min). As shown in **Figure 2.9c**, the treatments of Bu_2N-TTz-Py or VF2.1.Cl to HEK 293T cells both show insignificant cytotoxicity.

2.5 CONCLUSION

In conclusion, we have developed a family of asymmetric TTz dyes which exhibit remarkable solvatofluorochromism as a consequence of the unique structural features provided by the TTz core, namely its enhanced rigidity and planarity in which typical conjugated hydrocarbon bridges do not confer. Spectroscopic studies of these TTz dyes reveal large absorption coefficients, high quantum yields in nonpolar environments, significant Stokes shifts, and red-shifted absorption/emission peaks across a wide solvent range. Lippert-Mataga plots indicate that these TTz dyes have some of the largest dipole moments ever reported ($\Delta\mu$ = 13 – 18 D) - double that of Prodan and comparable to FR0 and 7AHC. Additionally, we have showed that the remarkable photophysical properties of the fused, bicyclic thiazolothiazole π-bridge make them ideal for polarity and/or temperature sensing applications. Furthermore, electrophysiological, *in-vitro* cell studies indicate promising voltage sensitivities, negligible cytotoxicity, and photostabilities 4 times higher than that of VF2.1.Cl. Thus, the strong ICT character and remarkable photophysical

properties of these new asymmetric TTz dyes make them attractive for a wide range of sensing applications.

2.6 REFERENCES

1. Klymchenko, A. S., Solvatochromic and Fluorogenic Dyes as Environment-Sensitive Probes: Design and Biological Applications. *Acc. Chem. Res.* **2017,** *50* (2), 366-375.

2. Kumar, M.; Kumar, A.; Singh, M. K.; Sahu, S. K.; John, R. P., A novel benzidine based Schiff base "turn-on" fluorescent chemosensor for selective recognition of Zn2+. *Sensor Actuat B-Chem* **2017,** *241*, 1218-1223.

3. Liu, Z.; He, W.; Guo, Z., Metal coordination in photoluminescent sensing. *Chem. Soc. Rev.* **2013,** *42* (4), 1568-1600.

4. Yang, Y.-S.; Ma, C.-M.; Zhang, Y.-P.; Xue, Q.-H.; Ru, J.-X.; Liu, X.-Y.; Guo, H.-C., A highly selective "turn-on" fluorescent sensor for zinc ion based on a cinnamyl pyrazoline derivative and its imaging in live cells. *Anal. Methods* **2018,** *10* (16), 1833-1841.

5. Narayanaswamy, N.; Chakraborty, K.; Saminathan, A.; Zeichner, E.; Leung, K.; Devany, J.; Krishnan, Y., A pH-correctable, DNA-based fluorescent reporter for organellar calcium. *Nature Methods* **2019,** *16* (1), 95-102.

6. Liu, F.; Tang, Y.; Kuang, Y.; Pan, D.; Liu, X.; Yu, R.-Q.; Jiang, J.-H., An activatable fluorescent probe with an ultrafast response and large Stokes shift for live cell bioimaging of hypochlorous acid. *RSC Adv.* **2016,** *6* (109), 107910-107915.

7. Yang, X.; He, L.; Xu, K.; Yang, Y.; Lin, W., The development of an ICT-based formaldehyde-responsive fluorescence turn-on probe with a high signal-to-noise ratio. *New J. Chem.* **2018,** *42* (15), 12361-12364.

8. Ermakova, Y. G.; Sen, T.; Bogdanova, Y. A.; Smirnov, A. Y.; Baleeva, N. S.; Krylov, A. I.; Baranov, M. S., Pyridinium Analogues of Green Fluorescent Protein Chromophore: Fluorogenic Dyes with Large Solvent-Dependent Stokes Shift. *J. Phys. Chem. Lett.* **2018,** *9* (8), 1958-1963.

9. Niko, Y.; Didier, P.; Mely, Y.; Konishi, G.-i.; Klymchenko, A. S., Bright and photostable push-pull pyrene dye visualizes lipid order variation between plasma and intracellular membranes. *Sci. Rep.* **2016,** *6*, 18870.

10. Miller, E. W.; Lin, J. Y.; Frady, E. P.; Steinbach, P. A.; Kristan, W. B.; Tsien, R. Y., Optically monitoring voltage in neurons by photo-induced electron transfer through molecular wires. *Proc. Natl. Acad. Sci. U. S. A.* **2012,** *109* (6), 2114-2119.

11. Zhu, L.; Younes, A. H.; Yuan, Z.; Clark, R. J., 5-Arylvinylene-2,2′-bipyridyls: Bright "push–pull" dyes as components in fluorescent indicators for zinc ions. *J. Photoche. Photobiol., A: Chem.* **2015,** *311*, 1-15.

12. Kucherak, O. A.; Didier, P.; Mély, Y.; Klymchenko, A. S., Fluorene Analogues of Prodan with Superior Fluorescence Brightness and Solvatochromism. *J. Phys. Chem. Lett.* **2010,** *1* (3), 616-620.

13. Niko, Y.; Kawauchi, S.; Konishi, G.-i., Solvatochromic Pyrene Analogues of Prodan Exhibiting Extremely High Fluorescence Quantum Yields in Apolar and Polar Solvents. *Chem. Eur. J.* **2013,** *19* (30), 9760-9765.

14. Yamaguchi, K.; Murai, T.; Hasegawa, S.; Miwa, Y.; Kutsumizu, S.; Maruyama, T.; Sasamori, T.; Tokitoh, N., 5-N-Arylaminothiazoles as Highly Twisted Fluorescent Monocyclic Heterocycles: Synthesis and Characterization. *J. Org. Chem.* **2015,** *80* (21), 10742-10756.

15. Dell'Acqua, M.; Ronda, L.; Piano, R.; Pellegrino, S.; Clerici, F.; Rossi, E.; Mozzarelli, A.; Gelmi, M. L.; Abbiati, G., MediaChrom: Discovering a Class of Pyrimidoindolone-Based Polarity-Sensitive Dyes. *J. Org. Chem.* **2015,** *80* (21), 10939-10954.

16. Woodward, A. N.; Kolesar, J. M.; Hall, S. R.; Saleh, N.-A.; Jones, D. S.; Walter, M. G., Thiazolothiazole Fluorophores Exhibiting Strong Fluorescence and Viologen-Like Reversible Electrochromism. *J. Am. Chem. Soc.* **2017,** *139* (25), 8467-8473.

17. Luo, J.; Hu, B.; Debruler, C.; Liu, T. L., A π-Conjugation Extended Viologen as a Two-Electron Storage Anolyte for Total Organic Aqueous Redox Flow Batteries. *Angew. Chem. Int. ed.* **2018,** *57* (1), 231-235.

18. Nazim, M.; Ameen, S.; Shaheer Akhtar, M.; Shin, H.-S., D-π-A-π-D type thiazolo[5,4-d]thiazole-core organic chromophore and graphene modified PEDOT:PSS buffer layer for efficient bulk heterojunction organic solar cells. *Sol. Energy* **2018,** *171*, 366-373.

19. Roy, I.; Bobbala, S.; Zhou, J.; Nguyen, M. T.; Nalluri, S. K. M.; Wu, Y.; Ferris, D. P.; Scott, E. A.; Wasielewski, M. R.; Stoddart, J. F., ExTzBox: A Glowing Cyclophane for Live-Cell Imaging. *J. Am. Chem. Soc.* **2018,** *140* (23), 7206-7212.

20. Reginato, G.; Mordini, A.; Zani, L.; Calamante, M.; Dessì, A., Photoactive Compounds Based on the Thiazolo[5,4-d]thiazole Core and Their Application in Organic and Hybrid Photovoltaics. *Eur. J. Org. Chem.* **2016,** *2016* (2), 233-251.

21. Dessi, A.; Calamante, M.; Mordini, A.; Peruzzini, M.; Sinicropi, A.; Basosi, R.; Fabrizi de Biani, F.; Taddei, M.; Colonna, D.; Di Carlo, A.; Reginato, G.; Zani, L., Organic dyes with intense light absorption especially suitable for application in thin-layer dye-sensitized solar cells. *Chem. Commun.* **2014,** *50* (90), 13952-13955.

22. Subramaniyan, S.; Xin, H.; Kim, F. S.; Murari, N. M.; Courtright, B. A. E.; Jenekhe, S. A., Thiazolothiazole Donor–Acceptor Conjugated Polymer Semiconductors for Photovoltaic Applications. *Macromol.* **2014,** *47* (13), 4199-4209.

23. Dessì, A.; Barozzino Consiglio, G.; Calamante, M.; Reginato, G.; Mordini, A.; Peruzzini, M.; Taddei, M.; Sinicropi, A.; Parisi, M. L.; Fabrizi de Biani, F.; Basosi, R.; Mori, R.; Spatola, M.; Bruzzi, M.; Zani, L., Organic Chromophores Based on a Fused Bis-Thiazole Core and Their Application in Dye-Sensitized Solar Cells. *Eur. J. Org. Chem.* **2013,** *2013* (10), 1916-1928.

24. Zhang, M.; Guo, X.; Wang, X.; Wang, H.; Li, Y., Synthesis and Photovoltaic Properties of D–A Copolymers Based on Alkyl-Substituted Indacenodithiophene Donor Unit. *Chem. Mater.* **2011,** *23* (18), 4264-4270.

25. Saito, M.; Osaka, I.; Suzuki, Y.; Takimiya, K.; Okabe, T.; Ikeda, S.; Asano, T., Highly Efficient and Stable Solar Cells Based on Thiazolothiazole and Naphthobisthiadiazole Copolymers. *Sci. Rep.* **2015,** *5*, 14202.

26. Amina Khatun, D. K. P. N. S. M. G. W. S. S., Thiazolothiazole-Based Luminescent Metal–Organic Frameworks with Ligand-to-Ligand Energy Transfer and Hg2+-Sensing Capabilities. *Inorganic Chemistry*.

27. Ando, S.; Nishida, J.-i.; Inoue, Y.; Tokito, S.; Yamashita, Y., Synthesis, physical properties, and field-effect transistors of novel thiophene/thiazolothiazole co-oligomers. *J. Mater. Chem.* **2004,** *14* (12), 1787-1790.

28. Cheng, C.; Yu, C.; Guo, Y.; Chen, H.; Fang, Y.; Yu, G.; Liu, Y., A diketopyrrolopyrrole-thiazolothiazole copolymer for high performance organic field-effect transistors. *Chem. Commun.* **2013,** *49* (20), 1998-2000.

29. Yan, L.; Zhao, Y.; Wang, X.; Wang, X.-Z.; Wong, W.-Y.; Liu, Y.; Wu, W.; Xiao, Q.; Wang, G.; Zhou, X.; Zeng, W.; Li, C.; Wang, X.; Wu, H., Platinum-Based Poly(Aryleneethynylene) Polymers Containing Thiazolothiazole Group with High Hole Mobilities for Field-Effect Transistor Applications. *Macromol. Rapid Commun.* **2012,** *33* (6-7), 603-609.

30. Osaka, I.; Zhang, R.; Liu, J.; Smilgies, D.-M.; Kowalewski, T.; McCullough, R. D., Highly Stable Semiconducting Polymers Based on Thiazolothiazole. *Chem. Mater.* **2010,** *22* (14), 4191-4196.

31. Dessì, A.; Calamante, M.; Mordini, A.; Peruzzini, M.; Sinicropi, A.; Basosi, R.; Fabrizi de Biani, F.; Taddei, M.; Colonna, D.; di Carlo, A.; Reginato, G.; Zani, L., Thiazolo[5,4-d]thiazole-based organic sensitizers with strong visible light absorption for transparent, efficient and stable dye-sensitized solar cells. *RSC Adv.* **2015,** *5* (41), 32657-32668.

32. Kudrjasova, J.; Herckens, R.; Penxten, H.; Adriaensens, P.; Lutsen, L.; Vanderzande, D.; Maes, W., Direct arylation as a versatile tool towards thiazolo[5,4-d]thiazole-based semiconducting materials. *Org. Biomol. Chem.* **2014,** *12* (26), 4663-4672.

33. Nazim, M.; Ameen, S.; Akhtar, M. S.; Seo, H.-K.; Shin, H. S., Novel liquid crystalline oligomer with thiazolothiazole-acceptor for efficient BHJ small molecule organic solar cells. *Syn. Met.* **2014,** *187*, 178-184.

34. Dessì, A.; Calamante, M.; Mordini, A.; Peruzzini, M.; Sinicropi, A.; Basosi, R.; Fabrizi de Biani, F.; Taddei, M.; Colonna, D.; Di Carlo, A.; Reginato, G.; Zani, L., Organic dyes with intense light absorption especially suitable for application in thin-layer dye-sensitized solar cells. *Chem. Commun.* **2014,** *50* (90), 13952-13955.

35. Zani, L.; Reginato, G.; Mordini, A.; Calamante, M.; Peruzzini, M.; Taddei, M.; Sinicropi, A.; Parisi, M. L.; Fabrizi de Biani, F.; Basosi, R.; Cavallaro, A.; Bruzzi, M., An unusual thiazolo[5,4-d]thiazole sensitizer for dye-sensitized solar cells. *Tetrahedron Lett.* **2013,** *54* (30), 3944-3948.

36. Kudrjasova, J.; Kesters, J.; Verstappen, P.; Brebels, J.; Vangerven, T.; Cardinaletti, I.; Drijkoningen, J.; Penxten, H.; Manca, J.; Lutsen, L.; Vanderzande, D.; Maes, W., A direct arylation approach towards efficient small molecule organic solar cells. *J. Mater. Chem. A* **2016,** *4* (3), 791-795.

37. Benin, V.; Yeates, A. T.; Dudis, D., Preparation of halogenated derivatives of thiazolo[5,4-d]thiazole via direct electrophilic aromatic substitution. *J. Heterocyclic Chem.* **2009,** *45* (3), 811-819.

38. Ziessel, R.; Nano, A.; Heyer, E.; Bura, T.; Retailleau, P., Rational Design of New Thiazolo-Thiazole Dyes as Input Energy Units in Molecular Dyads. *Chem. Eur. J.* **2013,** *19* (8), 2582-2588.

39. Weber, G.; Farris, F. J., Synthesis and spectral properties of a hydrophobic fluorescent probe: 6-propionyl-2-(dimethylamino)naphthalene. *Biochemistry.* **1979,** *18* (14), 3075-3078.

40. Brouwer, A. M., Standards for photoluminescence quantum yield measurements in solution (IUPAC Technical Report). *Pure and Applied Chemistry* **2011,** *83* (12), 2213-2228-2228.

41. Suzuki, K.; Kobayashi, A.; Kaneko, S.; Takehira, K.; Yoshihara, T.; Ishida, H.; Shiina, Y.; Oishi, S.; Tobita, S., Reevaluation of absolute luminescence quantum yields of standard solutions using a spectrometer with an integrating sphere and a back-thinned CCD detector. *Physical Chemistry Chemical Physics* **2009,** *11* (42), 9850-9860-9860.

42. Axel, D. B., Density-functional thermochemistry. III. The role of exact exchange. *J Chem Phys 98*, 5648-5652.

43. P J Stephens, F. J. D. C. F. C. M. J. F., Ab Initio Calculation of Vibrational Absorption and Circular Dichroism Spectra Using Density Functional Force Fields. *J Phys Chem 98*, 11623-11627.

44. W J Hehre, R. D. J. A. P., Self—Consistent Molecular Orbital Methods. XII. Further Extensions of Gaussian—Type Basis Sets for Use in Molecular Orbital Studies of Organic Molecules. *J Chem Phys 56*, 2257-2261.

45. Sheldrick, G. M., A short history of SHELX. *Acta Crystallogr Sect Found Crystallogr* **2008,** *64* (1), 112-122.

46. Dolomanov, O. V.; Bourhis, L. J.; Gildea, R. J.; Howard, J. A. K.; Puschmann, H., OLEX2: a complete structure solution, refinement and analysis program. *J Appl Crystallogr* **2009,** *42* (2), 339-341.

47. Yohei Ogiwara, K. T. T. K. N. S., Indium(III)-Catalyzed Knoevenagel Condensation of Aldehydes and Activated Methylenes Using Acetic Anhydride as a Promoter. *J Org Chem* **2015,** *80*, 3101-3110.

48. G Reginato, A. M. L. Z. M. C. A. D., Photoactive Compounds Based on the Thiazolo 5,4-d thiazole Core and Their Application in Organic and Hybrid Photovoltaics. *European Journal of Organic Chemistry 2016*, 233-251.

49. Lakowicz, J. R., *Principles of Fluorescence Spectroscopy*. Springer: Baltimore, 2006.

50. Bhattacharyya, K.; Chowdhury, M., Environmental and magnetic field effects on exciplex and twisted charge transfer emission. *Chemical Reviews* **1993,** *93* (1), 507-535-535.

51. Soujanya, T.; Fessenden, R. W.; Samanta, A., Role of Nonfluorescent Twisted Intramolecular Charge Transfer State on the Photophysical Behavior of Aminophthalimide Dyes. *J Phys Chem* **1996,** *100* (9), 3507-3512.

52. Singh, M. K.; Pal, H.; Bhasikuttan, A. C.; Sapre, A. V., Dual Solvatochromism of Neutral Red. *Photochemistry and Photobiology* **1998,** *68* (1), 32-38.

53. Mallick, S.; Pal, K.; Koner, A. L., Probing microenvironment of micelle and albumin using diethyl 6-(dimethylamino)naphthalene-2,3-dicarboxylate: An electroneutral solvatochromic fluorescent probe. **2016,** *467*.

54. Grabowski, Z. R.; Rotkiewicz, K.; Rettig, W., Structural Changes Accompanying Intramolecular Electron Transfer: Focus on Twisted Intramolecular Charge-Transfer States and Structures. *Chemical Reviews* **2003,** *103* (10), 3899-4032.

55. Hu, R.; Lager, E.; Aguilar-Aguilar, A. l.; Liu, J.; Lam, J. W. Y.; Sung, H. H. Y.; Williams, I. D.; Zhong, Y.; Wong, K.; Peña-Cabrera, E.; Tang, B., Twisted Intramolecular Charge Transfer and Aggregation-Induced Emission of BODIPY Derivatives. *The Journal of Physical Chemistry C* **2009,** *113* (36), 15845-15853.

56. E, L., Zeitschrift für physikalische Chemie. *Zeitschrift für physikalische Chemie.* **1956,** *6*, 125.

57. Mataga, N.; Kaifu, Y.; Koizumi, M., Solvent Effects upon Fluorescence Spectra and the Dipolemoments of Excited Molecules. 1956; Vol. 29, p 465-470.

58. Giordano, L.; Shvadchak, V. V.; Fauerbach, J. A.; Jares-Erijman, E. A.; Jovin, T. M., Highly Solvatochromic 7-Aryl-3-hydroxychromones. *The Journal of Physical Chemistry Letters* **2012,** *3* (8), 1011-1016.

59. Reichardt, C., Solvatochromism, thermochromism, piezochromism, halochromism, and chiro-solvatochromism of pyridinium N -phenoxide betaine dyes. *Chemical Society Reviews* **1992,** *21* (3), 147-153-153.

60. Viard, M.; Gallay, J.; Vincent, M.; Meyer, O.; Robert, B.; Paternostre, M., Laurdan solvatochromism: solvent dielectric relaxation and intramolecular excited-state reaction. *Biophysical Journal* **1997,** *73* (4), 2221-2234-2234.

61. Seeboth, A.; Kriwanek, J.; Vetter, R., The first example of thermochromism of dyes embedded in transparent polymer gel networks. *Journal of Materials Chemistry* **1999,** *9* (10), 2277-2278-2278.

62. Chen, K.; Catalano, V. J., Luminescent Thermochromism in a Gold(I)–Copper(I) Phosphine–Pyridine Complex. *European Journal of Inorganic Chemistry* **2015,** *2015* (31), 5254-5261-5261.

63. Burt, M. C.; Dave, B. C., An optical temperature sensing system based on encapsulation of a dye molecule in organosilica sol–gels. *Sensors and Actuators B: Chemical* **2005,** *107* (2), 552-556-556.

64. Bacci, M.; Brenci, M.; Conforti, G.; Falciai, R.; Mignani, A. G.; Scheggi, A. M., Thermochromic transducer optical fiber thermometer. *Applied Optics* **1986,** *25* (7), 1079.

65. Huang, Y.-L.; Walker, A. S.; Miller, E. W., A Photostable Silicon Rhodamine Platform for Optical Voltage Sensing. *Journal of the American Chemical Society* **2015**.

66. Kuhn, B.; Fromherz, P., Anellated Hemicyanine Dyes in a Neuron Membrane: Molecular Stark Effect and Optical Voltage Recording. *The Journal of Physical Chemistry B* **2003,** *107* (31), 7903-7913.

67. Kuhn, B.; Roome, C. J., Primer to Voltage Imaging With ANNINE Dyes and Two-Photon Microscopy. *Frontiers in Cellular Neuroscience* **2019,** *13*, 321.

68. Whitaker, J. E.; Haugland, R. P.; Ryan, D.; Hewitt, P. C.; Haugland, R. P.; Prendergast, F. G., Fluorescent rhodol derivatives: Versatile, photostable labels and tracers. *Analytical Biochemistry* **1992,** *207* (2), 267-279.

69. Kulkarni, R. U.; Kramer, D. J.; Pourmandi, N.; Karbasi, K.; Bateup, H. S.; Miller, E. W., Voltage-sensitive rhodol with enhanced two-photon brightness. *Proceedings of the National Academy of Sciences* **2017,** *114* (11), 2813-2818.

CHAPTER 3: Mechanistic and reaction kinetics studies via computational modeling and LC/PDA/ESI-MS

3.1 INTRODUCTION

Due to their desirable photophysical properties (high QY, fast hole mobilities, oxidative stability, etc.), thiazolothiazoles have proven useful for applications involving organic electronics and sensing. Despite their promise, however, one of the major limitations for more widespread adoption of TTzs (especially a-TTzs) in industry is their difficult purification and low yields.[1] Due to its straightforward, single-step synthesis, the Ketcham method has remained the most prevalent technique, but the harsh reaction conditions required can cause significant side-product formation and tarring; a problem further exacerbated in a mixed-pot a-TTz reaction where multiple TTzs are formed.[2] Attempts have been made throughout the literature to ease purification and improve yields, including the use of microwave synthesis, oxidative cleanup, catalysis, and/or different routes entirely, but accessing TTzs continues to remain less than ideal.[3-7]

Despite the prevalence of the Ketcham method, little is definitively known of its reaction mechanism, most likely due to its complexity.[1] Using a pyrrolidine catalyst, a 1984 East German patent claimed to have isolated an aryliminomercaptothiazole intermediate prone to disulfide oxidation,[8, 9] but it was not until very recently that such a side-product was confirmed to occur in the regular course of the Ketcham method (**Figure 3.1**).[1] Such a result suggests that the reaction mechanism first involves nucleophilic attack and then condensation/ring-closing to an aminomercaptothiazole (Tz) which is then condensed to the stable iminomercaptothiazole (imTz). The stable intermediate can then ring-close and oxidize to form the TTz. If true, subjecting the reaction to non-oxidizing conditions (i.e. inert atmosphere) should halt the reaction at the imTz. If reversible, addition of another aldehyde while maintaining anaerobic conditions should result in a

redistribution of thiazole products. If under thermodynamic control, an equilibrium can be engineered whereby reactant ratios, oxidation timing, and thermodynamic differences are exploited to favor the a-TTz. In order to probe these parameters, computational and experimental reaction studies were carried out.

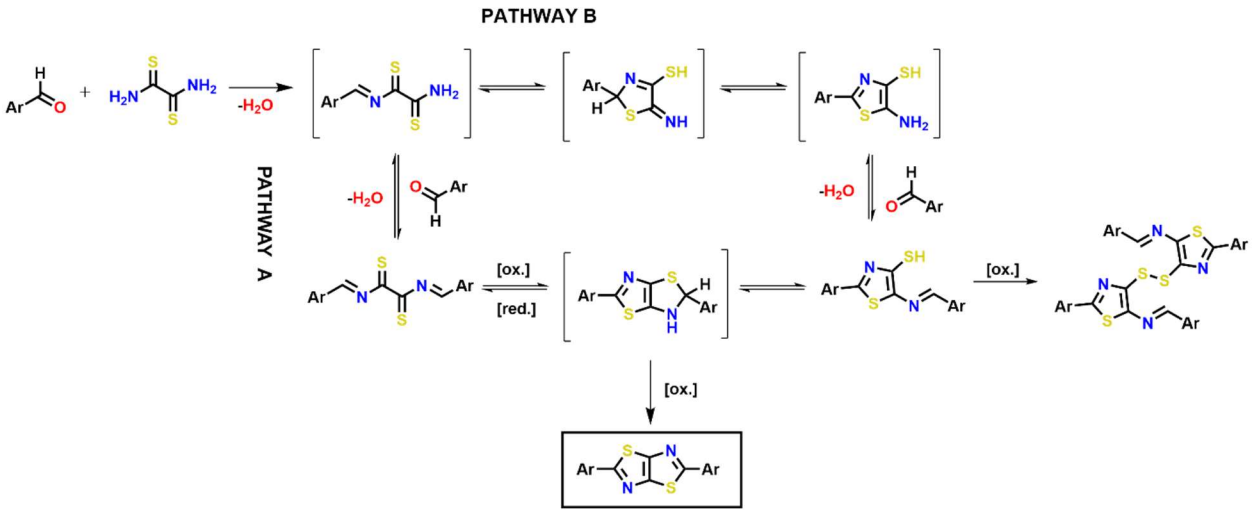

Figure 3.1. Proposed literature mechanisms of the Ketcham TTz reaction. **Pathway A:** Classically accepted mechanism proceeding through azomethines. **Pathway B:** Recently suggested mechanism proceeding through iminomercaptothiazole.[1]

For the computational studies, geometry and energy minimizations were carried out on a donor aldehyde (D-CHO), an acceptor aldehyde (A-CHO), rubeanic acid (RA), and the corresponding Tzs, TTzs, and plausible intermediates. 4-(N,N-dimethylamino)benzaldehyde (Me_2N-CHO) and 4-pyridinecarboxaldehyde (Py-CHO) were chosen as the donor and acceptor aldehydes, respectively. These aldehydes were chosen for their correspondence to Bu_2N-TTz-Py, i.e. our most promising 1st generation voltage sensitive dye (VSD) and building block for 2nd generation VSDs (**Chapter 1**). From the energies calculated it is possible to calculate the thermochemistry of a balanced chemical reaction; e.g. reaction energy, transition state energy, etc. Calculation of transition state geometries were attempted by first minimizing with Spartan's

Transition State tool, which "guesses" the transition state based on Spartan's reaction database. Failing to find a suitable reaction model, Spartan will revert to a fallback technique known as "linear synchronous transit" for its guess. This technique is meant to help with faster convergence at higher levels of theory. Despite finding plausible initial guesses using Spartan's tool, no transition state geometries successfully converged at higher levels of theory. Nevertheless, Spartan's 3D environment and specialized transition state tool still provided a convenient method to visualize likely transition states.

From geometry optimizations, also calculated were electrostatic potential maps, exposed electrostatic potential surfaces, local ionization potential maps, and HOMO/LUMO values and maps. The electrostatic potential maps help reveal sites of high electron density (red, negative ionizable group, hydrogen bond acceptor) and low electron density (blue, positive ionizable group, hydrogen bond donor), thus helping to deduce plausible reaction mechanisms. Their drawback, however, is that the electrostatic potential is mapped to the molecule's contact surface, and so, no information on the molecule's exposed sites (i.e. reactive sites) is given. More useful in this regard is visualizing the exposed electrostatic potential surface whereby a molecule's electron density surface is overlaid with 2 electron potential surfaces, diametrically opposed. This map helps visualize areas of both high and low electron density which lie outside the normal electron density, i.e. sites prone to either electrophilic or nucleophilic attack, respectively. Local ionization potential maps are useful for showing regions with easily ionizable electrons which are susceptibility to electrophilic attack; whereas, LUMO maps show regions with low electron density – those susceptible to nucleophilic attack. It should be noted that the LUMO does not always contribute significantly to the reaction of interest. In these cases, maps of higher energy LUMOs may contribute most significantly to the reaction.

Experimental reaction studies were performed under aerobic and anaerobic conditions by sampling the reaction at pre-determined time points and analyzing the samples via LC\PDA\ESI-MS. In this manner, obtained were reaction kinetics data and detailed information regarding product stoichiometry, oxidative effects, and side product formation. Such studies are inspired by the work of Lindsey et al. involving porphyrin synthesis optimization, whereby time-point chromatography-MS experiments were used to identify ideal solvents, acid catalysts, temperature, and oxidation parameters.[10-12] Due to thiazolothiazoles having a similar mechanism (condensation, ring-closing, oxidation) and tarring issues, the Ketcham TTz synthesis was hypothesized to benefit from time-point chromatography-MS experiments as well.

3.2 EXPERIMENTAL METHODS

General. 4-Pyridinecarboxaldehyde, dithiooxamide and all solvents used were purchased from Sigma-Aldrich. All were used without further purification except for 4-pyridinecarboxaldehyde which was filtered through glass wool before using. Density functional theory (DFT) calculations were performed with Spartan computational software using B3LYP.[15, 16] All LC/PDA/ESI-MS analysis was performed using a reverse phase ThermoFisher Accucore C4, 2.6 µm, 150 x 2.1 mm column on an Accela LC system with Accela photodiode array (2 channel: 260 and 350 nm) and MSQ Plus Mass Detector.

Reaction Monitoring of 2,5-bis(4-pyridine) thiazolo[5,4-d]thiazole (Py_2-TTz, aerobic). 4-Pyridinecarboxaldehyde (136.7 mg, 1.277 mmol) and dithiooxamide (72.5 mg, 0.0608 mmol) were added to a 4 dram vail with 2.5 mL anhydrous DMF. The reaction was stirred at 120 °C for 150 min. 200.0 µL of solution was sampled from the reaction and diluted to 1.000 mL and then

further diluted 10x at time points -30, 0, 5, 15, 30, 60, 90, 120, and 150 min. These aliquots were then immediately analyzed via LC\PDA\ESI-MS.

Reaction Monitoring of 2,5-bis(4-pyridine) thiazolo[5,4-d]thiazole (Py_2-TTz, anaerobic). 4-Pyridinecarboxaldehyde (200.0 mg, 1.868 mmol) and dithiooxamide (106.8 mg, 0.8897 mmol) were added to a 3-neck round bottom with 5.0 mL anhydrous DMF. After sparging for 30 min with N_2, the reaction was stirred at 120 °C for 120 min under N_2. 200.0 µL of solution was sampled from the reaction and diluted to 1.000 mL and then further diluted 10x at time points -30, 0, 5, 15, 30, 60, 90, and 120 min. These aliquots were then immediately analyzed via LC\PDA\ESI-MS. After 2 h, the reaction was allowed to cool before vacuum filtering, washing with H_2O, and drying under high vacuum (yellow-tan powder, 73.0 mg, 27.7 % yield).

3.3 RESULTS AND DISCUSSION

3.3.1 Computational Studies

Whereas the lowest energy conformer for the other proposed intermediates can be trivially determined, the DHTE intermediate shows considerably more flexibility. As such, a conformer search was performed on Py_2-DHTE. Since conformer searches are computationally costly, only Py_2-DHTE was chosen due to having a simpler substitution pattern than either a-DHTE and An_2-DHTE. It was reasoned that the optimal conformer for Py_2-DHTE would be a good blueprint for the other DHTE intermediates since the electronic properties of the distal functional groups have relatively little impact on overall equilibrium geometry. The conformer recipe was as follows: 1.) performing a systemic conformer search using MMFF model and Spartan's built-in searching operation, 2.) removing duplicated and conformers with relative energies > 40 kJ/mol, 3.) calculating equilibrium geometries using HF/3-21G, 4.) removing duplicates and conformers with relative energies > 30 kJ/mol, 5.) calculating conformer energies using B3LYP/6-31G*, 6.)

removing conformers with relative energies > 15 kJ/mol, 7.) calculating equilibrium geometries using B3LYP/6-31G*, and 8.) keeping only the lowest energy conformer. The azomethine and thioether intermediates were subjected a similar conformational search before comparing reaction energies.

According to the classically accepted mechanism for the Ketcham reaction, an azomethine intermediate is first formed from N-centered nucleophilic addition followed by condensation. Such behavior from a thioamide is unexpected due to the well-known phenomenon whereby the lone pair of electrons on the nitrogen atom is delocalized into the thiocarbonyl group, thus significantly weakening the nitrogen's nucleophilicity. Indeed, a SciFinder search returns no instances of imine formation which involves an aldehyde and thioamide, nor even an amide. On the contrary, imines are typically formed from amines (whose lone pairs are not significantly delocalized) - whether by condensation with carbonyl compounds, oxidative condensation, oxidation, or oxidative coupling with alcohols.[14] The EEPM, EPM, and LIPM of dithiooxamide corroborate such, showing that N-centered nucleophilic addition to the carbonyl is unlikely as evidenced by the low electron density and ionizability of the corresponding region (**Figure 3.2**). On the other hand, the same maps predict that the S-centered region has high electron density and ionizability, thus suggesting strong nucleophilicity. Therefore, if nucleophilic addition is N-centered then it would most likely involve tautomerization. Consequently, calculations were performed on dithiooxamide and its two tautomers using dual basis B3LYP/6-311++G(2df,2p). The extended basis set gives more accurate energies at the expense of computation time; however, using a dual basis set has been shown to reduce computation time considerably while still providing accurate relative energies, and therefore good estimations of the equilibrium constant (K_{eq}). As summarized in **Table 3.1**, the equilibrium constants of dithiooxamide's tautomers were calculated as 2.4×10^{-8} and 8.1×10^{-19}.

For reference, the K_{eq} and %enol of keto-enol tautomerization for ethyl acetoacetate based on ^{1}H NMR are 0.09 and 8.0%, respectively, at 32 ^{o}C.[17] In other words, tautomerization is almost non-existent, i.e. N-centered nucleophilic addition would proceed exceedingly slowly, if at all.

Table 3.1. Reaction energies and equilibrium constants for dithiooxamide tautomers

Compound	Reaction Energy (E_{rxn}, kJ/mol)	Equilibrium Constant (K_{eq}) @ 120 °C[a]	%tautomer
Imino-thiol	57.27	2.4×10^{-8}	9.2×10^{-9} %
Di(imino-thiol)	136.12	8.1×10^{-19}	1.4×10^{-20} %

[a] estimations from the Boltzmann equation. $K_{eq} \approx \exp(-\Delta E_{rxn}/RT)$

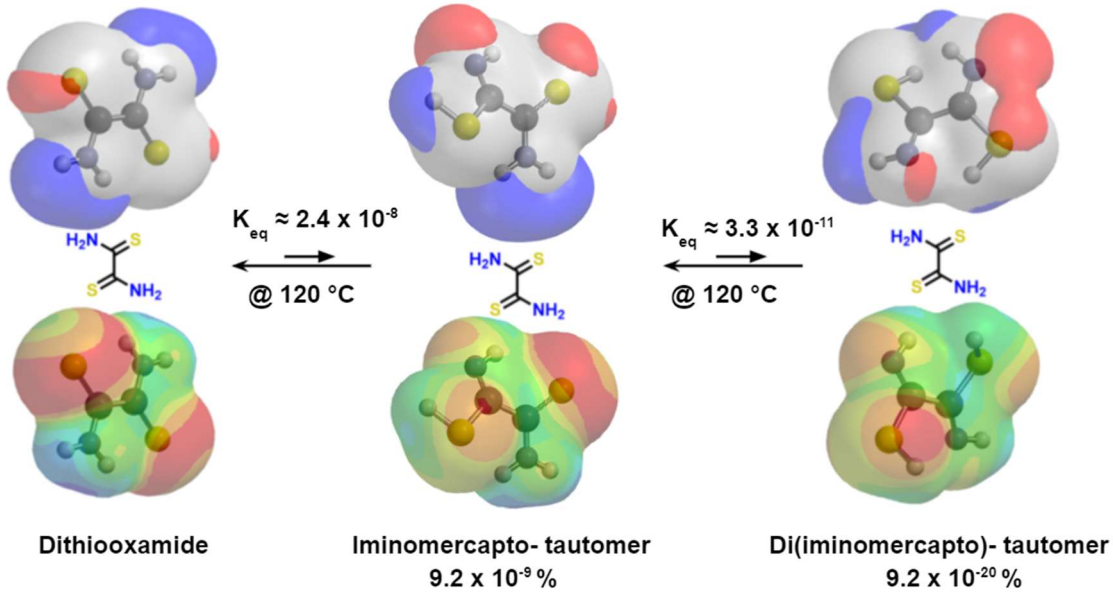

Figure 3.2. Dithiooxamide and its tautomers. Extended electrostatic potential map (top) and local ionization potential map (bottom). K_{eq} at 120 °C was estimated using the Boltzmann equation and energy calculations using B3LYP/6-31G* under the assumption that $\Delta H_{rxn} \approx \Delta E_{rxn}$ and the entropy difference between tautomers is negligible.

Furthermore, although the EEPMs, EPMs, and LIPMs of both tautomers do suggest increased N-centered nucleophilicity, electron density and ionizability are higher over the S-centered region. Consequently, proposed is an S-centered nucleophilic addition mechanism which proceeds through thioether intermediates as opposed to azomethine intermediates (**Figure 3.3**). Attempts were made to identify the transition state for S-centered nucleophilic addition to the

carbonyl; however, convergence failed at higher levels of theory. Nevertheless, a likely transition state was identified using MMFF. Similar attempts were made to identify the transition state of an N-centered nucleophilic addition with not even a reasonable guess being identified.

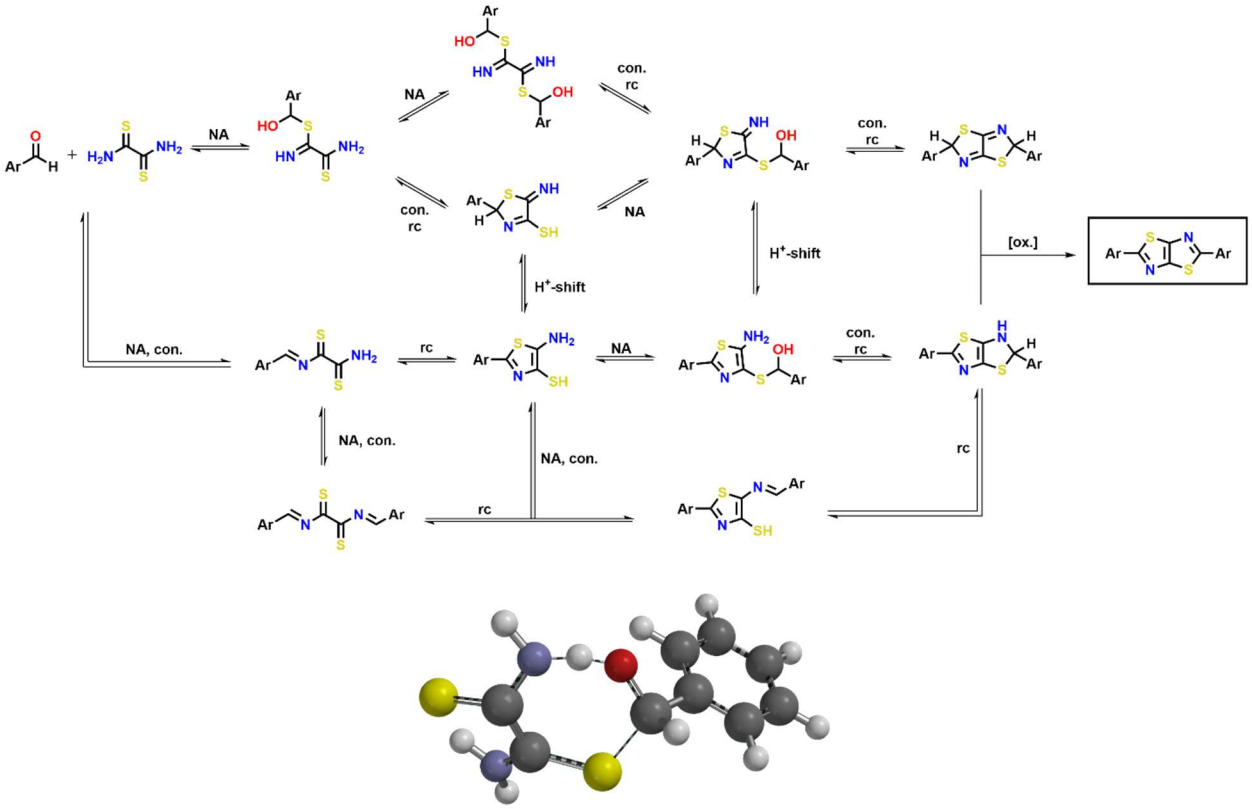

Figure 3.3. Proposed modification to Ketcham mechanism and transition state for the nucleophilic addition of sulfur. The first step involves an S-centered nucleophile as opposed to an N-centered nucleophile. NA = nucleophilic addition, con. = condensation, rc = ring closing

Multiple routes have been suggested because it is unclear in which order certain chemical operations occur. For example, after the first nucleophilic addition, it is possible for either another nucleophilic addition to occur second or for condensation and ring closing to occur second. To further investigate the most likely mechanism, computational calculations were performed on all feasible intermediates from both the N-centered and S-centered mechanisms. The trends are exemplified by the $(Me_2N)_2$-TTz reaction coordinate diagram seen in **Figure 3.4**. Reaction

energies of TTz and its feasible intermediates were calculated from the difference between the total energy of the products and reactants for the balanced chemical reaction (B3LYP/6-31G*).

$$\Delta E_{rxn} = \sum products - \sum reactant$$

$$2\ ArCHO + RA + \frac{1}{2}O_2 \rightarrow Ar_2TTz + 3H_2O$$

Somewhat surprisingly, all intermediates were found to be endothermic reactions. It was originally hypothesized that formation of the initial thiazole ring would be exothermic given its aromaticity. It would seem to be the case, however, that dithiooxamide is an exceptionally stable molecule. Such a result would seem to hinder the idea that thermodynamic exploitation under anaerobic conditions will lead to better TTz yields since the reagents are the most thermodynamically favored, and considerably so.

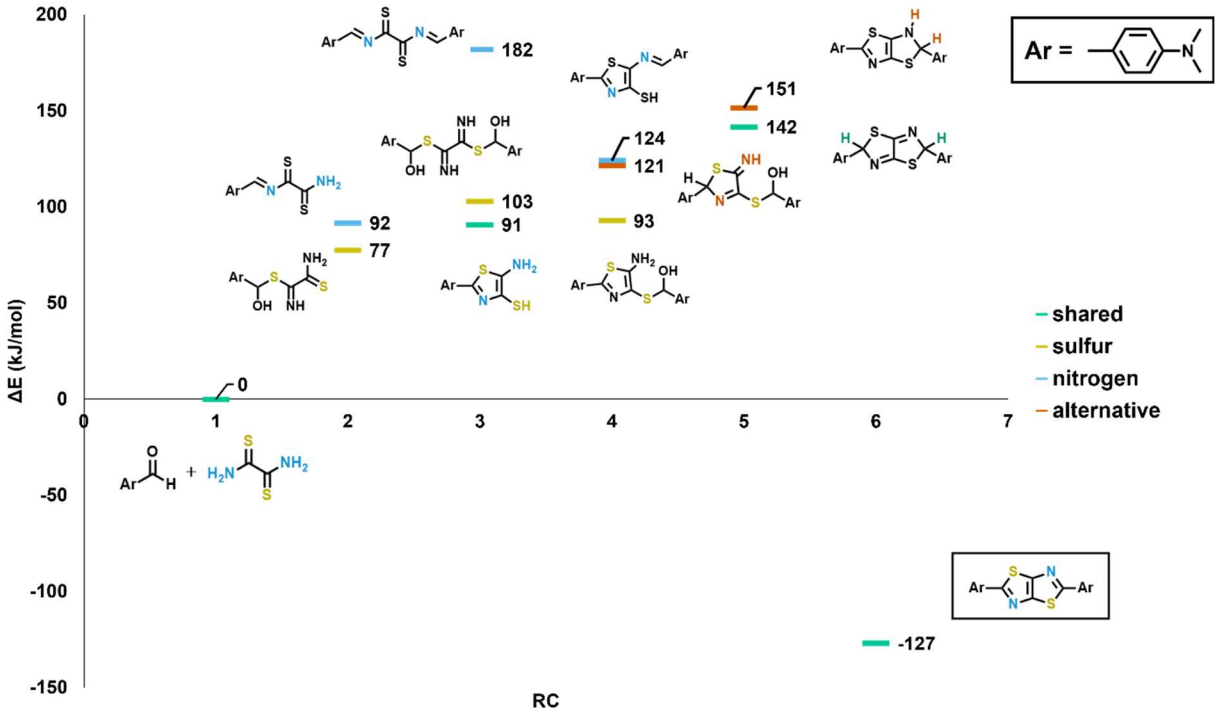

Figure 3.4. Reaction coordinate (RC) diagram of $(Me_2N)_2$-TTz showing shared (green), S-centered (yellow), N-centered (blue), and alternative (orange) intermediates. All intermediates are endothermic, but the S-centered pathway has the lowest energy intermediates.

Also apparent in the RC diagram of $(Me_2N)_2$-TTz is that intermediates derived from S-centered nucleophilic addition (NA) are considerably less endothermic (i.e. more energetically favorable) than intermediates resulting from N-centered NA. Surprisingly, the diazomethine intermediate (reaction coordinate 3) is predicted as the most unstable intermediate overall, and 80 and 90 kJ/mol more endothermic than either the dithioether (DTE) and aminomercaptothiazole (Tz) intermediates, respectively. Such a result is quite a contradiction to current literature where it is commonly thought that the diazomethine (DAM) intermediate is the most stable intermediate. Although thermochemical computation indicates that the Tz intermediate is more thermodynamically stable than the DTE intermediate, the preferred pathway under typical aerobic conditions (i.e. kinetic conditions) is unclear without transition state calculations. If the reaction does proceed mainly through Tz formation, then there exists another instance where either N-centered or S-centered NA is possible. And as was the case for understanding dithiooxamide nucleophilicity, EPMs, EEPMs, and LIPMs were computed for An-Tz and Py-Tz so to understand their nucleophilic behaviors. As seen in **Figure 3.5**, the N-centered region of both Tzs have more exposed negative electron densities and ionization potentials than dithiooxamide, thus suggesting N-centered NA is possible. This makes sense because, in contrast to diothiooxamide, Tz has amino functionality as opposed to amide functionality. Whereas amides are poor nucleophiles due to resonance, amines are well known for their nucleophilicity. Indeed, imines are commonly formed by NA/condensation reactions between amines and aldehydes. At the same time, sulfur is going from thioamide functionality to thiol functionality, thus reducing S-centered nucleophilicity in the Tz compared to that in dithiooxamide. Nevertheless, **Figure 3.5** also shows that the S-centered regions of both molecules have greater areas of exposed electronegativity and stronger ionizabilities than the N-centered region within the same compound. This is most likely because,

while aromatic amines and thiols both commonly donate electron density into the aromatic core thus reducing their nucleophilicities, thiols are weaker electron donors than amines. As such, computational calculations predict that S-centered NA is, again, more likely. Based on the Tz EEPMs, it also seems likely that tautomerization between the core N can lead to an iminium-thioxido intermediate which would increase the likelihood of S-centered NA drastically.

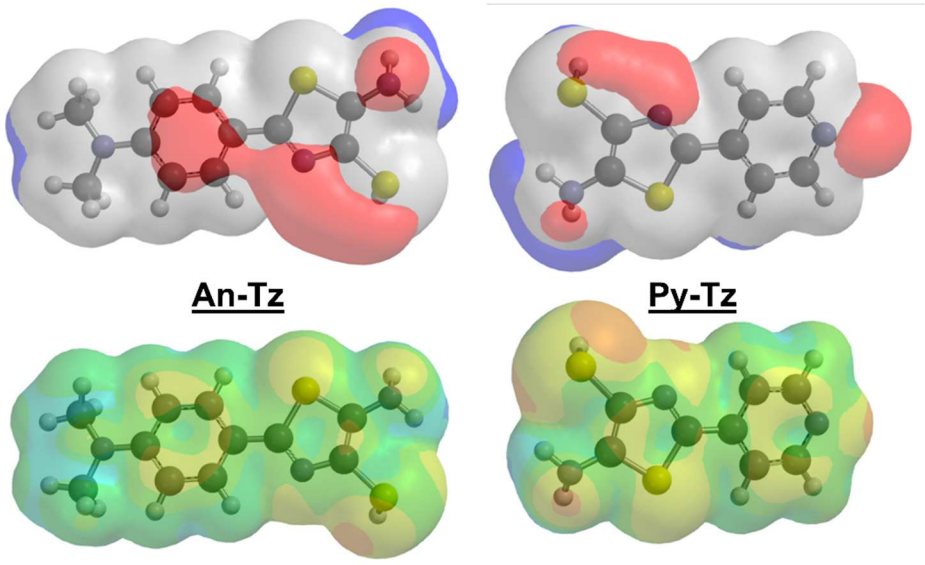

Figure 3.5. Extended electrostatic potential maps (EEPMs, top) and local ionization potential maps (LIPMs, bottom) of An-Tz and Py-Tz intermediates. Both compounds' EEPM and LIPM show that the S-centered region is more exposed and nucleophilic than the N-centered region.

Shown above reaction coordinates 5 and 6 are intermediates corresponding to an alternative route (orange) which precludes the proton shift necessary to form a thiazole intermediate. As depicted in the proposed mechanism (**Figure 3.3**), a proton shift can occur at the iminomercapto-5-hydrothiazole (HTz) intermediate, the iminothioether-5-hydrothiazole (te-HTz) intermediate, or not at all - thus forming the 2,5-dihydrothiazolothiazole (H_2-TTz) intermediate before oxidizing to the desired TTz product. Interestingly, the formation of te-HTz is much more endothermic than that of te-Tz; however, H_2-TTz (which can only be accessed via ring closure of te-HTz) is predicted to be more thermodynamically stable than the 2,3-dihydrothiazolothiazole (H_2Tz-Tz)

intermediate. If, after the first ring closure, proton shifting is rate limiting (which in aprotic solvents is likely), then the HTz to H_2-TTz route is most probably the main route under kinetically controlled reaction conditions.

Although transition states and activation barriers were unable to be calculated, the potential maps and energy profiles strongly suggest that S-centered nucleophilic addition is also more kinetically favored than N-centered NA. It is still theoretically possible, however, that S-centered NA has a higher activation barrier than N-centered NA despite thioether intermediates being considerably more thermodynamically favored. And so, without transition state calculations, conclusions concerning kinetic favorability are less than definitive.

In addition to calculating reaction energies for An_2-TTz and its intermediates, reaction energies were also calculated for Py_2-TTz, An-TTz-Py, and all their respective intermediates. In this way, the effect that electronic differences between donor and acceptor moieties have on thermodynamic stability can be predicted. As shown in **Figure 3.6**, an electron donating moiety tends to have a relatively destabilizing effect compared to an electron accepting moiety with the affect that asymmetric compounds have middling reaction energies, relatively speaking. Such is even true for TTz formation, and so, under thermodynamic reaction conditions symmetric acceptor compounds (e.g. Py_2-TTz) are expected to form in the highest yields. One interesting trend worth noting is that exchanging one or both An moieties for Py moieties significantly increases the stability of te-Tz intermediates. So much so that te-Py_2Tz is predicted to be the most thermodynamically favored intermediate, a reversal compared to the RC of An_2-TTz where calculations predict the thioether and thiazole intermediates as being the most thermodynamically favored intermediates.

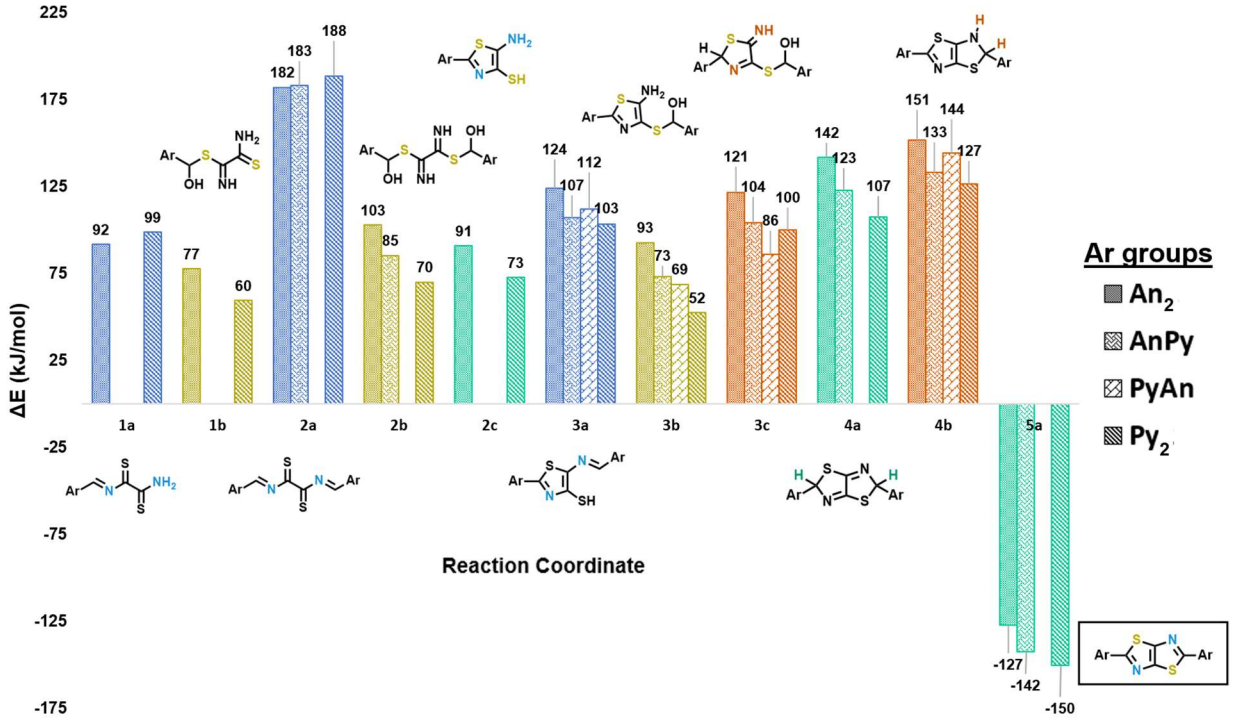

Figure 3.6. Reaction coordinate (RC) chart of An_2-TTz, a-TTz, and Py_2-TTz reactions showing shared (green), S-centered (yellow), N-centered (blue), and alternative (orange) intermediates.

A sulfur carbene structure may be possible. It would give a similar MS, NMR, and IR spectra as the azomethine intermediate. It would also help explain why the Ketcham reaction is thought to only work with aromatic aldehydes (unless under microwave conditions). The carbene stability would be increased by aromatic R groups. Another explanation for seeing the diazomethine intermediate in MS, NMR, and IR spectra is that cyclized and non-oxidized intermediates can revert to the diazomethine structure. Another possible explanation is that the H_2-TTz intermediate may look spectroscopically identically to the DAM intermediate.

3.3.2 Reaction monitoring via LC/PDA/ESI-MS

Reaction monitoring via LC/PDA/ESI-MS was performed on the Py_2-TTz reaction to 1.) better understand reaction kinetics, 2.) probe thermodynamic equilibriums under anaerobic

conditions, and 3.) elucidate the most probable reaction mechanism by identifying intermediates. Ultimately, each of the three goals serve to gain foundational knowledge which can be used to improve TTz yields. Micro-volume aliquots were taken at specified time points of front-loaded frequency and diluted in 10% ACN:H_2O for immediate LC injection. Micro-volume sampling was necessary to limit solvent depletion, and front-loading the frequency sampling ensured elucidation of initial reaction kinetics while also balancing against unnecessary data encumbrance.

The top of **Figure 3.7** summarizes the reaction kinetics for the Py_2-TTz reaction under both aerobic and anaerobic. Plotted are absorbance values measured through Channel UV-B (set to 350 nm) vs. reaction time. 350 nm was chosen because it is near the peak wavelengths of both dithiooxamide (AKA rubeanic acid, RA) and Py_2-TTz. Additionally, few other compounds absorb at 350 nm, thus in effect, filtering the chromatograms so that the consumption and formation of dithiooxamide and Py_2-TTz, respectively, can be clearly seen over the course of the reaction. Under both conditions, the rates of reaction prior to 15 min seemed independent of reaction rates after 15 min, thus possibly suggesting two different phases of the reaction. Indeed, looking at the difference between the total ion count (TIC) MS chromatograms at room temperature and set point (-30 and 0 min) under anaerobic conditions, the Py-CHO peak (retention time, rt = 2.05 min, total scan PDA chromatogram) seems to be completely replaced by a more intense and later eluting peak at rt = 2.58 min. The PDA spectra of the compound eluting at 2.58 min seems to be a combination of dithiooxamide (305 nm) and Py-CHO (262 nm) absorption peaks, while the mass spectra is identical to Py-CHO (note: dithiooxamide is not visible under +V, i.e. no mass spectra). One possible explanation is that the rate limiting step occurs after nucleophilic addition so that a stable intermediate is almost completely formed by the time the reaction temperature reaches its set point.

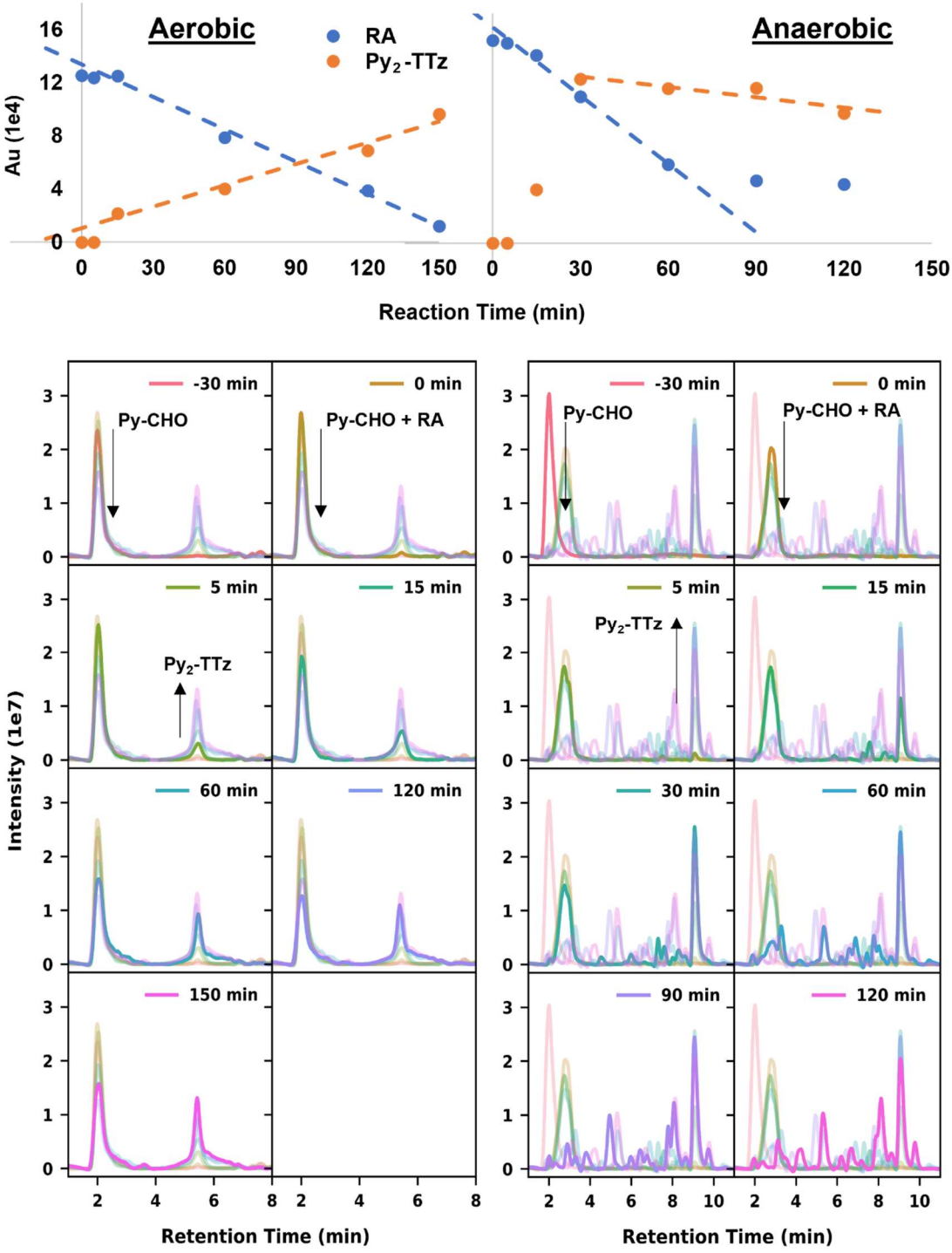

Figure 3.7. (top) Reaction profile summary of rubeanic acid (RA) and Py_2-TTz at 350 nm absorbance and (bottom) total ion count (TIC) MS chromatograms of the Py_2-TTz reaction under aerobic (left) and anerobic (right) conditions. Chromatogram legends refer to the reaction times when an aliquot was taken.

Under aerobic conditions, the concentration of dithiooxamide decreased linearly at a rate of 6.47 % of concentration at 15 min per 10 min, whereas the concentration of Py_2-TTz increased linearly at a rate of 5.56 % of final concentration per 10 min. The difference in consumption and formation rates of dithiooxamide and Py_2-TTz, respectively, can be attributed to the formation of side products. Under anaerobic conditions, the concentration of dithiooxamide decreased linearly from 5 to 60 min at a rate of 11.2 % of concentration at 5 min per 10 min before leveling off after 90 min, whereas the concentration of Py_2-TTz increased rapidly between 5 and 30 minutes before decreasing linearly from 30 to 120 min at a rate of 2.09 % of concentration at 30 min per 10 min. Although the reaction was sparged with N_2 for 30 min prior to heating and maintained throughout the reaction, oxidation to the TTz product was still observed within the first 30 min. Causes considered include 1.) insufficiently stringent anaerobic conditions, 2.) oxygen contamination during sampling, 3.) chemical oxidation via solvent or side products, and 4.) oxidation after sampling. With the current experimental setup, none can be ruled out. Freeze-pump-thaw and/or use of Ar may be required to achieve adequately anaerobic conditions. Oxygen contamination may have occurred since the sampling procedure involved opening the system to allow micropipette insertion. It was believed that positive N_2 pressure would shield the reaction from significant oxygen contamination during sampling, but that may not have been the case. Dehydrogenation involving DMF degradation products or reaction side products seems unlikely but cannot be ruled out. There are even reports claiming good TTz yields under anaerobic conditions so it would not be unprecedented if true. Finally, sample prep for LC analysis was done in open-air conditions, so it's possible that oxidation occurred after-the-fact. Although, Roethling patents suggest that dehydrogenation under aerobic conditions requires high temperatures in polar, aproptic solvents, whereas sample prep was done at room temperature in highly aqueous solutions (10 % ACN:H_2O).

A repeat experiment using Ar and freeze-pump-thaw conditions, stricter sampling procedures, and air-free dilution techniques with sealed autosampler vials would be required to determine a definitive reason for the TTz formation observed.

Nevertheless, the anaerobic reaction study still provides interesting insights concerning the TTz reaction. One interesting aspect worth noting is the slow reduction of Py_2-TTz concentration starting at 30 min and continuing for the rest of the experiment. While the reduction of Py_2-TTz concentration may be partly due to precipitation, the concomitant rise of side products seen in the TIC chromatogram of the anaerobic reaction (**Figure 3.7**, bottom right) suggests reversibility and/or derivatization of Py_2-TTz. Shown in **Figure 3.8** are attempts at structure identification based on mass fragmentation and PDA spectra (see **Appendix D** for spectra). The structure determination for peak A was difficult and the structure suggested is mostly to convey that the parent mass seems to correspond to nucleophilic addition of dithiooxamide to Py-CHO followed by condensation and lost of both H_2O and ammonia. Structures B and C seem to correspond to structures that offer good evidence for S-centered nucleophilic addition based on the presence of hydroxyl functionalization. Structure B also demonstrates, the nucleophilicity of both the amino and thiol groups of the Tz intermediate, which was predicted from computation. No direct evidence of Tz was found, suggesting that te-Tz formation is more thermodynamically stable as predicted computationally. Structure D corresponds to the mass of Py_2-TTz with the addition of another 4-methylpyridyl group, perhaps suggesting that Py_2-TTz can be derivatized at the core via alkylation and hydrogenation, or that the H_2Tz-Tz intermediate can alkylate before oxidation can occur.

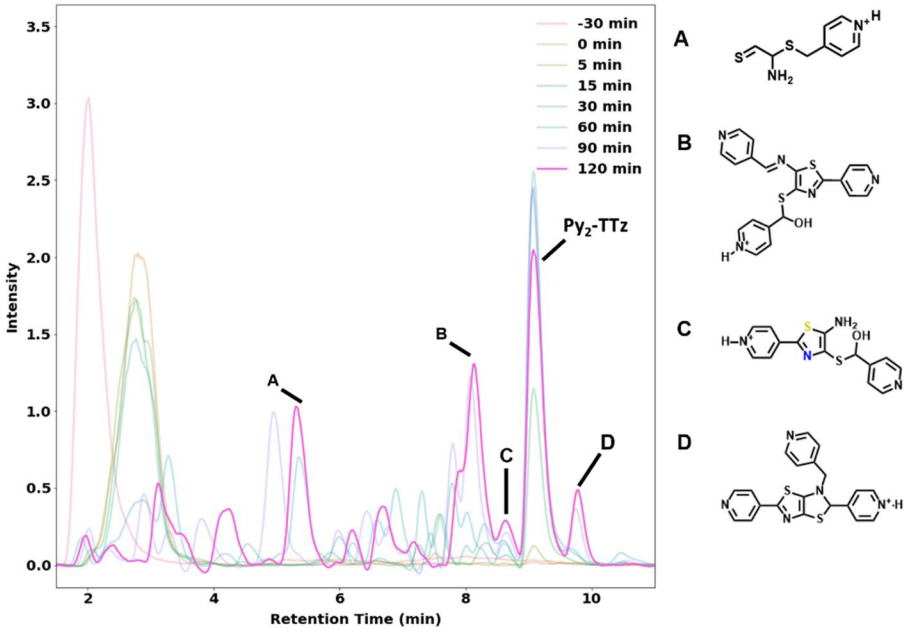

Figure 3.8. Structure assignments of chromatographic peaks based on mass fragmentation and PDA spectra.

3.4 CONCLUSION

In conclusion, poor a-TTz yields of the mixed-pot TTz reaction prompted further mechanistic analysis of the Ketcham reaction in the hopes that fundamental understanding may lead to increased yields. Further understanding was achieved via computational analysis and reaction studies using LC/PDA/ESI-MS. Computational calculations of reactants, products, and probable intermediates yielded various potential maps (EPMs, EEPMs, LIPMs, LMs) and reaction energies which were used to understand the kinetics and thermodynamics of the reaction. The potential maps and reaction coordinate diagrams suggest that the Ketcham TTz reaction most likely proceeds via S-centered nucleophilic addition to afford thioether intermediates, whereas it has been classically accepted that the reaction proceeds via N-centered nucleophilic addition to a diazomethine intermediate. Not only was the diazomethine intermediate found to be kinetically unfavorable, relying on the extremely slow tautomerization of dithiooxamide, but it was also found to be the most thermodynamically unfavorable intermediate as well. Reaction studies via

LC/PDA/ESI-MS provided compelling evidence corroborating computational predictions of thioether intermediates, while also lending additional insight into the formation of side products. Additionally, reaction kinetics were assessed under both aerobic and anaerobic conditions. Under aerobic conditions, it was found that the dithiooxamide and Py_2-TTz are consumed and formed, respectively, linearly over time after the rapid initial formation of an aldehyde-diothiooxamide intermediate. Under anaerobic conditions, PDA and mass spectra suggest that TTz formation is reversible, thus opening the possibility for new experimental designs with thermodynamic, as opposed to kinetic, control. Such foundational understanding can be exploited to increase a-TTz yields by, for example, adjusting reactant concentrations to be commensurate with the kinetic and thermodynamic differences of the products.

3.5 REFERENCES

1. Tokárová, Z.; Eckstein-Andicsová, A.; Balogh, R.; Tokár, K., Survey of the Ketcham reaction for series of furan-substituted thiazolo[5,4-d]thiazoles. *Tetrahedron* **2021,** *89*, 132155.

2. Sayresmith, N.; Saminathan, A.; Sailer, J. K.; Patberg, S. M.; Sandor, K.; Krishnan, Y.; Walter, M. G., Photostable Voltage Sensitive Dyes Based on Simple, Solvatofluorochromic, Asymmetric Thiazolothiazoles. *Journal of the American Chemical Society* **2019**.

3. Dessì, A.; Calamante, M.; Mordini, A.; Peruzzini, M.; Sinicropi, A.; Basosi, R.; Biani, F. d.; Taddei, M.; Colonna, D.; Carlo, A.; Reginato, G.; Zani, L., Organic dyes with intense light absorption especially suitable for application in thin-layer dye-sensitized solar cells. *Chemical Communications* **2014,** *50* (90), 13952-13955.

4. Dessì, A.; Calamante, M.; Mordini, A.; Zani, L.; Taddei, M.; Reginato, G., Microwave-activated synthesis of thiazolo[5,4- d]thiazoles by a condensation/oxidation sequence. *RSC Advances* **2013,** *4* (3), 1322-1328.

5. Papernaya, L. K.; Shatrova, A. A.; Kletskov, A. V.; Petkevich, S. K.; Sterkhova, I. V.; Klyba, L. V.; Levkovskaya, G. G., Microwave synthesis of new azolyl-substituted thiazolo[5,4-d]thiazoles. *Russian Journal of Organic Chemistry* **2016,** *53* (4), 550-556.

6. Papernaya, L. K.; Shatrova, A. A.; Sterkhova, I. V.; Levkovskaya, G. G.; Rozentsveig, I. B., Microwave-assisted synthesis of 2,5-diarylthiazolo[5,4-d]thiazoles from benzaldehydes and dithiooxamide. *Russian Journal of Organic Chemistry* **2015,** *51* (3), 373-377.

7. Reginato, G.; Mordini, A.; Zani, L.; Calamante, M.; Dessì, A., Photoactive Compounds Based on the Thiazolo[5,4-d]thiazole Core and Their Application in Organic and Hybrid Photovoltaics. *Eur. J. Org. Chem.* **2016,** *2016* (2), 233-251.

8. Roethling, T.; Schroeder, A.; Kibbel, H.; Kochmann, W.; Naumann, K. Thiazolothiazole. DD208354, 1984.

9. Witt, D., Recent developments in disulfide bond formation. *SYNTHESIS-STUTTGART* **2008,** (16), 2491-2509.

10. Laha, J. K.; Dhanalekshmi, S.; Taniguchi, M.; Ambroise, A.; Lindsey, J. S., A Scalable Synthesis of Meso-Substituted Dipyrromethanes. *Org Process Res Dev* **2003,** *7* (6), 799-812.

11. Lindsey, J. S.; Hsu, H. C.; Schreiman, I. C., Synthesis of tetraphenylporphyrins under very mild conditions. *Tetrahedron Letters* **1986,** *27* (41), 4969-4970.

12. Littler, B. J.; Ciringh, Y.; Lindsey, J. S., Investigation of Conditions Giving Minimal Scrambling in the Synthesis of trans -Porphyrins from Dipyrromethanes and Aldehydes. *J Org Chem* **1999,** *64* (8), 2864-2872.

13. Ziessel, R.; Nano, A.; Heyer, E.; Bura, T.; Retailleau, P., Rational Design of New Thiazolo□Thiazole Dyes as Input Energy Units in Molecular Dyads. *Chemistry - A European Journal* **2013,** *19* (8), 2582-2588.

14. Huang, J.-M.; Zhang, J.-F.; Dong, Y.; Gong, W., An Effective Method To Prepare Imines from Aldehyde, Bromide/Epoxide, and Aqueous Ammonia. *J Org Chem* **2011,** *76* (9), 3511-3514.

15. Axel, D. B., Density-functional thermochemistry. III. The role of exact exchange. *J Chem Phys 98*, 5648-5652.

16. P J Stephens, F. J. D. C. F. C. M. J. F., Ab Initio Calculation of Vibrational Absorption and Circular Dichroism Spectra Using Density Functional Force Fields. *J Phys Chem 98*, 11623-11627.

17. J.L, B.; Rogers; M.T, Keto-Enol Tautomerism in ß-Dicarbonyls Studied by Nuclear Magnetic Resonance Spectroscopy.1 I. Proton Chemical Shifts and Equilibrium Constants of Pure Compounds. *J. Am. Chem. Soc* **1963,** *86* (11), 2105-2109.

CHAPTER 4: Second generation of voltage sensitive dyes

4.1 INTRODUCTION

The electric potential changes across the cell membrane are indicative of many key cellular events involving cellular communication including differentiation, apoptosis, and gene expression. Additionally, ensemble electric potential changes in neuronal cells underly human information processing which dictate behavior and thought.[1] Consequently, developing methods capable of measuring transmembrane voltages (V_M) across many cells simultaneously has gained considerable interest recently. Such a method to measure the changes of V_M in the dynamics of cellular events requires high spatial and temporal resolution to even be possible.[2] Optical imaging using fluorescent indicators is one such method because mass imaging can occur simultaneously and fluorescence is fast enough to record the rapid membrane polarization events. Unfortunately, however, current dyes still lack sufficient sensitivity and selectivity due issues involving tissue absorption, autofluorescence, poor membrane staining, and low photostability.

To address current issues with voltage sensitive dyes (VSDs), we developed a family of asymmetric TTzs whose unique structure enables a large transition dipole moment, and therefore high environmental sensitivity (see **Chapter 1**). We showed that Bu_2N-TTz-Py has low background noise, excellent membrane staining characteristics, good photostability, and low cytotoxicity. Unfortunately, however, Bu_2N-TTz-Py also showed only a modest voltage sensitivity ($\Delta F/F$ = 10% per 100 mV) and wavelengths of excitation and emission too energetic for tissue transparency. For reference, current state-of-the-art VSDs have demonstrated fraction changes of fluorescence as high as 50% per 100 mV and wavelengths of excitation and emission as red-shifted as 681 nm.[3, 4]

For a-TTzs to achieve higher voltage sensitivities and red-shifted excitation wavelengths, one strategy is to incorporate a pyridinium head group.[5] Such a strategy has been shown to be effective for a variety of anellated hemicyanine dyes (e.g. ANNINE-6plus and di-4-ANEPBS).[6] Compared to pyridine, pyridinium salts and zwitterions are more electron withdrawing and hydrophilic. Having a stronger electron withdrawing group increases the transition dipole moment, thus enhancing environmental sensing. Having a more hydrophilic head group can also improve dye orientation with respect to the electric field of the membrane, thus increasing voltage sensitivity as well.[7] At the same time, increased water solubility of the dye also eases dye loading requirements, thus precluding the use of surfactants.

As such, efforts were made to synthesize an a-TTz VSD with a similar structurally motif as previous pyridinium dyes which include water-solubilizing quaternary ammonium salts. Two different synthetic routes for obtaining Me_2N-TTz-Py(NPr) were tried: 1.) mixed-pot synthesis of Me_2N-TTz-Py followed by alkylation with bromopropyltrimethylammonium bromide ($BrPrNMe_3$), and 2.) alkylation of pyridine carboxaldehyde (CHO-Py) by $BrPrNMe_3$ followed by mixed-pot synthesis to afford the desired pyridinium a-TTz product. Optimal solvent selection and temperature for the alkylation step in Method 1 was assessed via LC/PDA/ESI-MS. Unfortunately, no set of reaction conditions yielded conclusive evidence that Me_2N-TTz-Py(NPr) was successfully formed. Method 2, however, did provide compelling evidence for successful product formation as evidenced by LC/PDA/ESI-MS analysis.

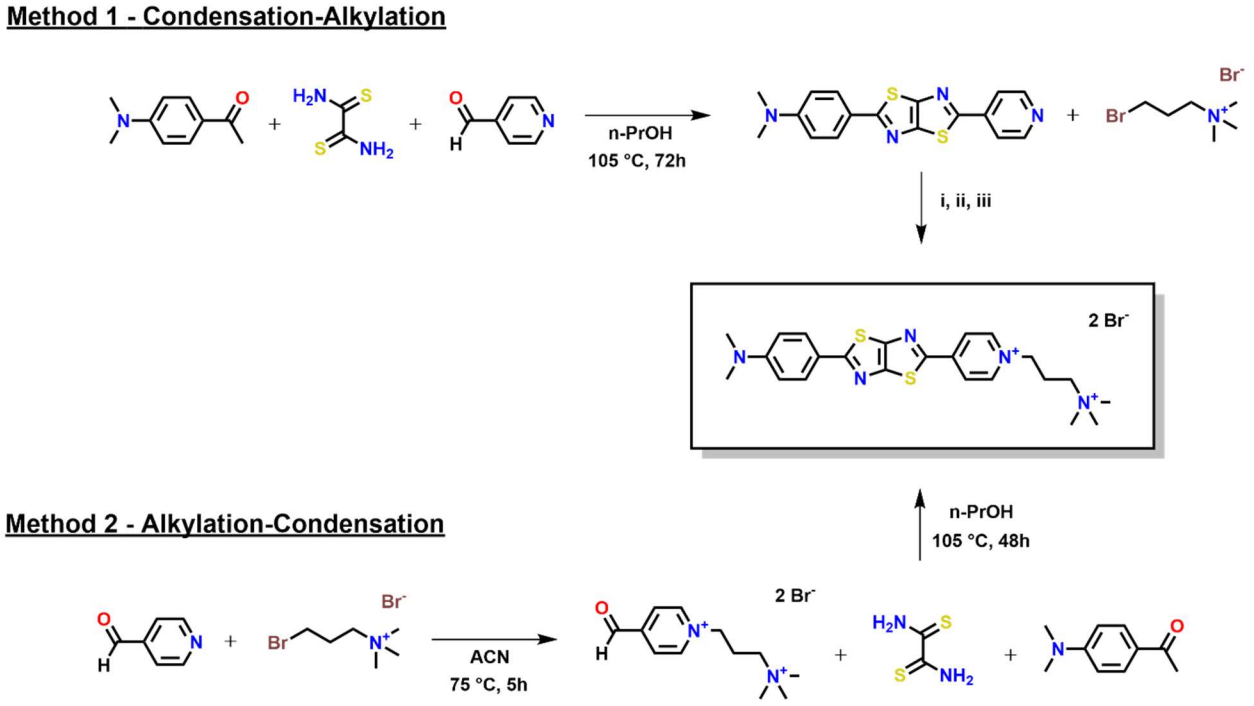

Figure 4.1. Two methods for accessing Me_2N-TTz-Py(NPr). i.) $CHCl_3$ at 40 °C for 24 h, ii.) DMF at 60 °C for 24 h, iii.) DMF at 80 °C for 24 h.

In addition to synthesizing second generation a-TTz VSDs addressing low sensitivity issues, the low selectivity of VSDs was also addressed by synthesizing an a-TTz VSD with click chemistry functionality. Previous reports have shown that clickable VSDs can be covalently tethered to DNA, thus enabling the non-invasive, organelle-specific measurement of V_M in live cells.[8, 9] This is important because the membrane potential of intracellular organelles is distinct from the membrane potential of the plasma membrane.[10] Therefore, to better understand intracellular and organelle-specific cellular events, it is necessary to develop dye systems capable of such specificity.

Specifically for our efforts, Me_2N-TTz-Ph pentynyl ester (click a-TTz) was synthesized by a mixed-pot condensation reaction involving the corresponding pentynyl benzaldehyde ester. The click a-TTz reaction was monitored via LC/PDA/ESI-MS, and the PDA and mass spectra provide compelling evidence of successful formation. While purification via column chromatography was

ultimately successful, the separation resolution was low and isolation difficult. The substituents chosen (i.e. dimethylaniline and pentynyl phenyl ester) were too similar in polarity for ideal column separation. Nevertheless, initial attempts provide a good basis for future directions, including the use of more nonpolar donating moieties and/or post-synthetic esterification.

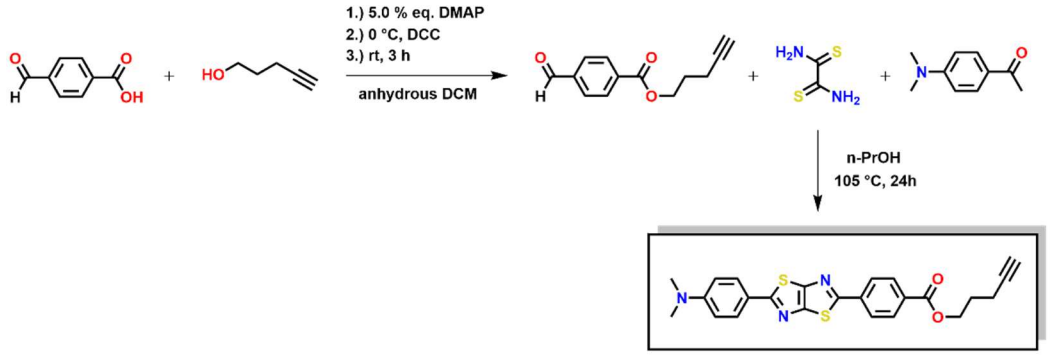

Figure 4.2. Two methods for accessing Me_2N-TTz-Py(NPr). i.) $CHCl_3$ at 40 °C for 24 h, ii.) DMF at 60 °C for 24 h, iii.) DMF at 80 °C for 24 h.

4.2 EXPERIMENTAL METHODS

4.2.1 Me_2N-TTz-Py(NPr)

2-(N,N-dimethyl-4-aminophenyl)-5-(4-pyridyl) thiazolo[5,4-d]thiazole (Me_2N-TTz-Py): 4-pyridinecarboxaldehyde (0.1730 g, 1.62 mmol), 4-(dimethylamino)benzaldehyde (0.2410 g, 1.62 mmol), and dithiooxamide (0.1765 g, 1.42 mmol) were mixed in 11.0 mL n-PrOH and refluxed while stirring for 72 h. The condenser was removed and solvent allowed to evaporate. After cooling for 1 h, the solid was dried under reduced pressure. To the solid was added ~1 g of silica gel and ~ 3 mL DCM. The mixture was dried under reduced pressure, dry loaded onto a column, and separated using 2:3 EtOAc:Hex. The clean Me_2N-TTz-Py fractions (yellow band on column, bright green in solution) were combined and dried to a yellow powder (34.6 mg, 6.92 % yield overall). **^{1}H NMR** (500 MHz, d-DCM, δ): 8.67 (d, J = 12.8 Hz, 2H), 7.86 (d, J = 18.3 Hz,

2H), 7.81 (d, J = 18.3 Hz, 2H), 6.74 (d, J = 13.7 Hz, 2H), 3.04 (s, 6H). **PDA λ_{max} (H_2O:ACN):** 476 nm. **ESI-MS**: calcd for $C_{17}H_{15}N_4S_2^+$ $[M + H]^+$, 339.07; found, 339.09.

1-[3-(Trimethylammonio)propyl]-4-formylpyridinium dibromide [CHO-Py(NPr)][11]: 4-pyridinecarboxaldehyde (0.3022 g, 2.82 mmol) and (3-bromopropyl)trimethylammonium bromide (0.7740 g, 2.96 mmol) were mixed in 5.0 mL ACN and sparged with Ar for 10 min. The mixture was refluxed at 75 °C and stirred for 5 h under Ar atmosphere, resulting in a highly viscous brown resin. The mixture was allowed to cool and stored under Ar atmosphere. ^{1}H NMR (500 MHz, MeOD-D4, δ): 9.09 (d, *J* = 12.8 Hz, 2H), 8.21 (d, *J* = 15.0 Hz, 2H), 6.06 (s, 0.3H), 5.74 (s, 0.7H), 4.77 (t, J = 6.2 Hz, 2H), 3.59 (t, J = 17.1 Hz, 2H), 3.20 (s, 9H), 2.60 (p, J = 8 Hz, 2H). ^{13}C NMR (126 MHz, MeOD-D4): 160.62, 144.88, 125.80, 94.25, 62.42, 57.52, (52.74, 52.71, 52.68), 24.92. PDA λ_{max} (H_2O:ACN): 258 nm. ESI-MS: calcd for $C_{12}H_{19}N_2O^+$ $[M – HBr – Br]^+$, 207.15; found, 207.18.

2-(N,N-dimethyl-4-aminophenyl)-5-(4-[3-(trimethylammonio)propyl]pyridinium thiazolo[5,4-d]thiazole dibromide [Me_2N-TTz-Py(NPr)][12]: *Procedure 1.* Me_2N-TTz-Py (6.0 mg, 17.2 μmol) and (3-bromopropyl)trimethylammonium bromide (4.9 mg, 18.1 mmol) were mixed in $CHCl_3$ and heated to 40 °C while stirring. After 24 h, 20 μL of the mixture was dissolved in 1.5 mL 10% H_2O:ACN and ran on LC/PDA/ESI-MS. $CHCl_3$ was removed under reduced pressure and 3.0 mL DMF was added. While stirring, the mixture was heated to 60 °C. After 24 h, an aliquot was taken for LC/PDA/ESI-MS. The solution was then raised to 80 °C. After 24 h, an aliquot was taken and the reaction was allowed to cool overnight. The mixture was gravity filtered and rinsed with water (3 x 10 mL). A yellow filtrate was collected and dried under high vacuum.

Procedure 2. Under Ar, CHO-Py(NPr) (1.0000 g, 2.73 mmol), and 4-(dimethylamino)benzaldehyde (0.4076 g, 2.73 mmol) were mixed in 20.0 mL n-PrOH, and the

mixture was sparged with Ar for 10 min. While stirring and maintaining Ar, the mixture was heated to 105 °C. After complete solvation, dithiooxamide (0.2985 g, 2.48 mmol) in 5.0 mL hot, Ar-sparged n-PrOH was added, and Ar was removed. Stirring and heat were maintained for 48h, after which the reaction was allowed to cool overnight. At 0, 3, 24, and 48 h; 20 µL aliquots were diluted in 1.5 mL 10% H_2O:ACN and analyzed via LC/PDA/ESI-MS. **PDA λ_{max} (H_2O:ACN):** 499 nm. **ESI-MS:** calcd for $C_{23}H_{29}N_5S_2^+$ $[M - 2Br]^+$, 439.19; found, 439.26.

4.2.2 Me_2N-TTz-Pentynyl Ester (click TTz)

2-(N,N-dimethyl-4-aminophenyl)-5-(4-carboxyphenyl) thiazolo[5,4-d]thiazole (Me_2N-TTz-COOH): 4-formylbenzoic acid (0.4331 g, 2.89 mmol), 4-(dimethylamino)benzaldehyde (0.4303 g, 2.89 mmol), and dithiooxamide (0.3149 g, 2.62 mmol) were mixed in 12.0 mL n-PrOH and refluxed while stirring for 24 h. After cooling for 1 h, the solution was gravity filtered and washed with cold n-PrOH. The solid was collected and dried under high vacuum overnight, yielding 309.9 mg of crude product. Crude material (15.9 mg) was purified via column chromatography starting with 2:5 EtOAc:Hex and finishing with 12 % MeOH in 2:5 EtOAc:Hex. Pure fractions of the middle-eluting yellow band were combined and dried under reduced pressure to afford a yellow solid (6.2 mg). **^{1}H NMR** (500 MHz, d-Ac, δ): 8.02 (d, 2H), 7.83 (d, *J* = 11.9 Hz, 2H), 6.82 (d, J = 20.2 Hz, 2H), 6.36 (d, 2H), 3.62 (s, 6H). **MALDI-TOF (m/z)**: calcd for $C_{19}H_{15}N_3O_2S_2$, 381.06; found, 380.84.

Pent-1-ynyl 4-formylbenzoate ester (modified Steglich esterification[13]): 4-Formylbenzoic acid (0.3471 g, 2.31 mmol) and 4-dimethylaminopyridine (0.0141 g, 5.0% mol/mol) were added to 5.0 mL anhydrous DCM. While stirring, the reaction was cooled to 0 °C and 4-pentyn-1-ol (0.215 mL, 2.31 mmol) and DCC were added subsurfacely. After stirring for 5 min, the reaction was stirred at rt for 3 h. The mixture was gravity filtered and washed with DCM. The supernatant

was washed with 0.5 N HCl (2 x 100 mL), saturated bicarbonate (aq., 2 x 100 mL), and dried over $MgSO_4$. After filtering, the solution was dried under reduced pressure. The solid was separated via column chromatography (1:5 EtOAc:Hex), giving a white solid (0.3891 g, 77.7% yield overall) upon drying under reduced pressure. ^{1}H NMR (500 MHz, d-DCM, δ): 10.06 (s, 1H), 8.15 (d, *J* = 14.7 Hz, 2H), 7.92 (d, J = 13.7 Hz, 2H), 4.41 (t, J = 12.8 Hz, 3H), 2.37 (p, J = 3.7 Hz, 2H), 1.99 (m, 3H). GC-MS (m/z): calcd for $C_{13}H_{11}O_3$ [M - H], 215.07; found, 215.1.

Pent-1-ynyl 2-(N,N-dimethyl-4-aminophenyl)-5-(4-benzoate) thiazolo[5,4-d]thiazole (Me_2N-TTz-pentynl ester): Pent-1-ynyl-4-formylbenzoate ester (0.3452 g, 1.60 mmol), 4-(dimethylamino)benzaldehyde (0.2397 g, 1.60 mmol), and dithiooxamide (0.1754 g, 1.45 mmol) were mixed in 10.0 mL n-PrOH and refluxed while stirring for 48 h. After cooling, the crude mixture was gravity filtered and washed with cold n-PrOH (3 x 10 mL). The solid was collected and dried. Mixed in 1.0 mL 5:2 Hex:EtOAc, 19.9 mg of crude material was vortexed. The supernatant was separated via column chromatography (5:2 Hex:EtOAc). The yellow band was collected, concentrated, and dried under reduced pressure - yielding 0.7 mg yellow solid (4 % column yield). **^{1}H NMR** (500 MHz, $CDCl_3$, δ): 8.13 (d, J = 17.4 Hz, 2H), 8.05 (d, J = 17.4 2H), 7.88 (d, J = 17.3 Hz, 2H), 6.75 (d, J = 18.3 Hz, 2H), 4.46 (t, 2H), 3.06 (s, 6H), 2.40 (p, 2H), 2.03 (m, 3H). **PDA λ_{max} (H_2O:ACN):** 421 nm. **ESI-MS**: calcd for $C_{24}H_{22}N_3O_2S_2^+$ $[M + H]^+$, 448.12; found, 448.20.

4.3 RESULTS AND DISCUSSION

4.3.1 Pyridinium a-TTzs

From the reaction studies of the Ketcham TTz synthesis, it became clear that solvent selection influenced the formation of side-products and ease of purification. Typically, the Ketcham TTz reaction is performed in high boiling, aprotic solvents such as dimethylformamide

(DMF) and dimethylsulfoxide (DMSO). For TTzs insoluble in such solvents (e.g. bispyridyl TTz, Py_2-TTz) it is typical that the desired product crystalizes out of solution while side-products remain dissolved, thus easing purification. However, it was found through reaction studies that a significant portion the a-TTz VSDs are soluble in such solvents. Crashing out with an H_2O workup is certainly possible, but it was found that further purification was made difficult by coprecipitating, tar-like side-products which also demonstrated nearly identical polarities to the desired a-TTzs. Inspired by a previous modification found in the literature, n-propanol (n-PrOH) was investigated as an alternative solvent.[14] Although requiring reaction times 4x longer, it was found that side-product formation was reduced. Additionally, the desired a-TTzs were found to precipitate more readily than the side-products that were formed, thus easing purification. Finally, difficulties involving solvent removal were greatly diminished – requiring relatively mild rotoevaporatory conditions compared to the solvents typically used in the Ketcham synthesis. For these reasons, second generation VSDs were synthesized using n-PrOH instead of DMF.

To increase voltage sensitivity and ease dye loading requirements, efforts were made to synthesize a pyridinium derivative of Me_2N-TTz-Py with quaternary ammonium functionality [Me_2N-TTz-Py(NPr)]. Our first thought for preparing pyridinium a-TTzs was to follow a procedure analogous to alkylation of bispyridinium TTzs.[12] Briefly, this procedure first involves the Ketcham synthesis of the TTz followed by SN_2 alkylation using a halocarbon. For bispyridinium, it is necessary to use relatively high temperatures (100 – 130 °C) and long reaction times (6+ hours) to ensure dialkylation. And because pyridine is an electron withdrawing group, the core of Py_2-TTz is electron deficient, thus decreasing the probability of overalkylation. For a-TTzs, on the other hand, the donating moiety activates the core nitrogens for increased reactivity. Consequently, alkylation of the pyridine should be much easier, but so too should alkylation of the

core nitrogens. The extended electrostatic potential and local ionizations potentials maps are useful for demonstrating this phenomenon (**Figure 4.3**).

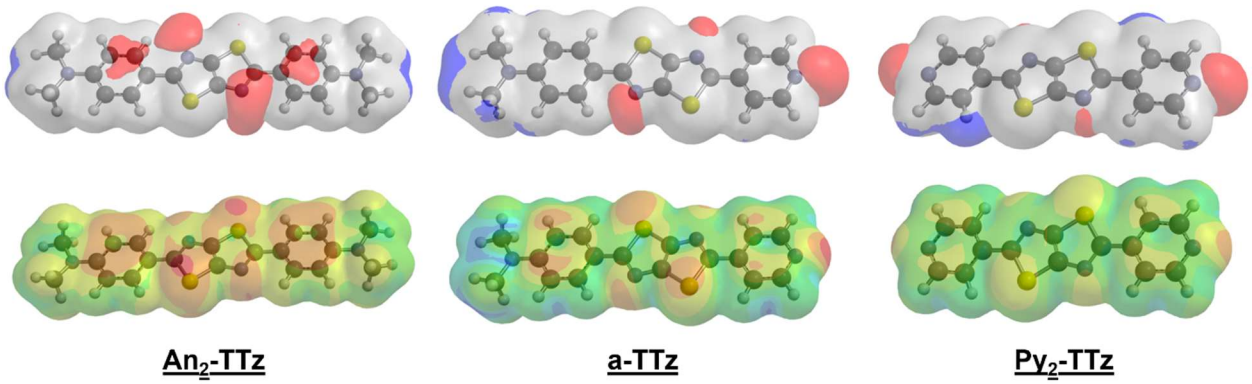

Figure 4.3. Extended electrostatic potential maps (EEPMs) and local ionization potential maps (LIPMs) of An_2-TTz, a-TTz, and Py_2-TTz demonstrating substituent effects on TTz-core activation.

To find optimal conditions which avoid overalkylation, a series of temperature and time studies were carried out whereby the alkylation reaction of pure Me_2N-TTz-Py was sampled at 40, 60, and 80 °C after 24 h reacting at each temperature. The samples were then diluted and analyzed via LC/PDA/ESI-MS (**Figure 4.4**). Additionally, the reaction at 40 °C was performed in $CHCl_3$, whereas DMF was used for the higher temperatures. $CHCl_3$ was investigated as a possible solvent in the hopes that using a relatively volatile solvent would ease purification, especially if Me_2N-TTz-Py(NPr) proved to be soluble in DMF. Unfortunately, chromatograms of samples taken at 24 h reaction time in $CHCl_3$ at 40 °C indicated that no reaction had occurred. Consequently, the reaction solvent was gently evaporated under reduced pressure, replaced by the same amount of anhydrous DMF, and reacted for 24 h at 60 °C. The reaction seemed to be proceeding slowly as evidenced by the large amount of starting material remaining, so the temperature was increased to 80 °C and stirring continued for an additional 24 h. After 24 h at 80 °C, no more of the haloalkane starting material could be detected by neither the PDA nor MS detectors. There was, however, a significant amount of starting TTz leftover despite using an excess molar amount of

bromopropyltrimethylammonium bromide ($BrPrNMe_3$). It was, at first, believed that the rapid consumption of the haloalkane compared to the starting a-TTz was due to over alkylation. The number of extra peaks formed seem to corroborate this hypothesis, corresponding to the mono-, di-, and tri- alkylated TTz derivatives. Unfortunately, however, the mass spectra for each new peak is inconclusive, and none of their fragmentation patterns directly correspond to any alkylated derivative (**Appendix D**).

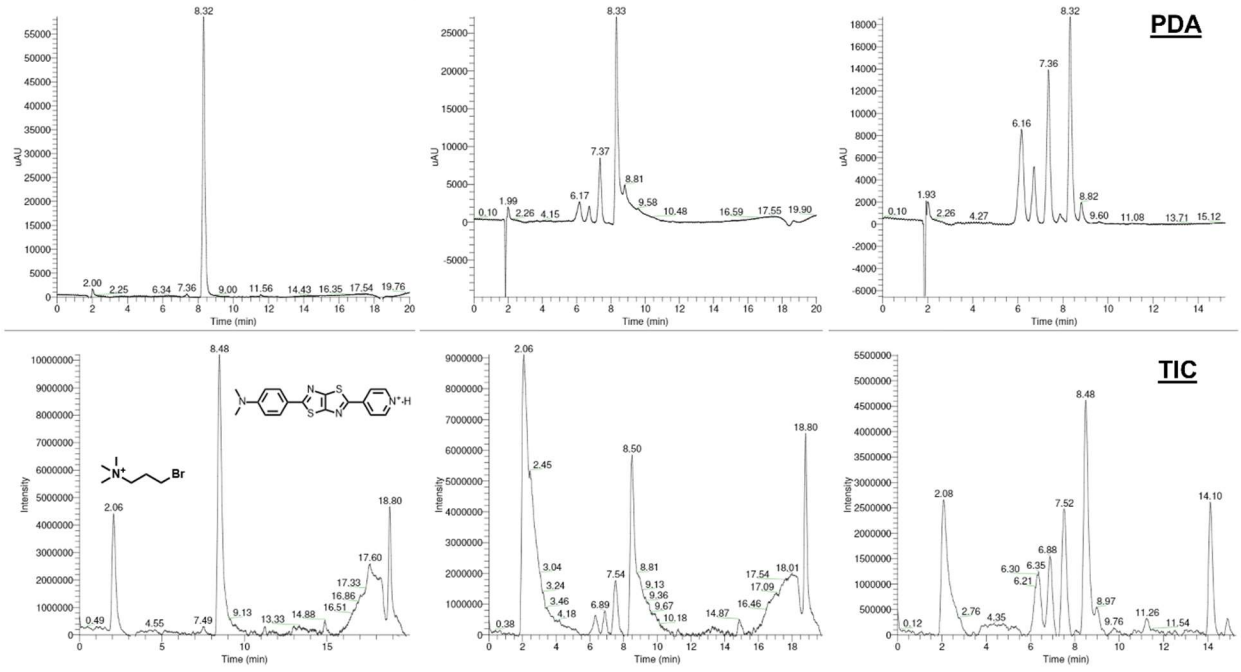

Figure 4.4. Total scan PDA (top) and TIC (bottom) chromatograms of Me_2N-TTz-Py(NPr) alkylation reaction at 40 °C in $CHCl_3$ (left), 60 °C in DMF (middle), and 80 °C in DMF (right).

With unclear results concerning the Me_2N-TTz-Py alkylation reaction, an alternative route was attempted involving alkylation of CHO-Py to form CHO-Py(NPr) and then reacting the pyridinium benzaldehyde with Me_2N-PhCHO and dithiooxamide in a mixed-pot condensation reaction. The alkylation of CHO-Py was adapted from literature procedure.[11] Briefly, CHO-Py and $BrPrNMe_3$ were refluxed in ACN for 5h while under Ar resulting in a highly viscous brown liquid. The reaction was allowed to cool while maintain Ar and as such, so to avoid oxidation of CHO-

Py(NPr). Whereas LC/PDA/ESI-MS gave credible evidence of successful alkylation, the ^{1}H NMR of the crude material lacked the characteristic singlet of aldehyde moieties and instead showed 2 anomalous singlets at 6.06 and 5.74 ppm whose areas summed to 1H. Despite lacking definitive aldehyde evidence, however, the condensation reaction was performed regardless. Without any further steps but maintaining Ar, to the crude CHO-Py(NPr) was added Me_2N-PhCHO, dithiooxamide, and n-PrOH. After the addition, Ar was removed and the reaction was stirred at 105 °C until aliquots analyzed via LC/PDA/ESI-MS indicated the near-full conversion of dithiooxamide (**Figure 4.5**). Somewhat surprisingly, PDA and mass spectra indicated the presence of Me_2N-TTz-Py(NPr) and $(PyNPr)_2$-TTz despite the anomalous ^{1}H and ^{13}C peaks of the CHO-Py(NPr) NMR spectra. Interestingly, the PDA and MS spectra of Me_2N-TTz-Py(NPr) match none of the peaks' spectra of the alkylation reaction first attempted, thus suggesting that the monoalkylation of Me_2N-TTz-Py was unsuccessful at all temperatures and solvents.

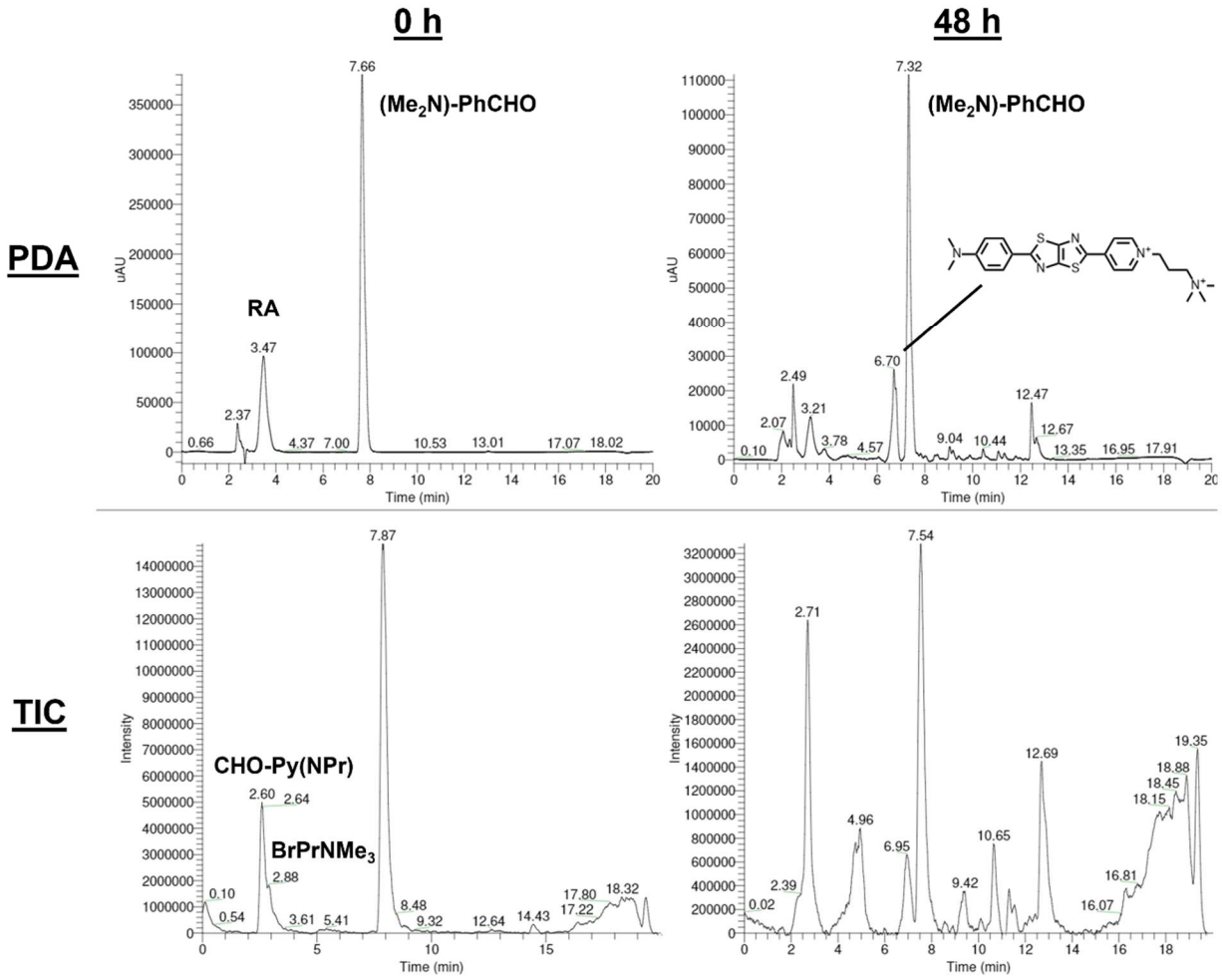

Figure 4.5. Total scan PDA (top) and TIC (bottom) chromatograms of Me_2N-TTz-Py(NPr) condensation reaction at 0 h (left) and 48 h (right).

4.3.2 Click-TTzs

Besides increasing voltage sensitivity and easing dye loading requirements, another aspect which VSDs need improvement is in their specificity. In this regard, an a-TTz comprising a clickable pentynyl ester moiety was pursued. Such a strategy to improve VSD specificity has been reported in the literature whereby click chemistry is used to covalently tether VSDs to DNA or RNA, taking advantage of the inherent specificity of genetic sequences.[15-17] One strategy is to first form the pentynyl benzaldehyde ester (CHO-Ph pentynyl ester) to serve as the electron

withdrawing moiety in a mixed-pot TTz reaction. CHO-Ph pentynyl ester was formed via Steglich esterification of 4-formylbenzoic acid and the corresponding alcohol.[13] Upon successful formation of CHO-Ph pentynyl ester (verified by GC-MS and ^{1}H NMR), Me_2N-TTz-Ph pentynyl ester was synthesized under mixed-pot conditions. The reaction was monitored via LC/PDA/ESI-MS and halted once dithiooxamide was mostly consumed (48 h). The corresponding PDA and mass spectra provide good evidence for the formation of the a-TTz and both $(Me_2N)_2$-TTz and (Ph-pentynyl ester)$_2$-TTz (**Figure 4.6**).

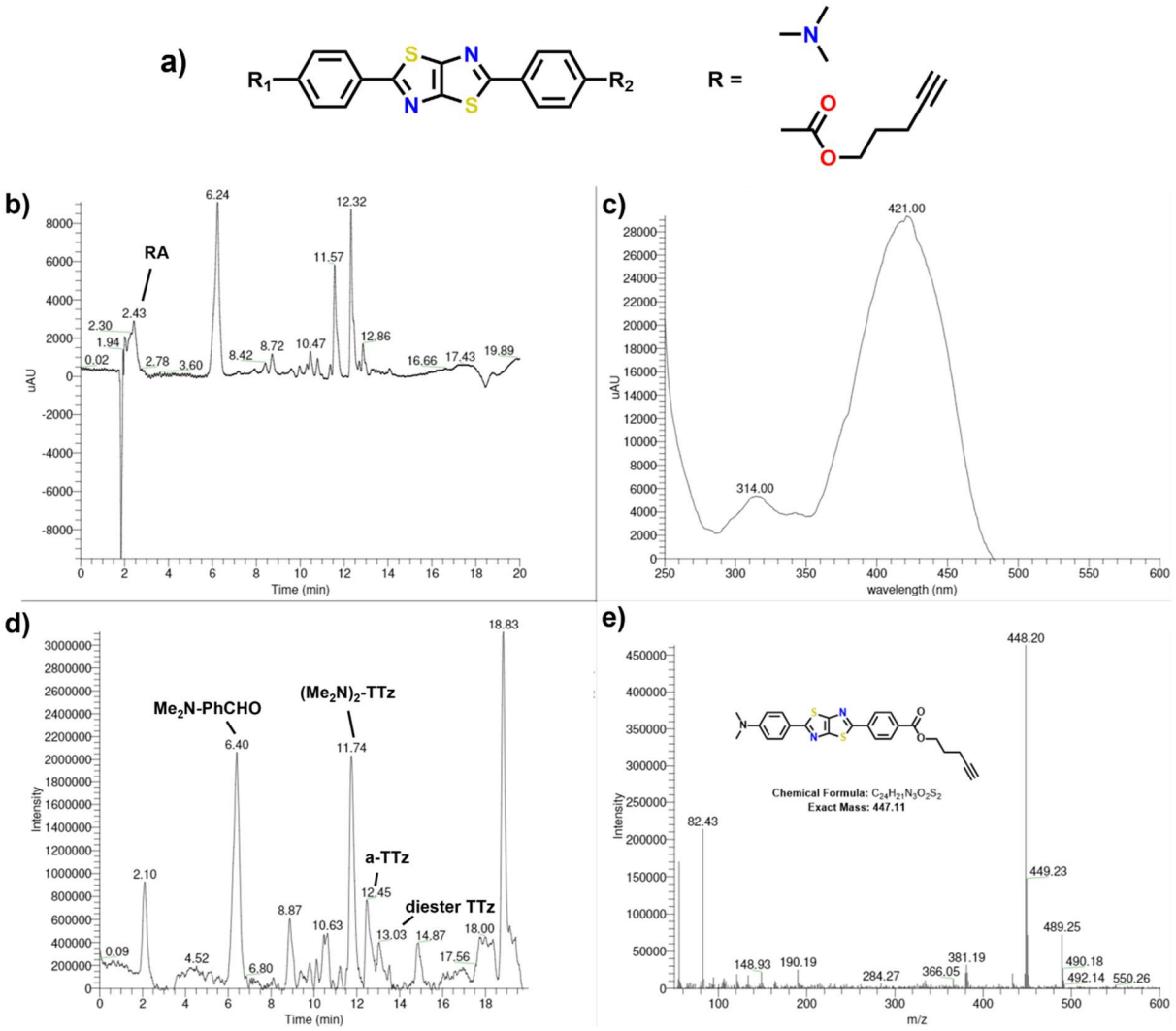

Figure 4.6. TTz structure depicting $(Me_2N)_2$-TTz, a-TTz, and diester TTz (a). Total scan PDA chromatogram (b) and TIC chromatogram (d) of click a-TTz reaction after 48 h. PDA and mass spectra (c and e, respectively) of rt = 12.32, 12.45 min peak corresponding to Me_2N-TTz-Ph pentynyl ester.

Purification via column chromatography was made difficult by the tendency for the three TTz products to closely elute. In contrast to previous a-TTzs, the substituents chosen for the click-TTz reaction (i.e. dimethylaniline and phenyl pentynyl ester) do not differ enough in their polarity to allow easy separation. One solution is to use longer chain aniline derivatives (e.g. dibutylaniline) to make the a-TTz more nonpolar and the donor symmetric TTz even more so. Another strategy is to first synthesize and isolate an a-TTz with carboxylic acid functionality and perform a Steglich esterification on said a-TTz.

4.4 CONCLUSION

In conclusion, current VSDs suffer from low sensitivity, nonideal dye loading requirements, and low specificity. In response, pyridinium a-TTzs with water-solubilizing quaternary ammonium groups and clickable a-TTzs with alkynyl functionality were synthesized. Two different routes were attempted to access Me_2N-TTz-Py(NPr): 1.) alkylation of Me_2N-TTz-Py, and 2.) mixed-pot condensation involving CHO-Py(NPr). The alkylation of Me_2N-TTz-Py was monitored via LC/PDA/ESI-MS at various temperatures and in either $CHCl_3$ or DMF. Unfortunately, PDA and mass spectra provided no definitive evidence for alkylation of any sort. On the other hand, PDA and mass spectra of the reaction via method 2 did provide compelling evidence for the formation of Me_2N-TTz-Py(NPr). Efforts are underway to isolate and characterize Me_2N-TTz-Py(NPr).

As for the click-TTz, LC/PDA/ESI-MS analysis of the corresponding mixed-pot reaction provided compelling evidence for the successful formation of Me_2N-TTz-Ph pentynyl ester. Additionally, isolation of the click a-TTz was successful via column chromatography and

confirmed by NMR and MALDI-TOF spectroscopy. Though successful, column separation was difficult owing to the polarity similarities between the three TTz products. Future efforts will involve exploring more non-polar donating substituents and/or the esterification a-TTz carboxylic acid derivatives as opposed to the direct condensation reaction used.

4.5 REFERENCES

1. Kulkarni, R. U.; Vandenberghe, M.; Thunemann, M.; James, F.; Andreassen, O. A.; Djurovic, S.; Devor, A.; Miller, E. W., In Vivo Two-Photon Voltage Imaging with Sulfonated Rhodamine Dyes. *ACS Central Science* **2018**.

2. Woodford, C. R.; Frady, P. E.; Smith, R. S.; Morey, B.; Canzi, G.; Palida, S. F.; Araneda, R. C.; Kristan, W. B.; Kubiak, C. P.; Miller, E. W.; Tsien, R. Y., Improved PeT Molecules for Optically Sensing Voltage in Neurons. *Journal of the American Chemical Society* **2015,** *137* (5), 1817-24.

3. Huang, Y.-L.; Walker, A. S.; Miller, E. W., A Photostable Silicon Rhodamine Platform for Optical Voltage Sensing. *Journal of the American Chemical Society* **2015,** *137* (33), 10767-10776.

4. Franke, J. M.; Raliski, B. K.; Boggess, S. C.; Natesan, D. V.; Koretsky, E. T.; Zhang, P.; Kulkarni, R. U.; Deal, P. E.; Miller, E. W., BODIPY Fluorophores for Membrane Potential Imaging. *Journal of the American Chemical Society* **2019,** *141* (32), 12824-12831.

5. Loew, L. M.; Scully, S.; Simpson, L.; Waggoner, A. S., Evidence for a charge-shift electrochromic mechanism in a probe of membrane potential. *Nature* **1979,** *281* (5731), 497-499.

6. Kuhn, B.; Roome, C. J., Primer to Voltage Imaging With ANNINE Dyes and Two-Photon Microscopy. *Frontiers in Cellular Neuroscience* **2019,** *13*, 321.

7. Kulkarni, R. U.; Yin, H.; Pourmandi, N.; James, F.; Adil, M. M.; Schaffer, D. V.; Wang, Y.; Miller, E. W., A Rationally Designed, General Strategy for Membrane Orientation of Photoinduced Electron Transfer-Based Voltage-Sensitive Dyes. *ACS chemical biology* **2016,** *12* (2), 407-413.

8. Saminathan, A.; Devany, J.; Veetil, A. T.; Suresh, B.; Pillai, K. S.; Schwake, M.; Krishnan, Y., A DNA-based voltmeter for organelles. *Nat Nanotechnol* **2021,** *16* (1), 96-103.

9. Chakraborty, K.; Veetil, A. T.; Jaffrey, S. R.; Krishnan, Y., Nucleic Acid–Based Nanodevices in Biological Imaging. *Annu Rev Biochem* **2016,** *85* (1), 349-373.

10. Ramzan, R.; Staniek, K.; Kadenbach, B.; Vogt, S., Mitochondrial respiration and membrane potential are regulated by the allosteric ATP-inhibition of cytochrome c oxidase. *Biochimica Et Biophysica Acta Bba - Bioenergetics* **2010,** *1797* (9), 1672-1680.

11. Gibbs-Strauss, S. L.; Vooght, C.; Fish, K. M.; Nasr, K. A.; Siclovan, T. M.; Barnhardt, N. E.; Hehir, C. A. T.; Frangioni, J. V., Molecular Imaging Agents Specific for the Annulus Fibrosus of the Intervertebral Disk. *Mol Imaging* **2010,** *9* (3), 7290.2010.00009.

12. Woodward, A. N.; Kolesar, J. M.; Hall, S. R.; Saleh, N. A.; Jones, D. S.; Walter, M. G., Thiazolothiazole Fluorophores Exhibiting Strong Fluorescence and Viologen-Like Reversible Electrochromism. *Journal of the American Chemical Society* **2017,** *139* (25), 8467-8473.

13. Engel, N.; Steglich, W., Einfache Synthese von 2-Aryl- und 2-Heteroaryl-pyrrolen aus N-Allylcarbonsäureamiden. *Angew Chem-ger Edit* **1978,** *90* (9), 719-720.

14. Ziessel, R.; Nano, A.; Heyer, E.; Bura, T.; Retailleau, P., Rational Design of New Thiazolo□Thiazole Dyes as Input Energy Units in Molecular Dyads. *Chemistry - A European Journal* **2013,** *19* (8), 2582-2588.

15. Veetil, A. T.; Zou, J.; Henderson, K. W.; Jani, M. S.; Shaik, S. M.; Sisodia, S. S.; Hale, M. E.; Krishnan, Y., DNA-based fluorescent probes of NOS2 activity in live brains. *Proceedings of the National Academy of Sciences* **2020**.

16. Narayanaswamy, N.; Chakraborty, K.; Saminathan, A.; Zeichner, E.; Leung, K.; Devany, J.; Krishnan, Y., A pH-correctable, DNA-based fluorescent reporter for organellar calcium. *Nature Methods* **2019,** *16* (1), 95-102.

17. Leung, K.; Chakraborty, K.; Saminathan, A.; Krishnan, Y., A DNA nanomachine chemically resolves lysosomes in live cells. *Nat Nanotechnol* **2019,** *14* (2), 176-183.

CHAPTER 5: Conclusion

Asymmetric thiazolothiazoles (a-TTzs) with electron donor-acceptor functionalities are planar, rigid, heterocycles whose structural motif enables large transition dipole moments, high quantum yields, and large photostability. As such, a-TTzs make for promising environmental, pH, temperature, and membrane voltage sensors. In Chapter 2, reported are a first generation of a-TTzs comprising either diphenyl amino or dibutyl amino donor groups combined with either pyridyl, benzoic acid, or benzaldehyde withdrawing groups. From these donor/acceptor functionalities 4 a-TTzs were synthesized (Bu_2N-TTz-Py, Ph_2N-TTz-Py, Ph_2N-TTz-COOH, and Ph_2N-TTz-CHO) using a mixed-pot variation of the classic Ketcham TTz synthesis. All four derivatives showed remarkable solvatofluorochromism, large molar absorptivities, and near unit quantum efficiencies in nonpolar solvents. Bu_2N-TTz-Py was shown to be a promising membrane voltage sensor, demonstrating 10 % $\Delta F/F$ per 100 mV in HEK cells, negligible cytotoxicity, excellent membrane staining, and photostabilities 4 times higher than current state-of-the-art voltage sensitive dyes (VSDs). However, the main drawbacks of 1st generation TTzs regarding voltage sensing applications include low synthetic yields, subpar voltage sensitivities, poor water-solubility, and blue-shifted wavelengths of excitation and emission.

The ultimate goal of Chapter 3 was to develop a method for increasing a-TTz yields by first gaining a deeper mechanistic and thermochemical understanding of the mixed-pot TTz reaction. Computational calculations were performed on an electron donating aromatic aldehyde (4-N,N'-dimethylformylaniline, Me_2N-PhCHO), an electron accepting aromatic aldehyde (4-pyridinecarboxaldehyde, Py-CHO), dithiooxamide, the 3 corresponding TTz products [$(Me_2N)_2$-TTz, Me_2N-TTz-Py, Py_2-TTz], and two series of probable intermediates stemming from either N-centered or S-centered nucleophilic addition (NA). Based on a combination of various potential

maps and thermochemical calculations, a new mechanism was suggested which involves S-centered NA and thioether intermediates as opposed to the classically accepted N-centered NA leading to diazomethane intermediates. Additionally, a reaction coordinate (RC) diagram was constructed which details the thermodynamic differences of all intermediates and the substituent effects within each intermediate. Calculations predict that all intermediates are endothermic while the overall reaction is exothermic. Also predicted is that electron withdrawing groups have a stabilizing effect across all intermediates and products, such that Py_2-TTz should be the most thermodynamically stable product in a mixed-pot reaction. Unfortunately, no transition states were successfully calculated, and so little kinetic information was be gleaned from the computational studies. Computational calculations were reinforced by aerobic and anaerobic reaction studies of Py_2-TTz involving LC/PDA/ESI-MS analysis at several time points. The PDA and mass spectra of the peaks corresponding to side-products and intermediates provided compelling evidence for S-centered NA. Also gained from these reaction studies were kinetic insights such as the linearity of consumption/formation of dithiooxamide/Py_2-TTz under aerobic conditions, and the apparent reversibility of the oxidation of Py_2-TTz under anaerobic conditions. Such studies provide a more detailed understanding of the TTz reaction, from which changes to the experimental design are more substantiated, and therefore more likely to successfully increase a-TTz yields.

The focus of Chapter 4 involved synthesizing a second generation of a-TTz VSDs with increased voltage sensitivity, water-solubility, and specificity. Efforts to increase the voltage sensitivity and water-solubility of a-TTz VSDs are similar to previous efforts whereby the pyridine head group is alkylated with an alkyl quaternary ammonium salt. In this regard, the synthesis of Me_2N-TTz-Py(NPr) was explored via two separate route: 1.) formation of the a-TTz followed by its alkylation, and 2.) alkylation of Py-CHO followed by the corresponding mixed-pot reaction.

Care was given to avoid overalkylation in Method 1 by optimizing reaction conditions for temperature and solvent. Unfortunately, however, LC/PDA/ESI-MS analysis provided no conclusive evidence that the alkylation of Me_2N-TTz-Py was successful for any reaction condition interrogated. Fortunately, Method 2 did provide compelling evidence for the formation of Me_2N-TTz-Py(NPr). Future efforts will involve scaling up Method 2, obtaining pure a-TTz, and assessing voltage sensitivity improvements.

Also, reported in Chapter 4 are efforts towards synthesizing an a-TTz VSD with click functionality, thus enabling DNA and/or RNA tethering. Such molecular paradigms (i.e. dye-nucleic acid compounds) take advantage of the specificity of nucleic acids and the photophysical properties of small molecules to elucidate specific cellular events (e.g. organellar polarization). In this regard, Me_2N-TTz-Ph pentynyl ester was synthesized by first esterifying 4-formylbenzoic acid followed by the corresponding mixed-pot a-TTz reaction. LC/PDA/ESI-MS was able to verify successful product formation and isolation of the click a-TTz was achieved via column chromatography. However, polarity similarities between the click a-TTz and its corresponding symmetric TTzs complicated purification. Consequently, improvements for future efforts include using more non-polar donor groups (e.g. dibutylaniline) and/or post-esterification.

Overall, a-TTzs have a host of desirable photophysical properties which make them highly suitable for applications involving imaging and sensing. While the 1st generation of a-TTzs demonstrated promising membrane voltage sensing characteristics, they lacked high synthetic yields and sensitivity. Considerable effort was made to better understand the TTz reaction, but more insight and experimental verification is needed to increase a-TTz yields. Likewise, 2nd generation VSDs require further molecular tailoring and/or method optimization. Such efforts are important for streamlining voltage sensing characterization and achieving wide-spread adoption.

Appendix A – Mass Spectra

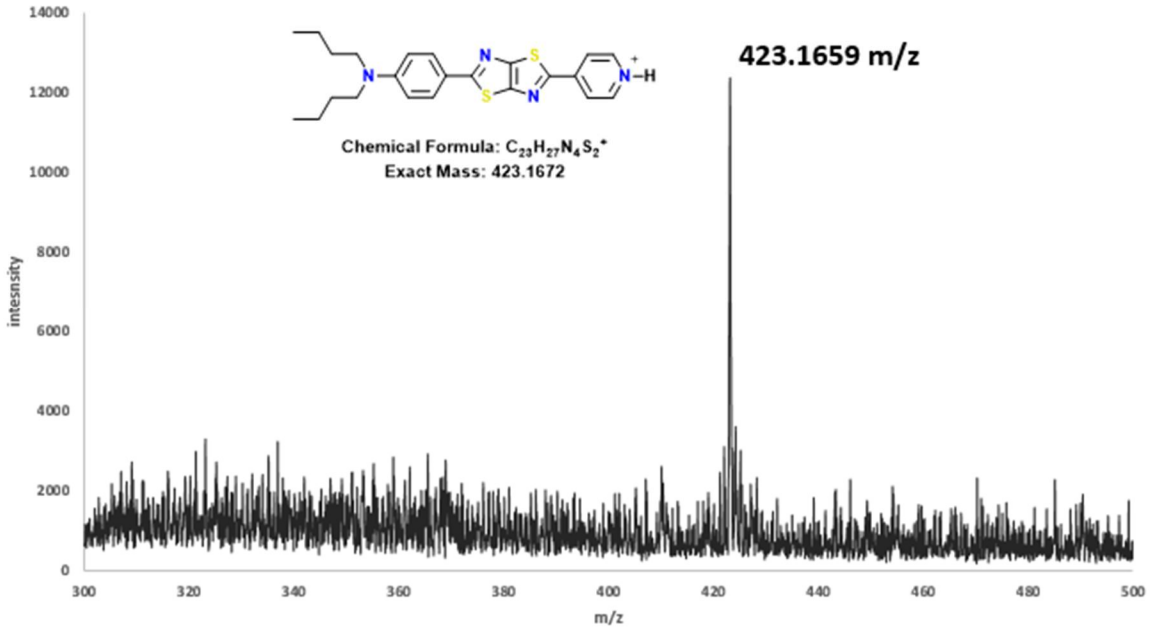

Figure A1. ESI-MS of Bu_2N-TTz-PyH^+ (calcd for $C_{23}H_{27}N_4S_2^+$, 423.1677 m/z; found, 423.1659 m/z).

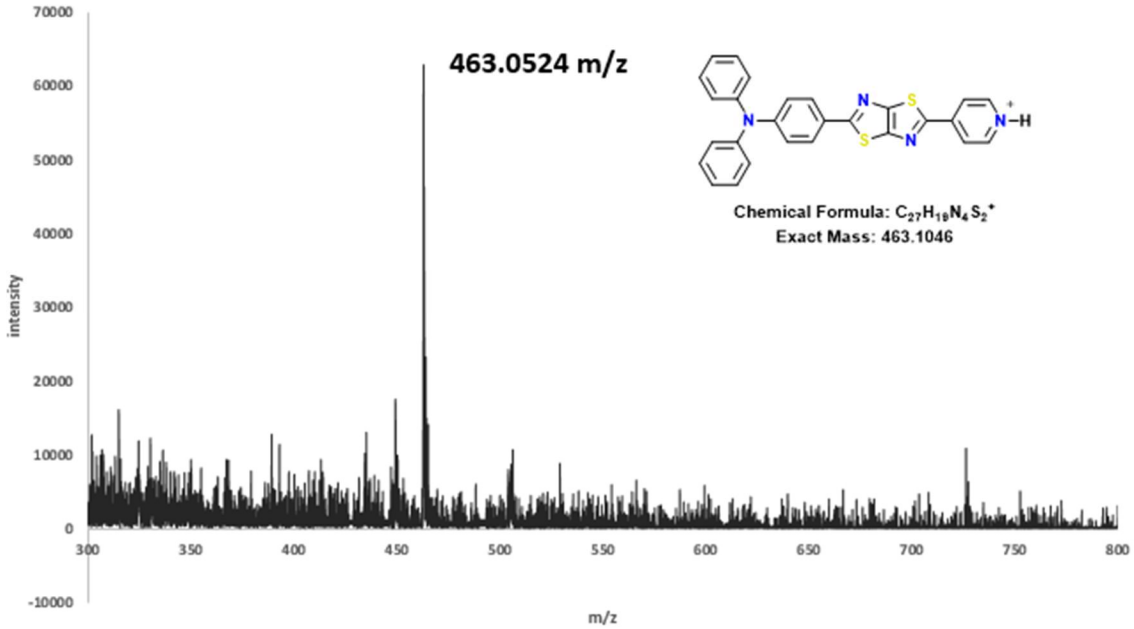

Figure A2. ESI-MS of Ph2N-TTz-PyH+ (calcd for C27H19N4S2+, 463.1051 m/z; found, 463.0524 m/z).

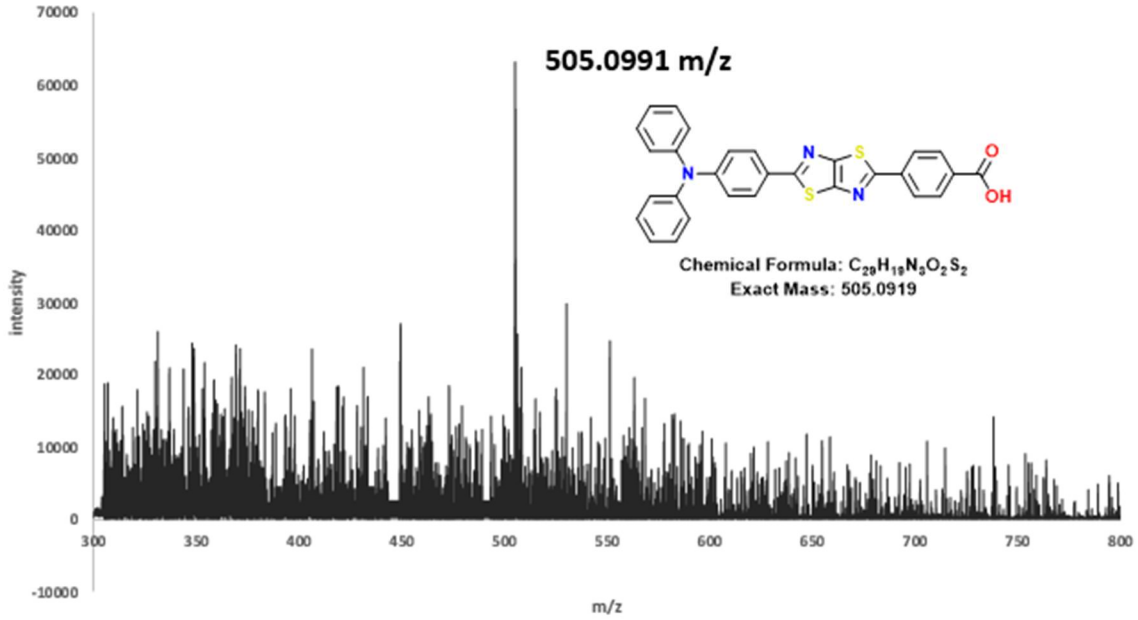

Figure A3. ESI-MS of Ph_2N-TTz-COOH (calcd for $C_{29}H_{19}N_3O_2S_2$, 505.0919 m/z; found, 505.0991 m/z).

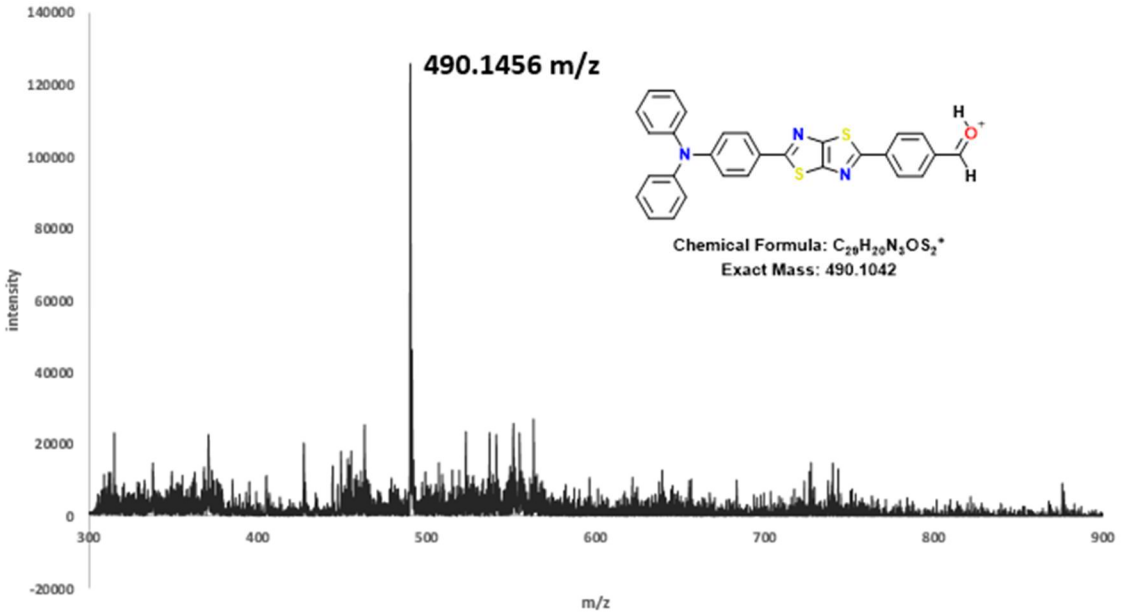

Figure A4. ESI-MS of Ph_2N-TTz-$CHOH^+$ (calcd for $C_{29}H_{20}N_3OS_2^+$: 490.1048 m/z; found, 490.1456 m/z).

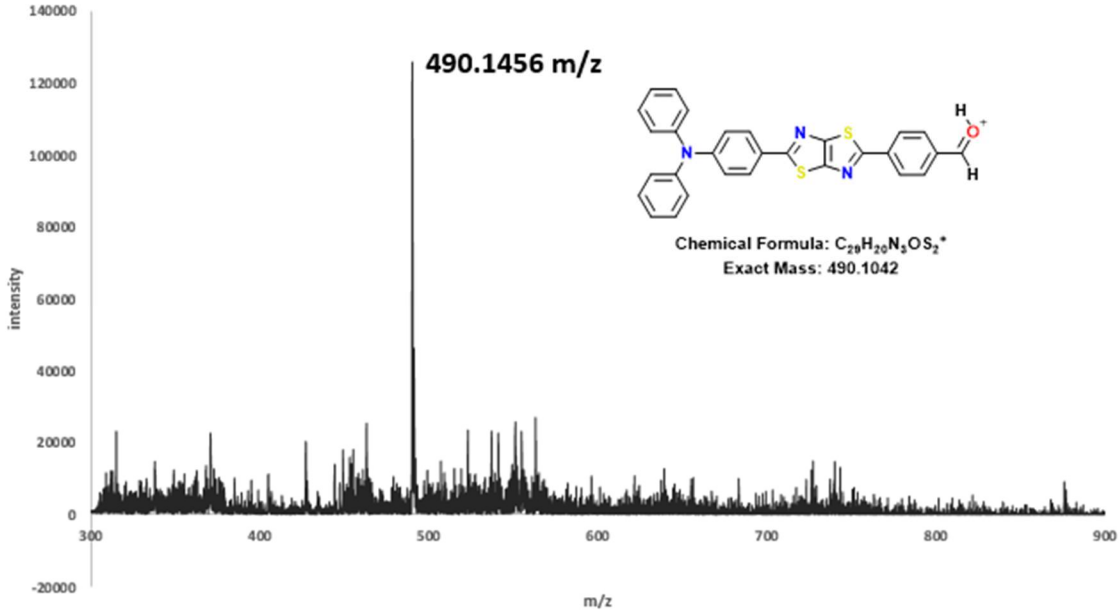

Figure A5. ESI-MS of Ph_2N-TTz-$CHOH^+$ (calcd for $C_{29}H_{20}N_3OS_2^+$: 490.1048 m/z; found, 490.1456 m/z).

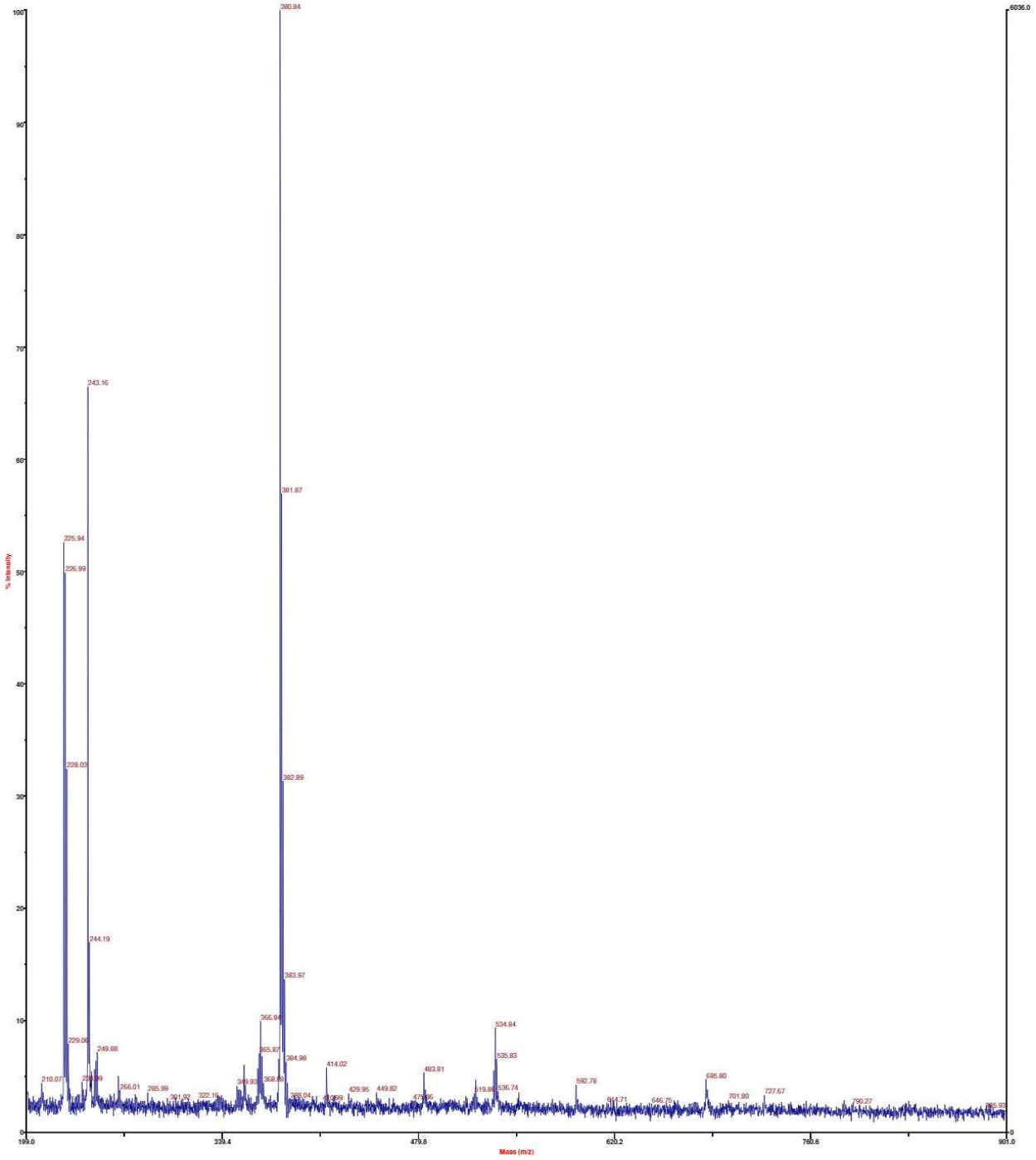

Figure A6. MALDI-TOF of Me_2N-TTz-COOH (calcd for $C_{19}H_{15}N_3O_2S_2$, 381.06 m/z; found, 380.84 m/z).

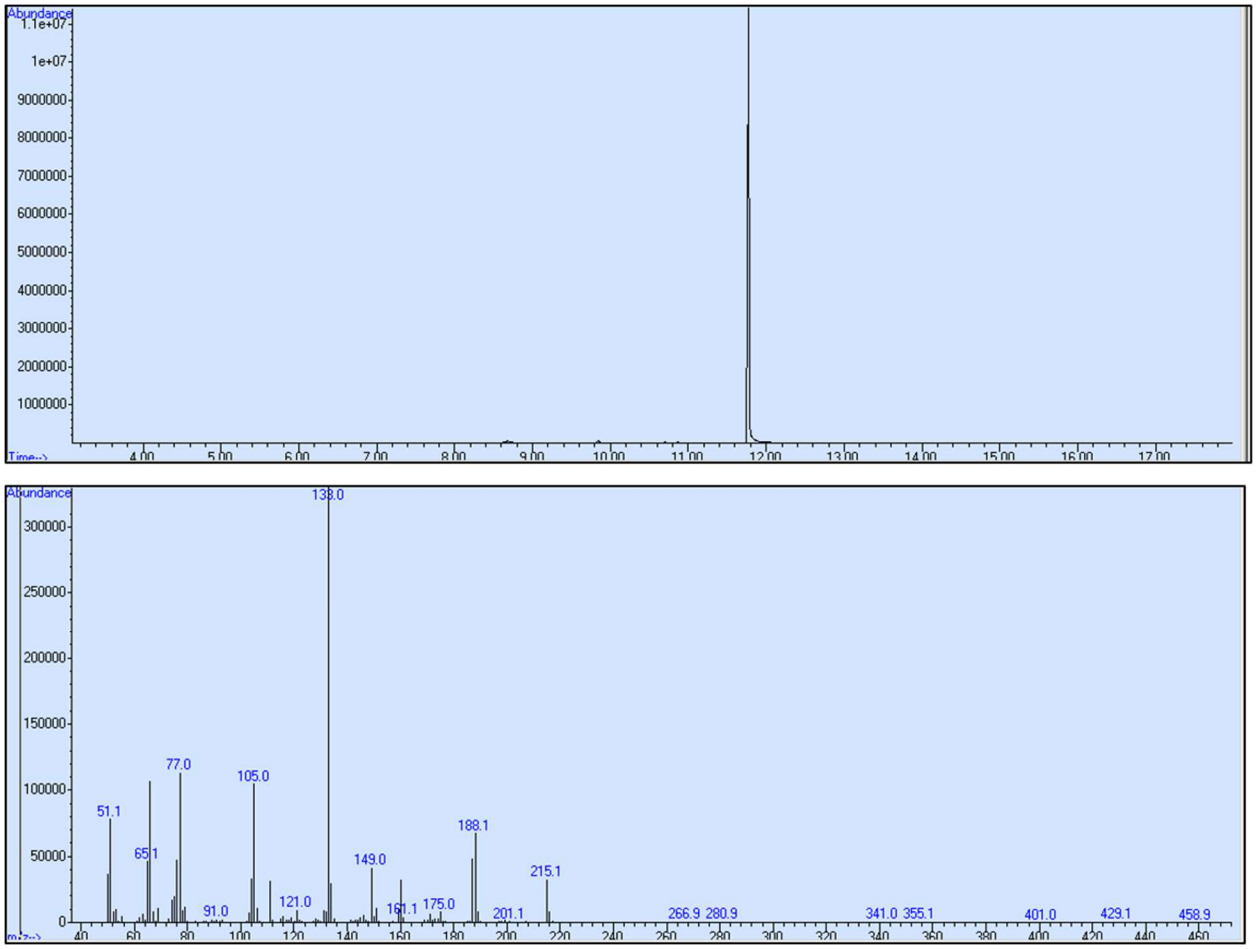

Figure A7. GC-MS of Pent-1-ynyl 4-formylbenzoate ester (GC, top. MS, bottom).

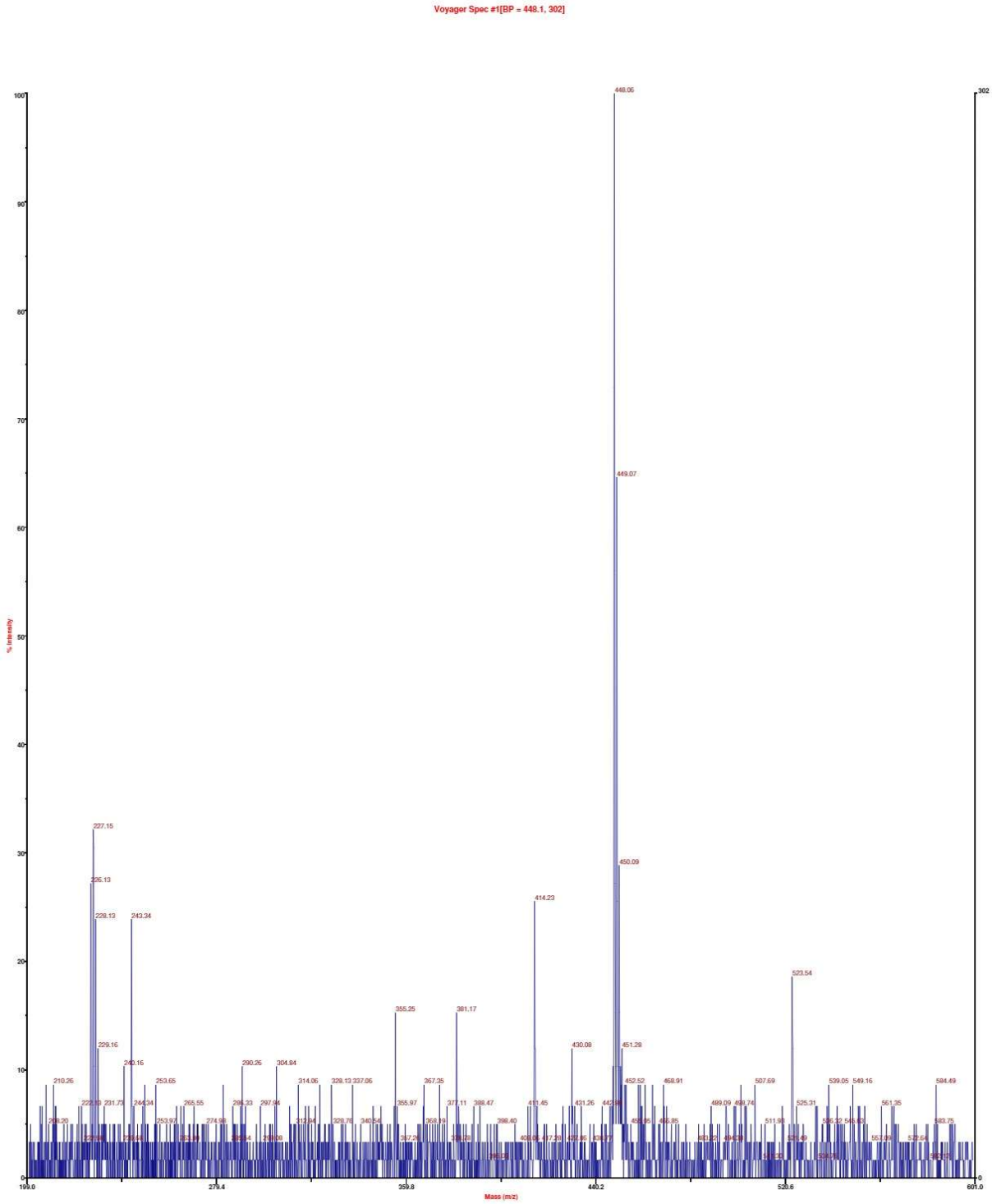

Figure A8. MALDI-TOF of Me_2N-TTz-pentynyl ester (calcd for $[M+H]^+$, 448.11 m/z; found, 448.06 m/z).

Appendix B – ^{1}H NMR

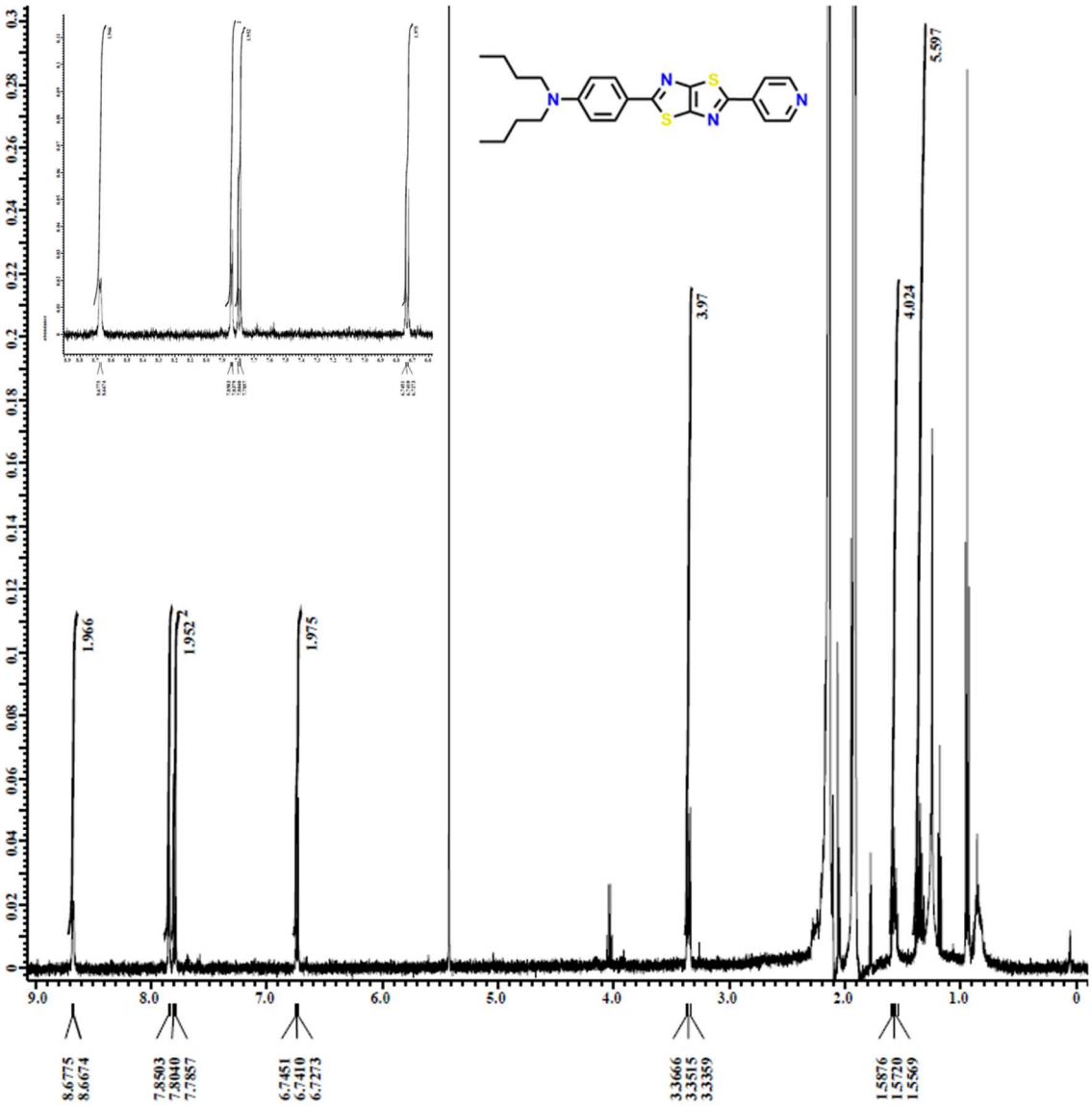

Figure B1. ^{1}H NMR of Bu_2N-TTz-Py in acetonitrile. Inset shows aryl region.

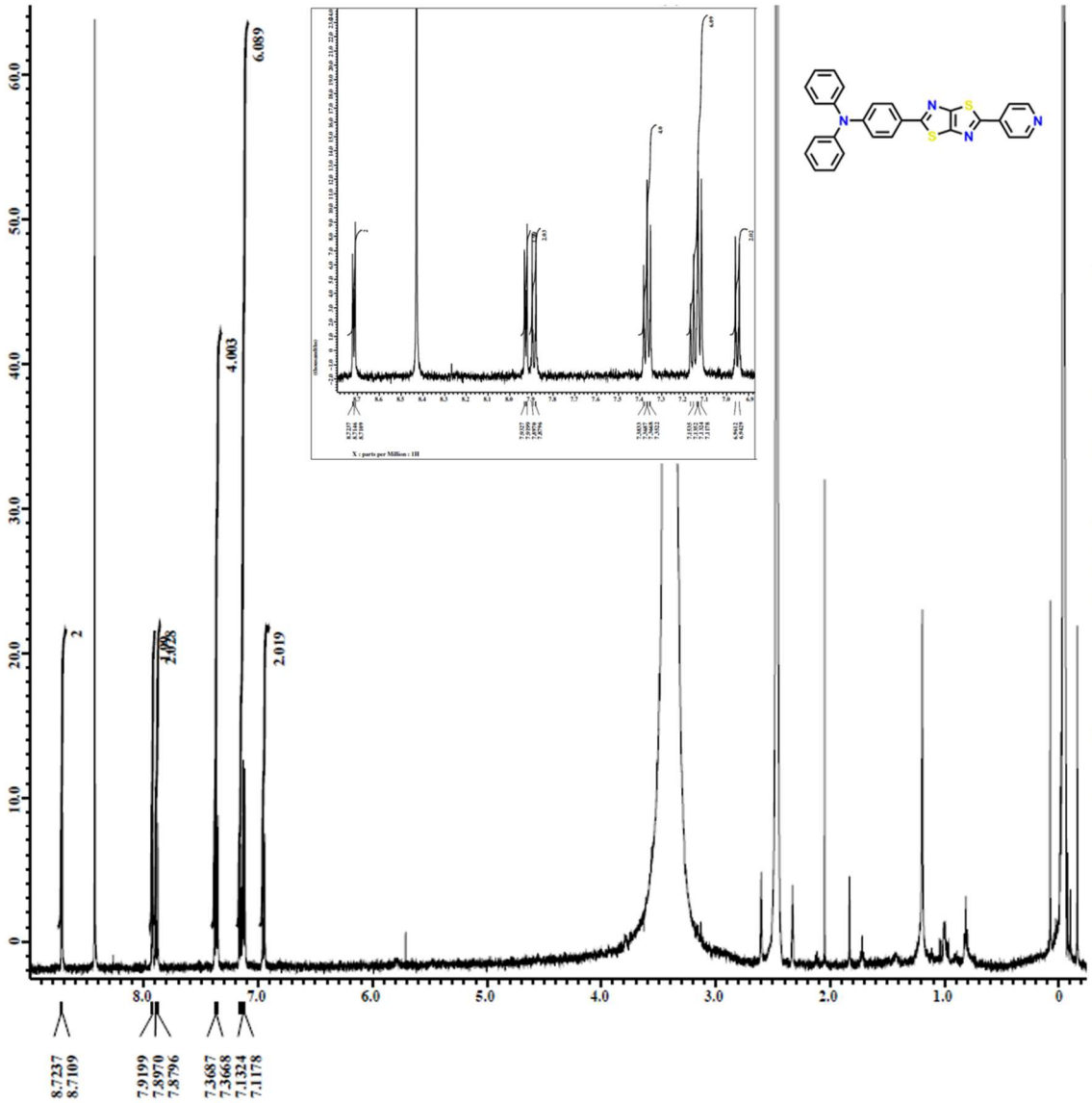

Figure B2. ^{1}H NMR of Ph_2N-TTz-Py in DMSO. Inset shows aryl region.

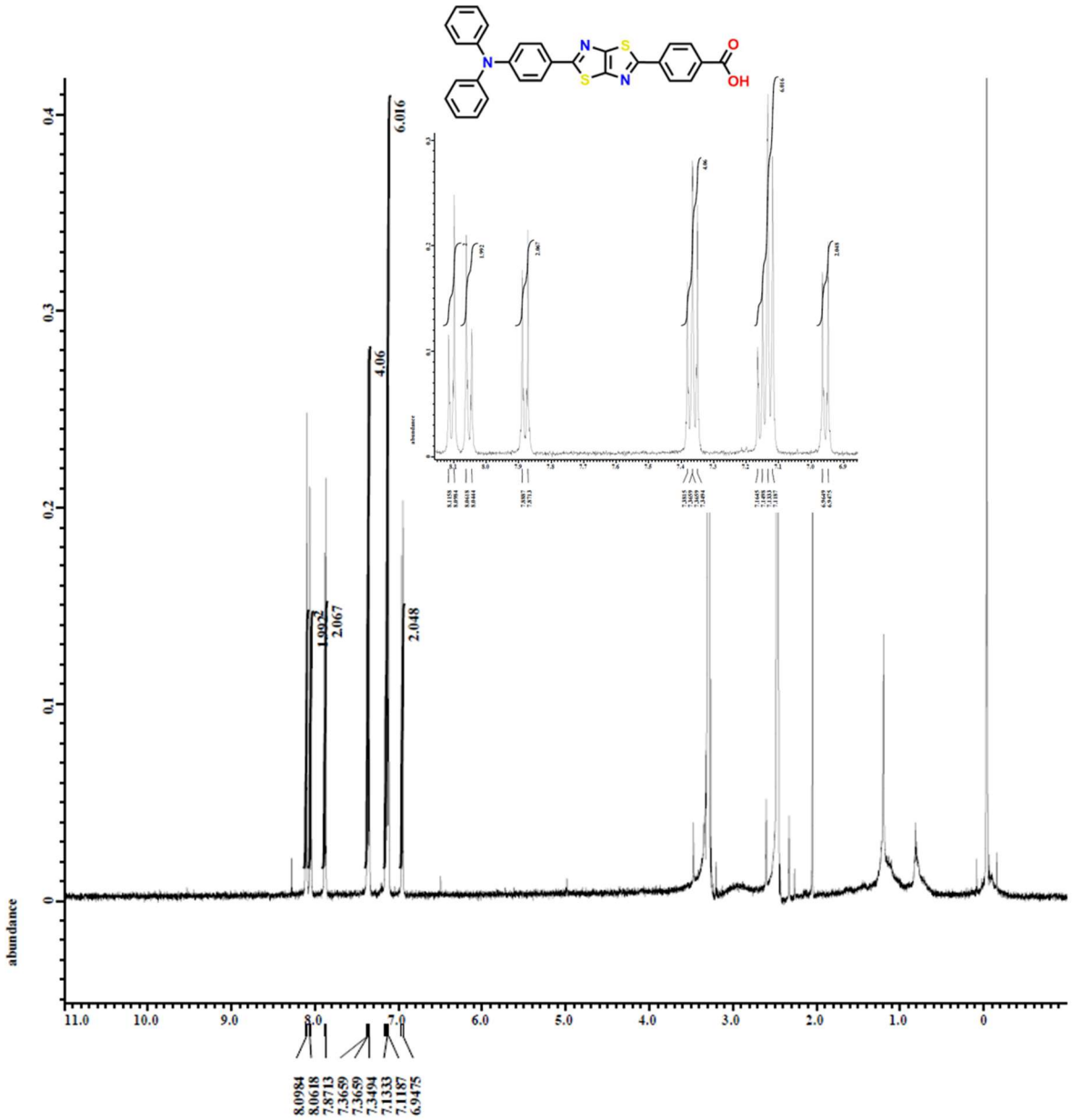

Figure B3. ^{1}H NMR of Ph_2N-TTz-COOH in DMSO. Inset shows aryl region.

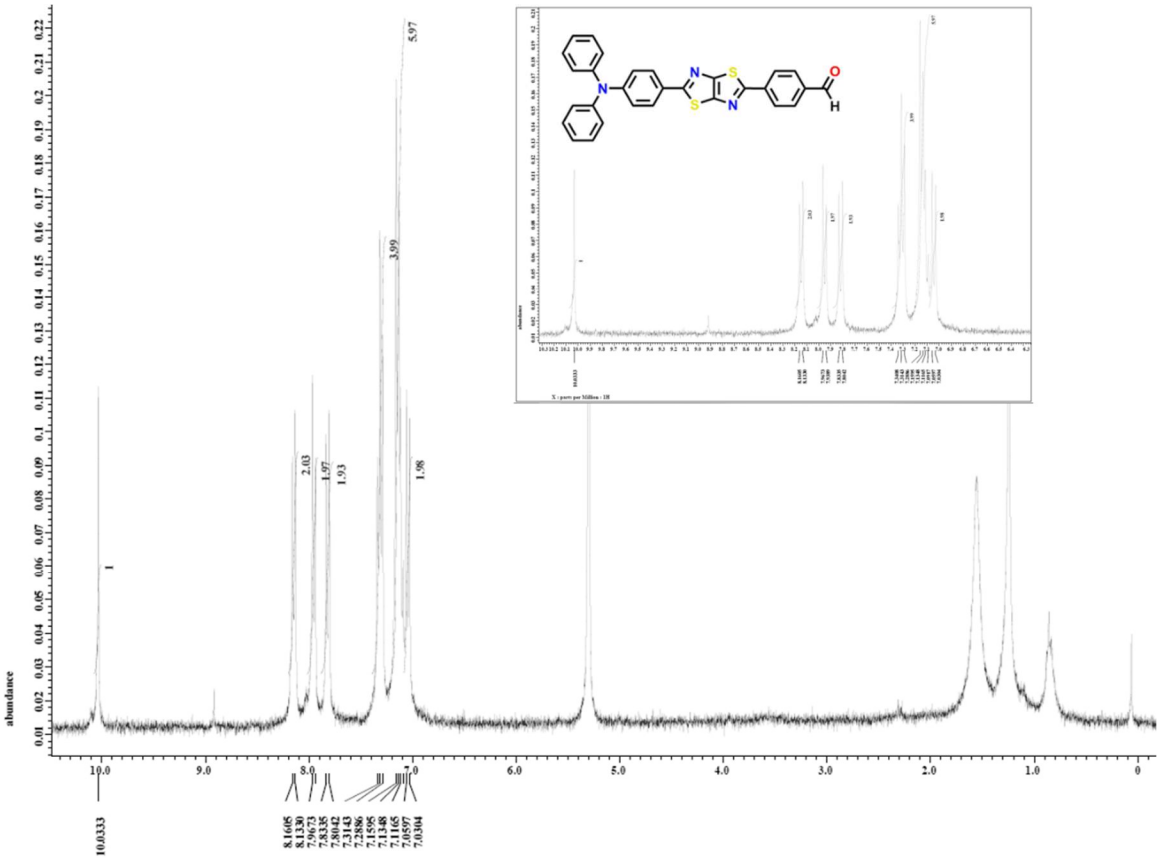

Figure B4. ^{1}H NMR of Ph_2N-TTz-CHO in DCM. Inset shows aryl region.

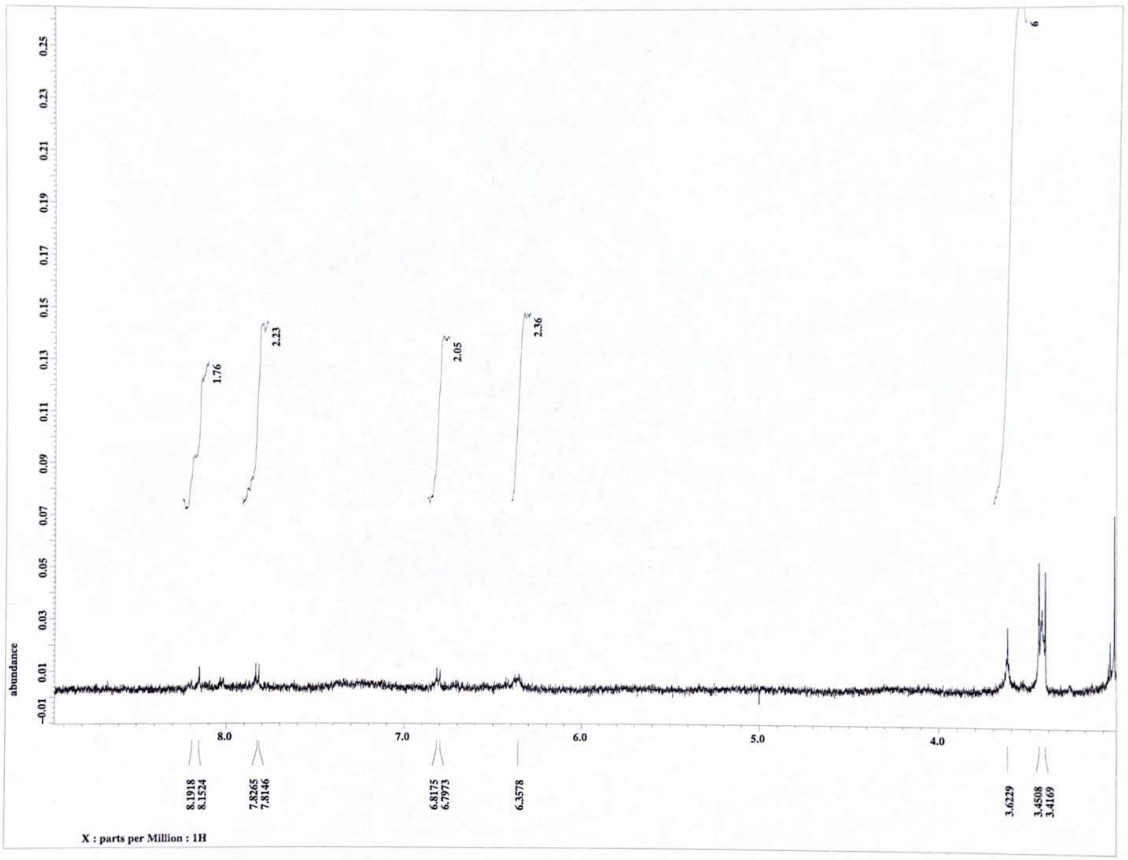

Figure B5. ^{1}H NMR of Me_2N-TTz-COOH in d-Acetone.

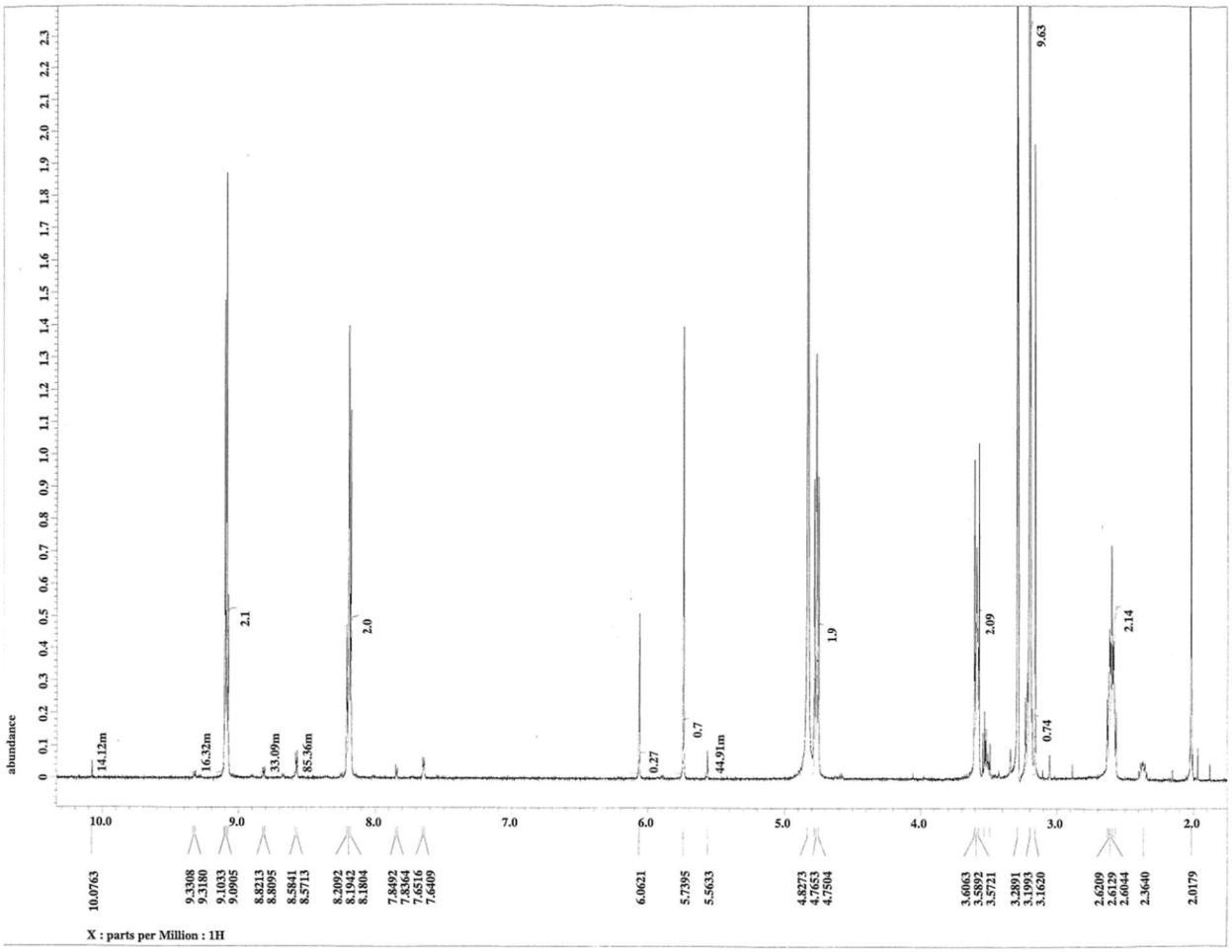

Figure B6. ^{1}H NMR of CHO-Py(NPr) in d_4-MeOD.

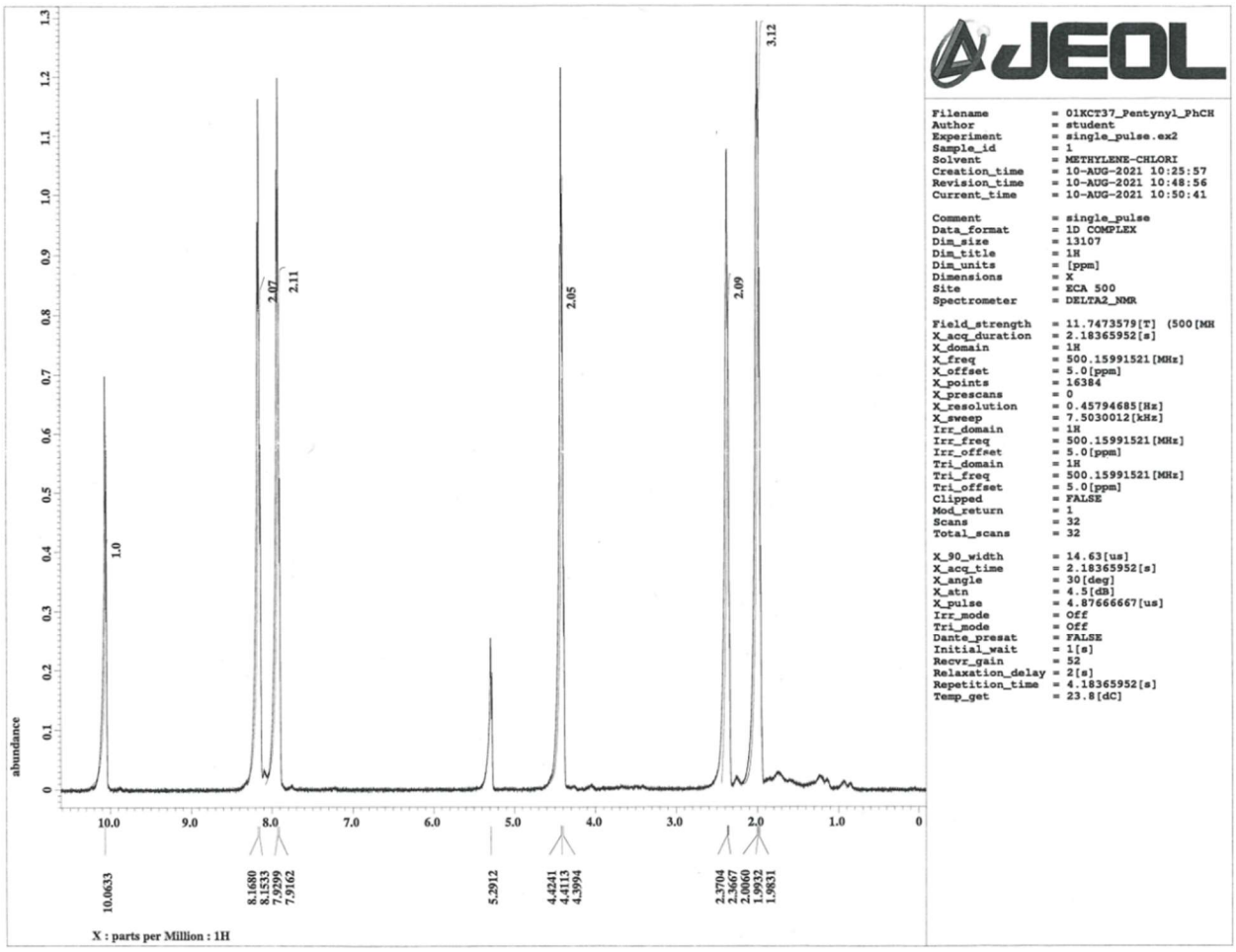

Figure B7. ^{1}H NMR of CHO-Ph pentynyl ester in d_4-MeOD.

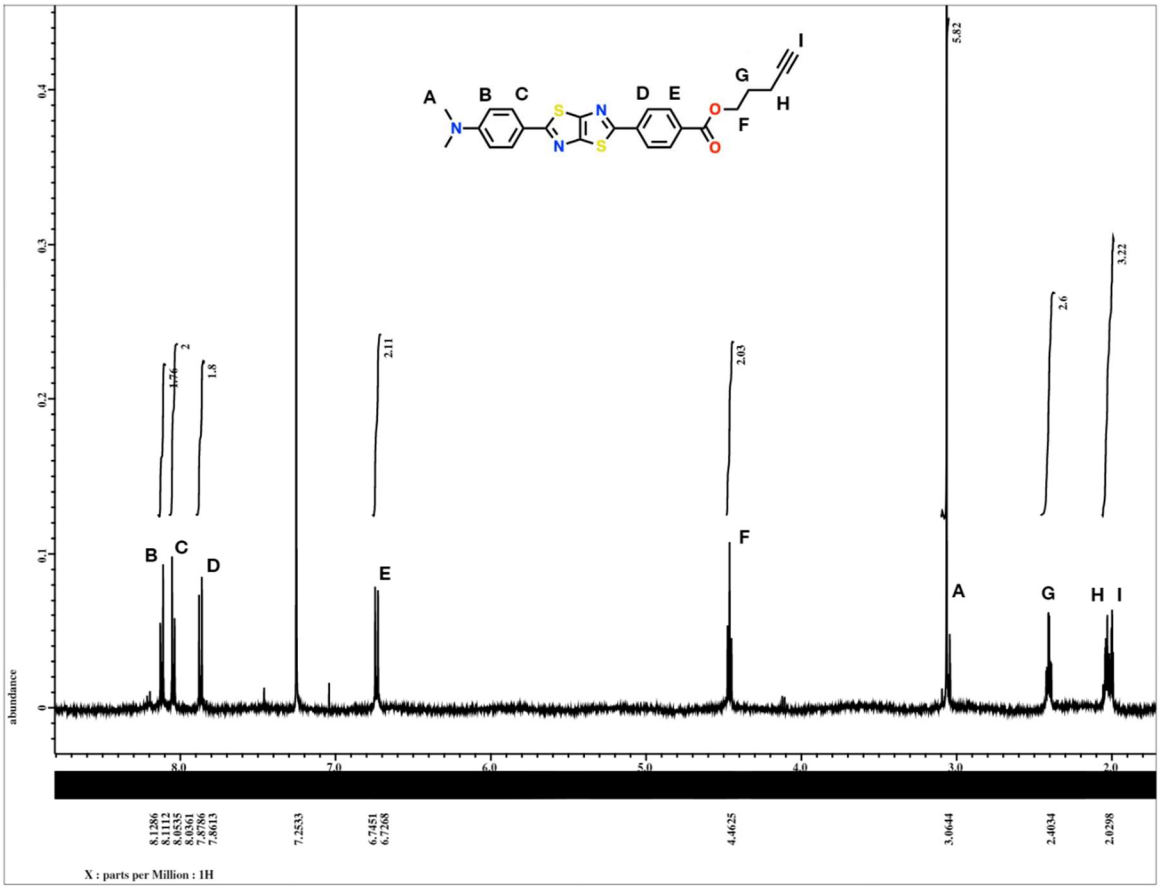

Figure B8. ^{1}H NMR of Me_2N-TTz-pentynyl ester in $CDCl_3$.

Appendix C – ^{13}C NMR

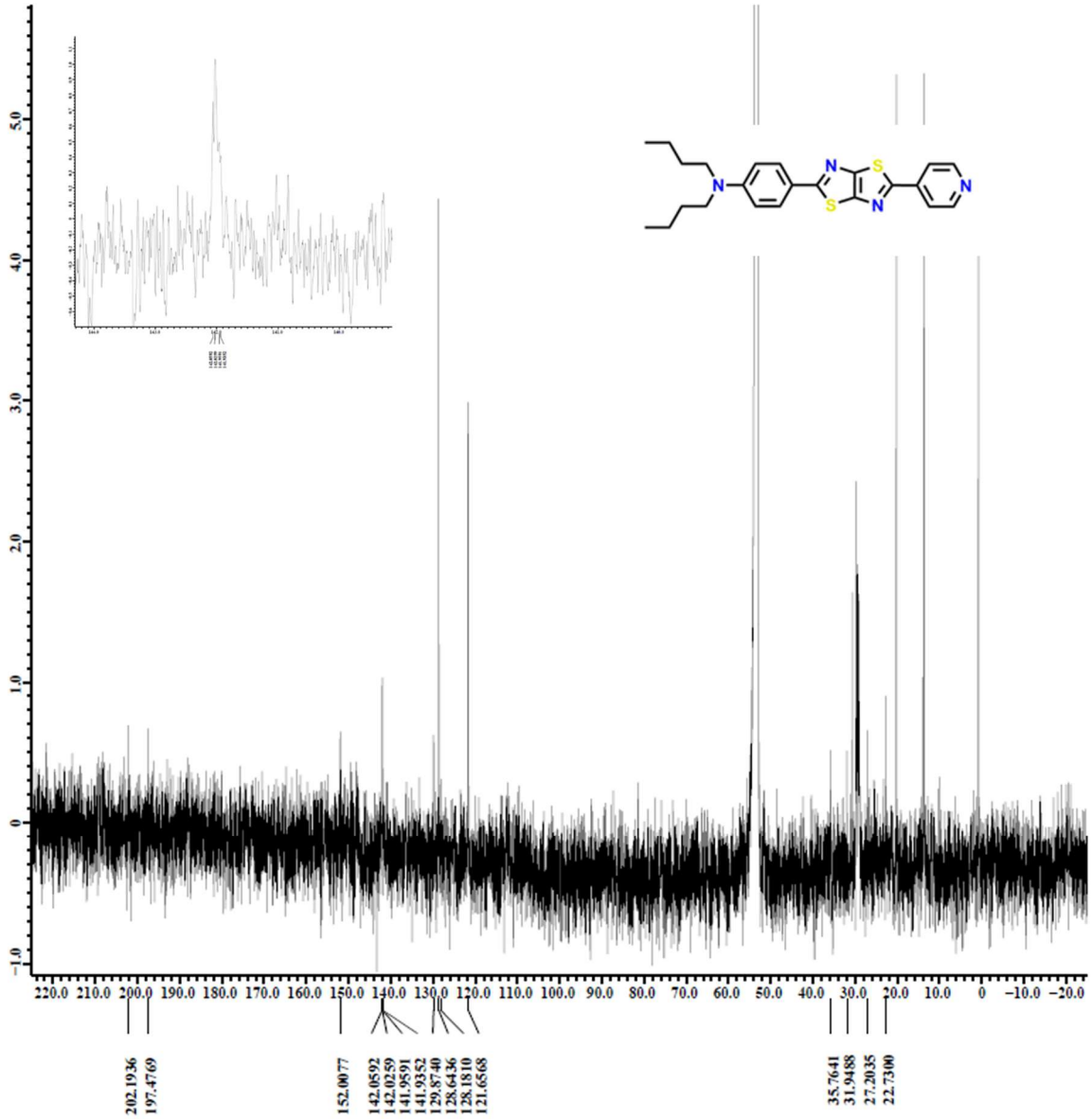

Figure C1. ^{13}C NMR of Bu_2N-TTz-Py·HCl in DCM. Inset shows quaternary carbon region.

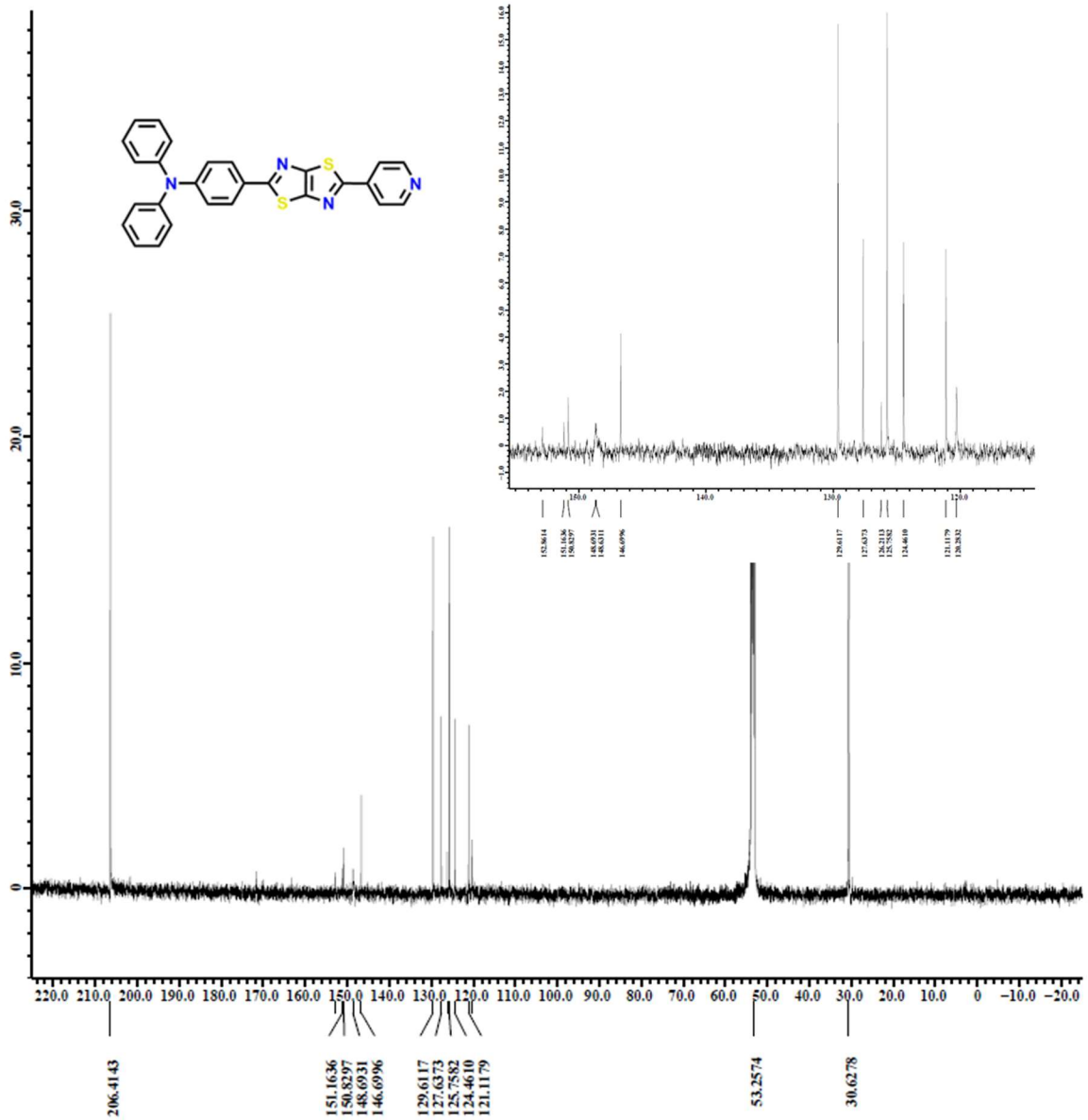

Figure C2. ^{13}C NMR of Ph_2N-TTz-Py·HCl in DCM. Inset shows aryl region.

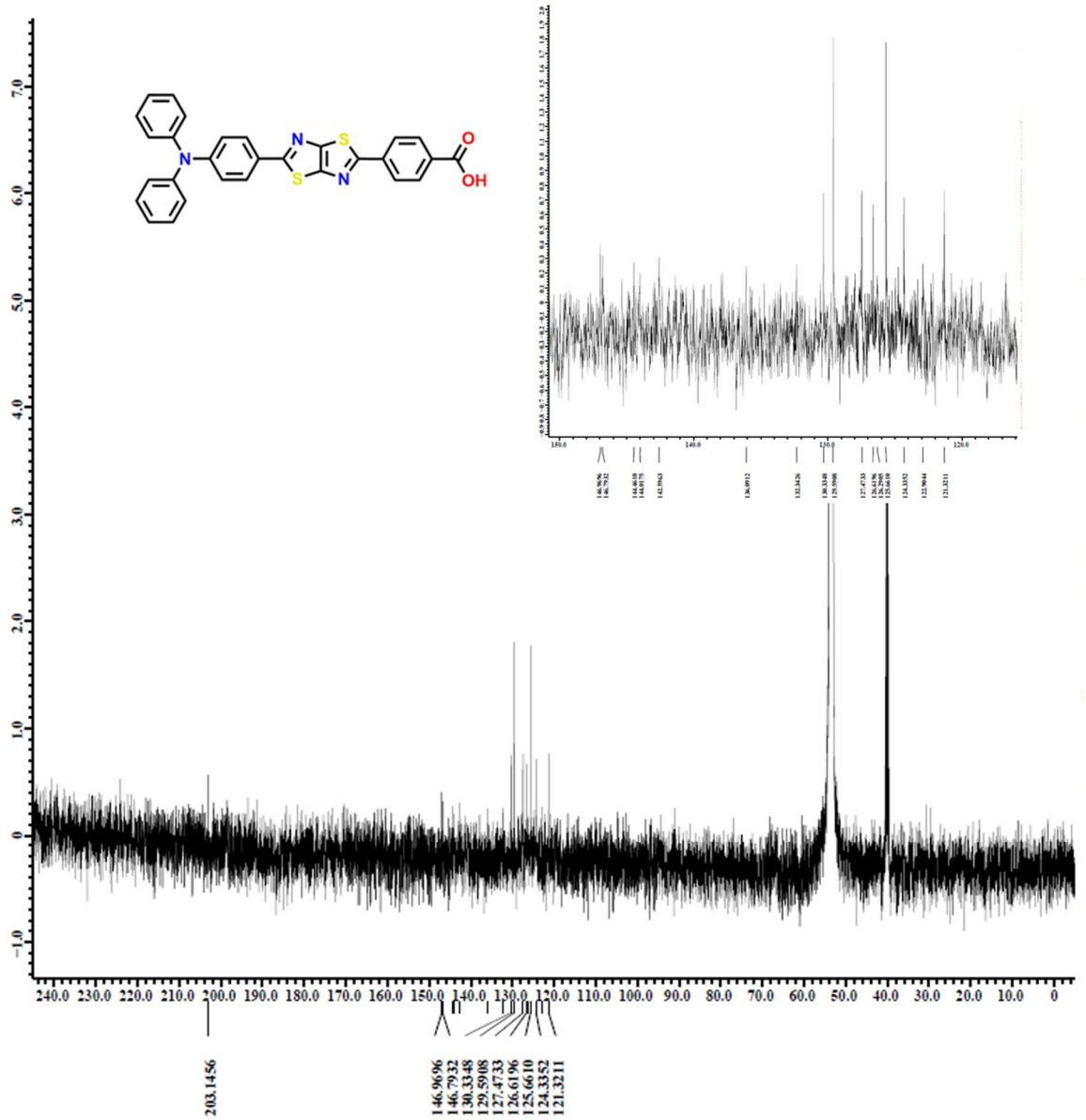

Figure C3. ^{13}C NMR of Ph_2N-TTz-COOH in DCM. Inset shows aryl region.

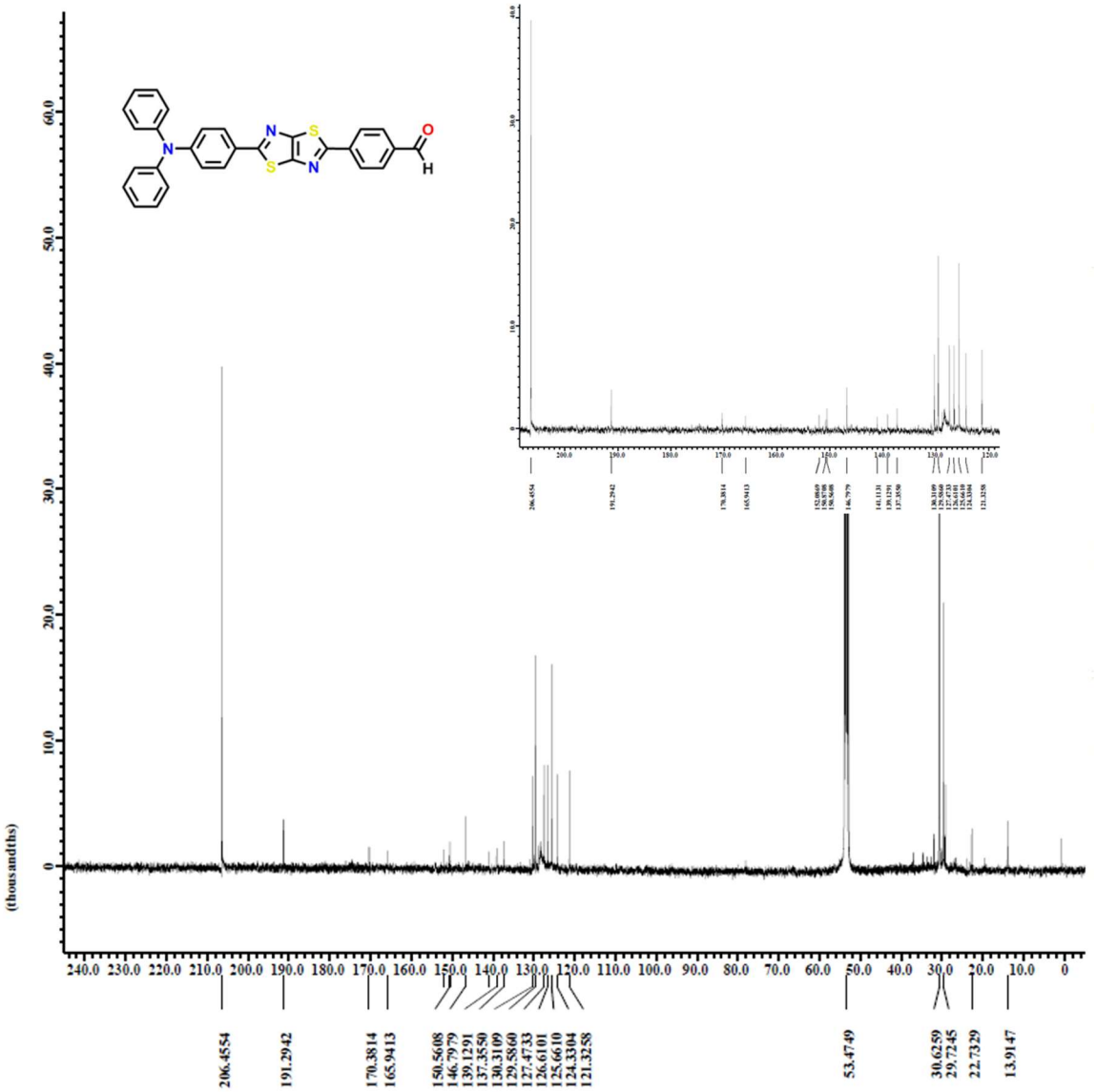

Figure C4. ^{13}C NMR of Ph_2N-TTz-CHO in DCM. Inset shows aryl region.

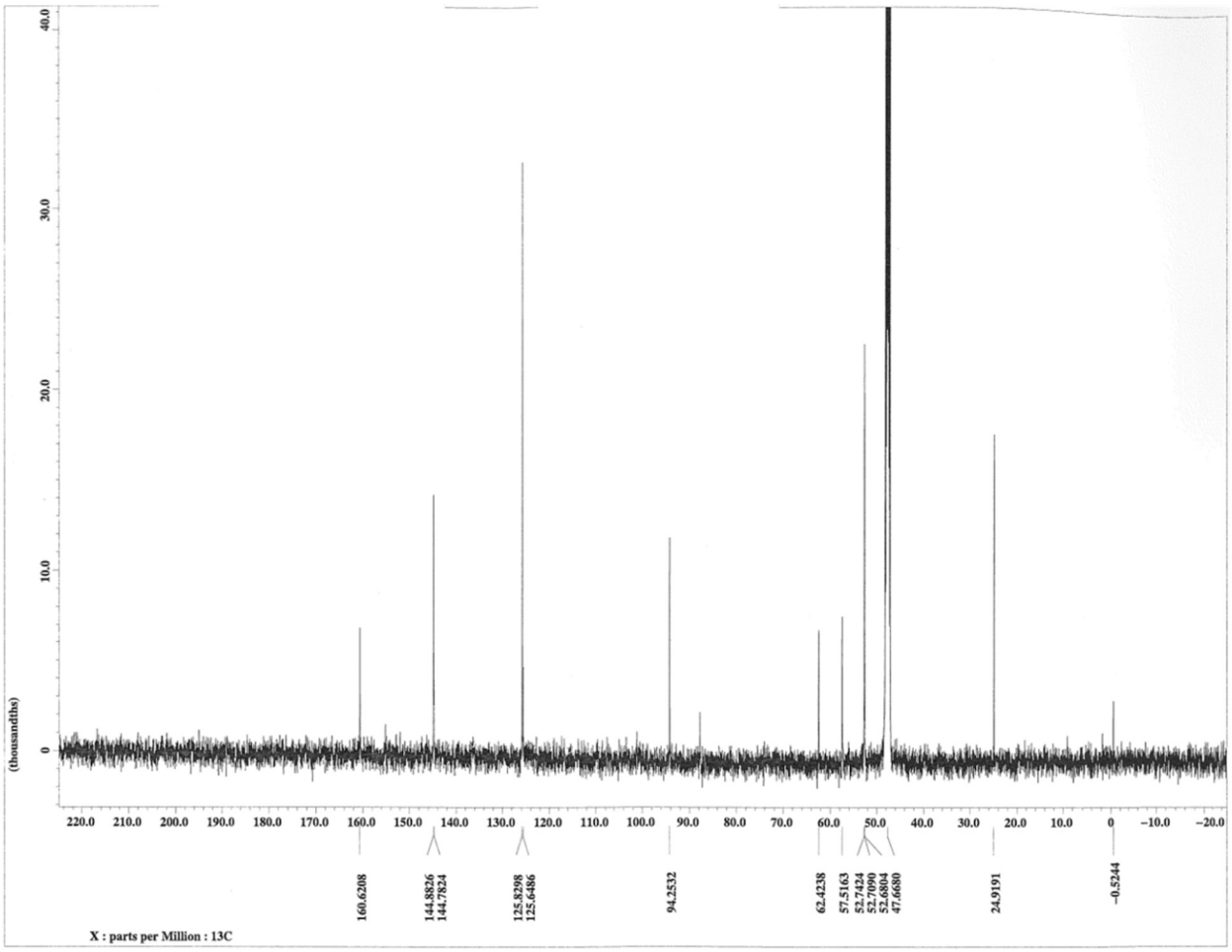

Figure C5. ^{13}C NMR of CHO-Py(NPr) in d_4-MeOD.

Appendix D – Chromatographic Analysis

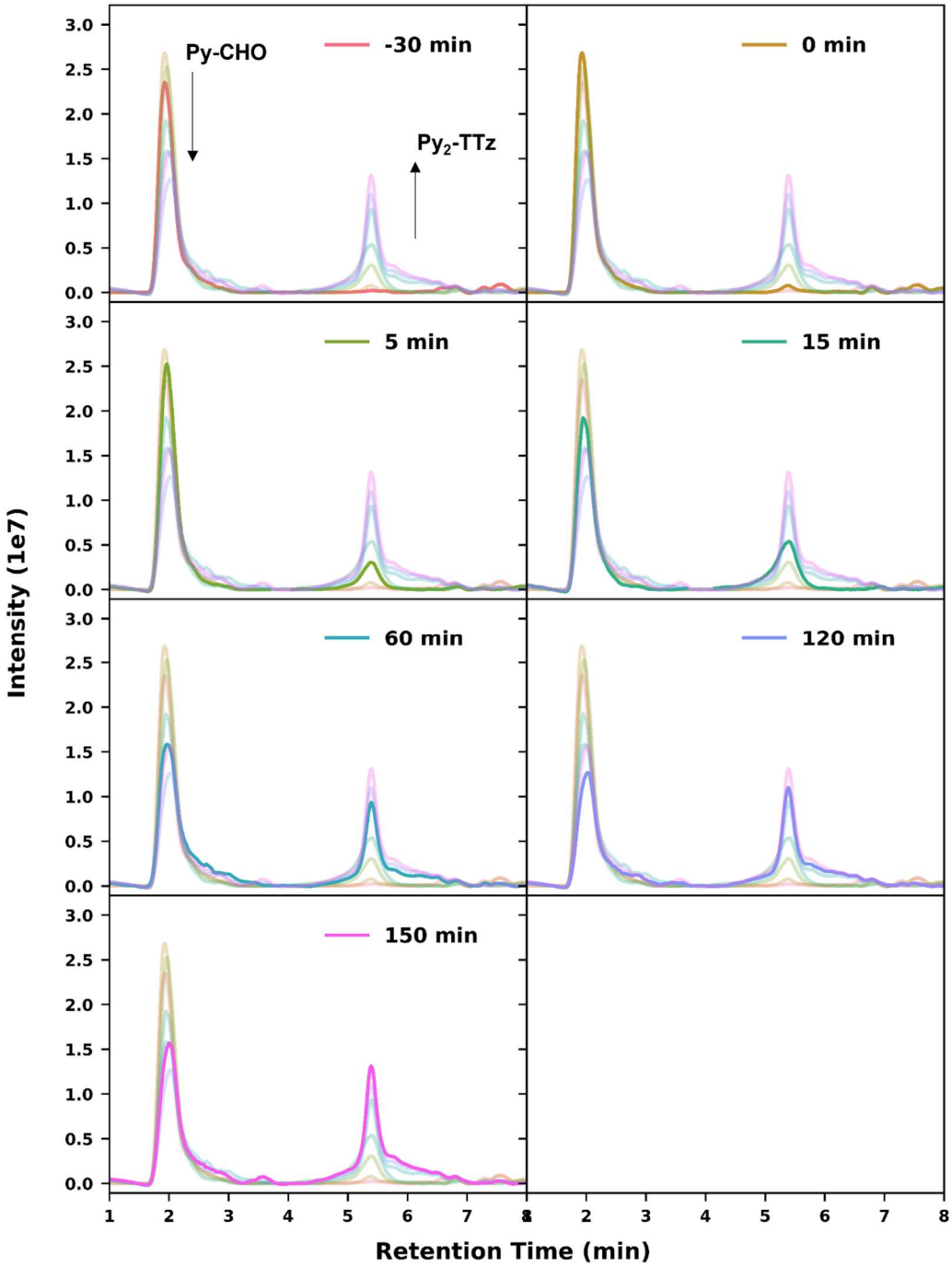

Figure D1. Total ion count (TIC) chromatograms of the Py_2-TTz reaction under aerobic conditions. Labels refer to the reaction time when an aliquot was taken.

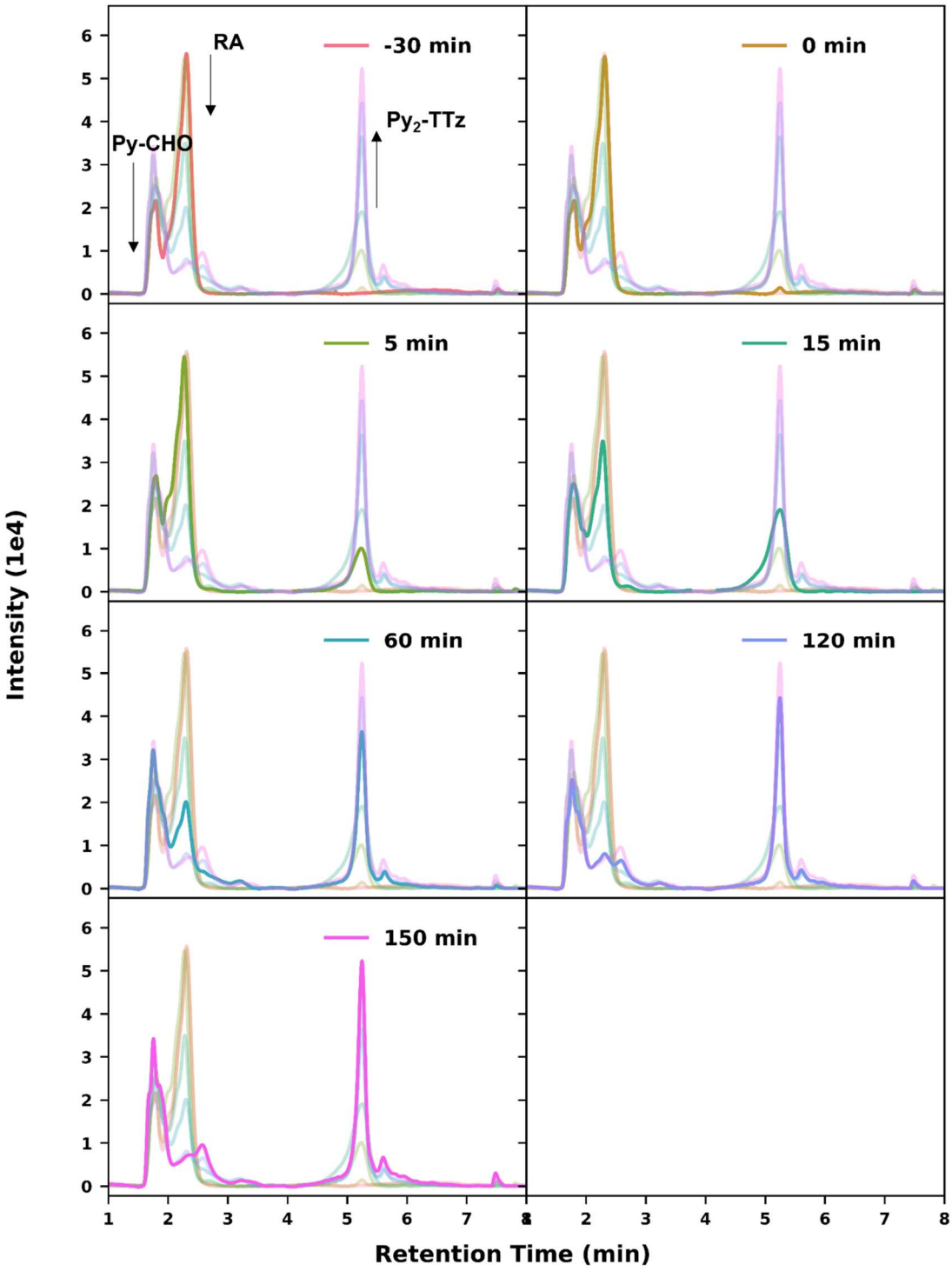

Figure D2. Total scan photodiode array (PDA) chromatograms of the Py_2-TTz reaction under aerobic conditions. Labels refer to the reaction time when an aliquot was taken.

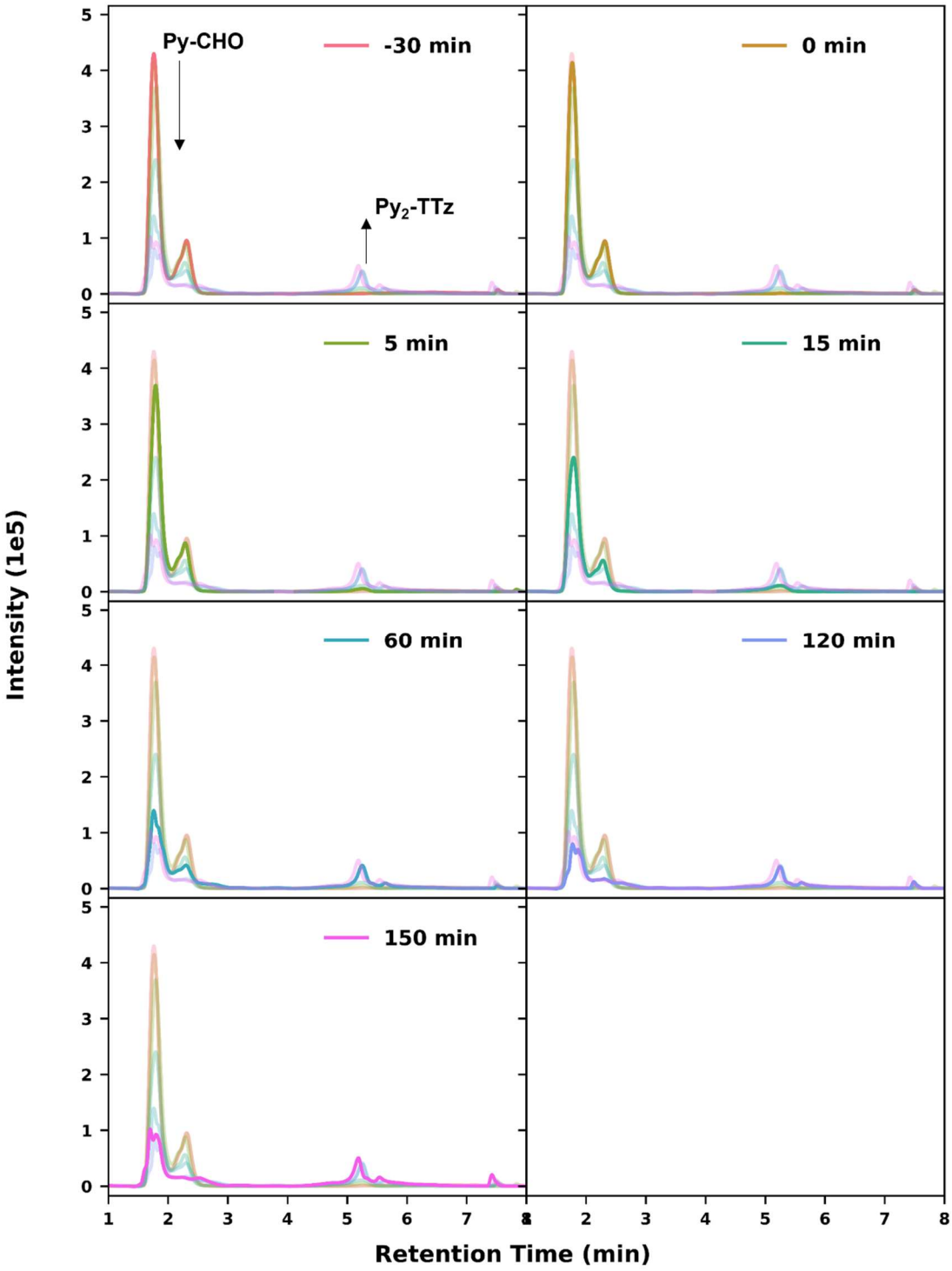

Figure D3. UV-A channel (260 nm) chromatograms of the Py_2-TTz reaction under aerobic conditions. Labels refer to the reaction time when an aliquot was taken.

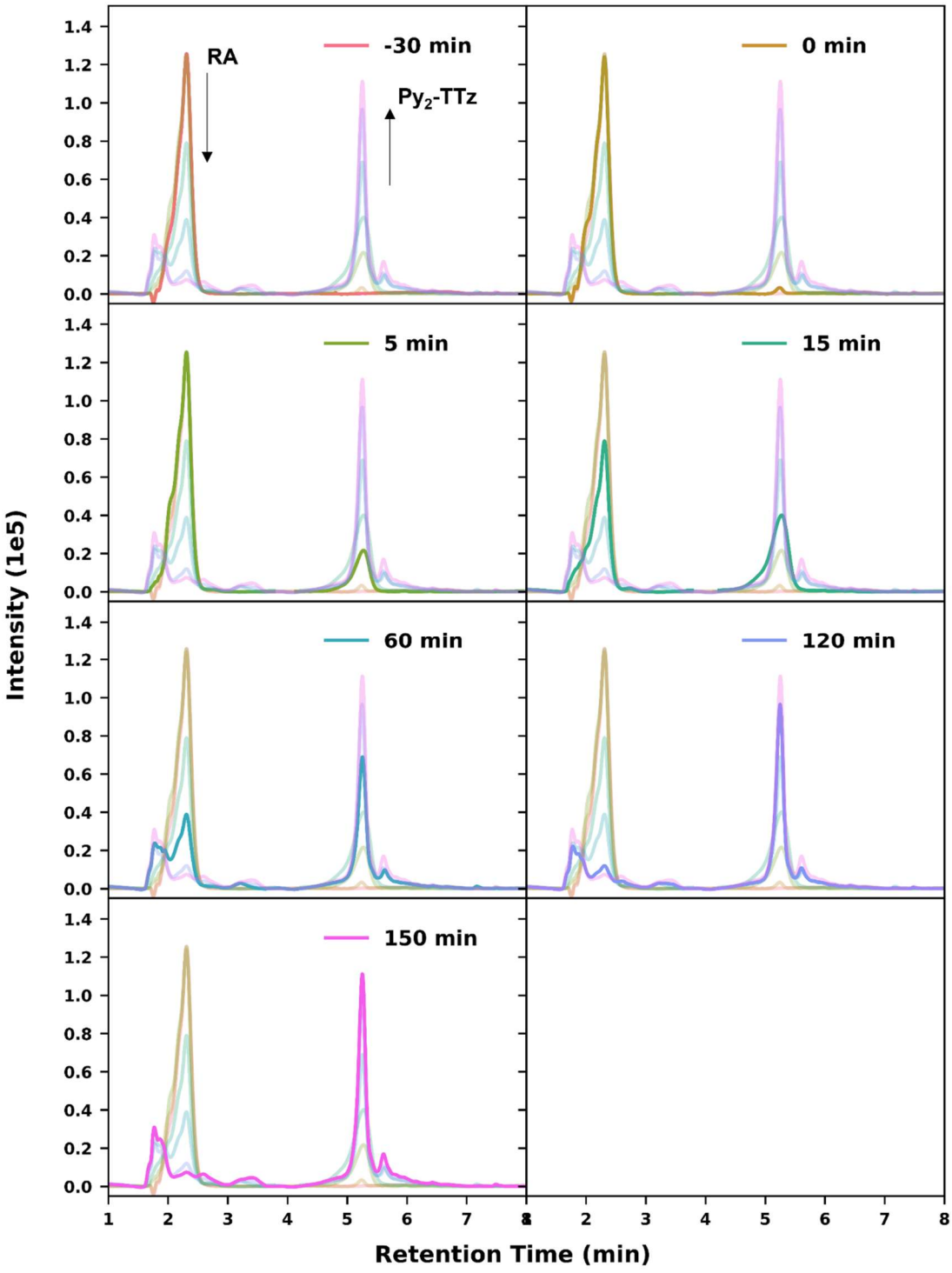

Figure D4. UV-B channel (350 nm) chromatograms of the Py_2-TTz reaction under aerobic conditions. Labels refer to the reaction time when an aliquot was taken.

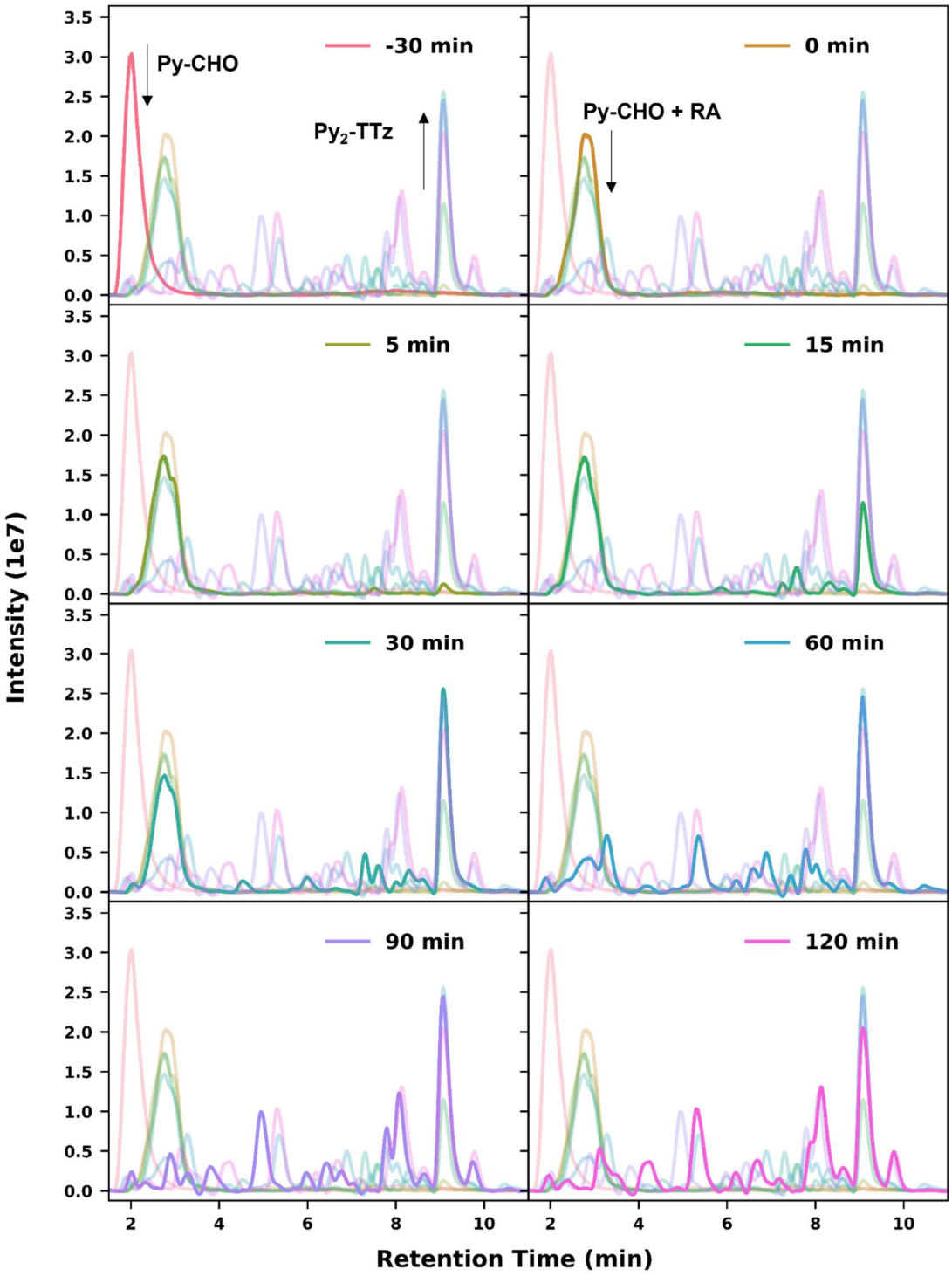

Figure D5. Total ion count (TIC) chromatograms of the Py_2-TTz reaction under anaerobic conditions (N_2). Labels refer to the reaction time when an aliquot was taken.

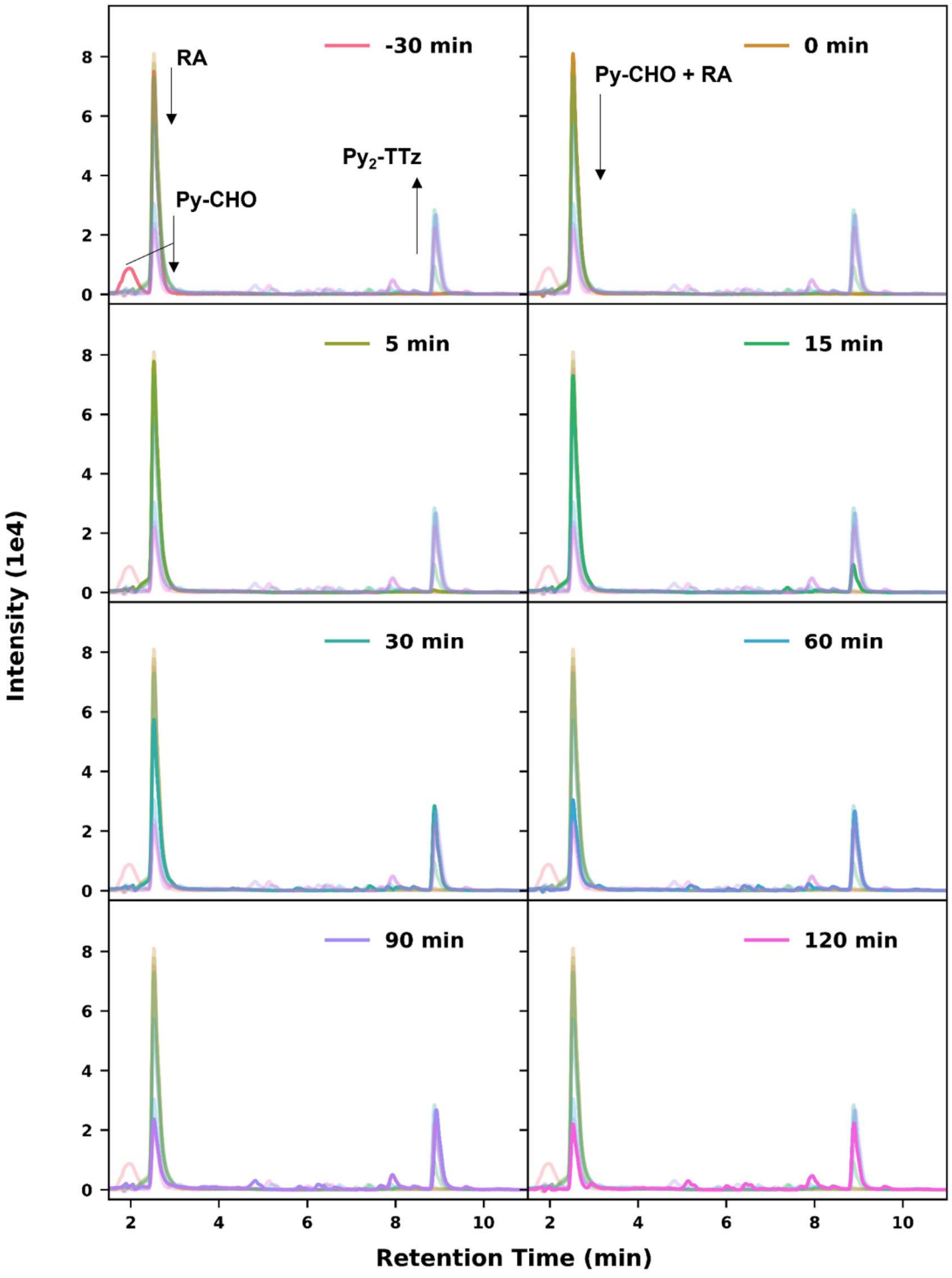

Figure D6. Total scan photodiode array (PDA) chromatograms of the Py_2-TTz reaction under anaerobic conditions (N_2). Labels refer to the reaction time when an aliquot was taken.

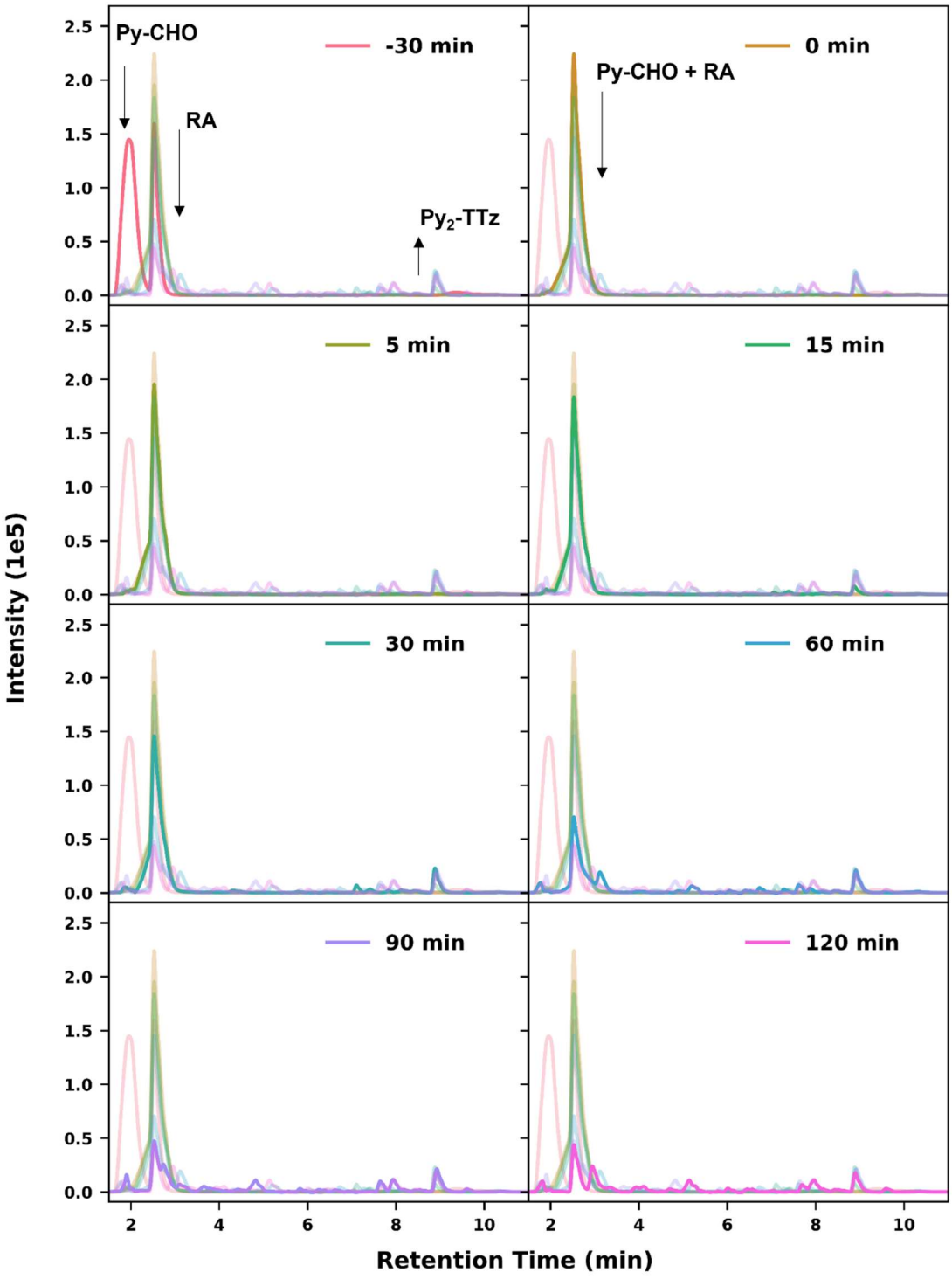

Figure D7. UV-A channel (260 nm) chromatograms of the Py_2-TTz reaction under anaerobic conditions (N_2). Labels refer to the reaction time when an aliquot was taken.

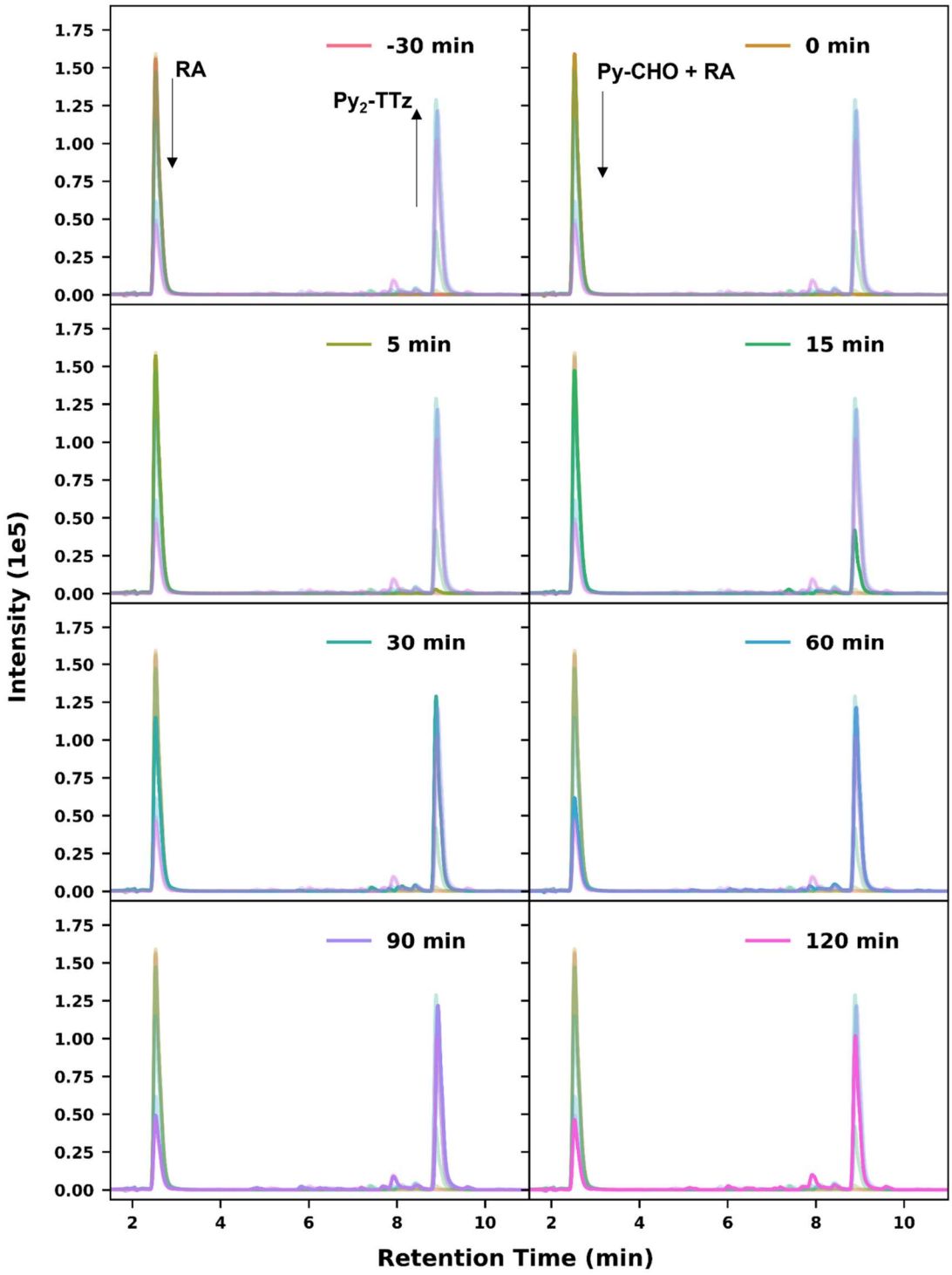

Figure D8. UV-B channel (350 nm) chromatograms of the Py_2-TTz reaction under anaerobic conditions (N_2). Labels refer to the reaction time when an aliquot was taken.

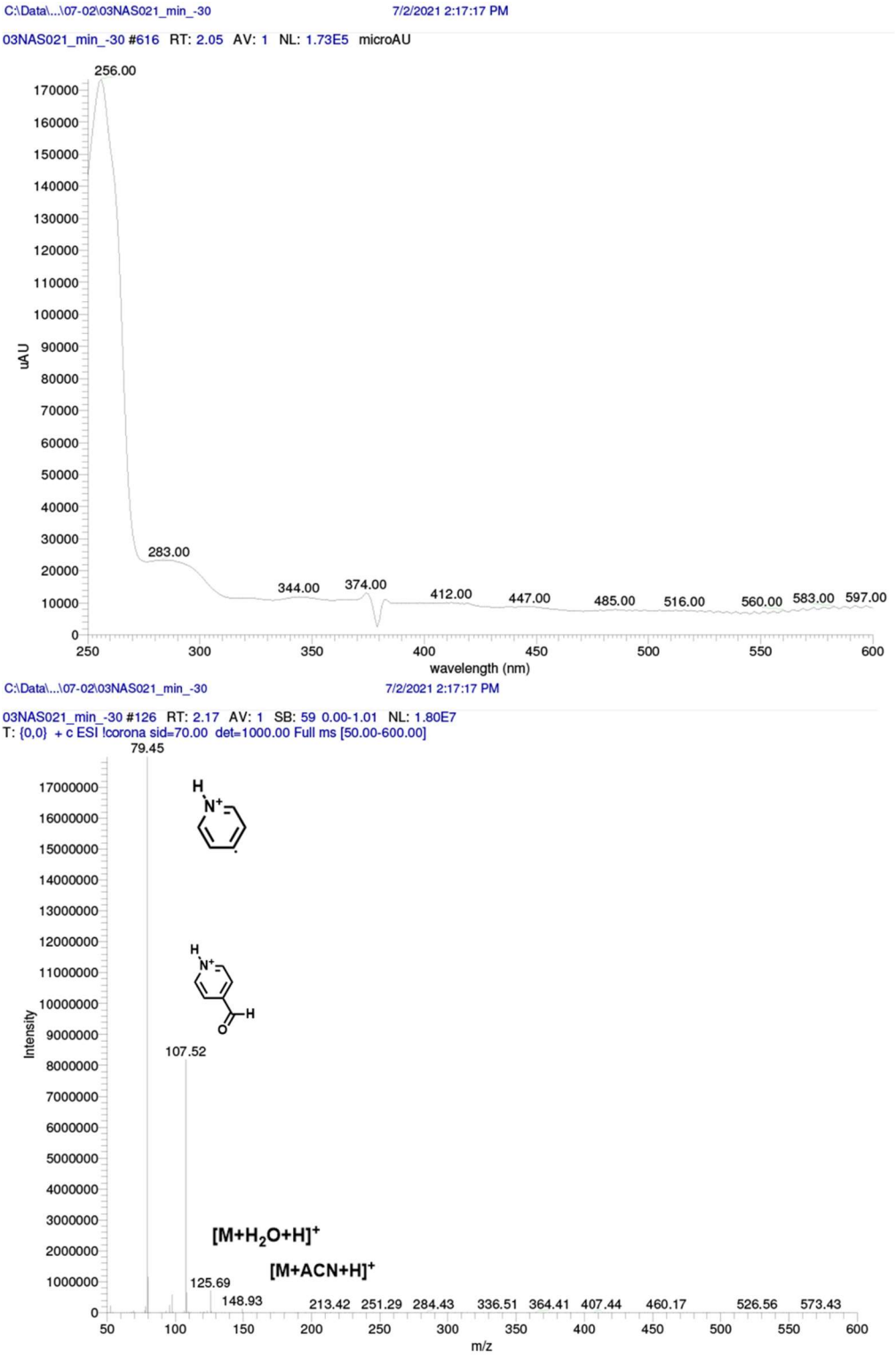

Figure D9. UV-B channel (350 nm) chromatograms of the Py_2-TTz reaction under anaerobic conditions (N_2). Labels refer to the reaction time when an aliquot was taken.

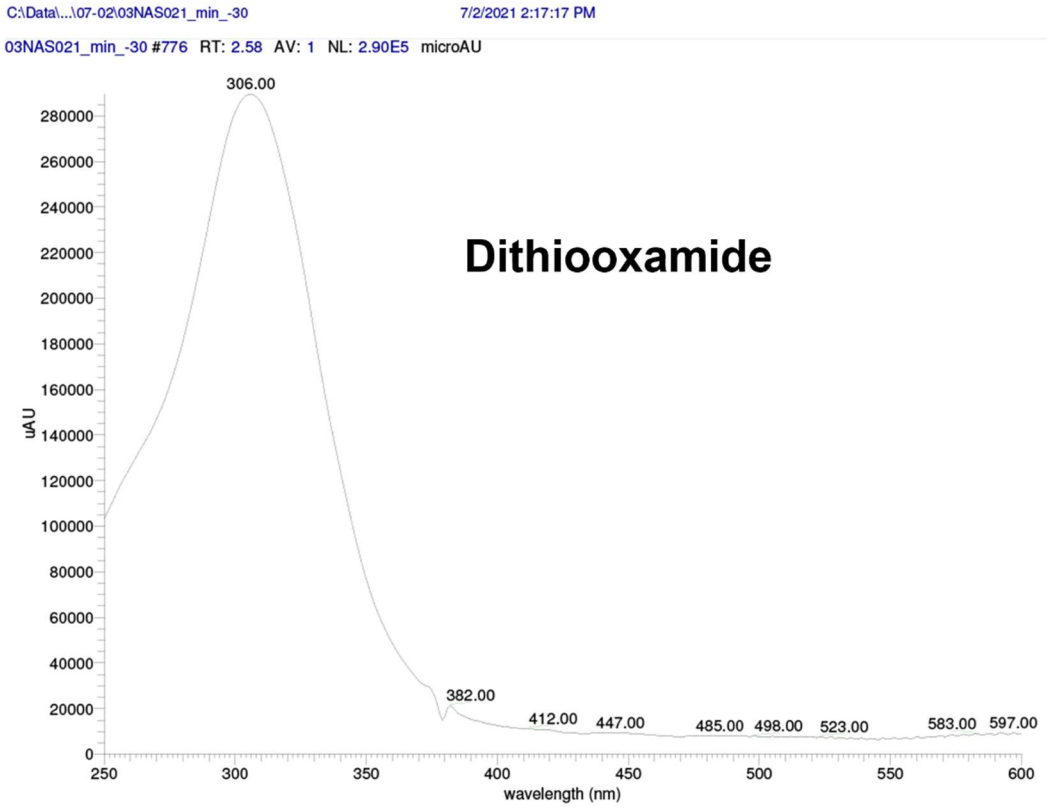

Figure D10. UV-B channel (350 nm) chromatograms of the Py_2-TTz reaction under anaerobic conditions (N_2). Labels refer to the reaction time when an aliquot was taken.

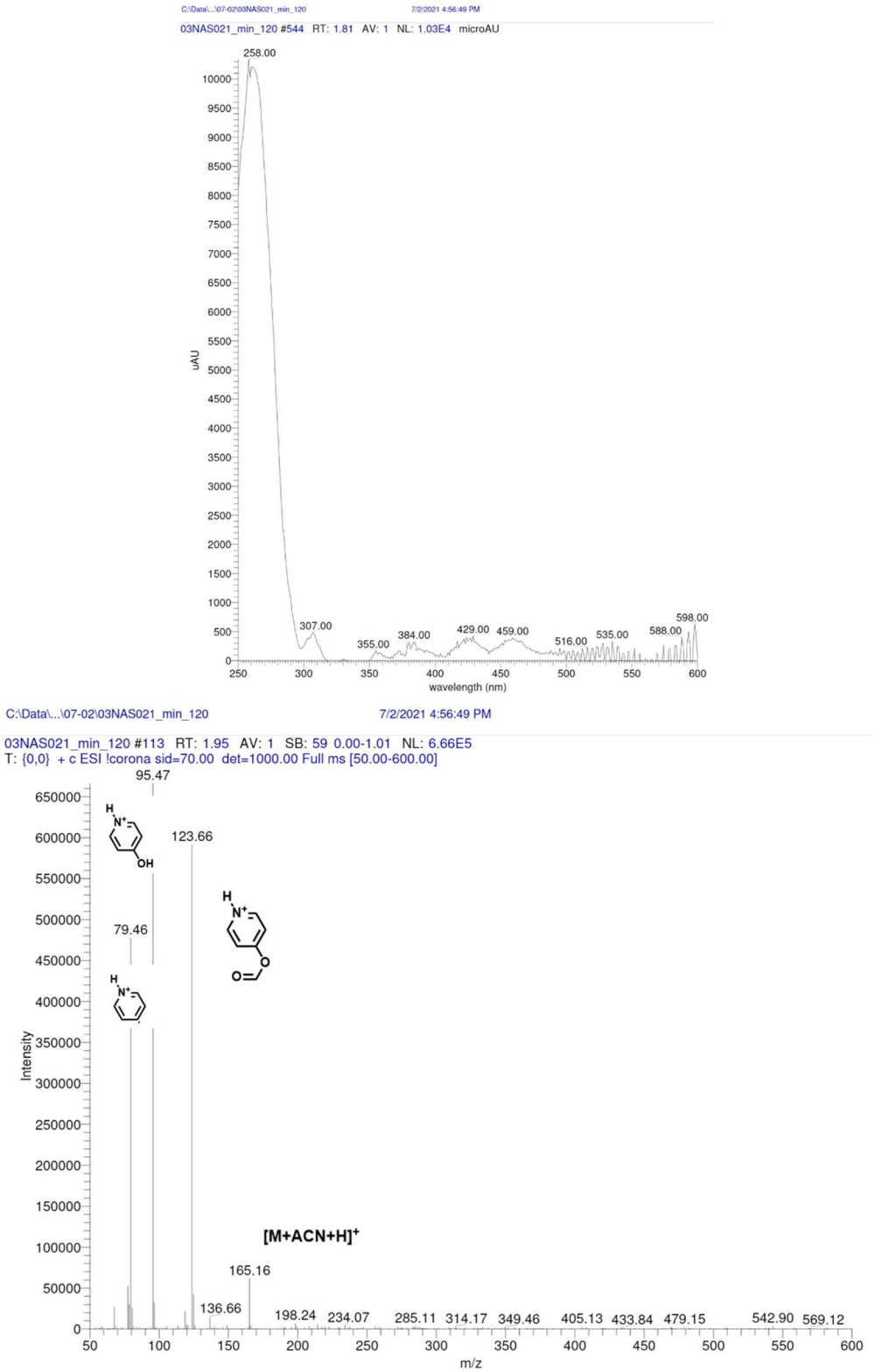

Figure D11. UV-B channel (350 nm) chromatograms of the Py_2-TTz reaction under anaerobic conditions (N_2). Labels refer to the reaction time when an aliquot was taken.

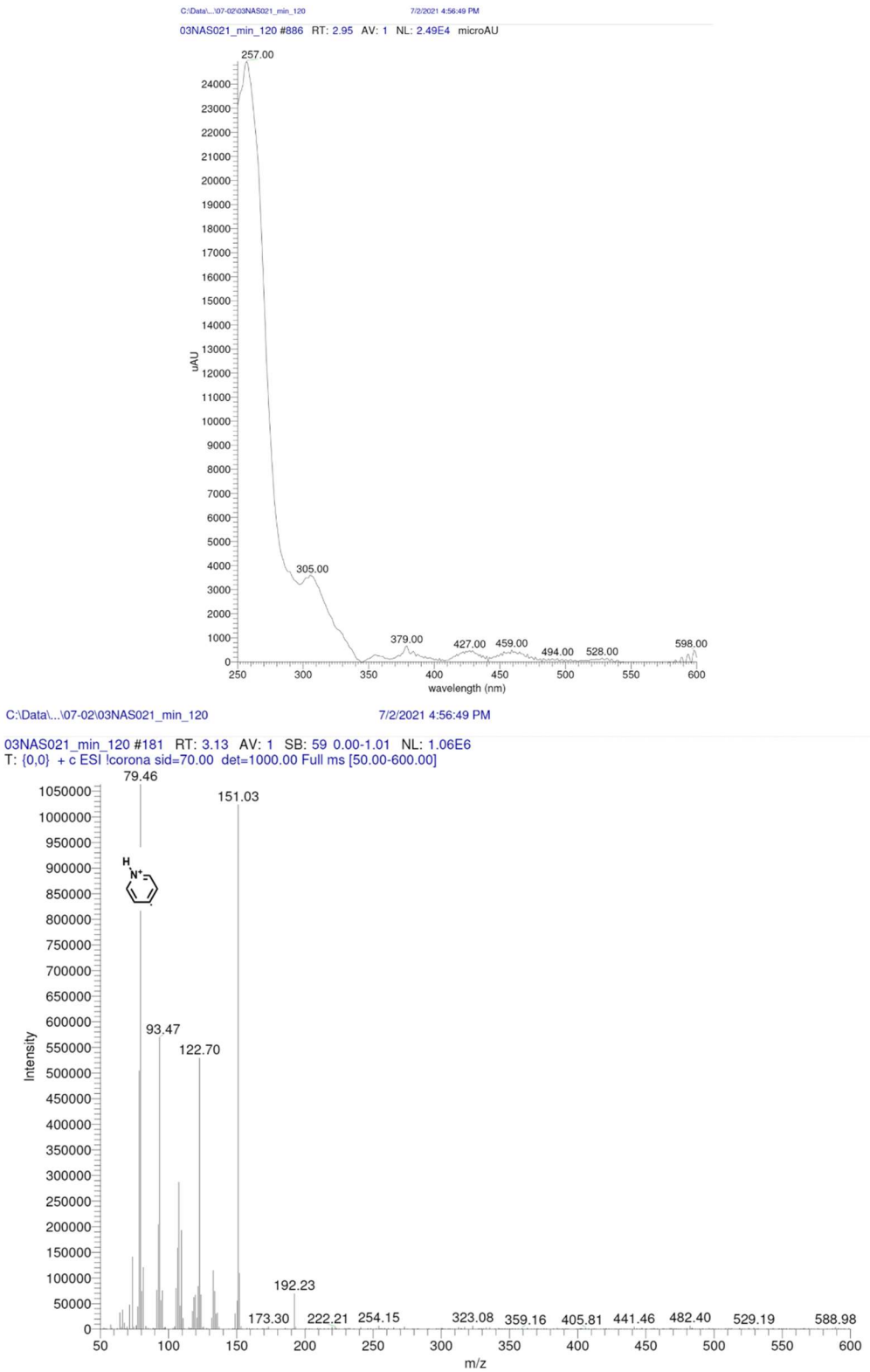

Figure D12. UV-B channel (350 nm) chromatograms of the Py_2-TTz reaction under anaerobic conditions (N_2). Labels refer to the reaction time when an aliquot was taken.

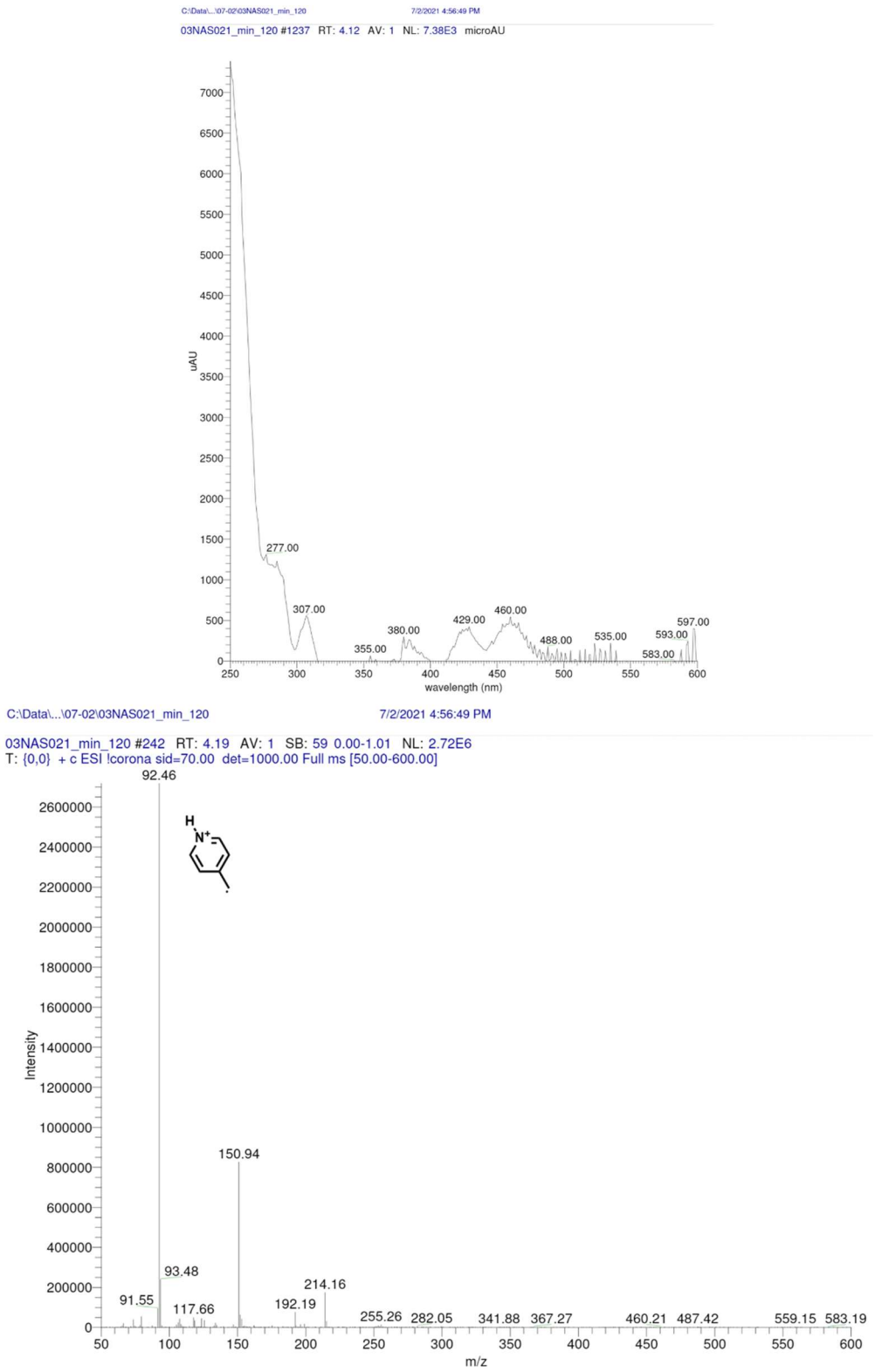

Figure D13. UV-B channel (350 nm) chromatograms of the Py_2-TTz reaction under anaerobic conditions (N_2). Labels refer to the reaction time when an aliquot was taken.

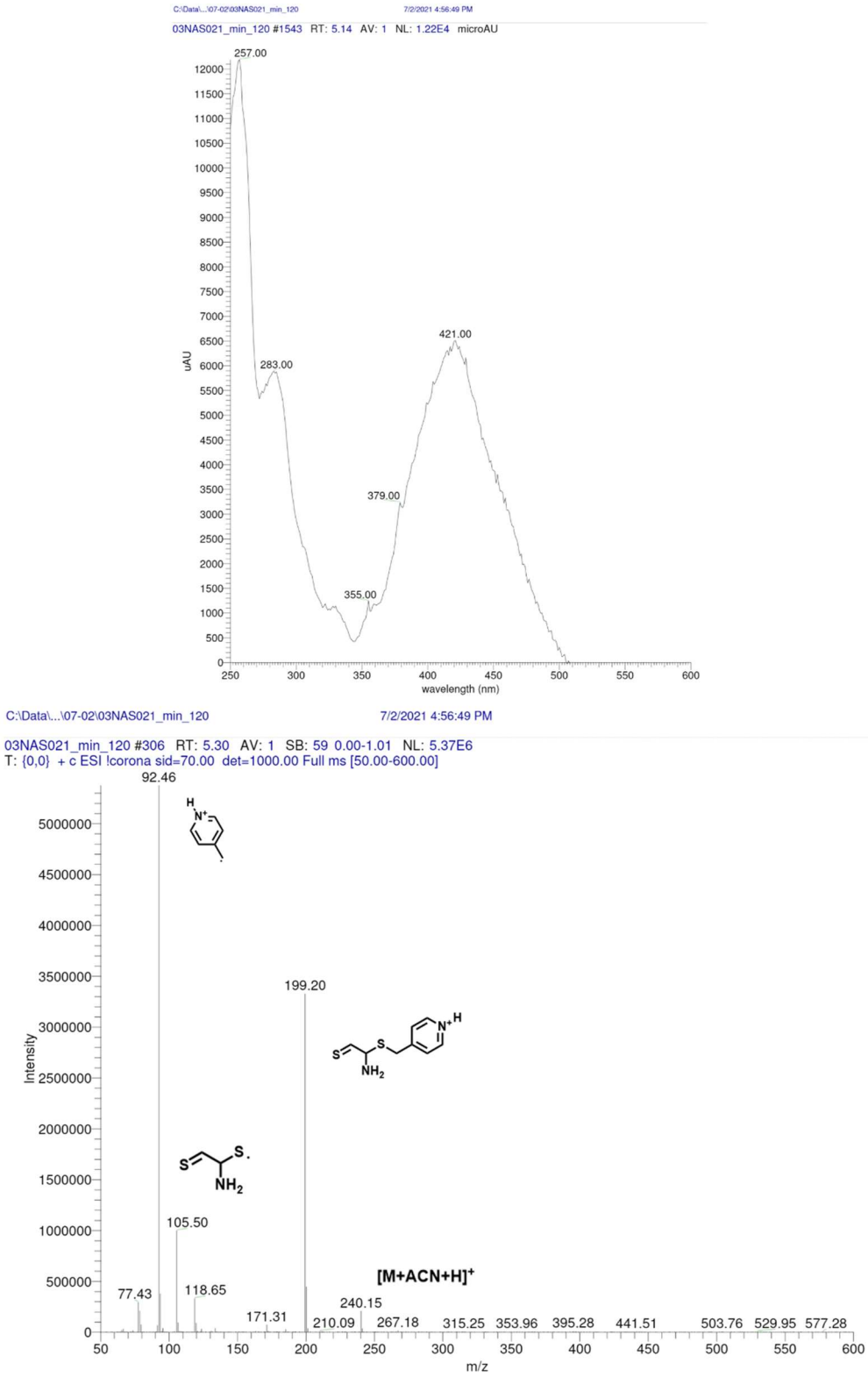

Figure D14. UV-B channel (350 nm) chromatograms of the Py_2-TTz reaction under anaerobic conditions (N_2). Labels refer to the reaction time when an aliquot was taken.

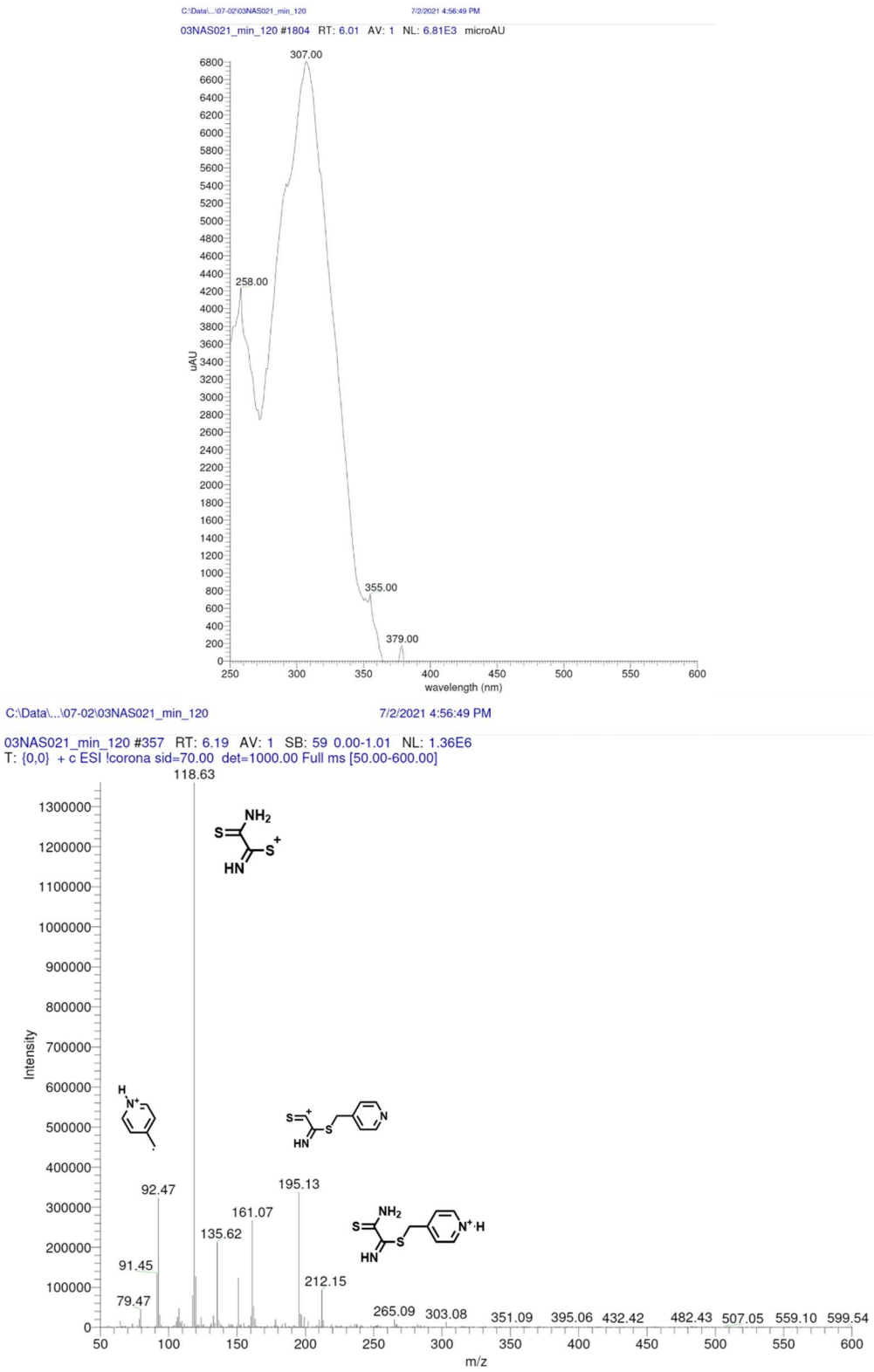

Figure D15. UV-B channel (350 nm) chromatograms of the Py_2-TTz reaction under anaerobic conditions (N_2). Labels refer to the reaction time when an aliquot was taken.

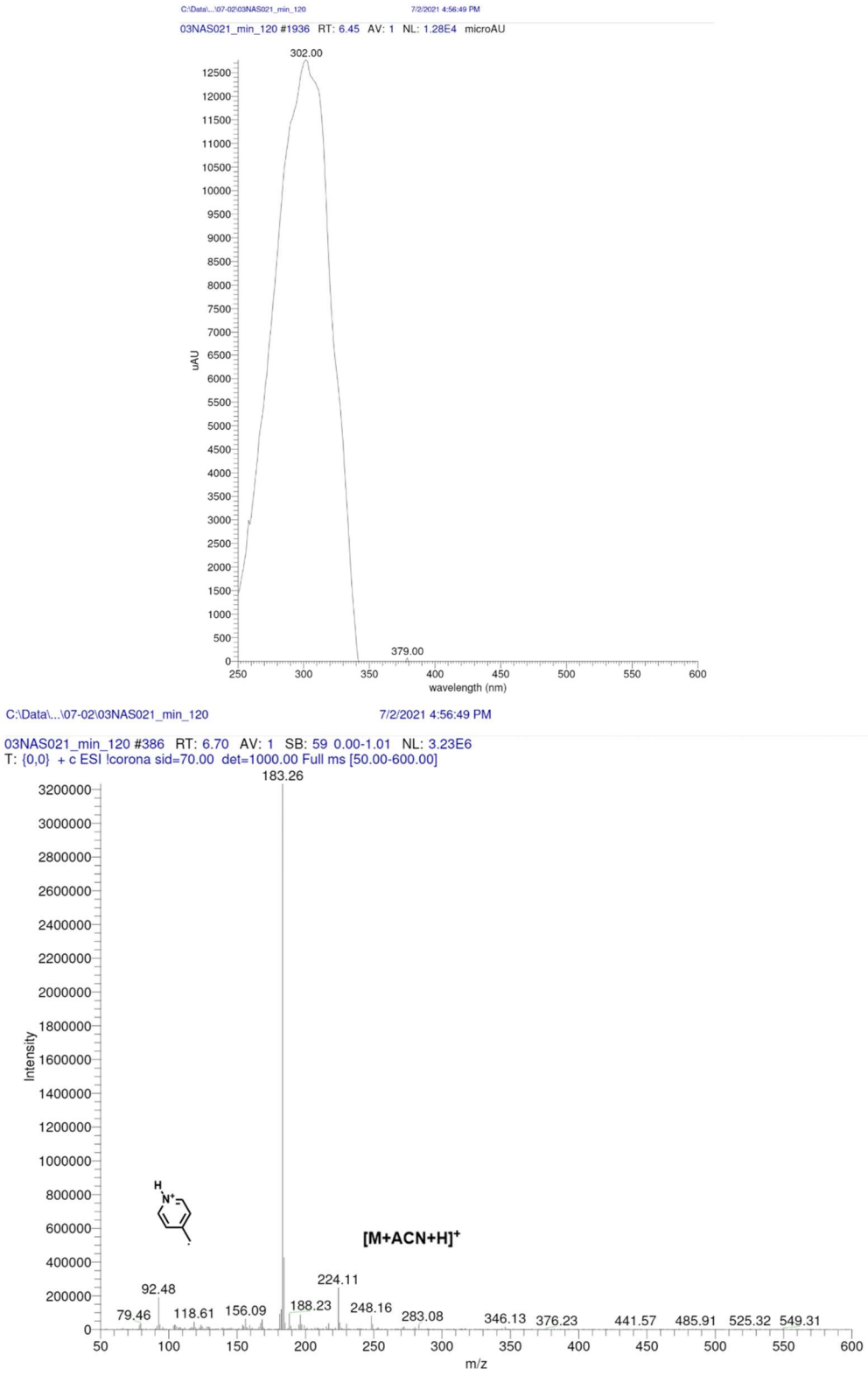

Figure D16. UV-B channel (350 nm) chromatograms of the Py_2-TTz reaction under anaerobic conditions (N_2). Labels refer to the reaction time when an aliquot was taken.

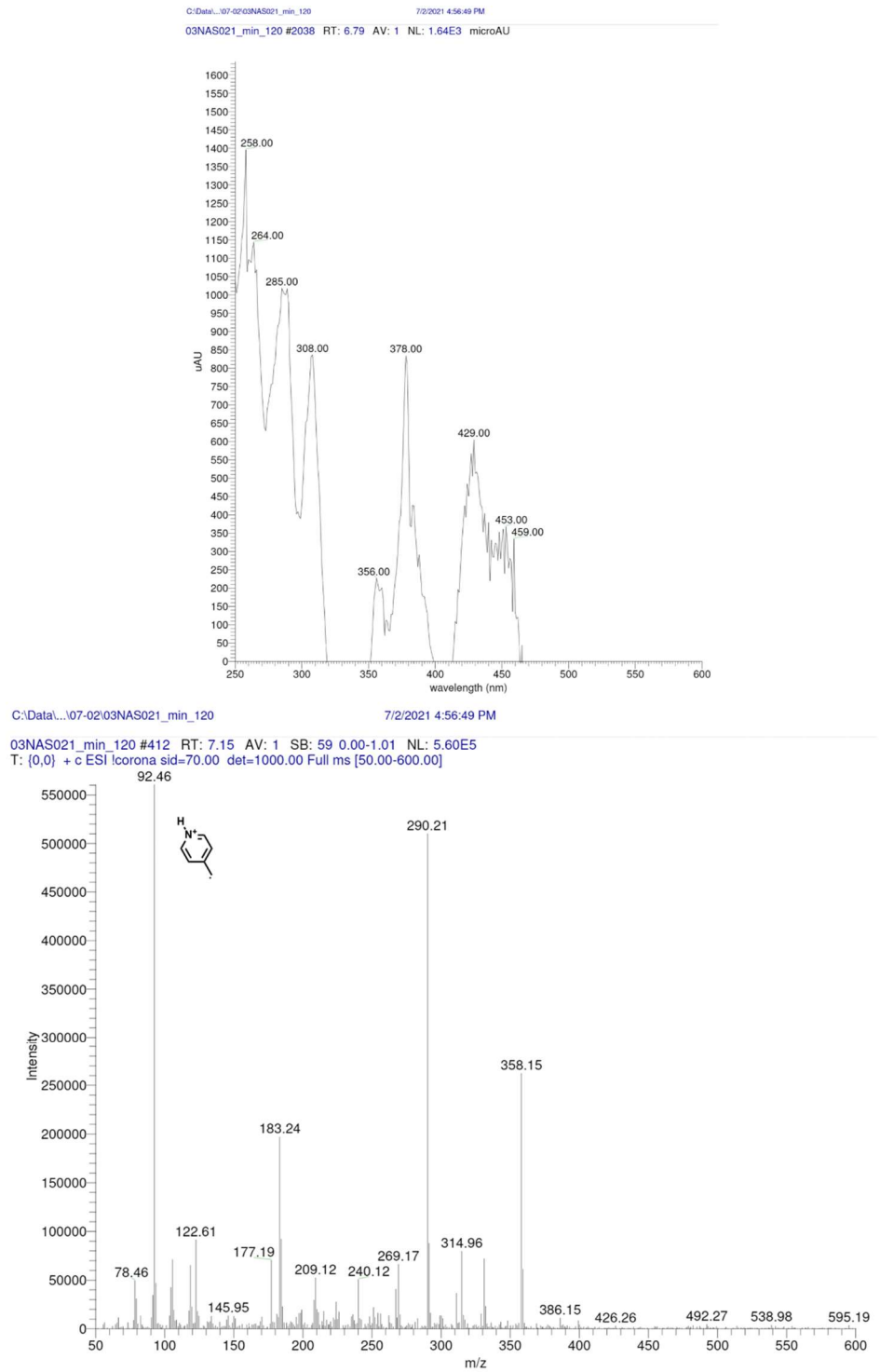

Figure D17. UV-B channel (350 nm) chromatograms of the Py_2-TTz reaction under anaerobic conditions (N_2). Labels refer to the reaction time when an aliquot was taken.

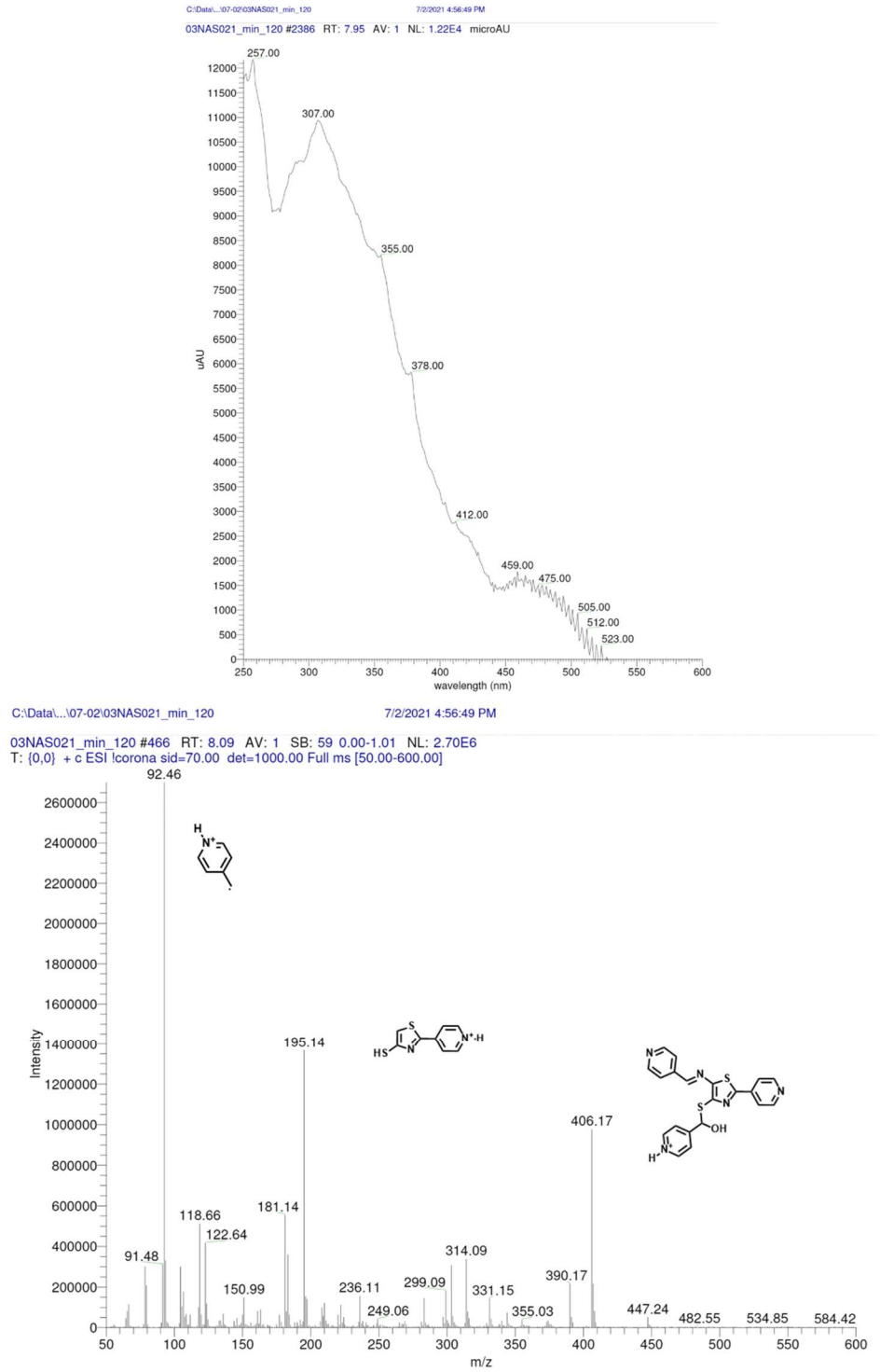

Figure D18. UV-B channel (350 nm) chromatograms of the Py_2-TTz reaction under anaerobic conditions (N_2). Labels refer to the reaction time when an aliquot was taken.

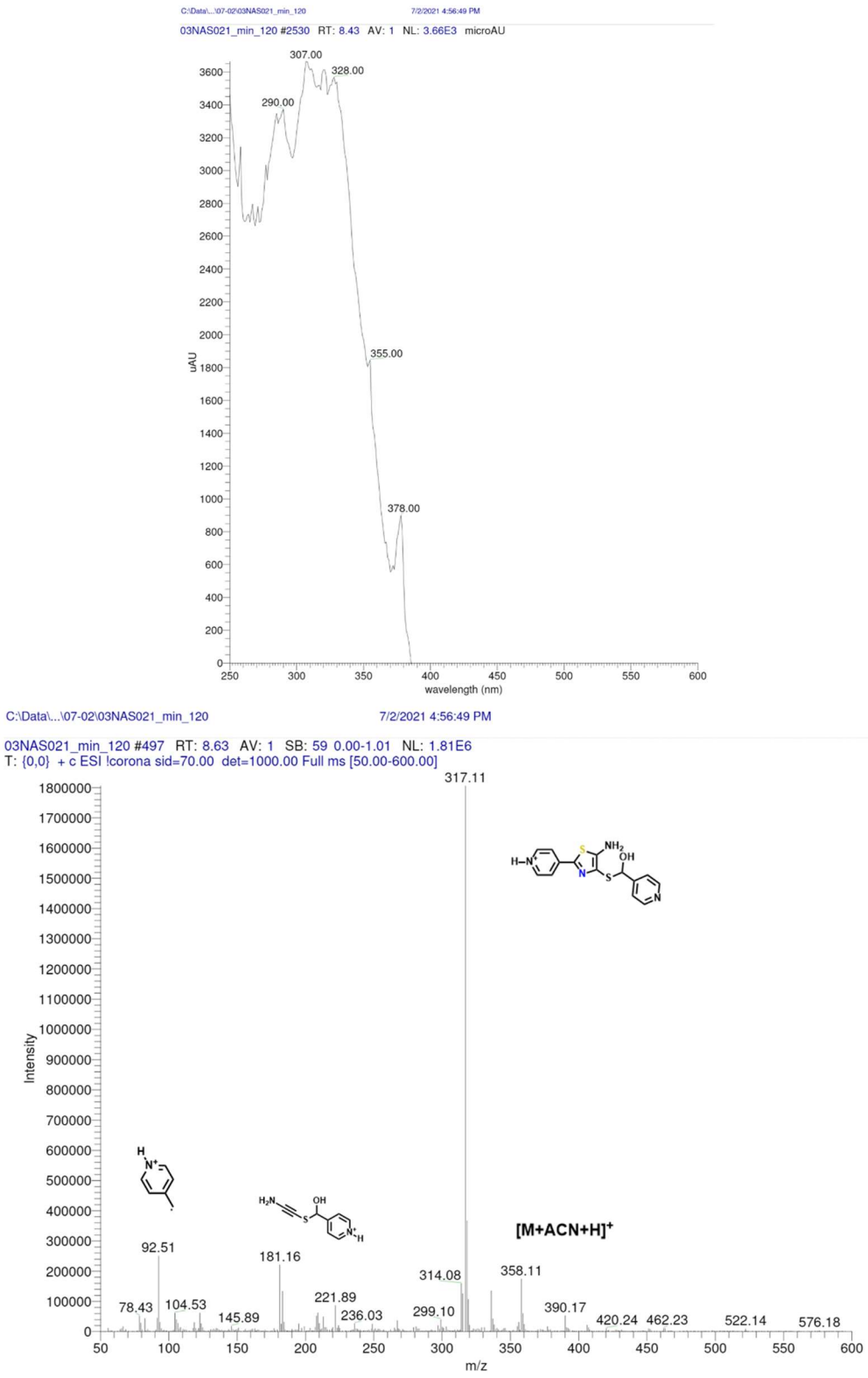

Figure D19. UV-B channel (350 nm) chromatograms of the Py_2-TTz reaction under anaerobic conditions (N_2). Labels refer to the reaction time when an aliquot was taken.

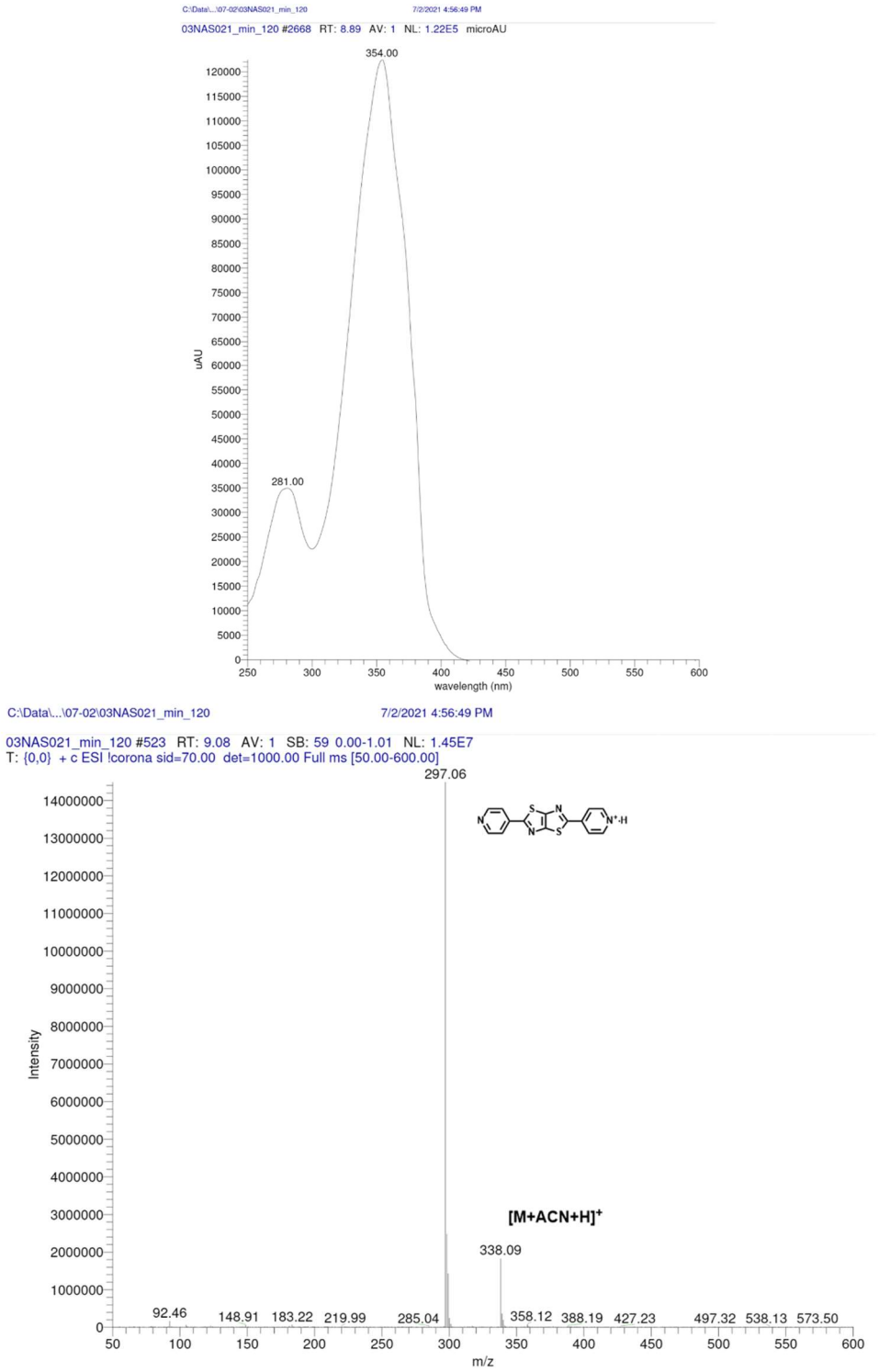

Figure D20. UV-B channel (350 nm) chromatograms of the Py_2-TTz reaction under anaerobic conditions (N_2). Labels refer to the reaction time when an aliquot was taken.

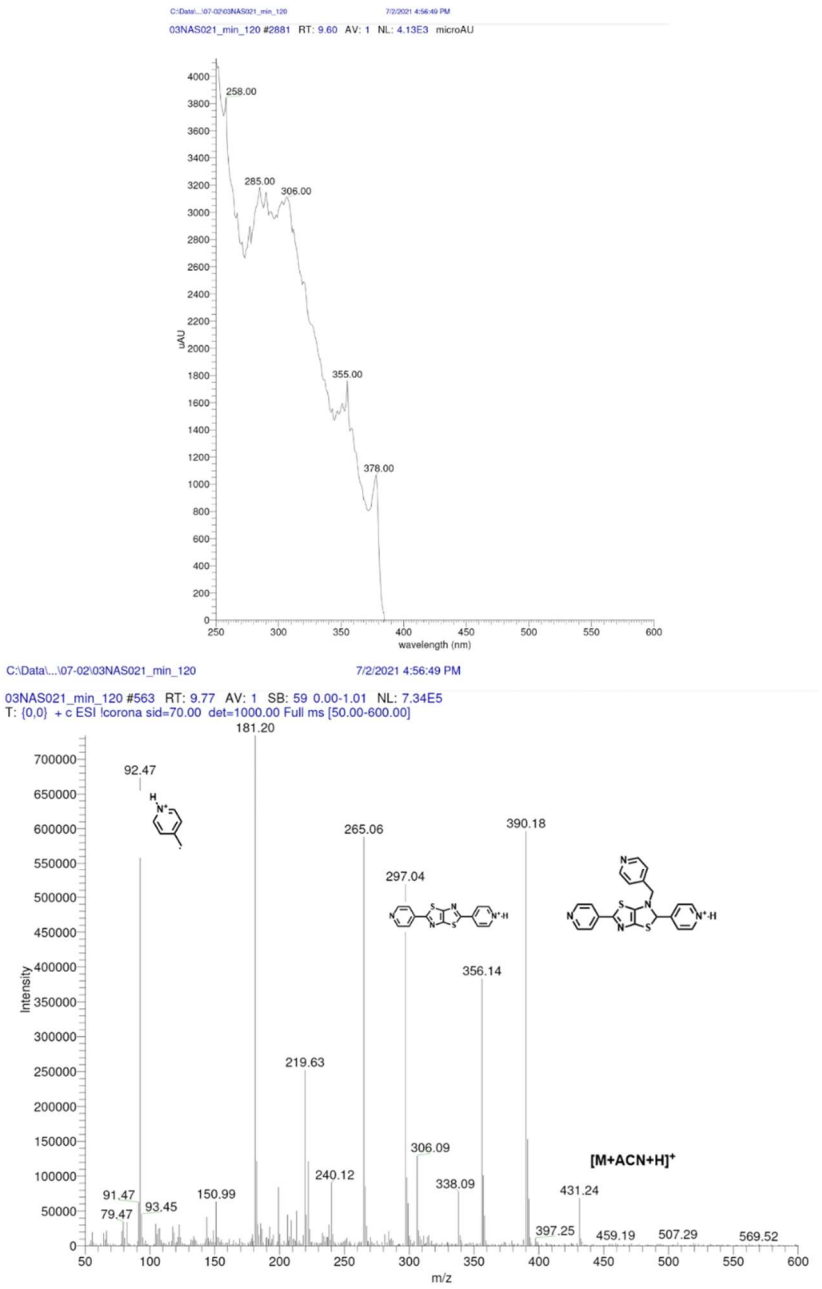

Figure D21. UV-B channel (350 nm) chromatograms of the Py_2-TTz reaction under anaerobic conditions (N_2). Labels refer to the reaction time when an aliquot was taken.

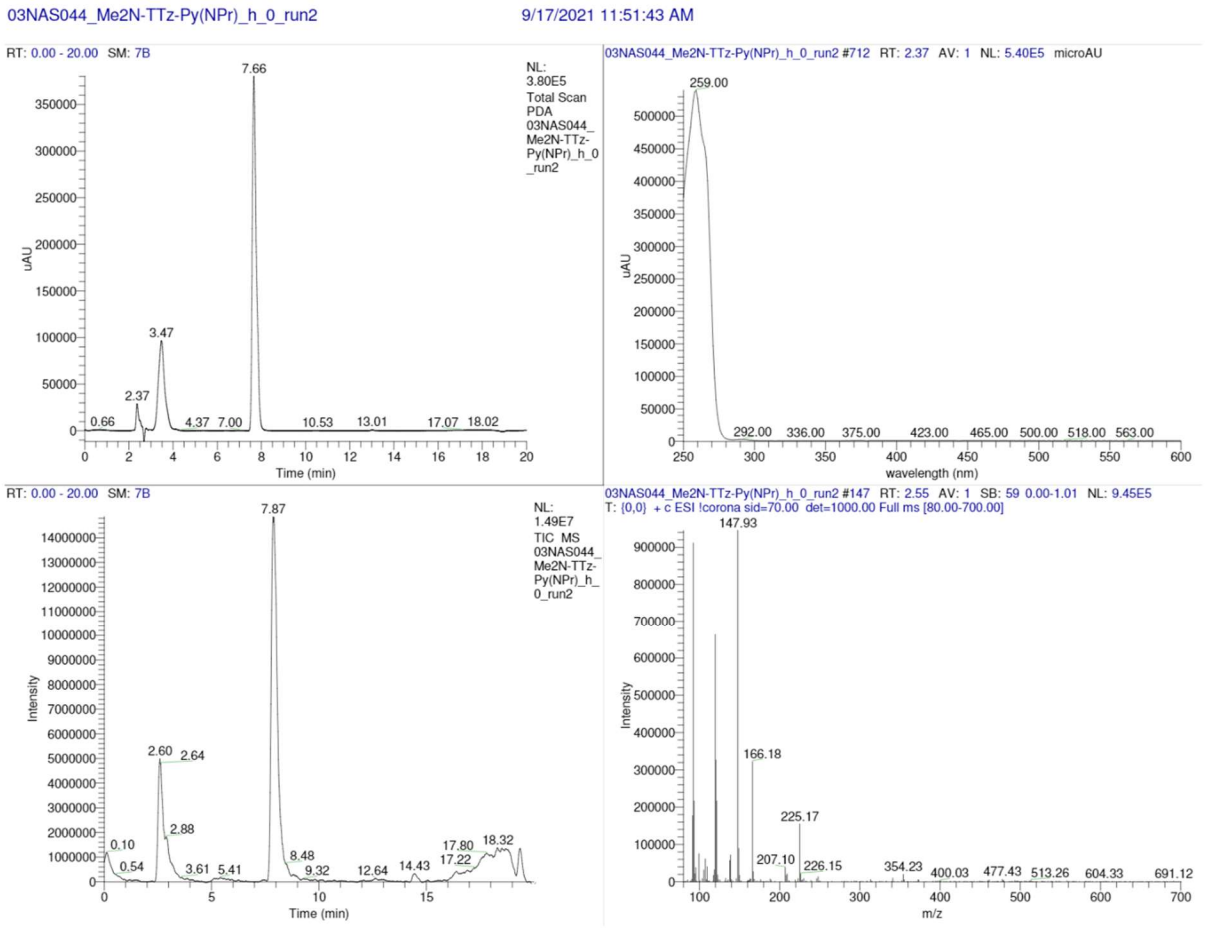

Figure D22. Me_2N-TTz-Py(NPr) condensation reaction chromatograms (left) and OHCPy(NPr) spectra (right, rt = 2.37, 2.55 min) at beginning of reaction (0 h). Total scan PDA (top), TIC MS (bottom).

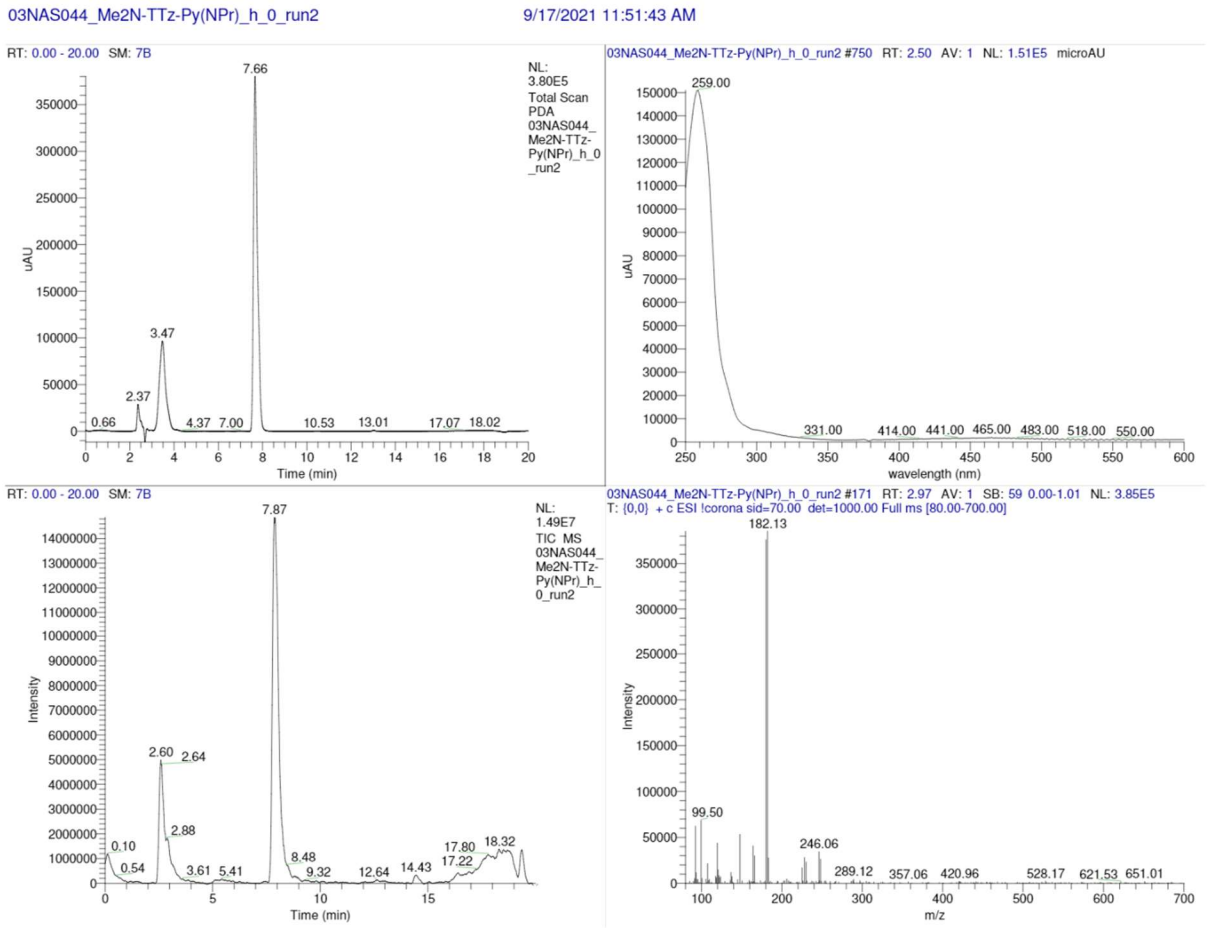

Figure D23. Me_2N-TTz-Py(NPr) condensation reaction chromatograms (left) and NPrBr impurity spectra (right, rt = 2.50, 2.97 min) at beginning of reaction (0 h). Total scan PDA (top), TIC MS (bottom).

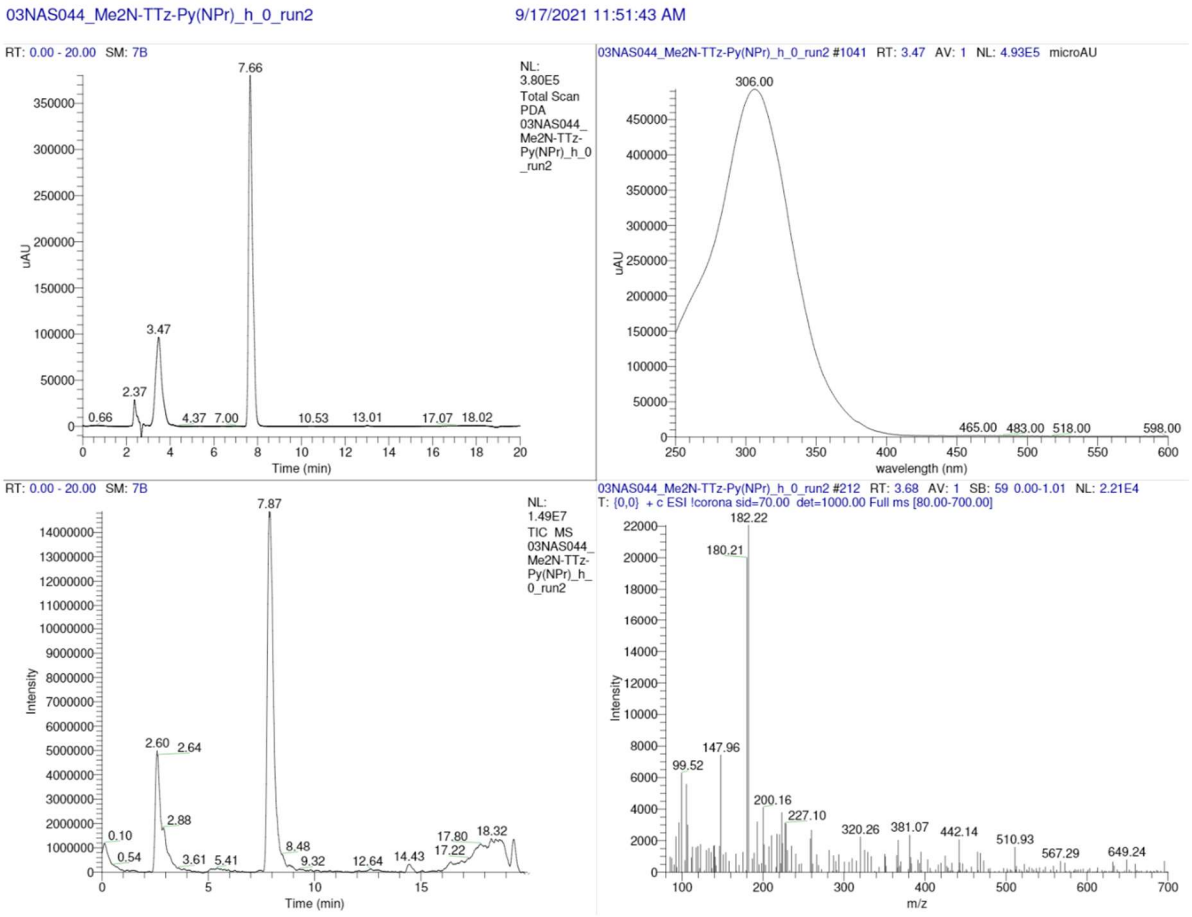

Figure D24. Me_2N-TTz-Py(NPr) condensation reaction chromatograms (left) and dithiooxamide spectra (right, rt = 3.47, 3.68 min) at beginning of reaction (0 h). Total scan PDA (top), TIC MS (bottom).

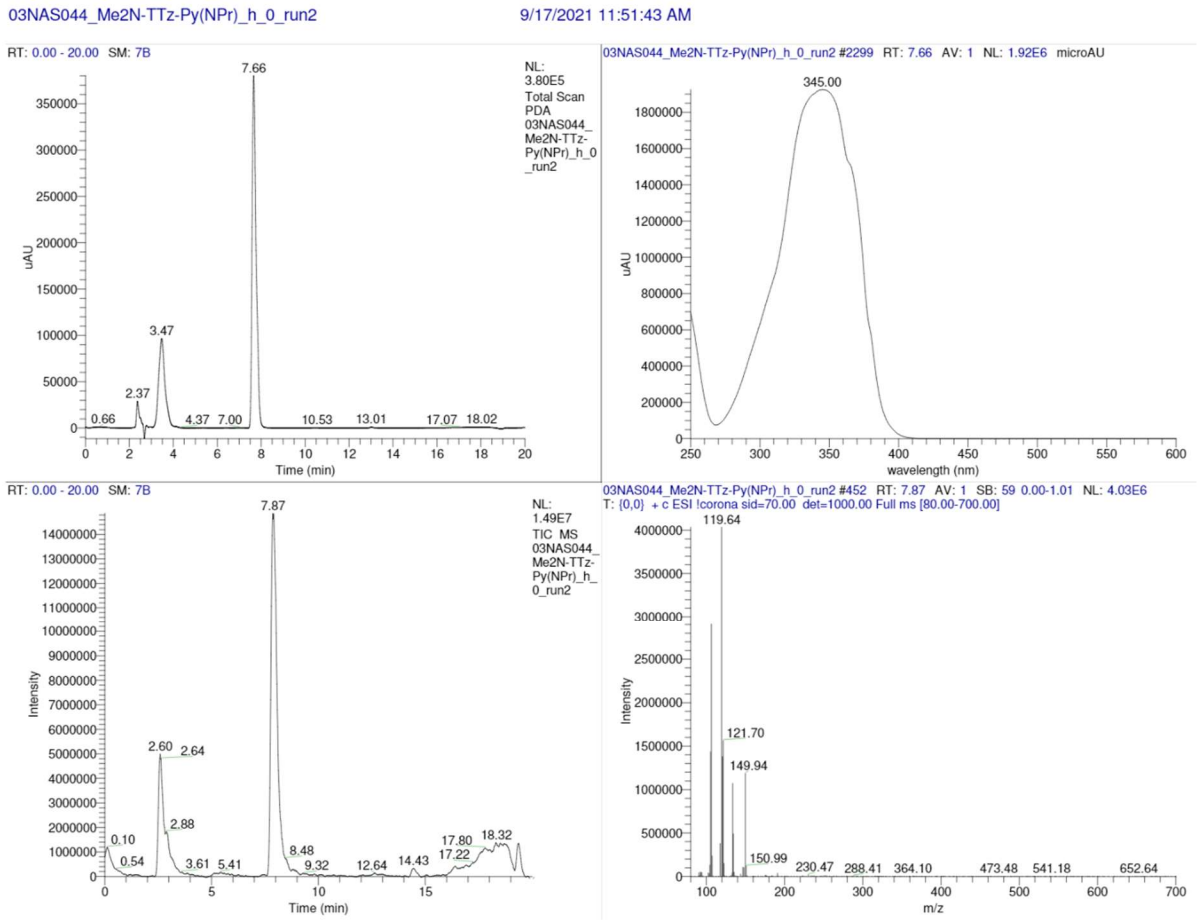

Figure D25. Me_2N-TTz-Py(NPr) condensation reaction chromatograms (left) and $Me_2NPhCHO$ spectra (right, rt = 7.66, 7.87 min) at beginning of reaction (0 h). Total scan PDA (top), TIC MS (bottom).

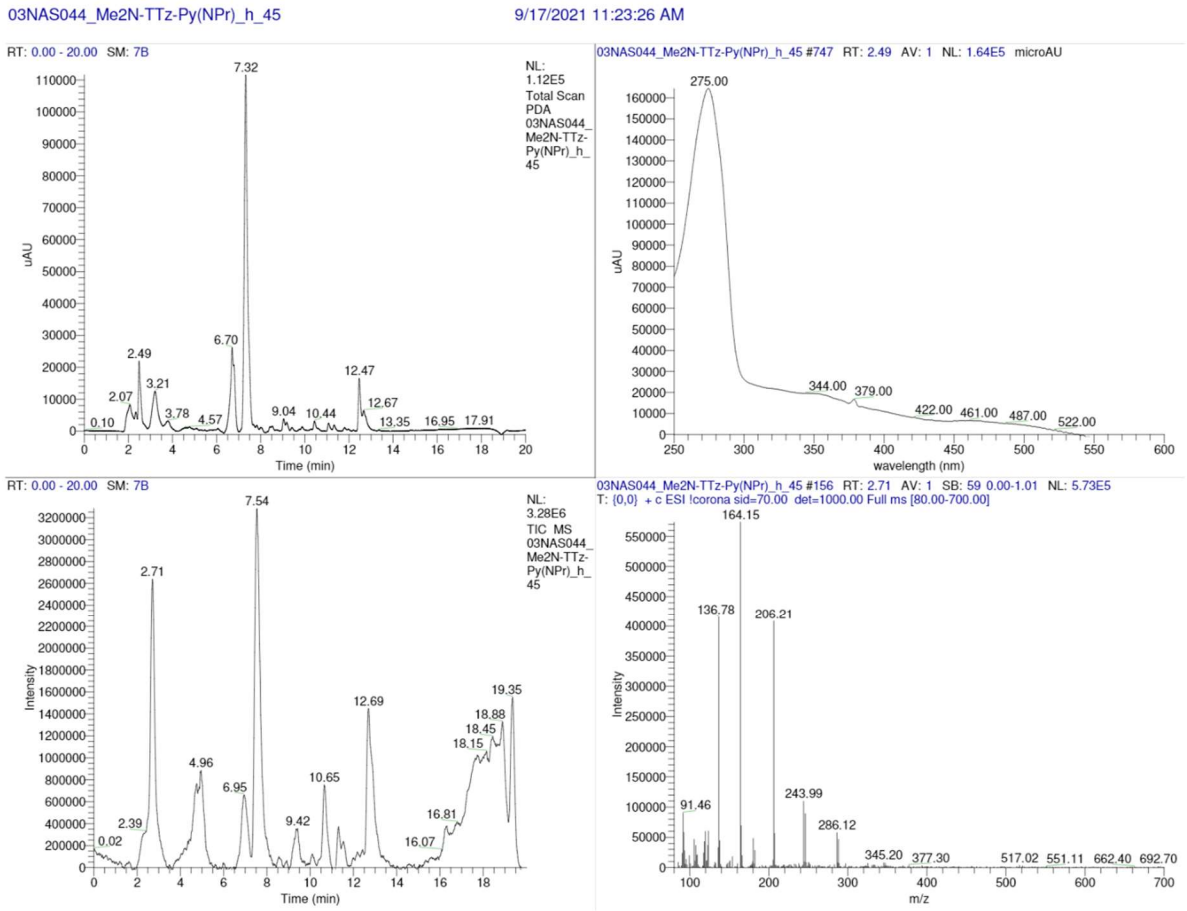

Figure D26. Me_2N-TTz-Py(NPr) condensation reaction chromatograms (left) and unknown side product spectra (right, rt = 2.49, 2.71 min) at end of reaction (48 h). Total scan PDA (top), TIC MS (bottom).

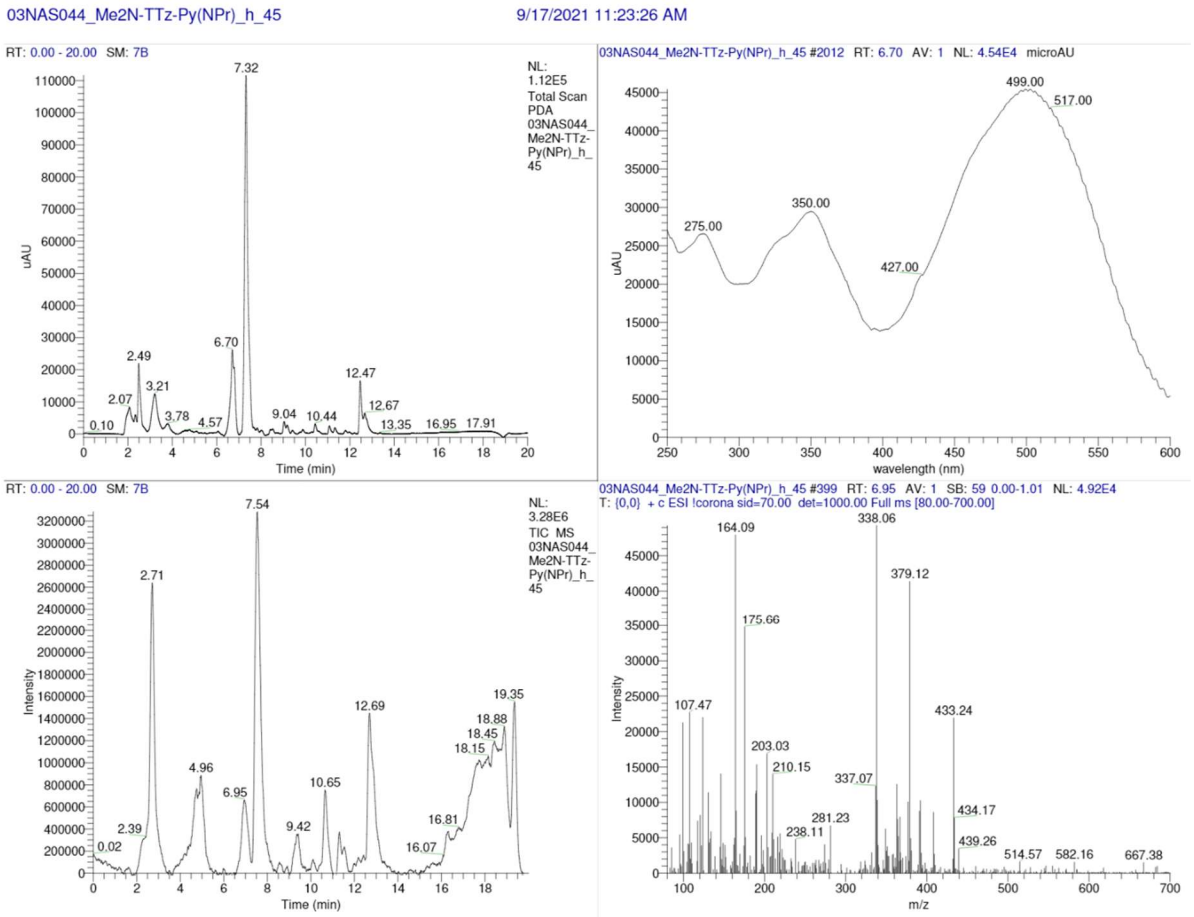

Figure D27. Me_2N-TTz-Py(NPr) condensation reaction chromatograms (left) and Me_2N-TTz-Py(NPr) spectra (right, rt = 6.70, 6.95 min) at end of reaction (48 h). Total scan PDA (top), TIC MS (bottom).

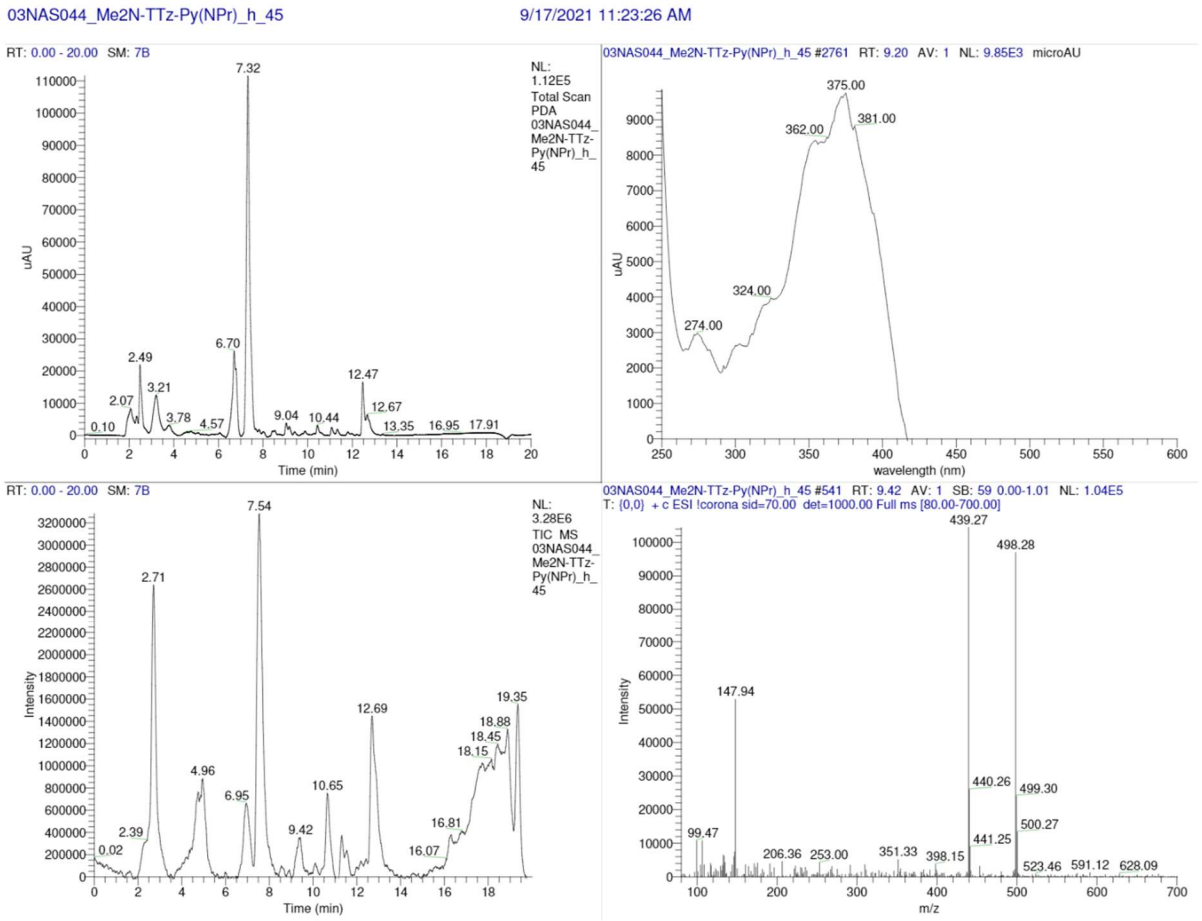

Figure D28. Me_2N-TTz-Py(NPr) condensation reaction chromatograms (left) and $[Py(NPr)]_2$-TTz spectra (right, rt = 9.20, 9.42 min) at end of reaction (48 h). Total scan PDA (top), TIC MS (bottom).

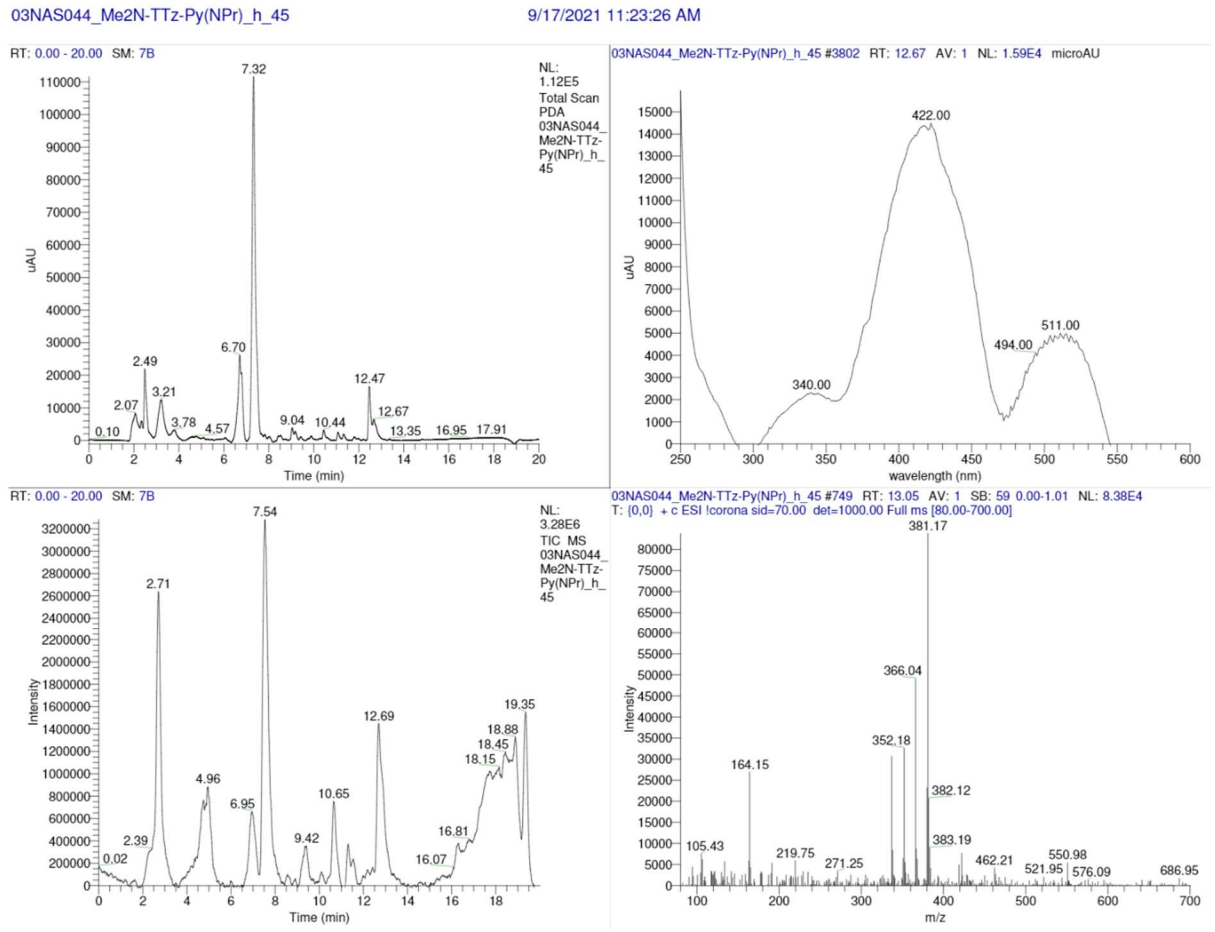

Figure D29. Me_2N-TTz-Py(NPr) condensation reaction chromatograms (left) and $(Me_2N)_2$-TTz spectra (right, rt = 12.67, 13.05 min) at end of reaction (48 h). Total scan PDA (top), TIC MS (bottom).

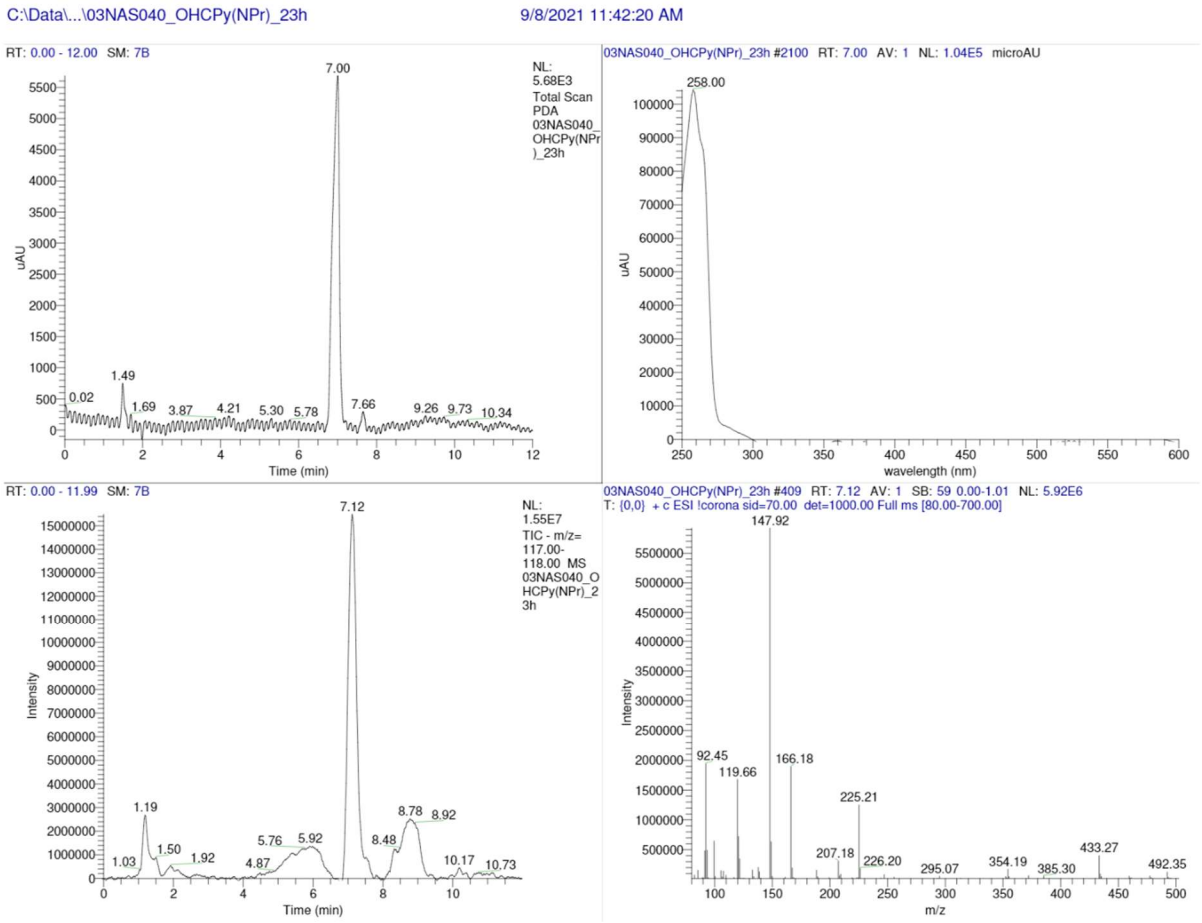

Figure D30. OHCPy(NPr) alkylation reaction chromatograms (left) and OHCPy(NPr) spectra (right, rt = 7.00, 7.12 min) at end of reaction (48 h). Total scan PDA (top), TIC MS (bottom).

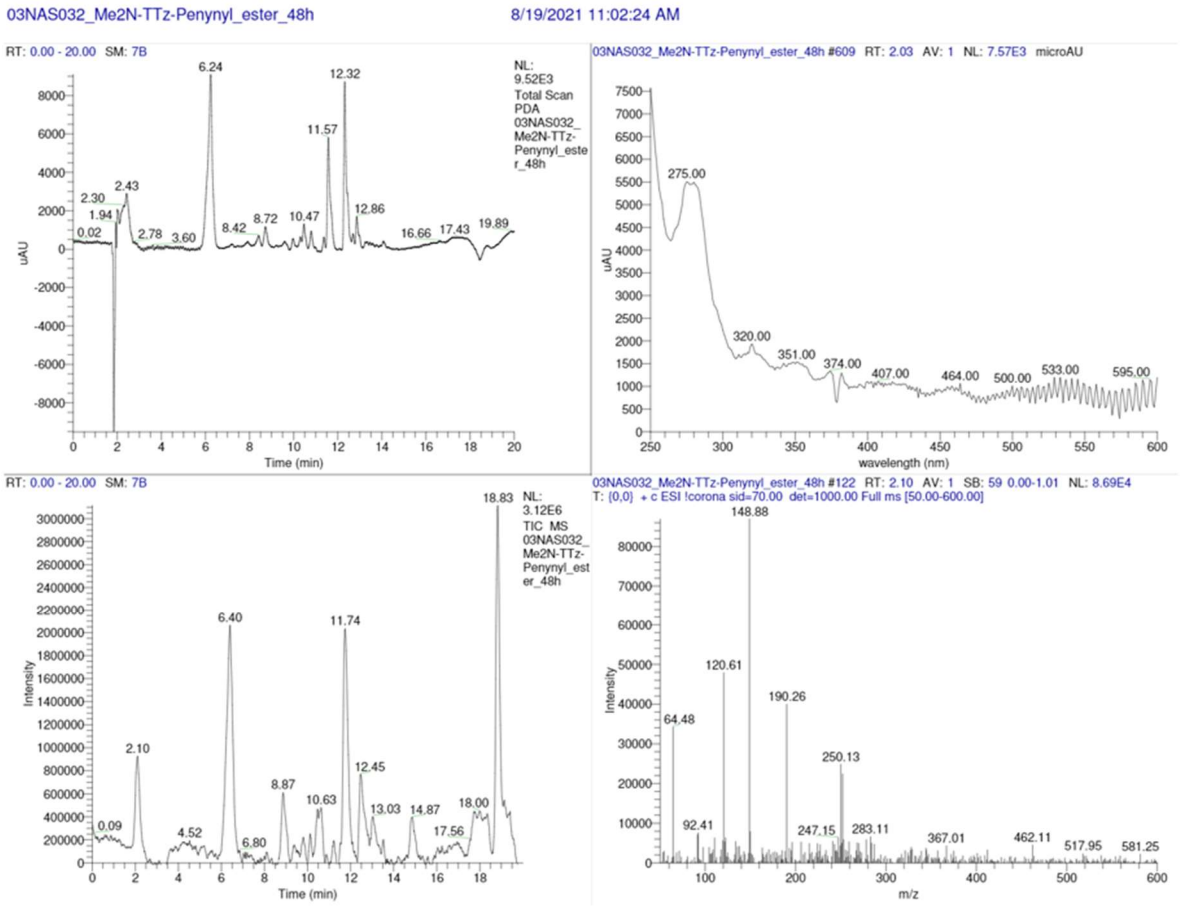

Figure D31. Click TTz reaction chromatograms (left) and spectra (right, rt = 2.03, 2.10 min) at end of reaction (48 h). Total scan PDA (top), TIC MS (bottom).

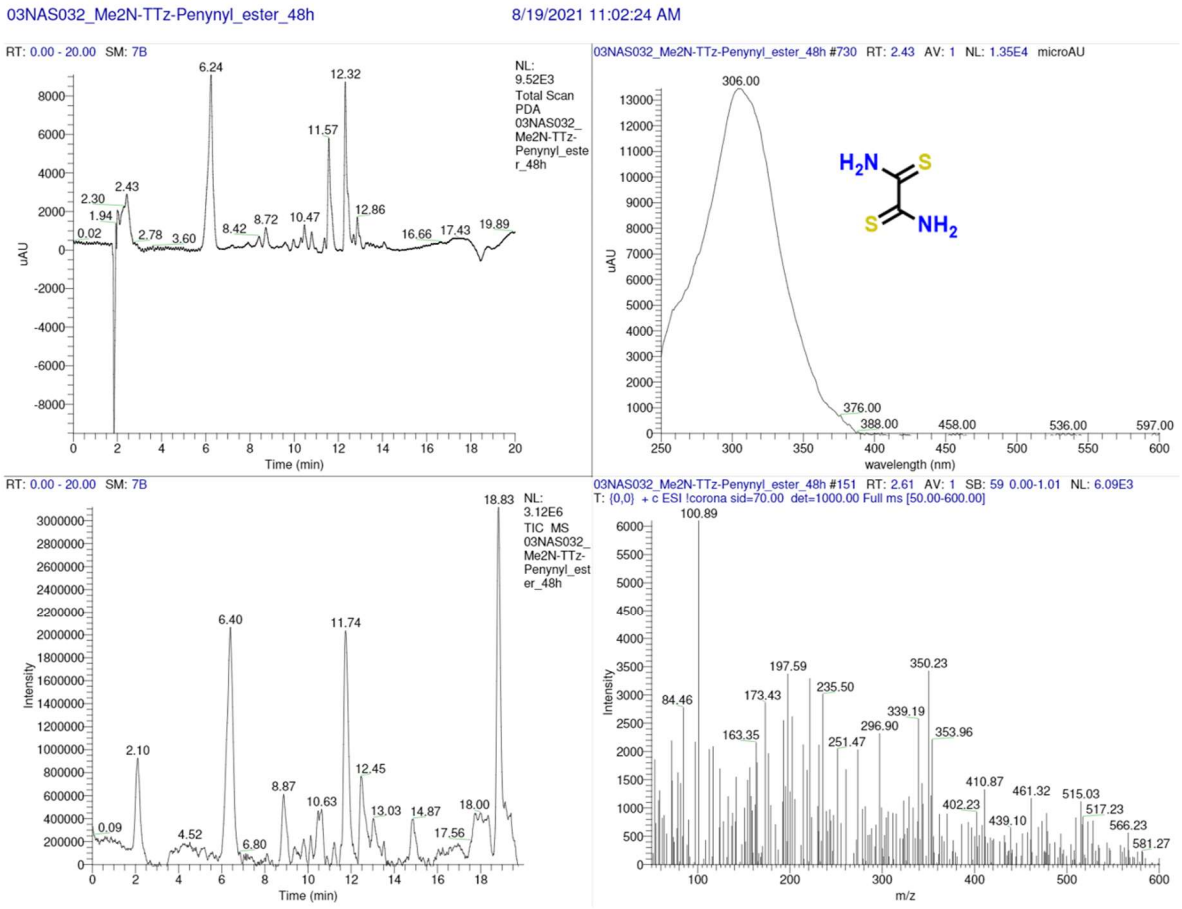

Figure D32. Click TTz reaction chromatograms (left) and dithiooxamide spectra (right, rt = 2.43, 2.61 min) at end of reaction (48 h). Total scan PDA (top), TIC MS (bottom).

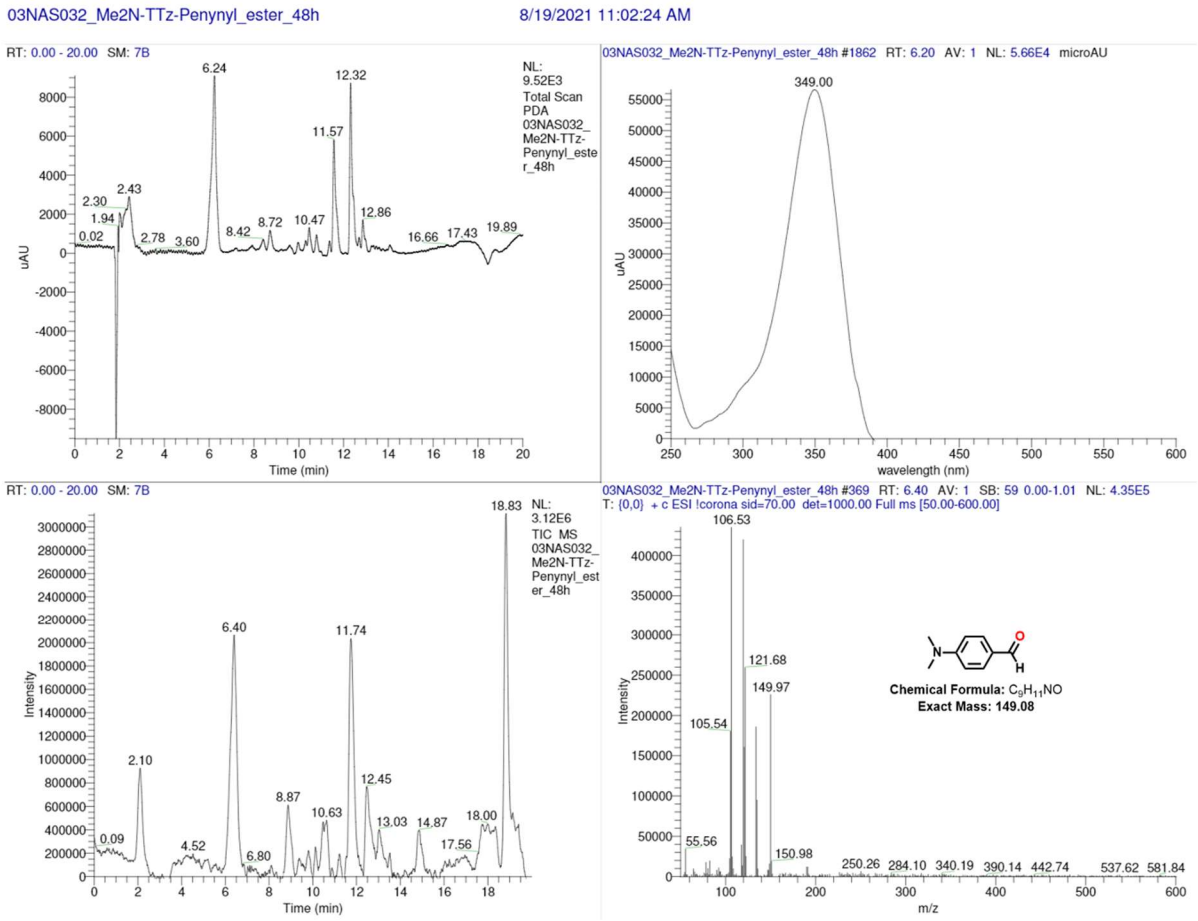

Figure D33. Click TTz reaction chromatograms (left) and Me_2N-PhCHO spectra (right, rt = 6.20, 6.40 min) at end of reaction (48 h). Total scan PDA (top), TIC MS (bottom).

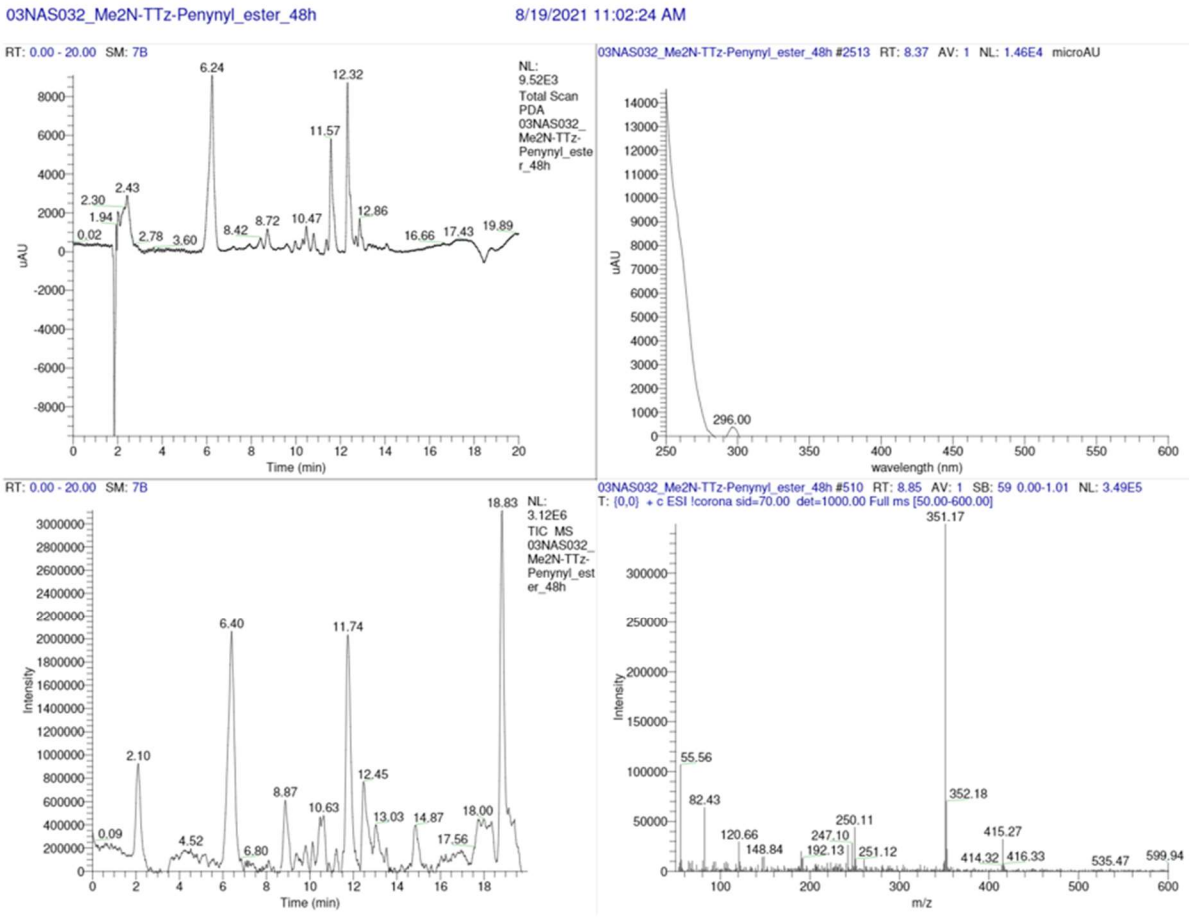

Figure D34. Click TTz reaction chromatograms (left) and spectra (right, rt = 8.37, 8.85 min) at end of reaction (48 h). Total scan PDA (top), TIC MS (bottom).

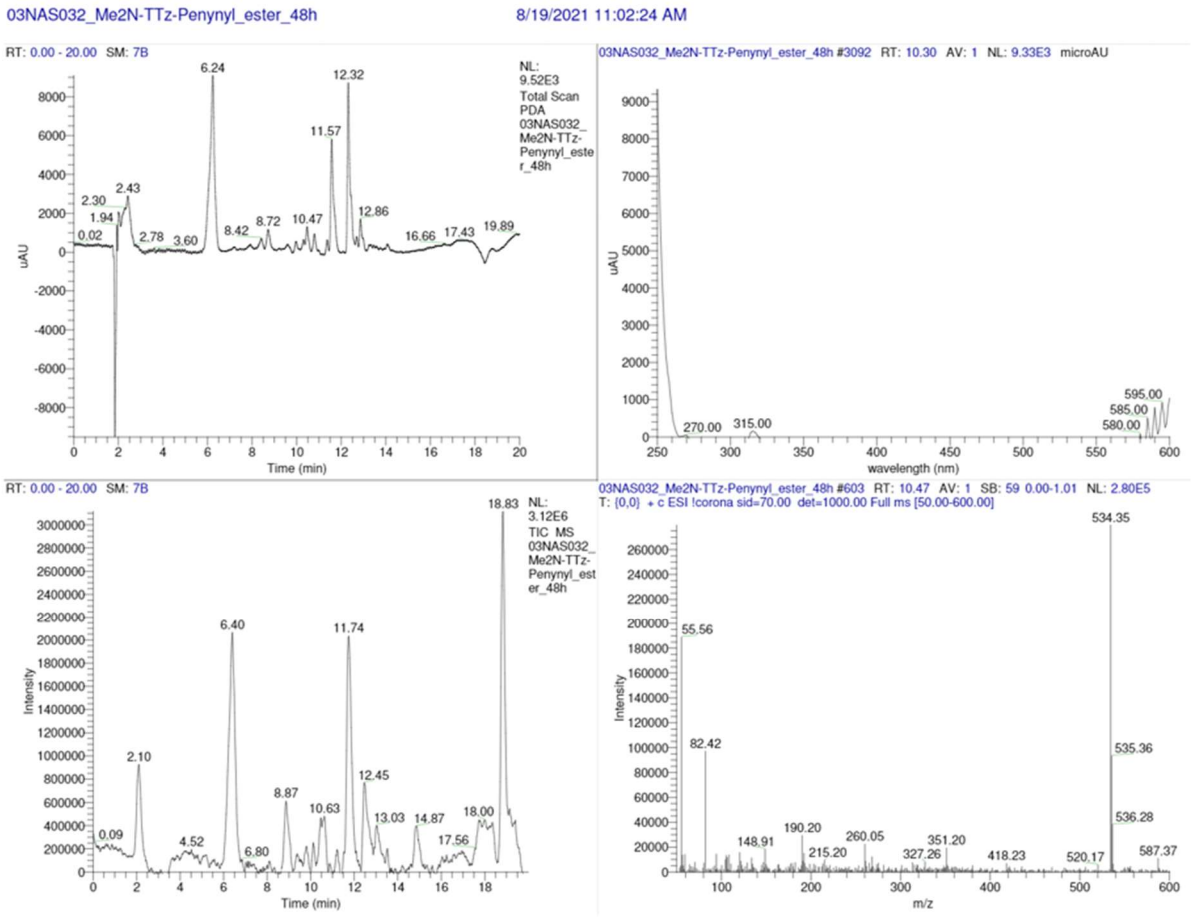

Figure D35. Click TTz reaction chromatograms (left) and spectra (right, rt = 10.30, 10.47 min) at end of reaction (48 h). Total scan PDA (top), TIC MS (bottom).

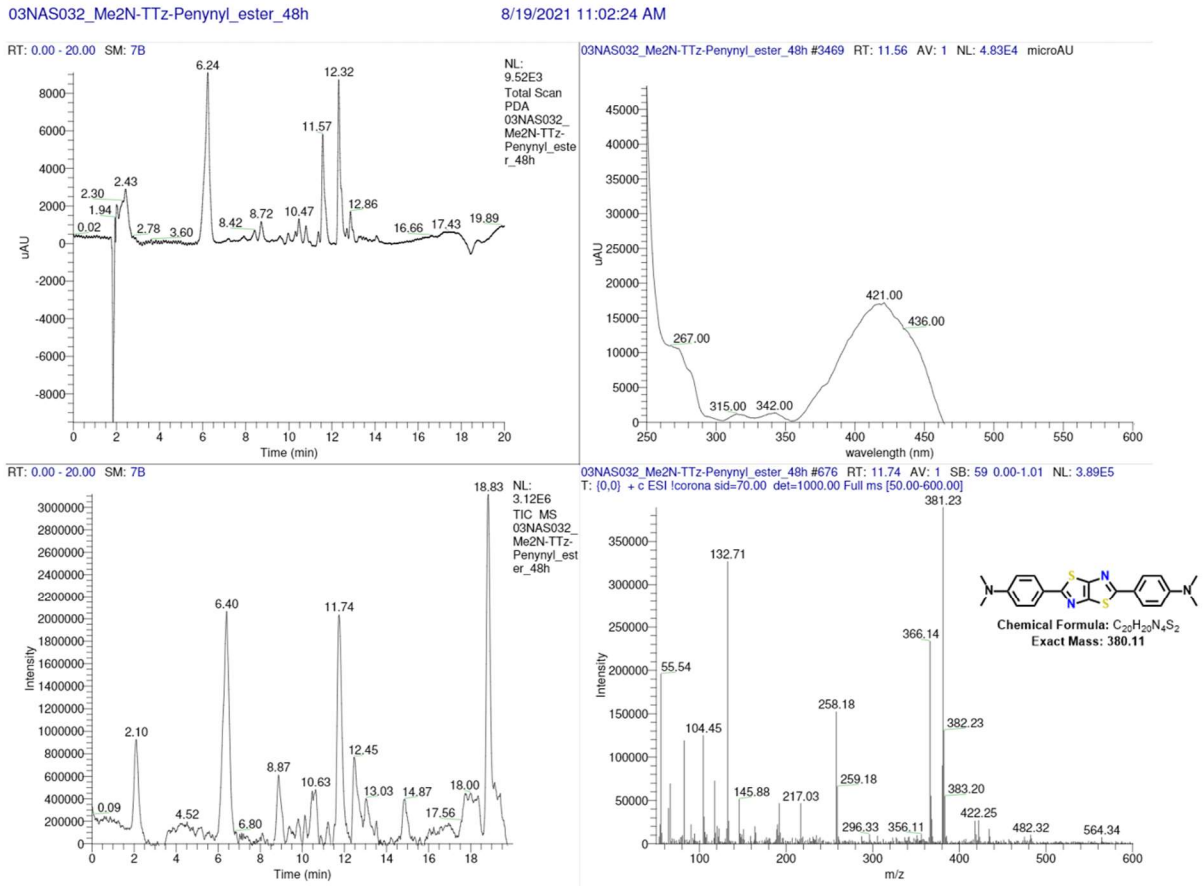

Figure D36. Click TTz reaction chromatograms (left) and $(Me_2N)_2$-TTz spectra (right, rt = 11.56, 11.74 min) at end of reaction (48 h). Total scan PDA (top), TIC MS (bottom).

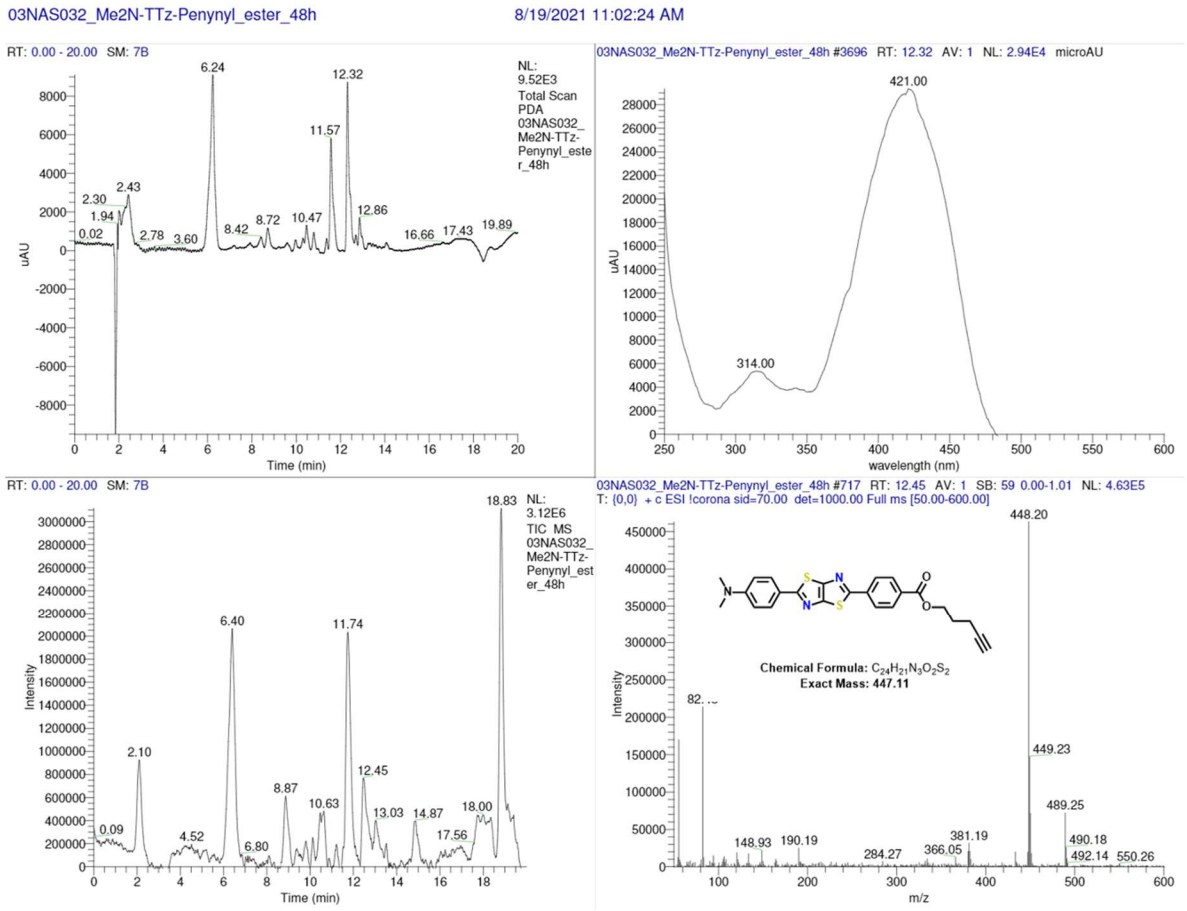

Figure D37. Click TTz reaction chromatograms (left) and Me_2N-TTz-Ph pentynyl ester spectra (right, rt = 12.32, 12.45 min) at end of reaction (48 h). Total scan PDA (top), TIC MS (bottom).

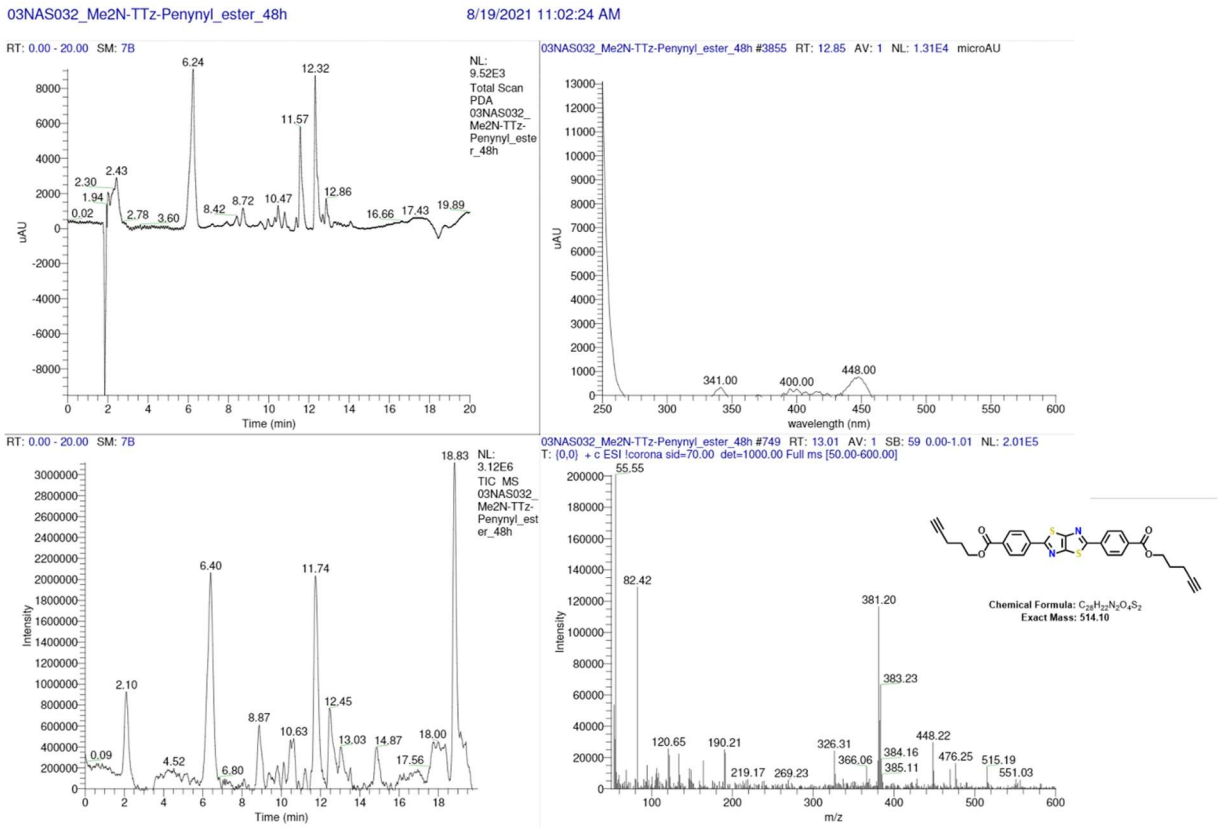

Figure D38. Click TTz reaction chromatograms (left) and diester TTz spectra (right, rt = 12.85, 13.01 min) at end of reaction (48 h). Total scan PDA (top), TIC MS (bottom).

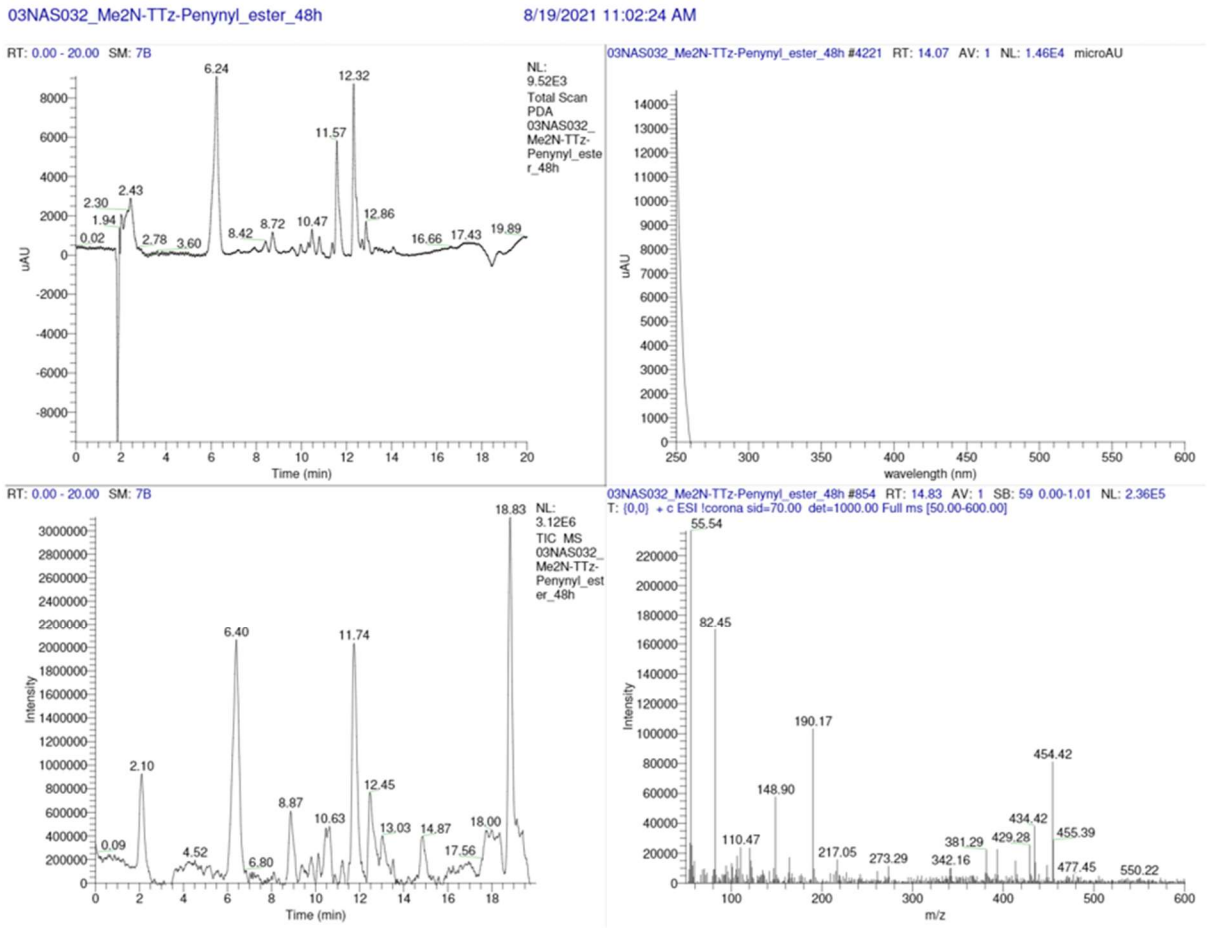

Figure D39. Click TTz reaction chromatograms (left) and spectra (right, rt = 14.07, 14.83 min) at end of reaction (48 h). Total scan PDA (top), TIC MS (bottom).

Appendix E – Mechanistic Computational Studies

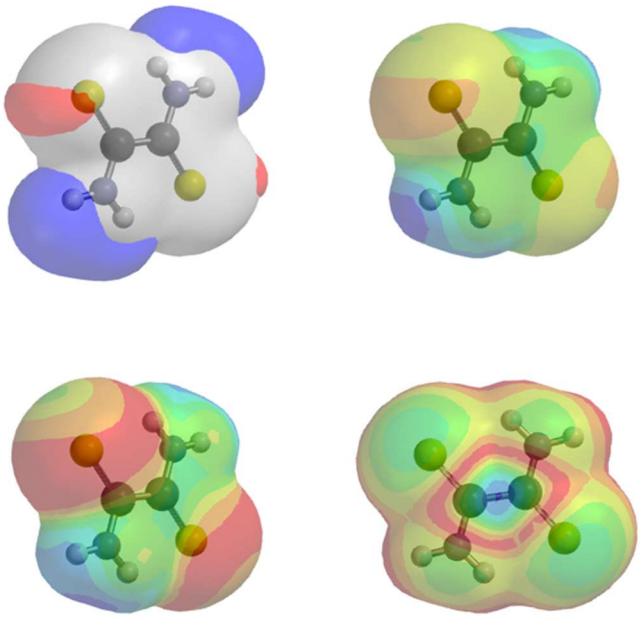

Figure E1. Dithiooxamide major form. (clockwise) Extended electrostatic potential map, electrostatic potential map, LUMO map, local ionization potential map.

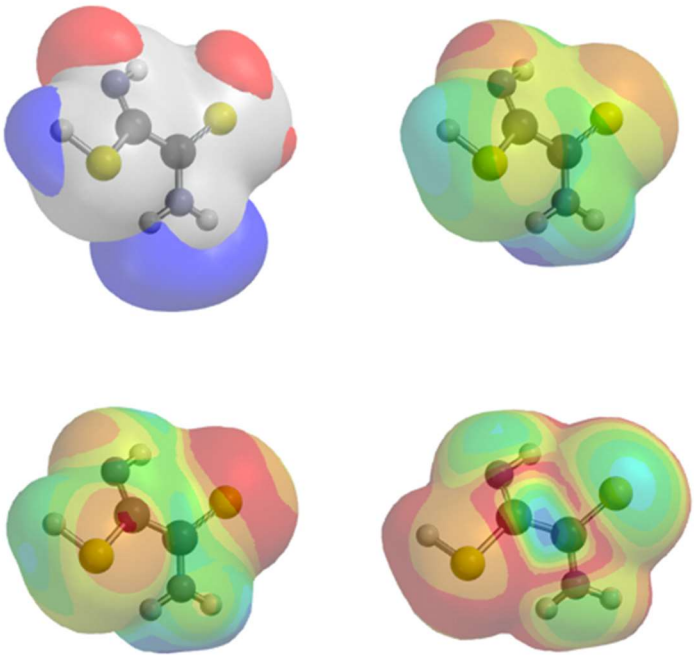

Figure E2. Dithiooxamide minor form (half). (clockwise) Extended electrostatic potential map, electrostatic potential map, LUMO map, local ionization potential map.

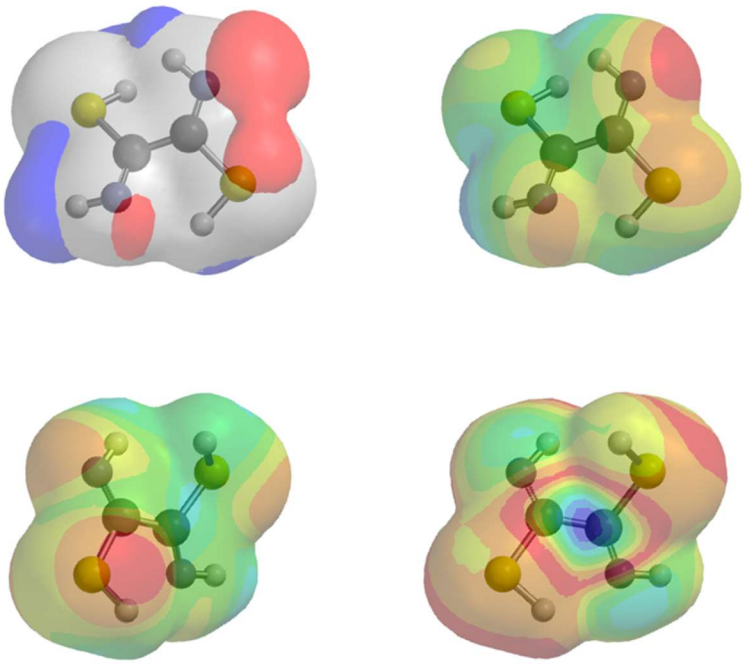

Figure E3. Dithiooxamide minor form (half). (clockwise) Extended electrostatic potential map, electrostatic potential map, LUMO map, local ionization potential map.

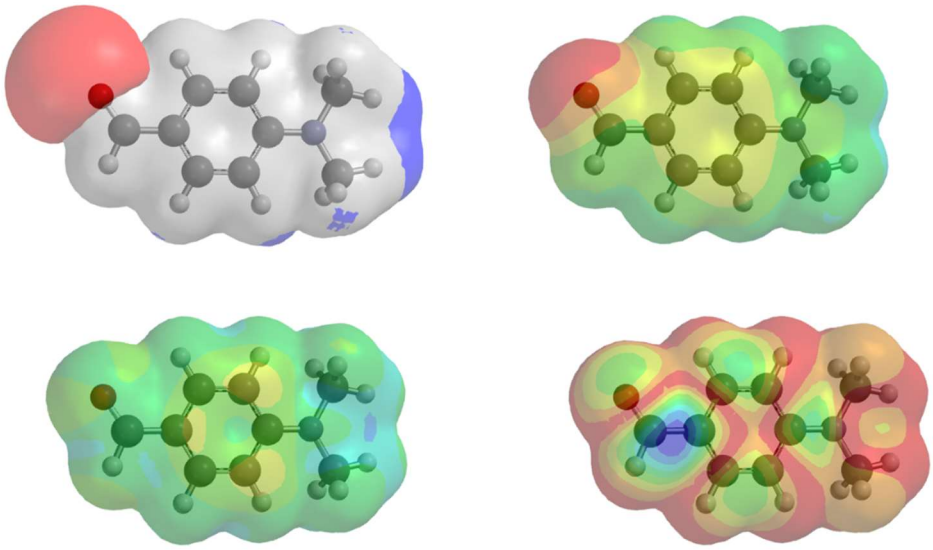

Figure E4. 4-(N,N-Dimethylamino)benzaldehyde (Me_2NPh-CHO). (clockwise) Extended electrostatic potential map, electrostatic potential map, LUMO map, local ionization potential map.

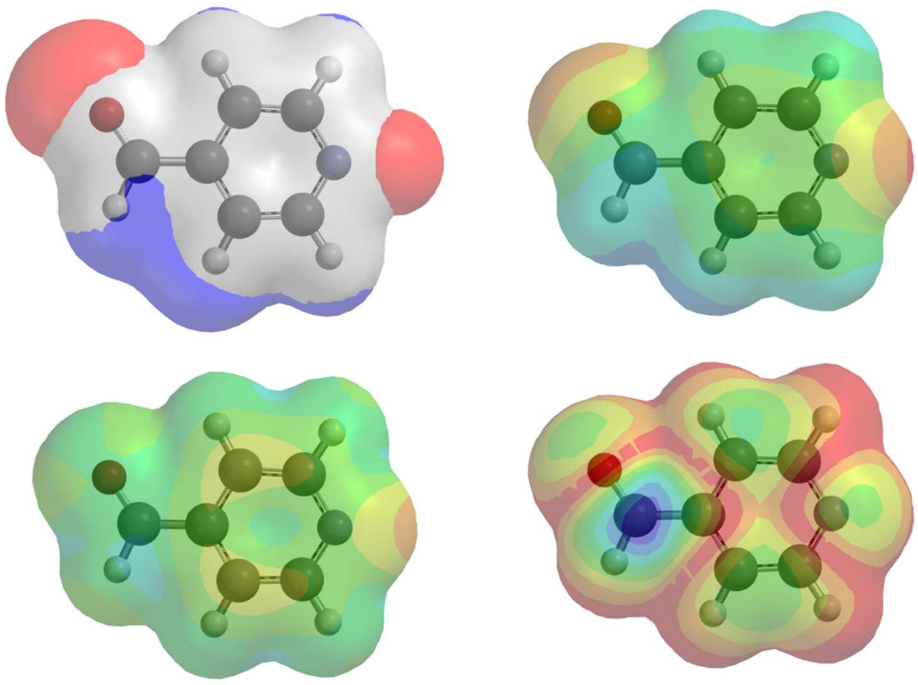

Figure E5. 4-Pyridinecarboxaldehyde (Py-CHO). (clockwise) Extended electrostatic potential map, electrostatic potential map, LUMO map, local ionization potential map.

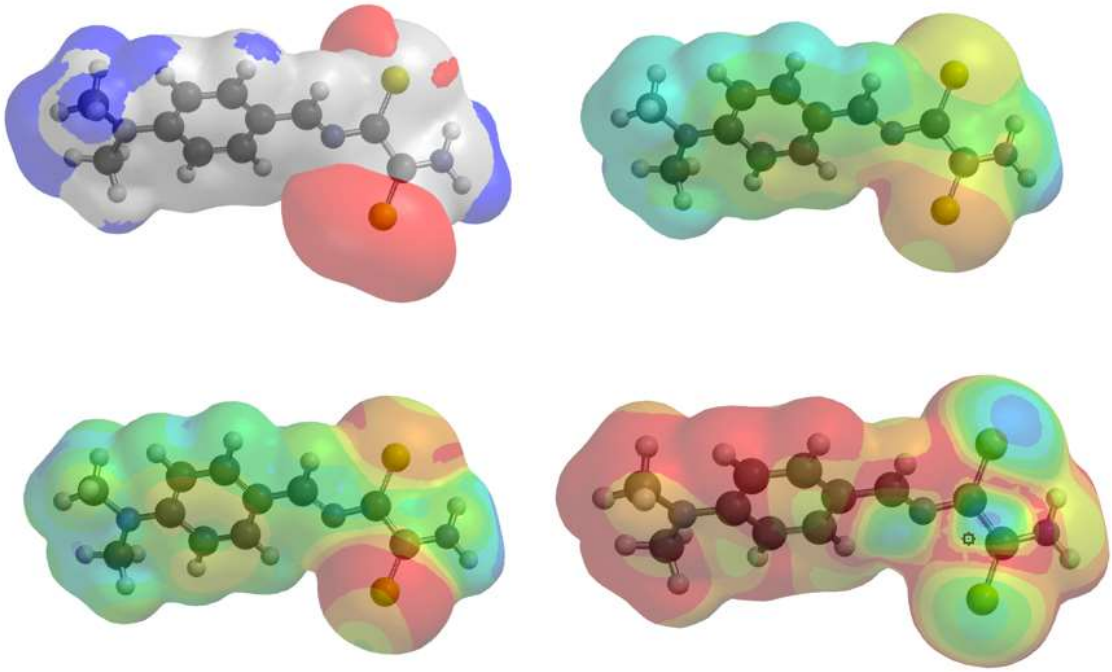

Figure E6. N-[(N,N'-4-dimethylaniline)methylene]-ethanedithioamide (amAn). (clockwise) Extended electrostatic potential map, electrostatic potential map, LUMO map, local ionization potential map.

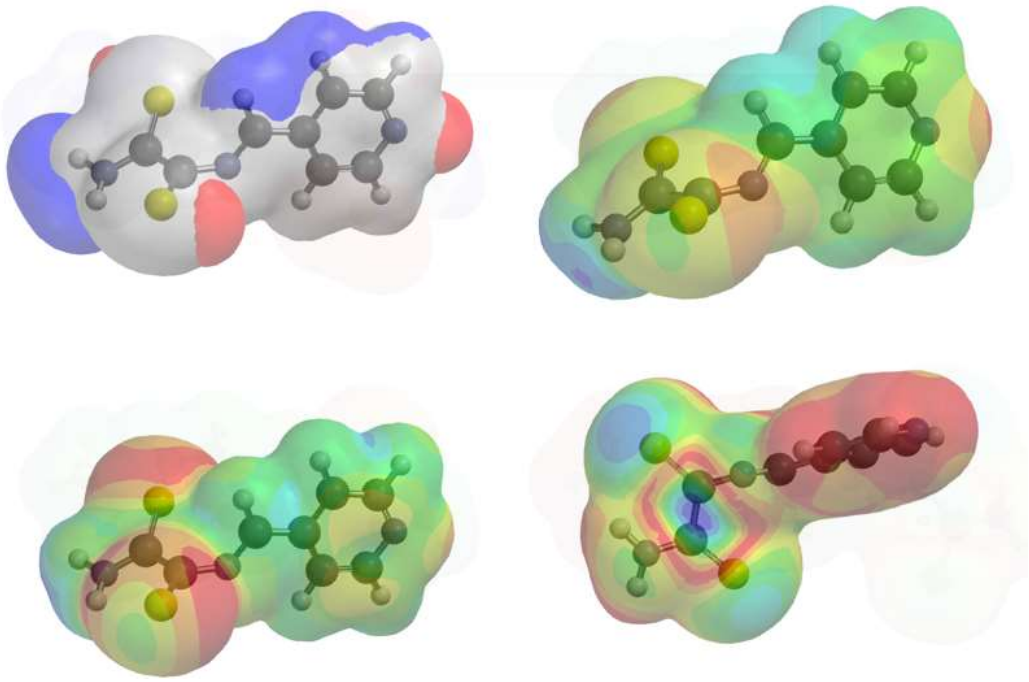

Figure E7. N-[4-pyridylmethylene]-ethanedithioamide (amPy). (clockwise) Extended electrostatic potential map, electrostatic potential map, LUMO map, local ionization potential map.

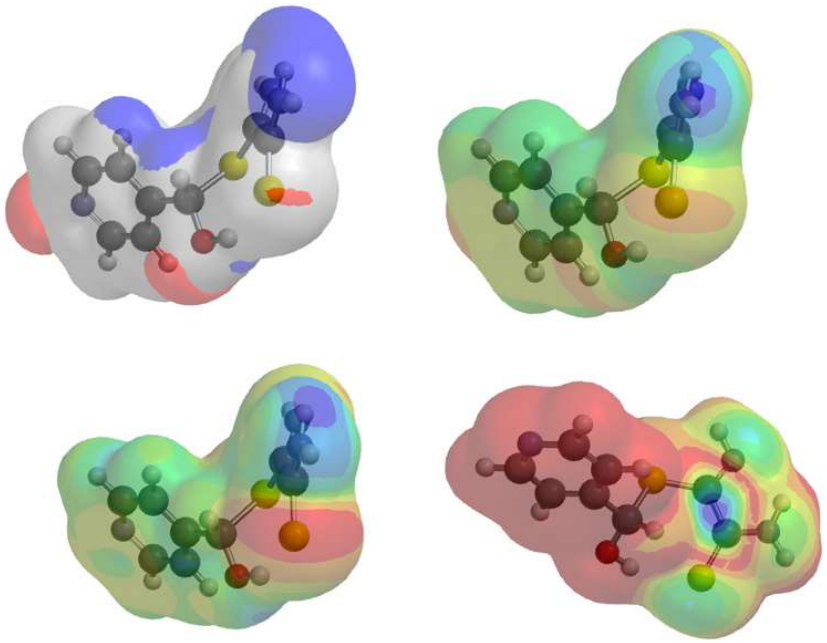

Figure E8. 4-Pyridyl hydroxylthioether intermediate (Py-HTE). (clockwise) Extended electrostatic potential map, electrostatic potential map, LUMO map, local ionization potential map.

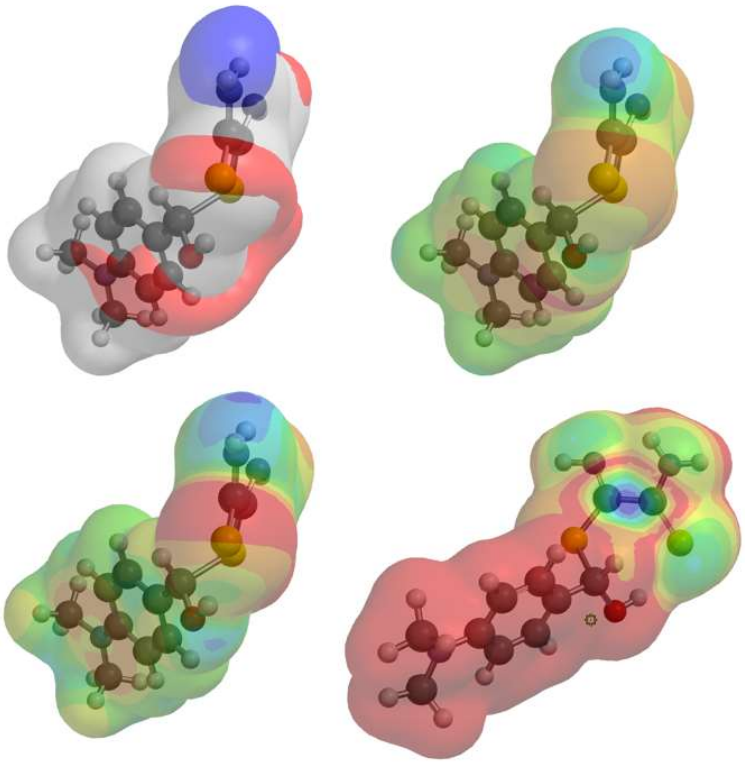

Figure E9. 4-Dimethylaniline hydroxylthioether intermediate (An-HTE). (clockwise) Extended electrostatic potential map, electrostatic potential map, LUMO map, local ionization potential map.

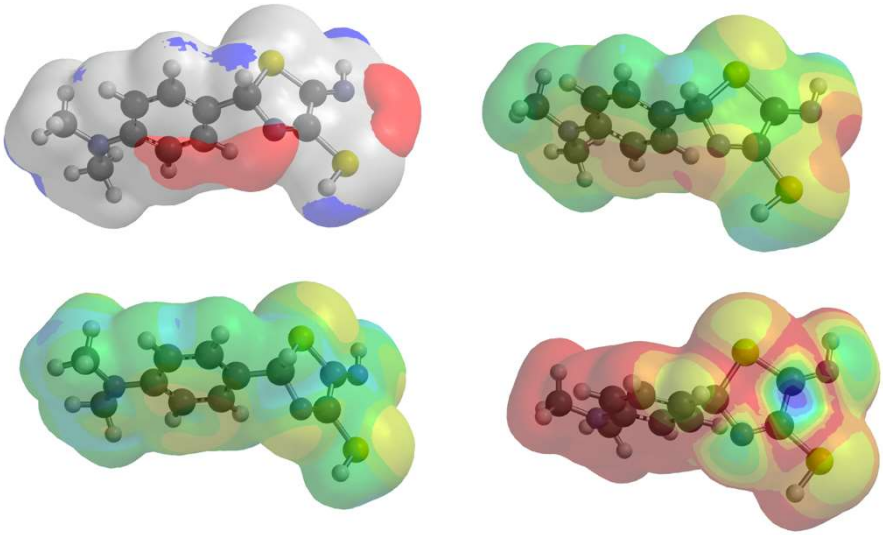

Figure E10. 5-(4-dimethylaniline)-2-imino-3-mercapto-5-hydrothiazole (An-HTz). (clockwise) Extended electrostatic potential map, electrostatic potential map, LUMO map, local ionization potential map.

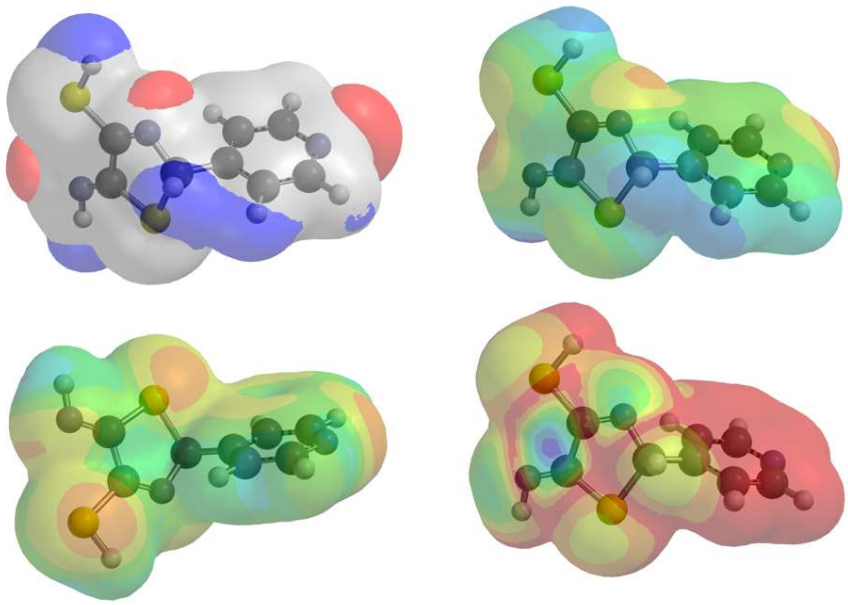

Figure E11. 5-(4-pyridyl)-2-imino-3-mercapto-5-hydrothiazole (An-HTz). (clockwise) Extended electrostatic potential map, electrostatic potential map, LUMO map, local ionization potential map.

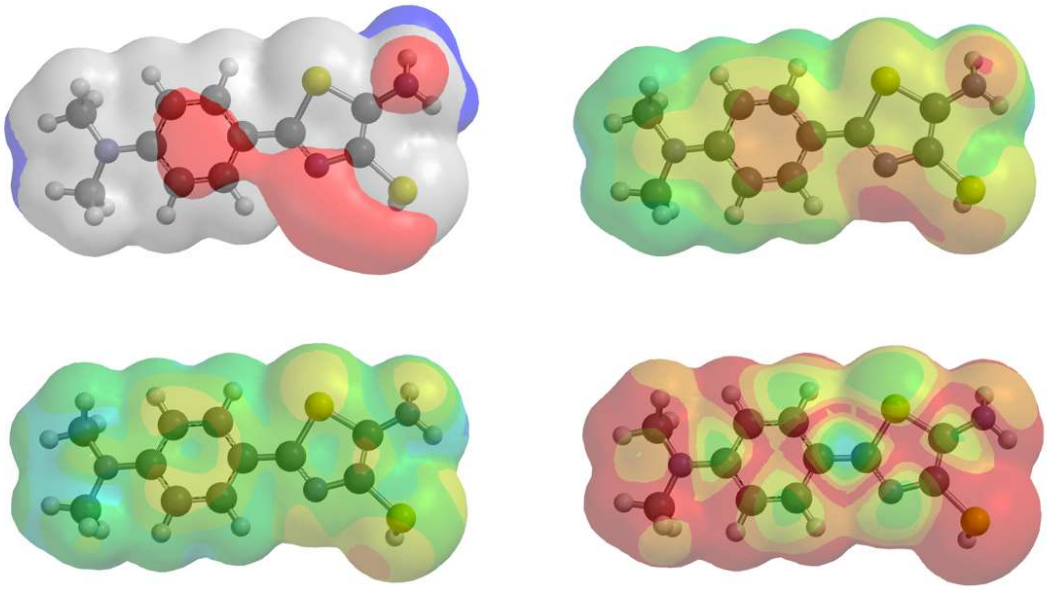

Figure E12. 5-(4-dimethylaniline)-2-imino-3-mercaptothiazole (An-Tz). (clockwise) Extended electrostatic potential map, electrostatic potential map, LUMO map, local ionization potential map.

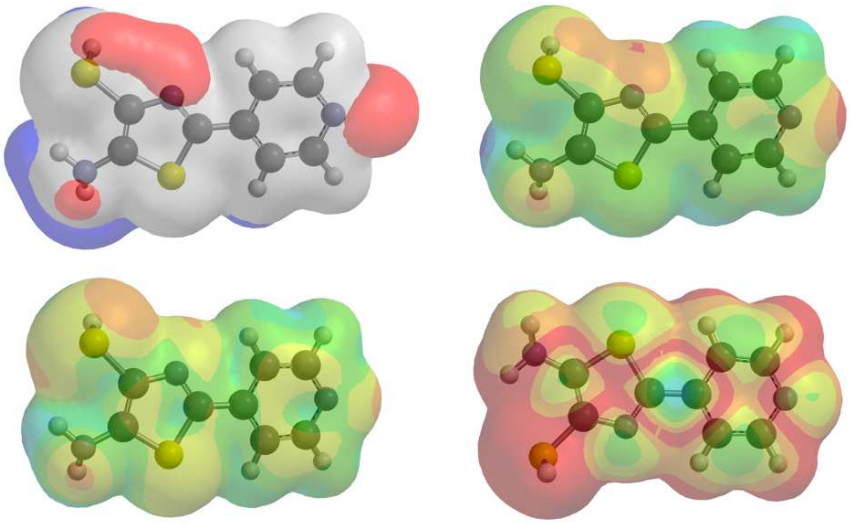

Figure E13. 5-(4- pyridyl)-2-imino-3-mercaptothiazole (An-Tz). (clockwise) Extended electrostatic potential map, electrostatic potential map, LUMO map, local ionization potential map.

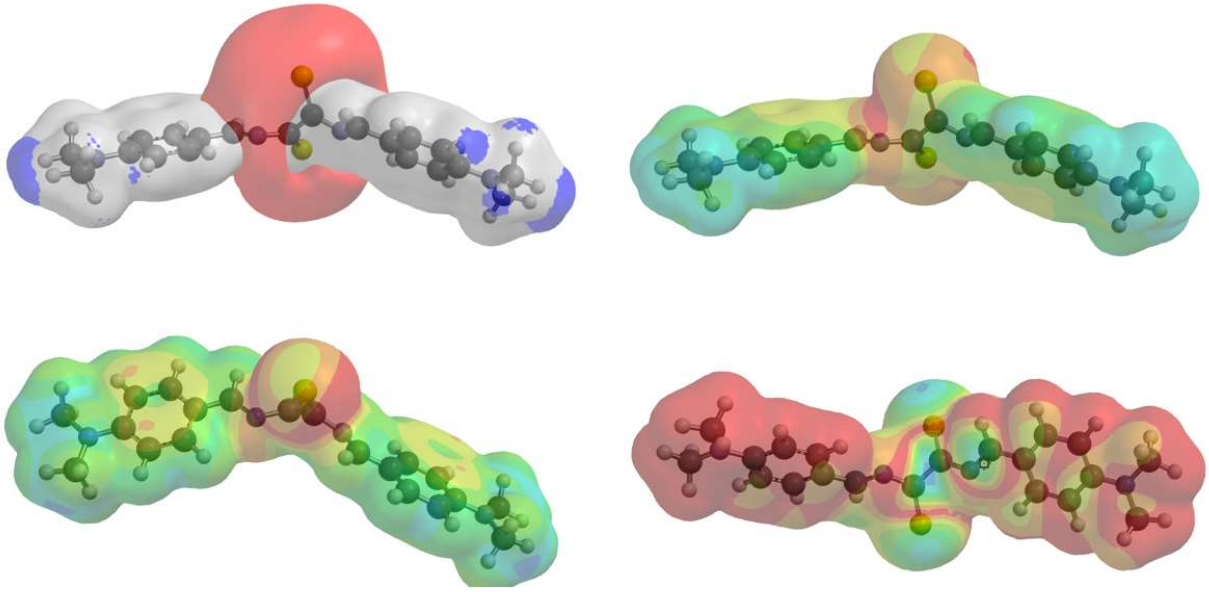

Figure E14. Dianiline diazomethine intermediate (An_2-DAM) (clockwise) Extended electrostatic potential map, electrostatic potential map, LUMO map, local ionization potential map.

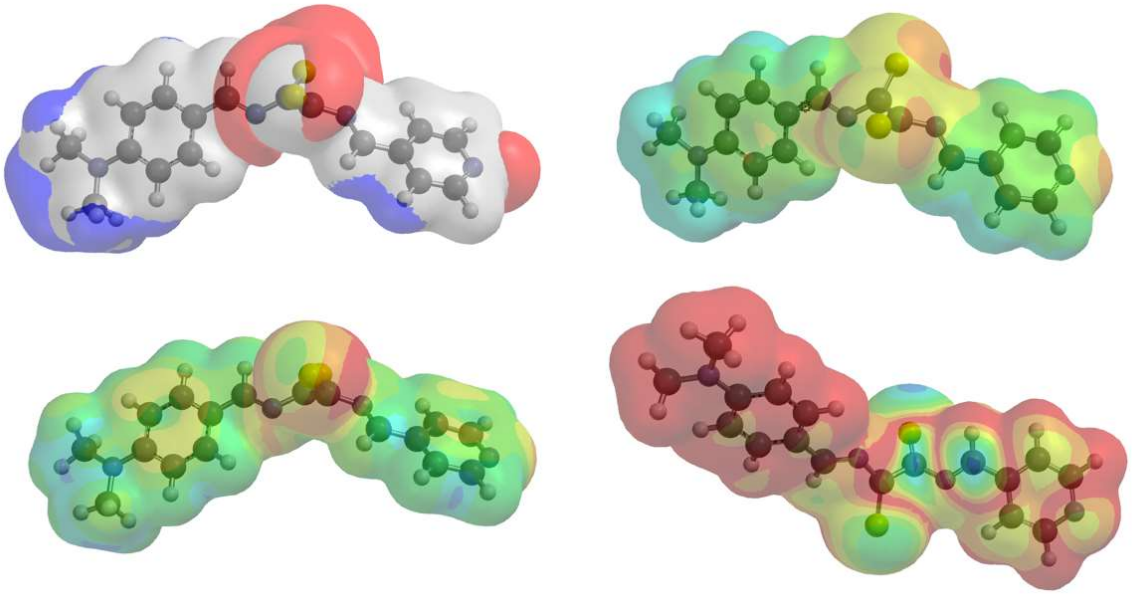

Figure E15. Asymmetric diazomethine intermediate (a-DAM) (clockwise) Extended electrostatic potential map, electrostatic potential map, LUMO map, local ionization potential map.

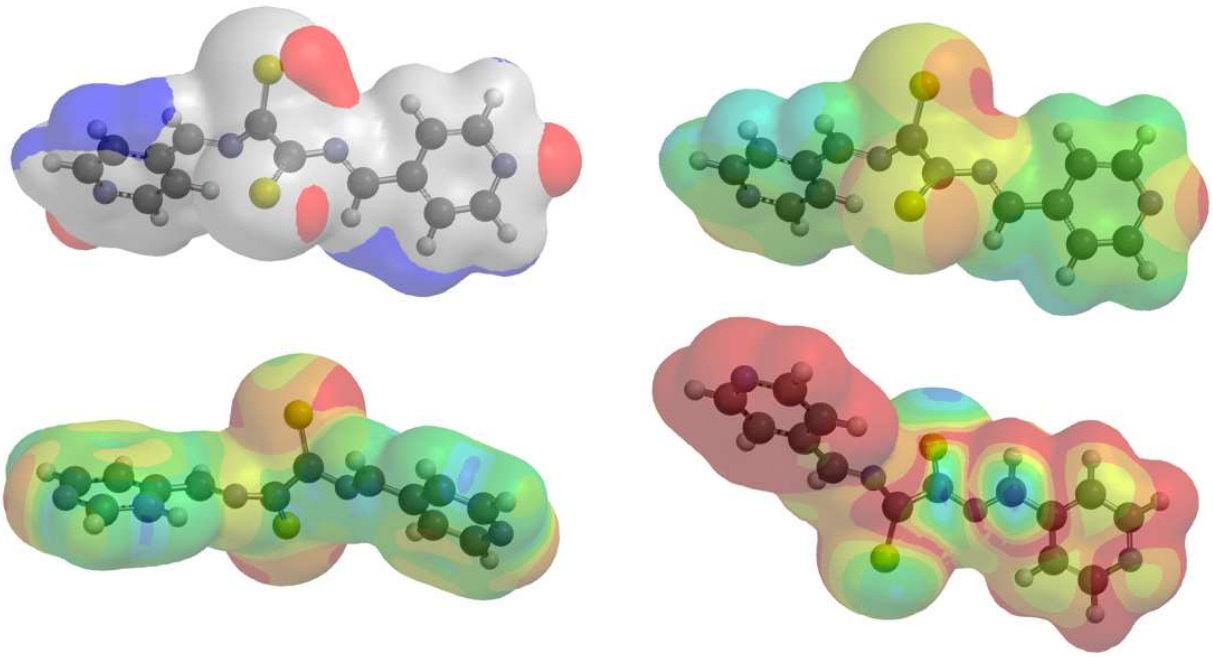

Figure E16. Dipyridyl diazomethine intermediate (Py_2-DAM) (clockwise) Extended electrostatic potential map, electrostatic potential map, LUMO map, local ionization potential map.

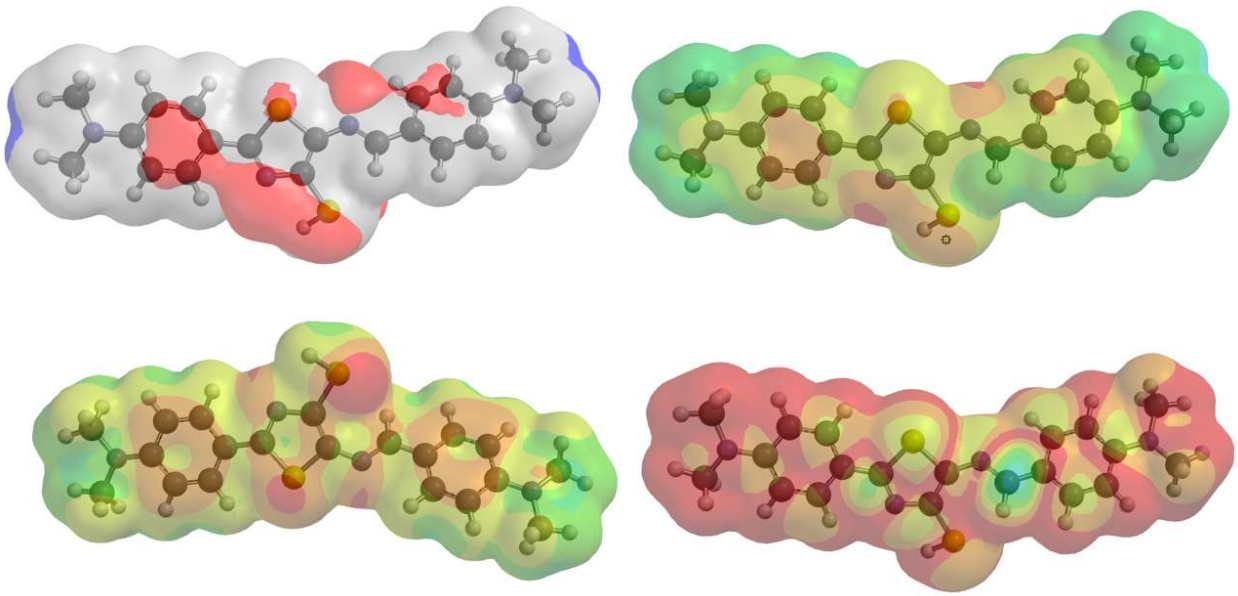

Figure E17. Azomethineaniline anilinethiazole intermediate (amAn-AnTz). (clockwise) Extended electrostatic potential map, electrostatic potential map, LUMO map, local ionization potential map.

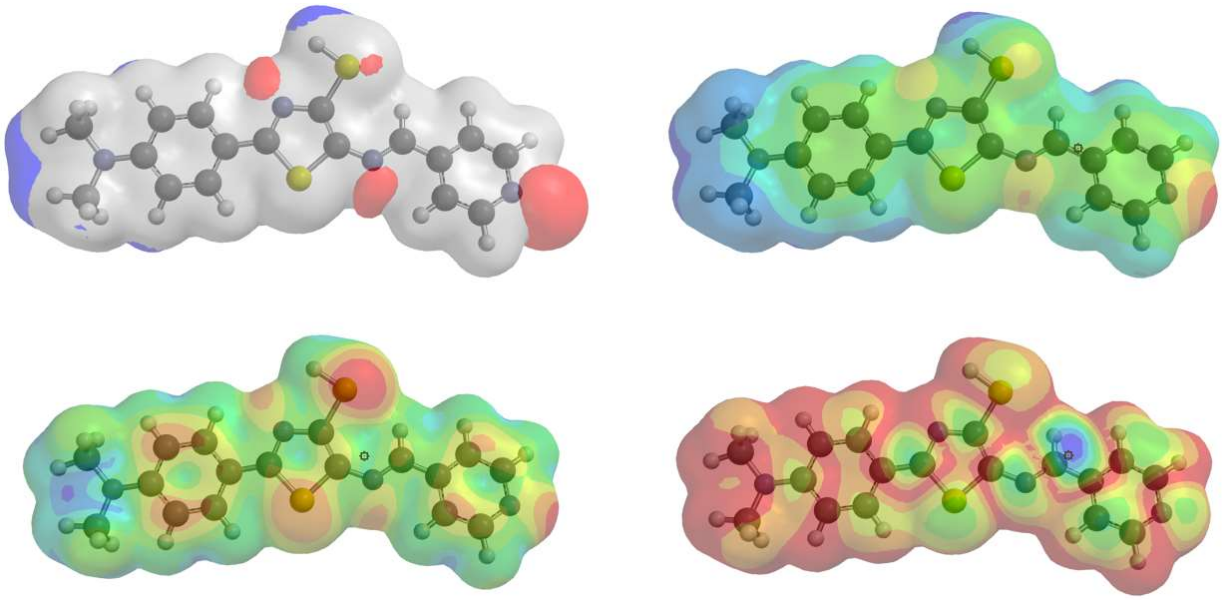

Figure E18. Azomethinepyridyl anilinethiazole intermediate (amPy-AnTz). (clockwise) Extended electrostatic potential map, electrostatic potential map, LUMO map, local ionization potential map.

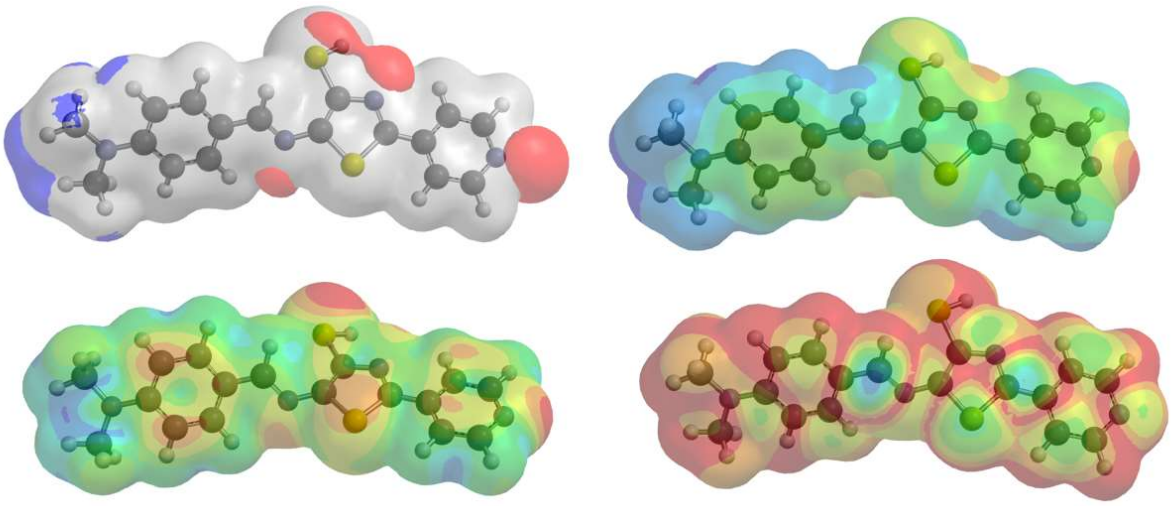

Figure E19. Azomethineaniline pyridylthiazole intermediate (amAn-PyTz). (clockwise) Extended electrostatic potential map, electrostatic potential map, LUMO map, local ionization potential map.

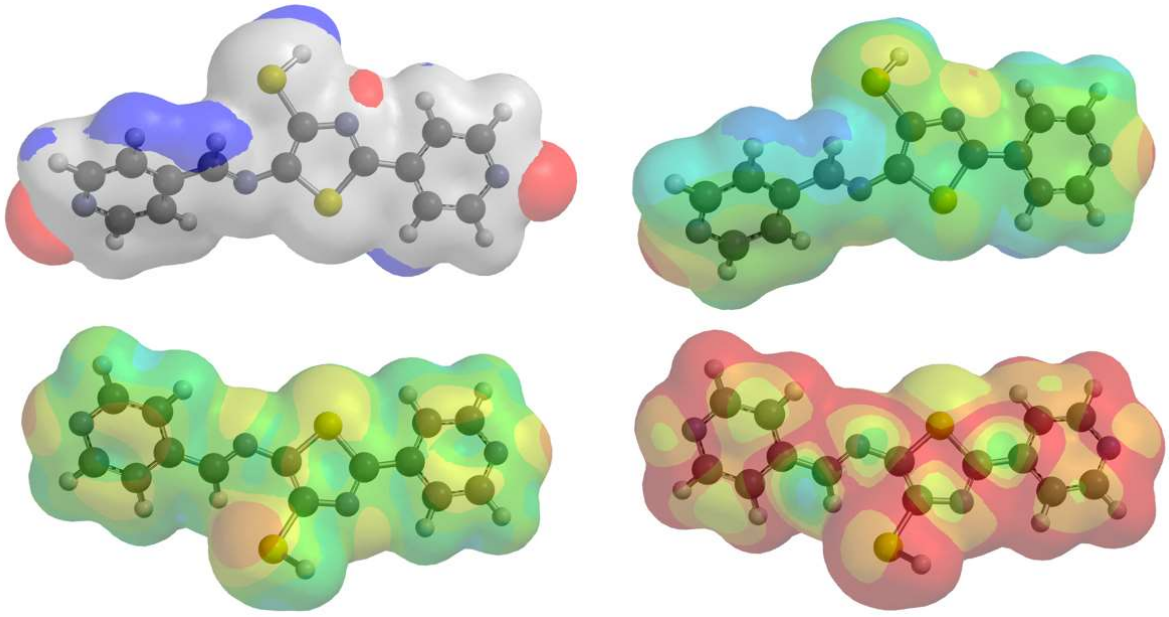

Figure E20. Azomethinepyridyl pyridylthiazole intermediate (amPy-PyTz). (clockwise) Extended electrostatic potential map, electrostatic potential map, LUMO map, local ionization potential map.

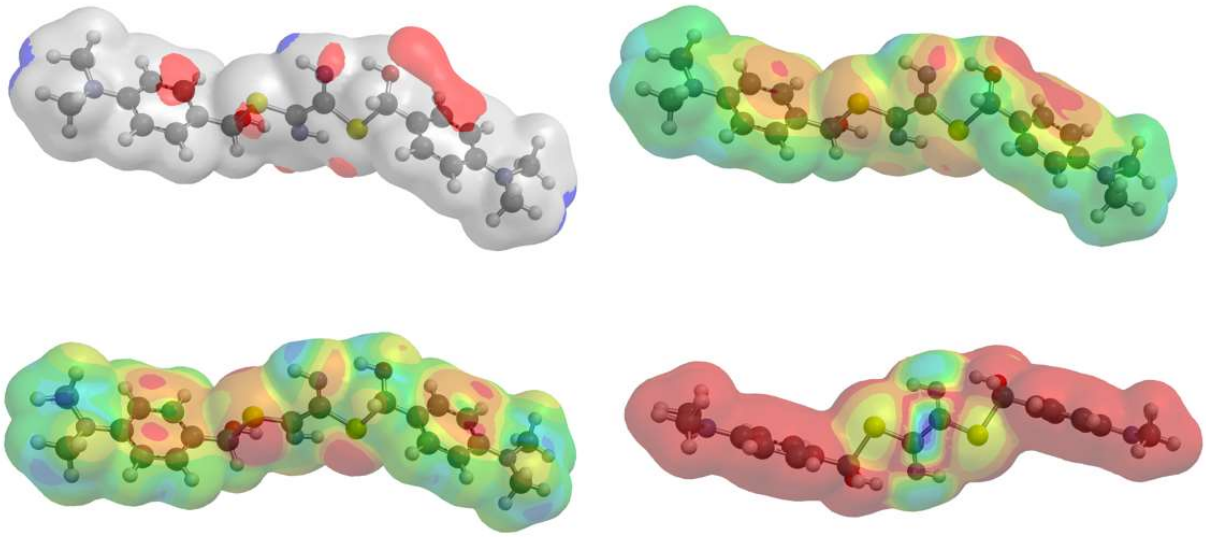

Figure E21. Di(anilinehydroxylthioether) intermediate (An-DHTE). (clockwise) Extended electrostatic potential map, electrostatic potential map, LUMO map, local ionization potential map.

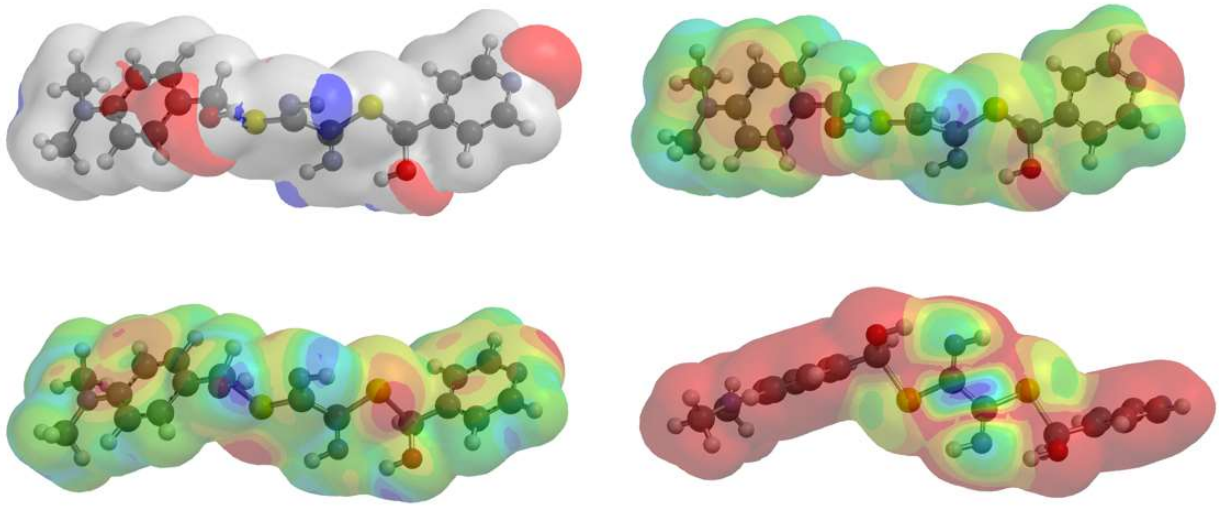

Figure E22. asymmetric hydroxylthioether intermediate (a-DHTE). (clockwise) Extended electrostatic potential map, electrostatic potential map, LUMO map, local ionization potential map.

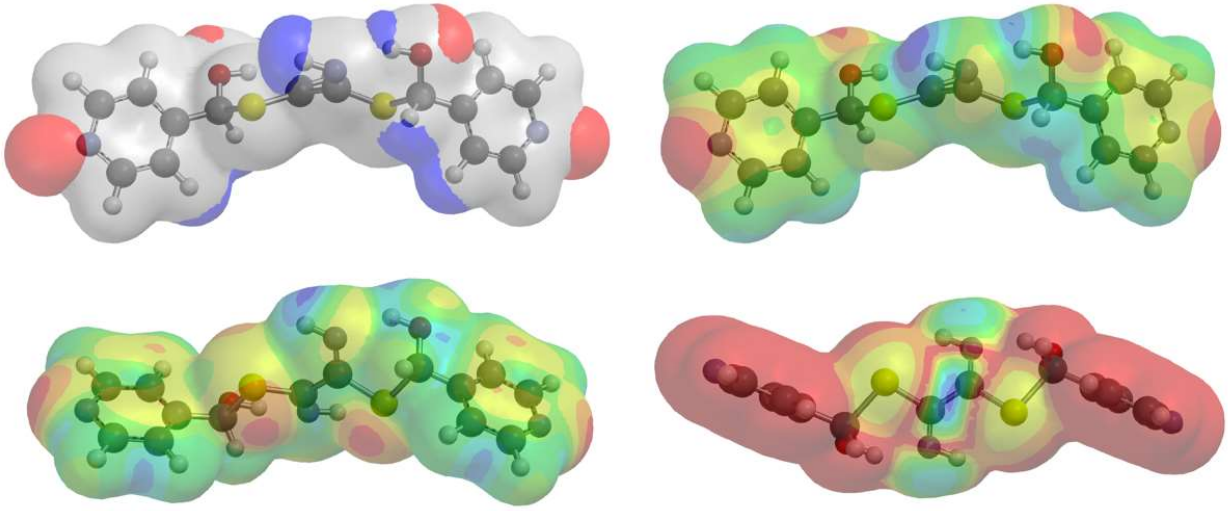

Figure E23. Di(pyridylhydroxylthioether) intermediate (An-DHTE). (clockwise) Extended electrostatic potential map, electrostatic potential map, LUMO map, local ionization potential map.

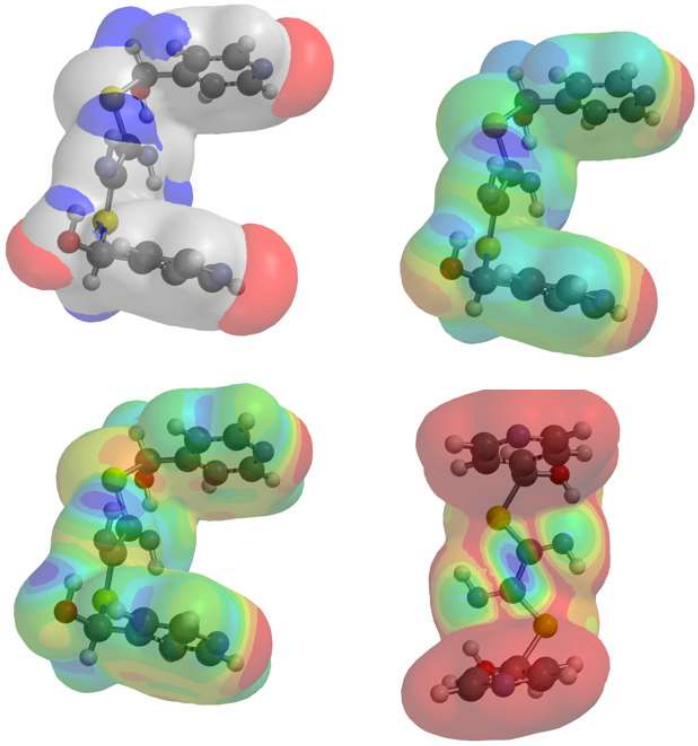

Figure E24. Cofacial di(pyridylhydroxylthioether) intermediate (An-DHTE). (clockwise) Extended electrostatic potential map, electrostatic potential map, LUMO map, local ionization potential map.

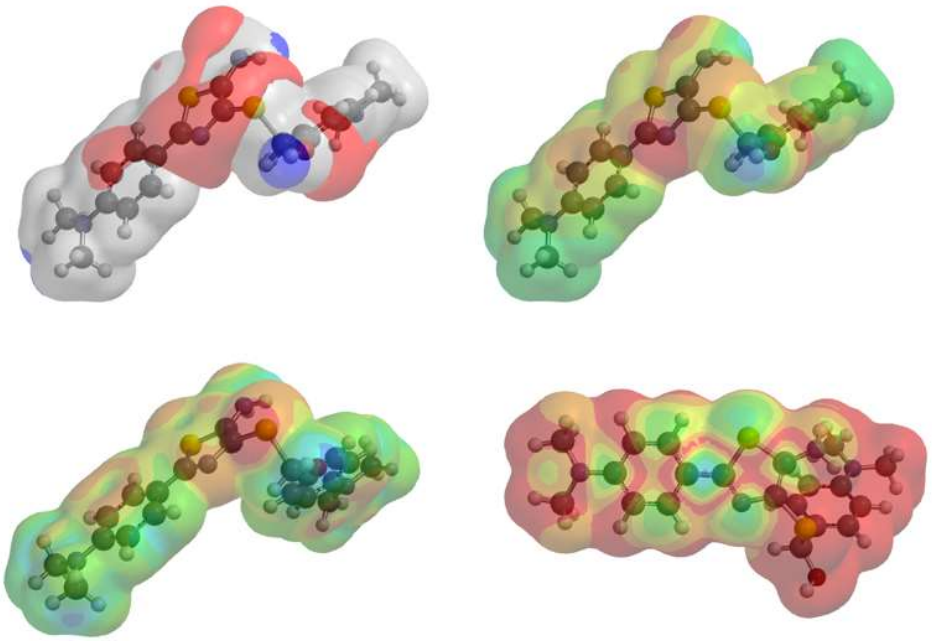

Figure E25. Thioetheraniline anilinethiazole intermediate (teAn-AnTz). (clockwise) Extended electrostatic potential map, electrostatic potential map, LUMO map, local ionization potential map.

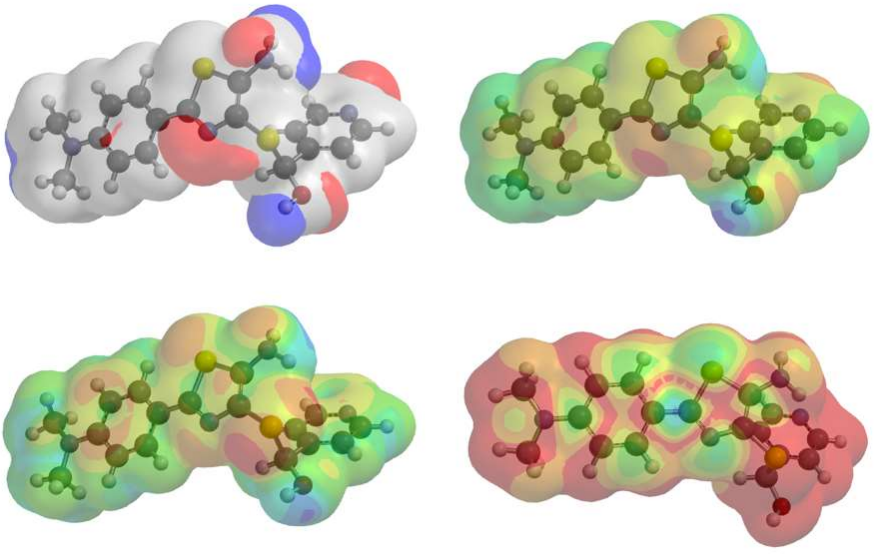

Figure E26. Thioetherpyridyl anilinethiazole intermediate (tePy-AnTz). (clockwise) Extended electrostatic potential map, electrostatic potential map, LUMO map, local ionization potential map.

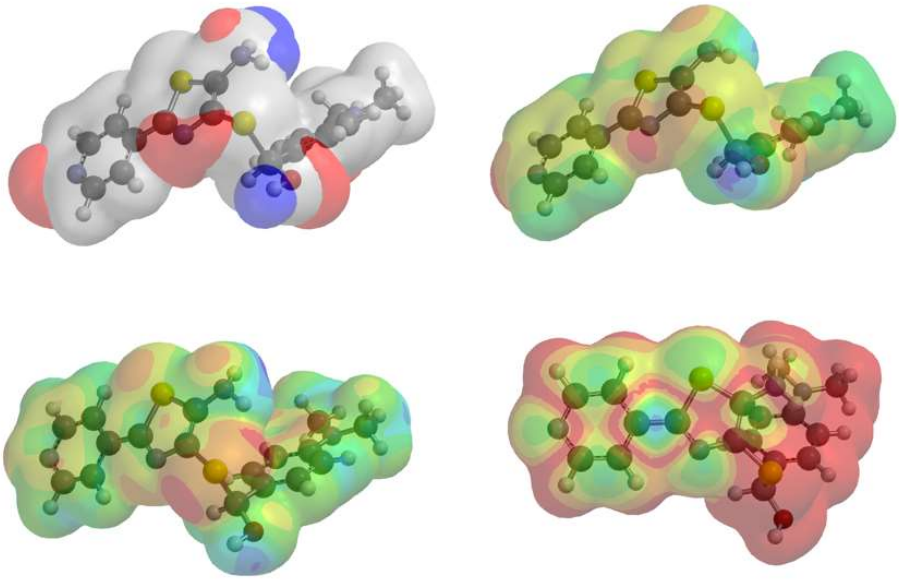

Figure E27. Thioetheraniline pyridylthiazole intermediate (teAn-PyTz). (clockwise) Extended electrostatic potential map, electrostatic potential map, LUMO map, local ionization potential map.

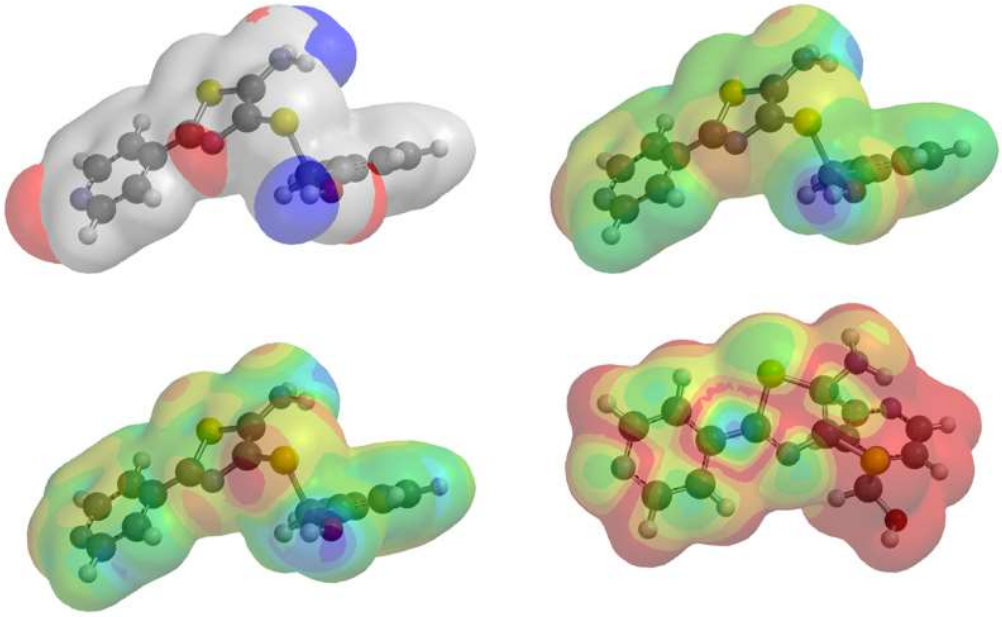

Figure E28. Thioetherpyridyl pyridylthiazole intermediate (tePy-PyTz). (clockwise) Extended electrostatic potential map, electrostatic potential map, LUMO map, local ionization potential map.

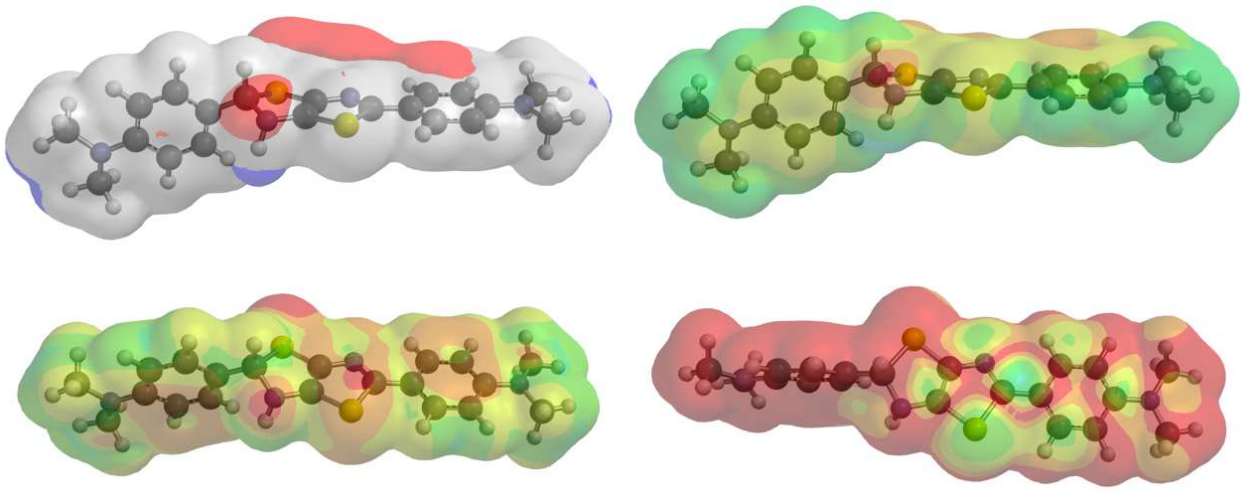

Figure E29. Anilinedihydrothiazolo-anilinethiazole intermediate (AnHTz-AnTz). (clockwise) Extended electrostatic potential map, electrostatic potential map, LUMO map, local ionization potential map.

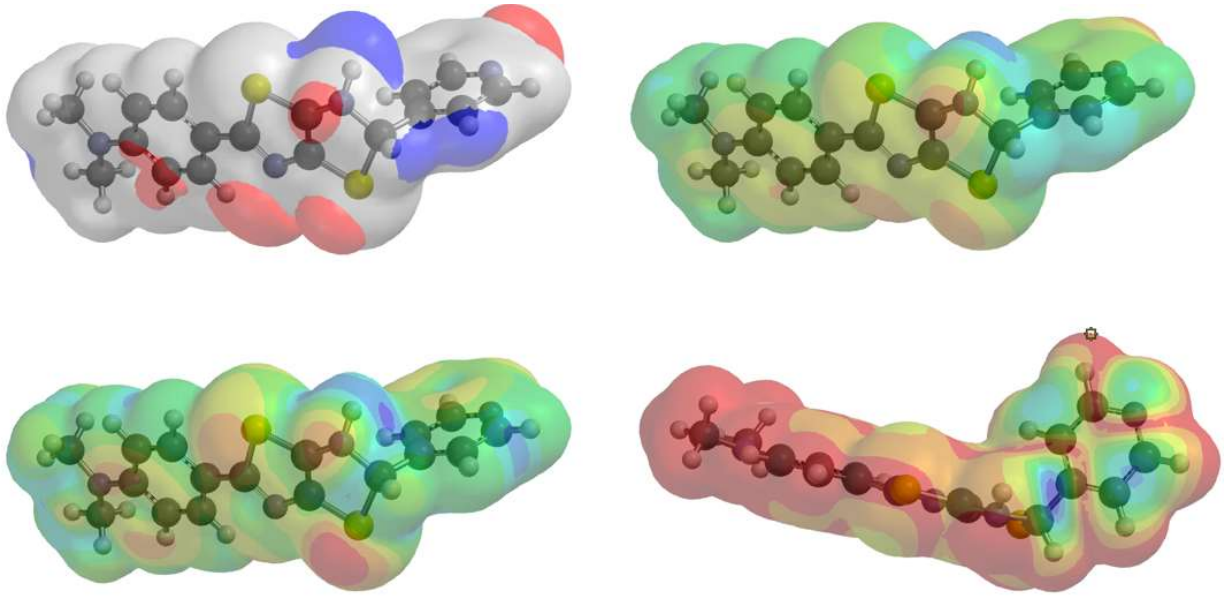

Figure E30. Pyridyldihydrothiazolo-anilinethiazole intermediate (PyHTz-AnTz). (clockwise) Extended electrostatic potential map, electrostatic potential map, LUMO map, local ionization potential map.

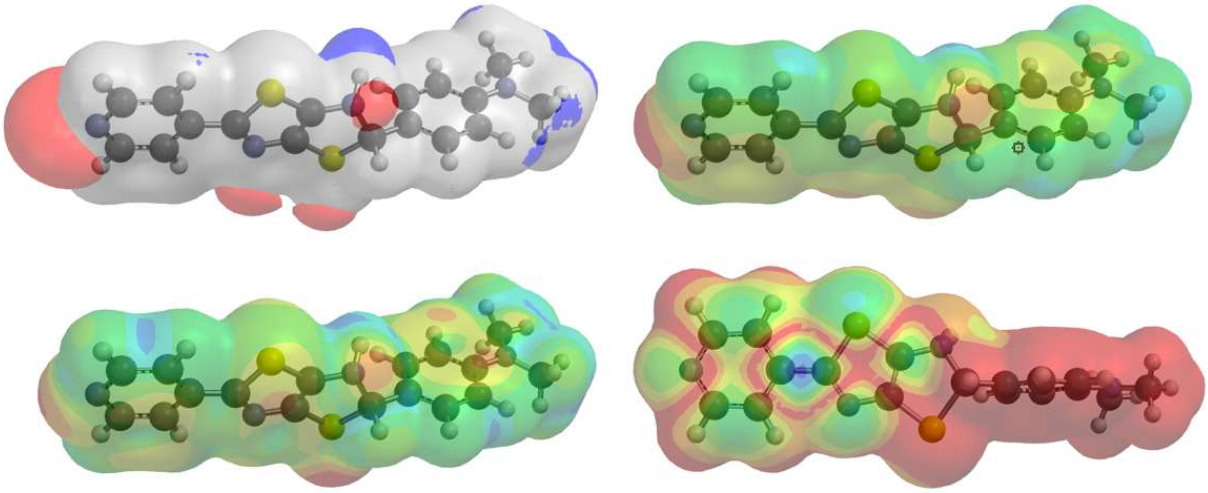

Figure E31. Anilinedihydrothiazolo-pyridylthiazole intermediate (AnHTz-PyTz). (clockwise) Extended electrostatic potential map, electrostatic potential map, LUMO map, local ionization potential map.

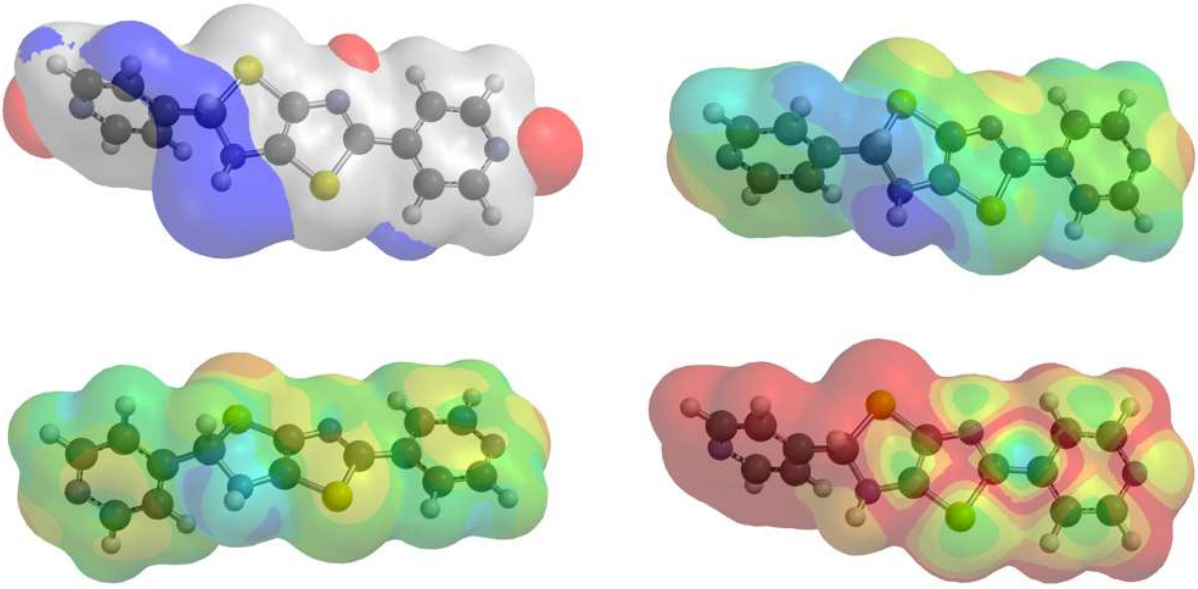

Figure E32. Anilinedihydrothiazolo-pyridylthiazole intermediate (PyHTz-PyTz). (clockwise) Extended electrostatic potential map, electrostatic potential map, LUMO map, local ionization potential map.

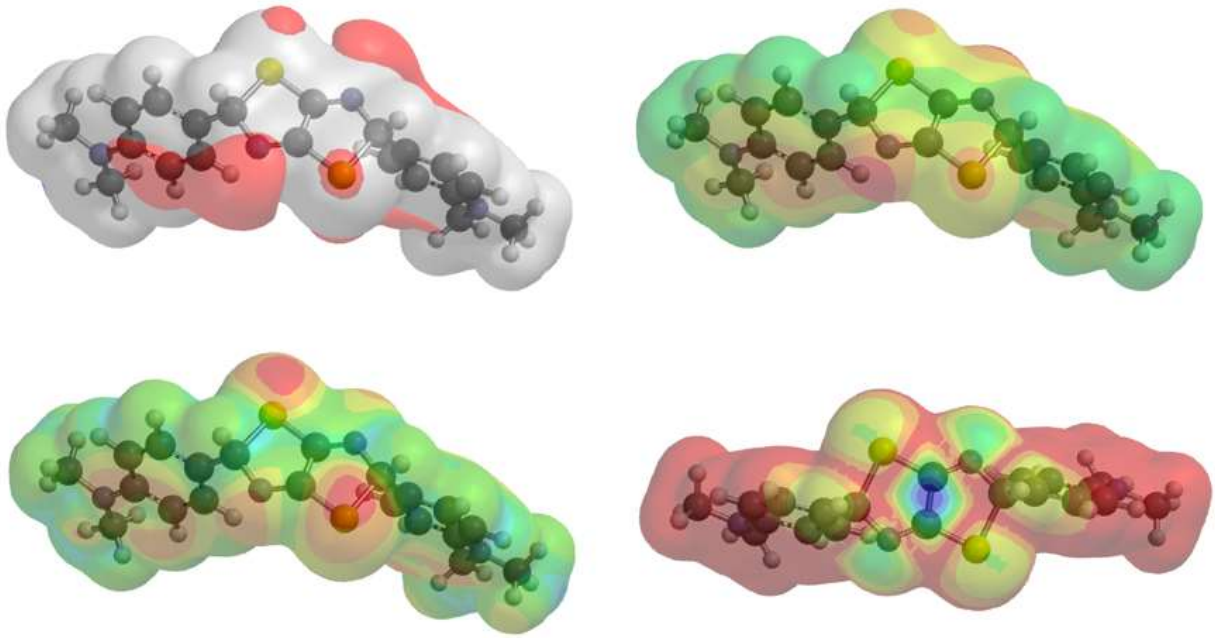

Figure E33. Dianilinedihydrothiazolothiazole intermediate (An_2-H_2TTz). (clockwise) Extended electrostatic potential map, electrostatic potential map, LUMO map, local ionization potential map.

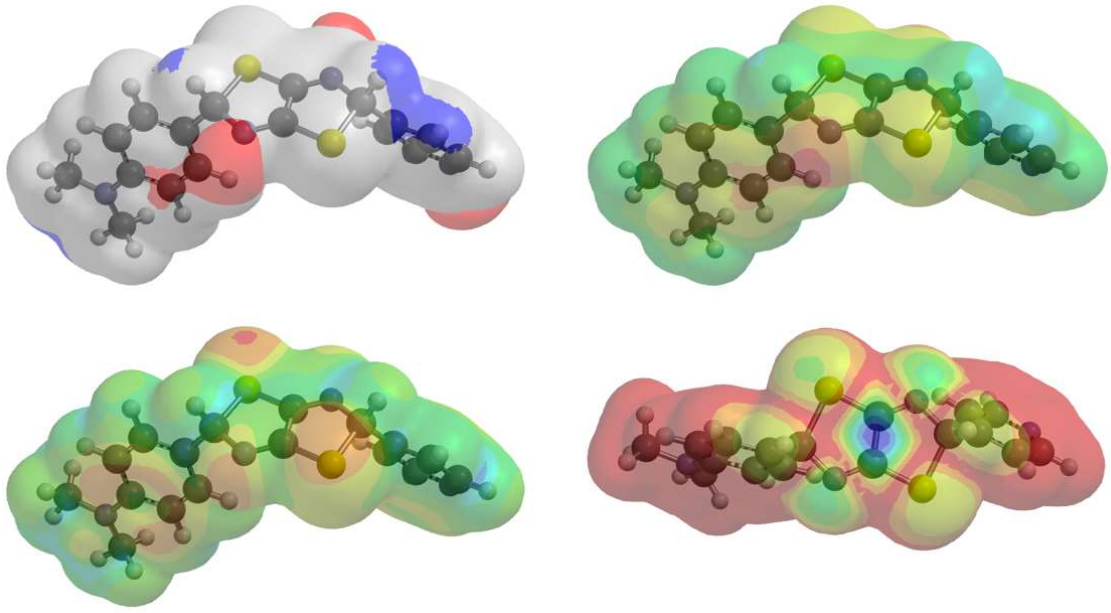

Figure E34. Asymmetric dihydrothiazolothiazole intermediate (a-H_2TTz). (clockwise) Extended electrostatic potential map, electrostatic potential map, LUMO map, local ionization potential map.

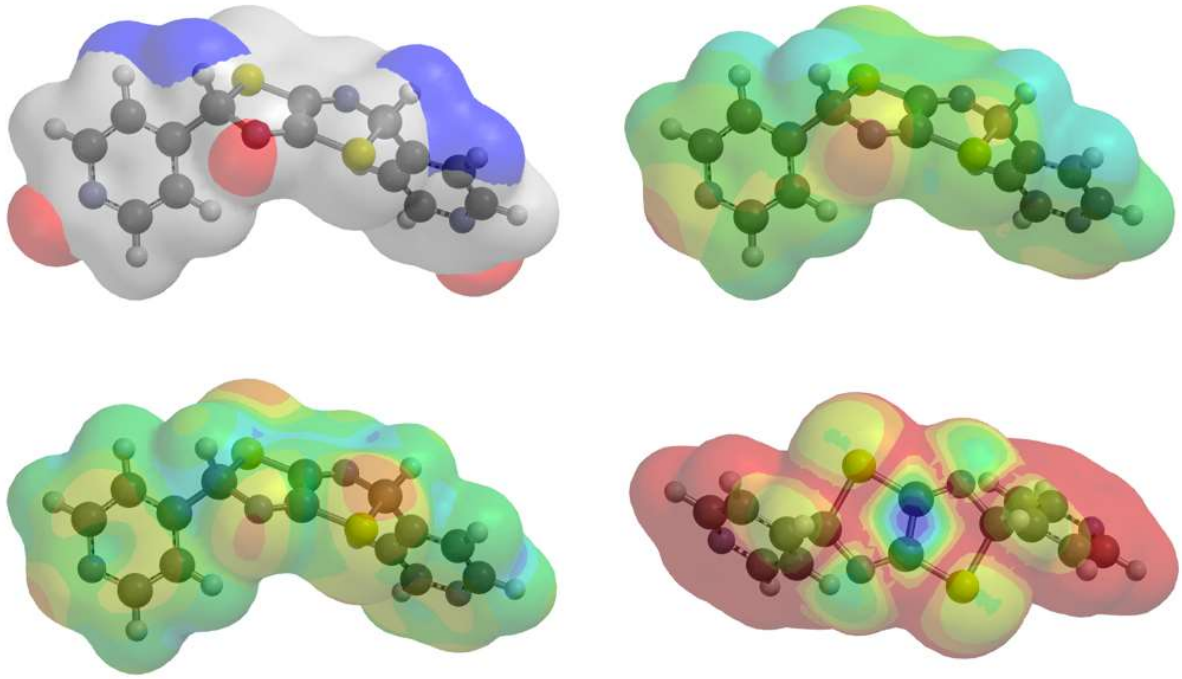

Figure E35. Dipyridyldihydrothiazolothiazole intermediate (Py_2-H_2TTz). (clockwise) Extended electrostatic potential map, electrostatic potential map, LUMO map, local ionization potential map.

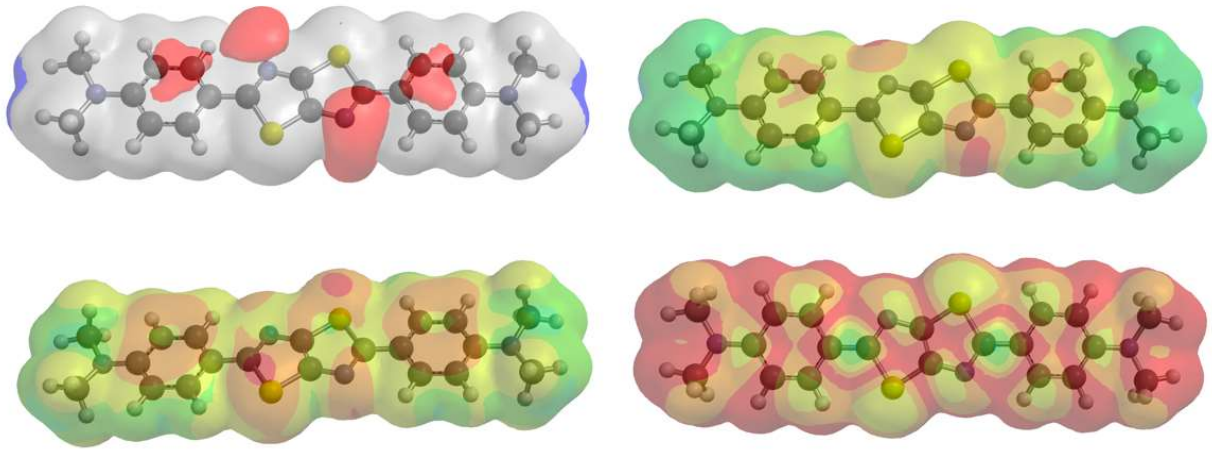

Figure E36. Dianilinethiazolothiazole (An_2-TTz). (clockwise) Extended electrostatic potential map, electrostatic potential map, LUMO map, local ionization potential map.

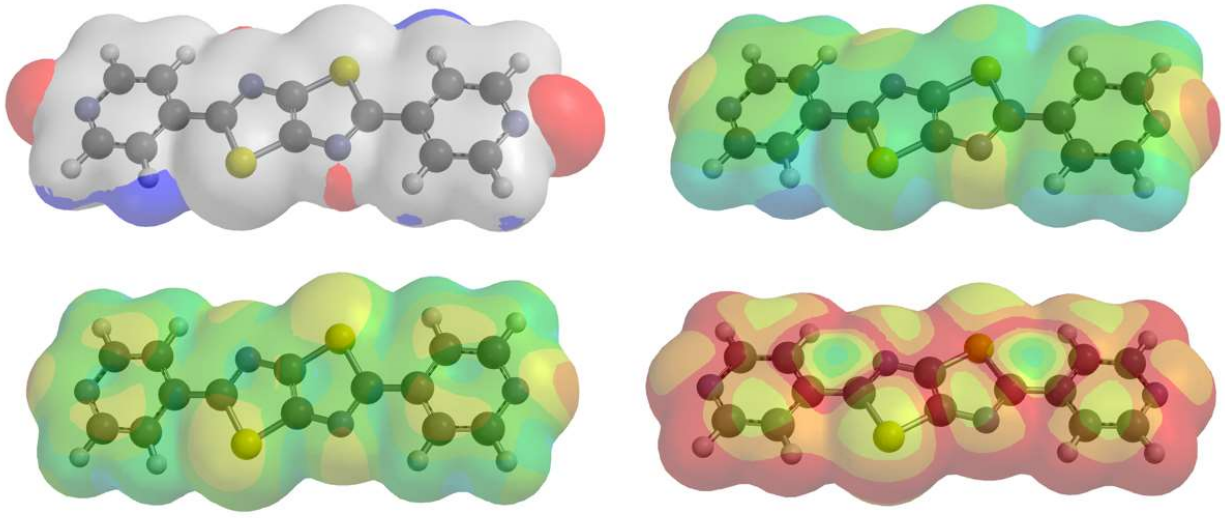

Figure E37. Asymmetric thiazolothiazole (a-TTz). (clockwise) Extended electrostatic potential map, electrostatic potential map, LUMO map, local ionization potential map.

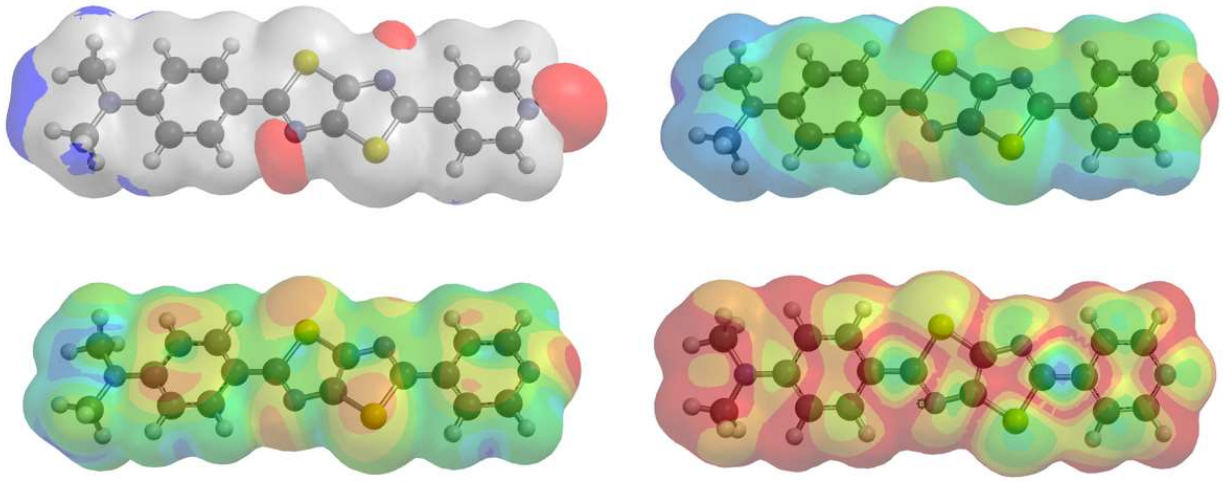

Figure E38. Dipyridylthiazolothiazole (Py_2-TTz). (clockwise) Extended electrostatic potential map, electrostatic potential map, LUMO map, local ionization potential map.

Appendix F – Supplemental Information for Chapter 2

Table F1. Optical and theoretical band gaps of 1st generation TTzs

compound	optical band gap (eV)[a]	theoretical band gap (eV)[b]
Bu_2N-TTz-Py	2.58	3.10
Ph_2N-TTz-Py	2.61	2.97
Ph_2N-TTz-COOH	2.58	2.83
Ph_2N-TTz-CHO	2.52	2.75

[a] From the onset absorption in $CHCl_3$. [b] DFT (B3LYP density functional with 6-31G* basis set) calculations

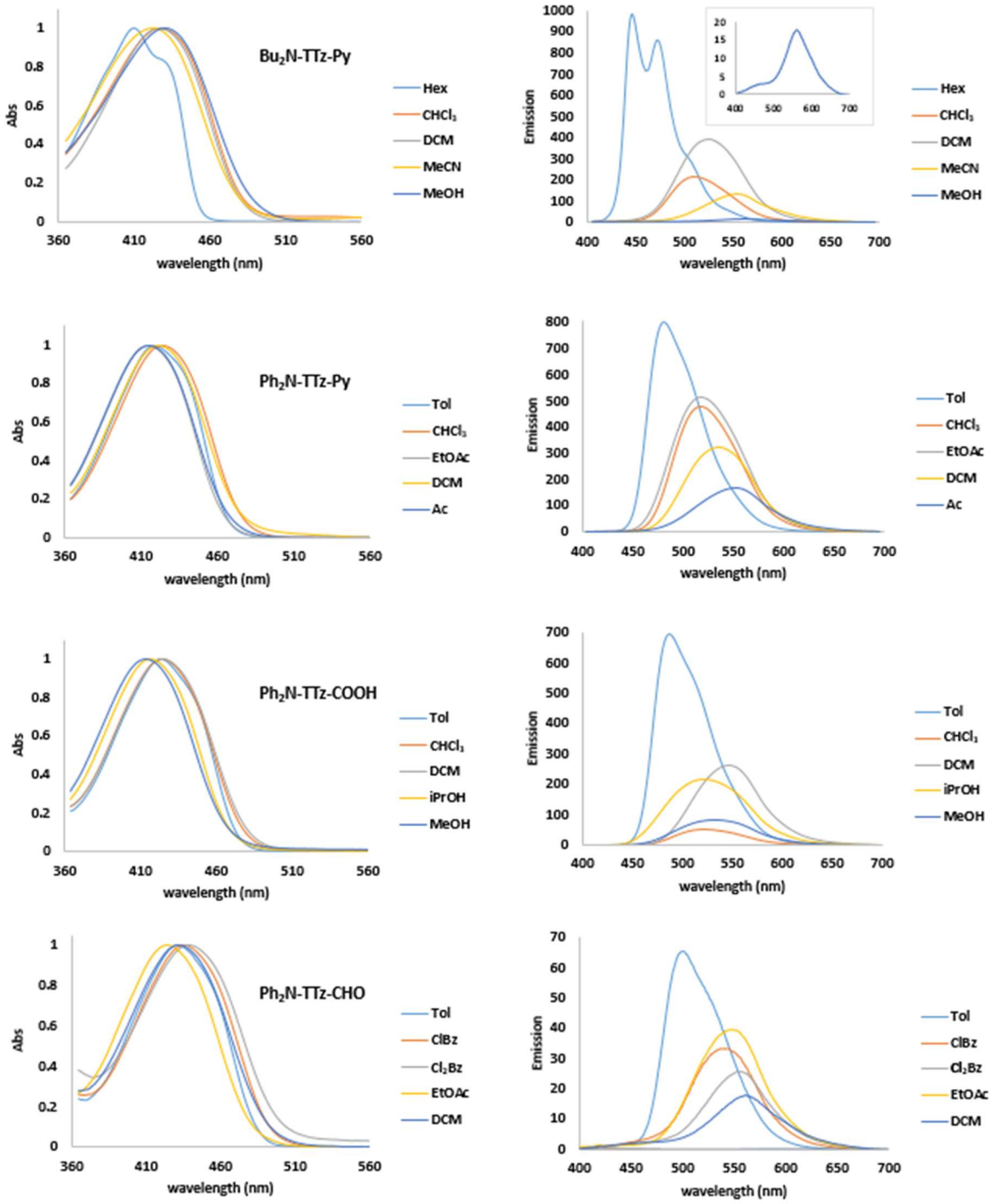

Figure F1. Absorbance and Emission plots of TTz Dyes

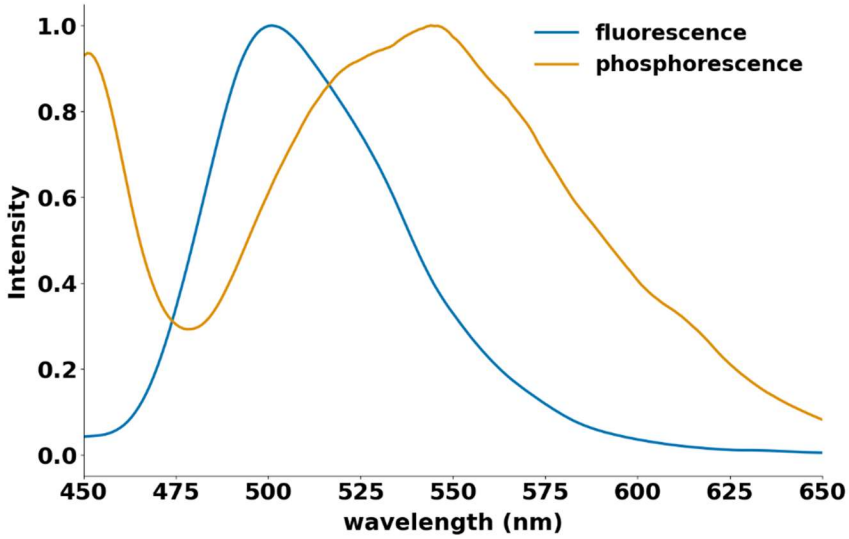

Figure F2. Normalized phosphorescence emission intensity of Bu_2N-TTz-Py in MeTHF at -196 ºC (excited with 385-400 nm LED lamp), spectrum acquired ~2 s after irradiation.

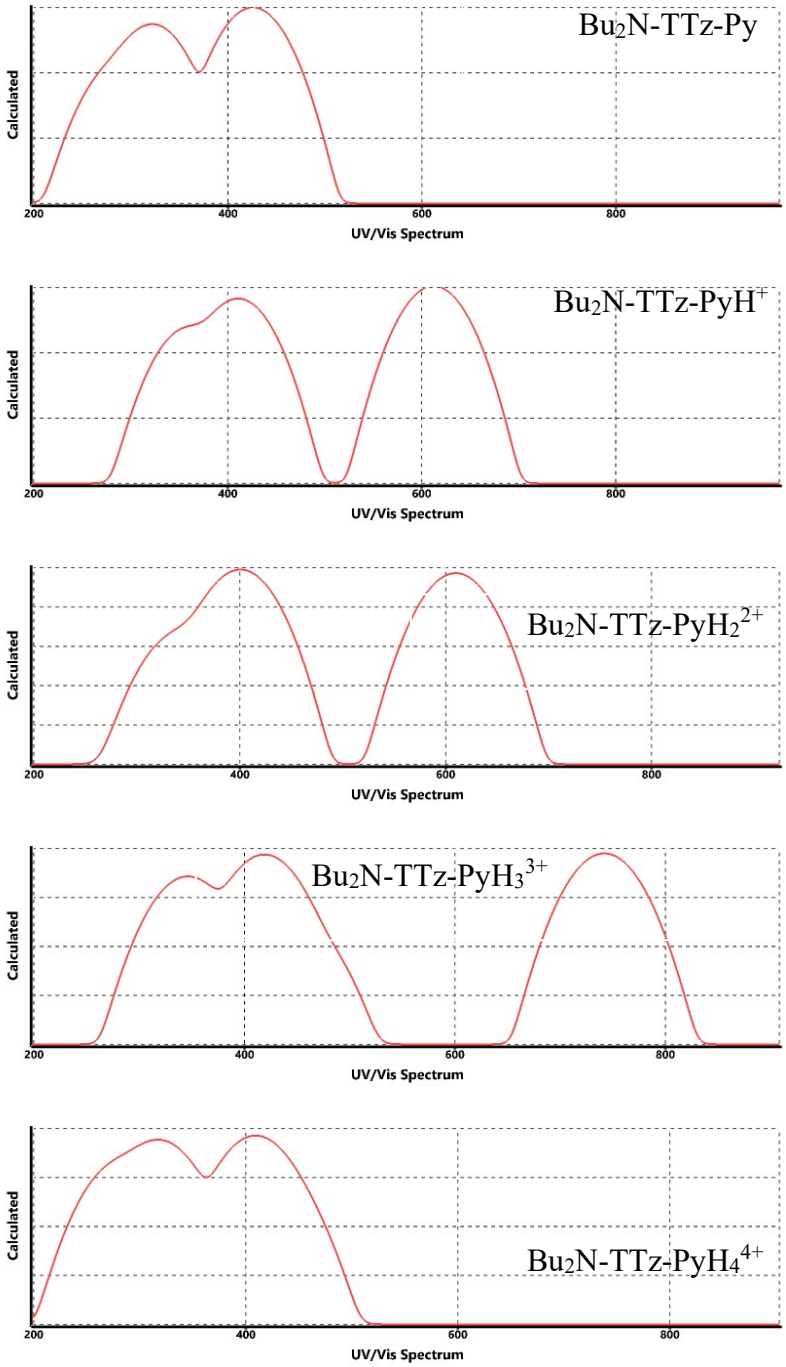

Figure F3. TD-DFT (B3LYP density functional with 6-31G* basis set) calculations of Bu_2N-TT-Py and its protonated forms.

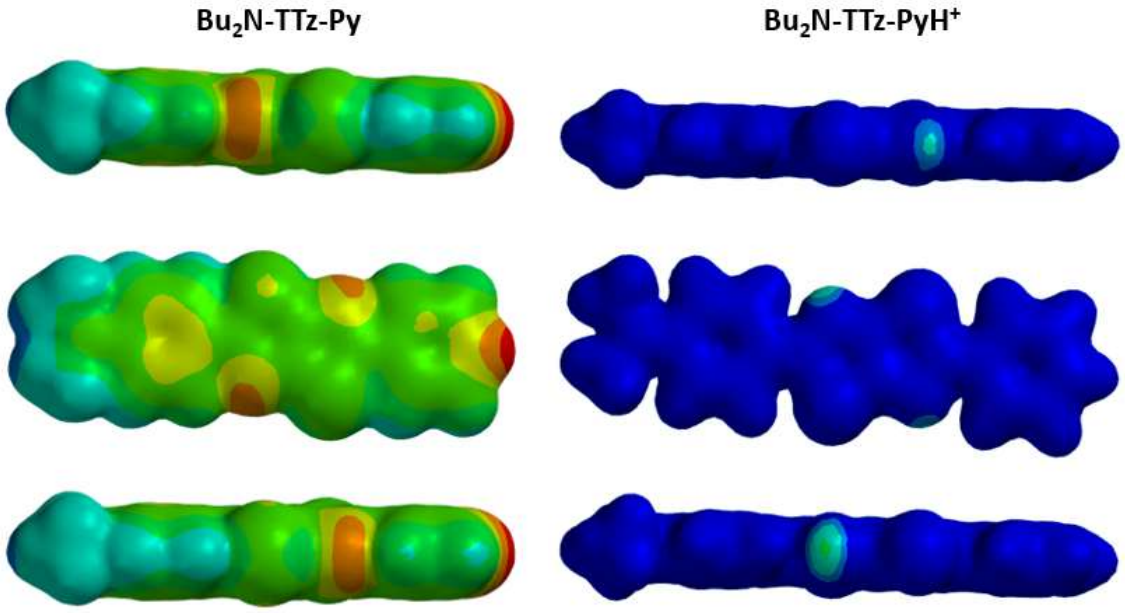

Figure F4. Calculated electrostatic potential maps of Bu_2N-TTz-Py and Bu_2N-TTz-PyH^+ (B3LYP density functional with 6-31G* basis set).

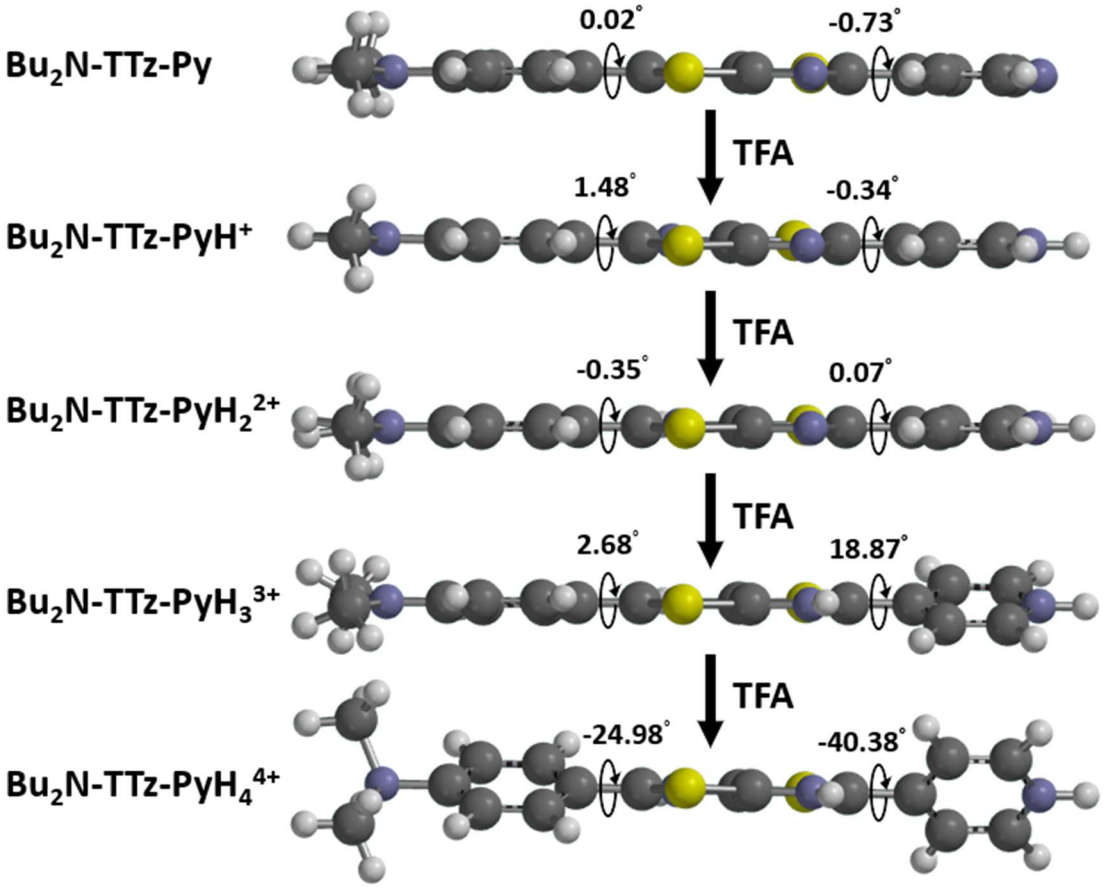

Figure F5. DFT (B3LYP density functional with 6-31G* basis set) calculations of the NCCC dihedral angles of Bu_2N-TTz-Py and its protonated forms. An increased dihedral angle between the TTz bridge and pyridyl constituent disrupts optimal π-π overlap. . Previous studies by Kai Wang et al. show a similar disruption of π-π overlap upon protonation of the TTz core as evidenced by their crystal structures of a highly similar, albeit, symmetrical TTz, di(triphenylamine)-thiazolo[5,4-d]thiazole.[68]

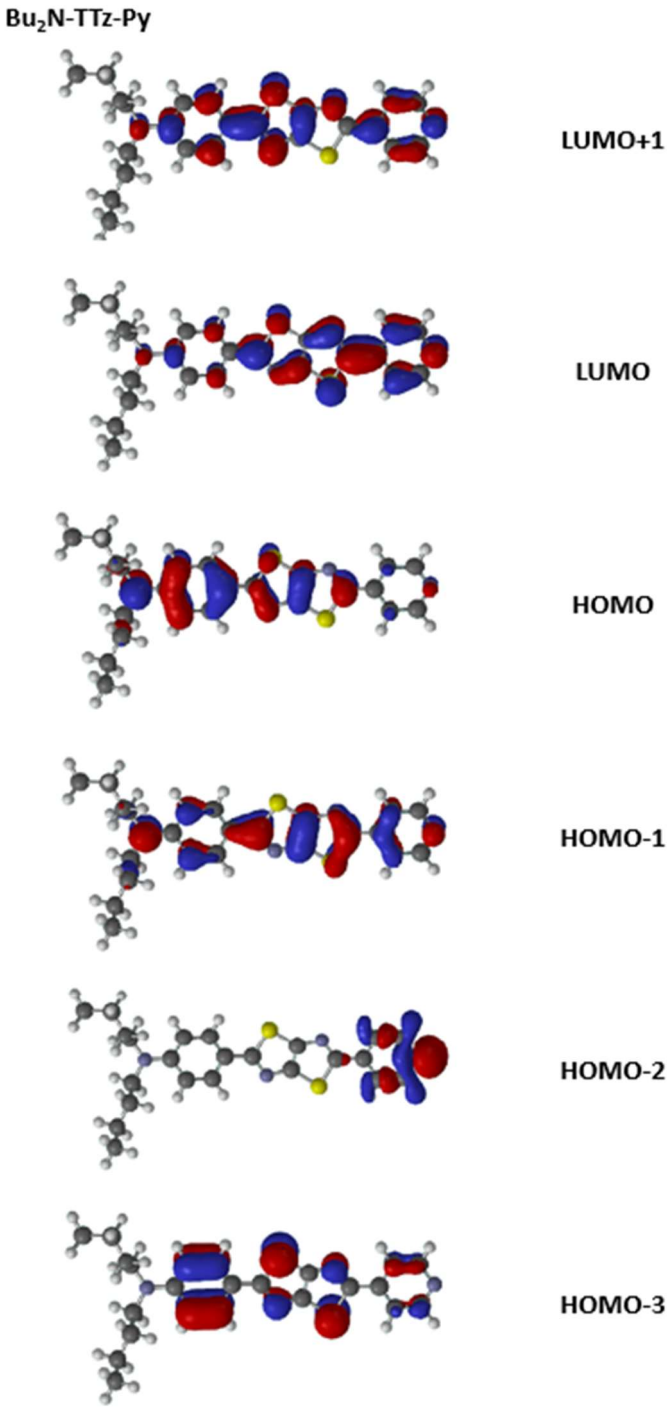

Figure F6. DFT (B3LYP density functional with 6-31G* basis set) calculations for Bu_2N-TTz-Py

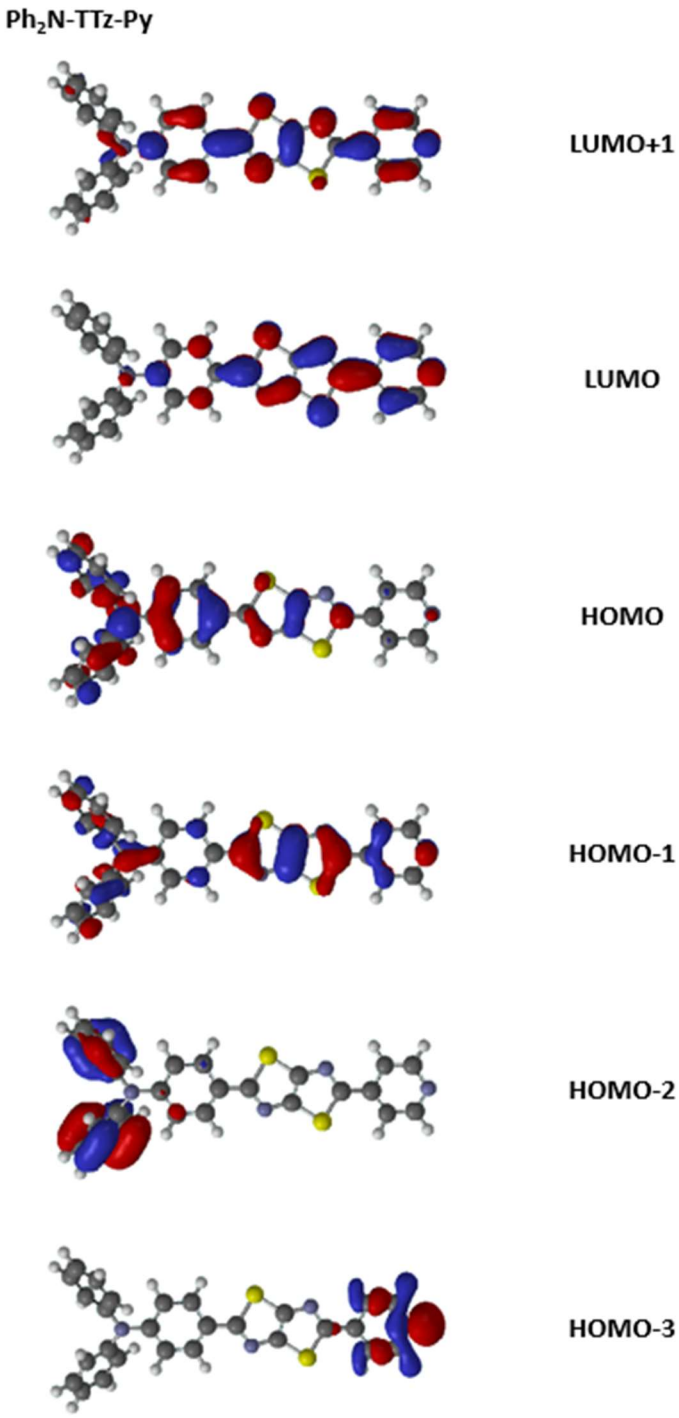

Figure F7. DFT (B3LYP density functional with 6-31G* basis set) calculation for Ph_2N-TTz-Py

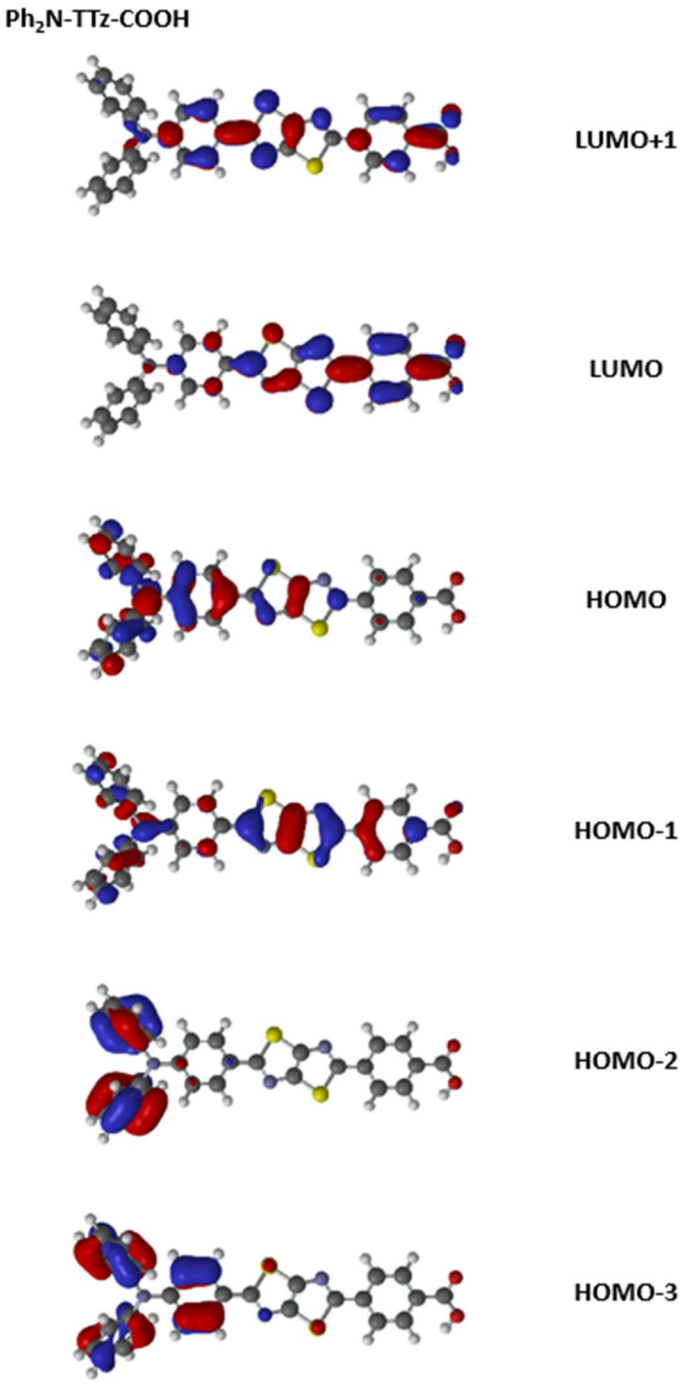

Figure F8. DFT (B3LYP density functional with 6-31G* basis set) calculations for Ph_2N-TTz-COOH

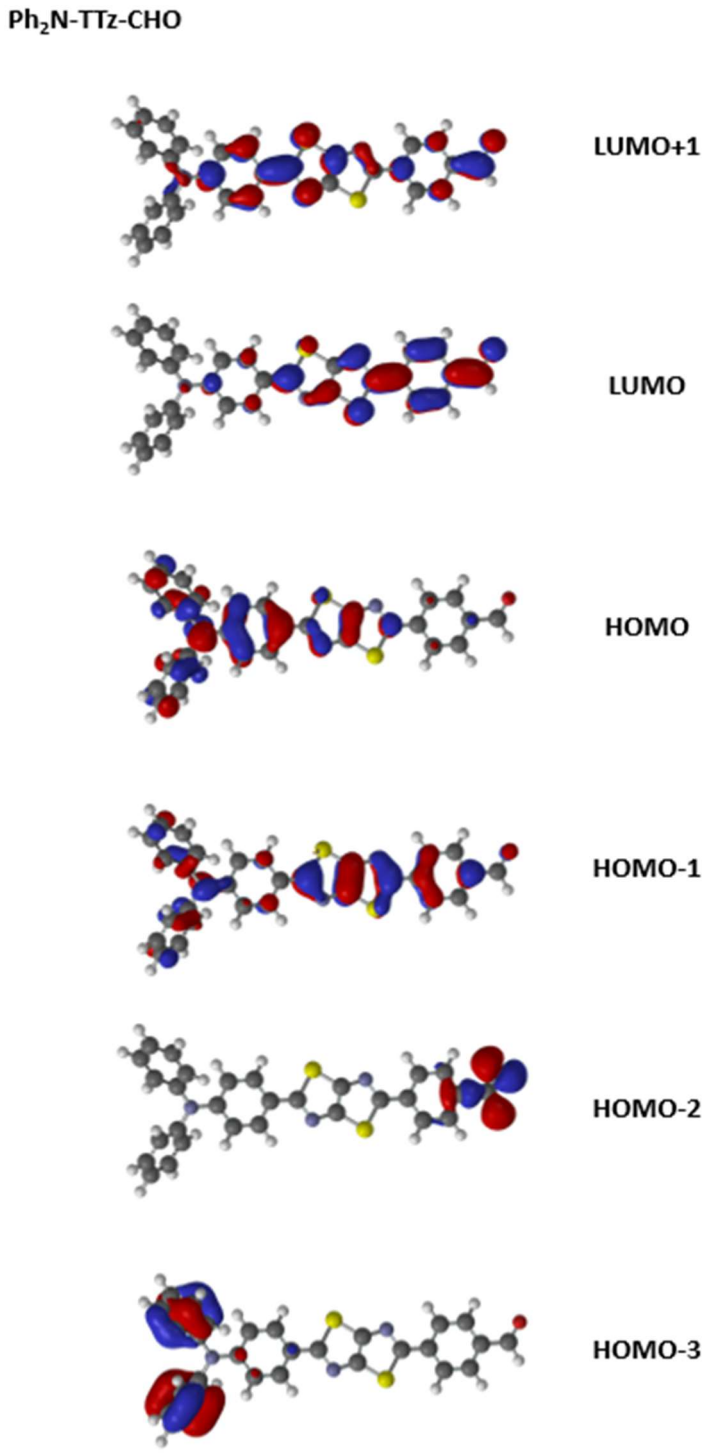

Figure F9. DFT (B3LYP density functional with 6-31G* basis set) calculations for Ph_2N-TTz-CHO

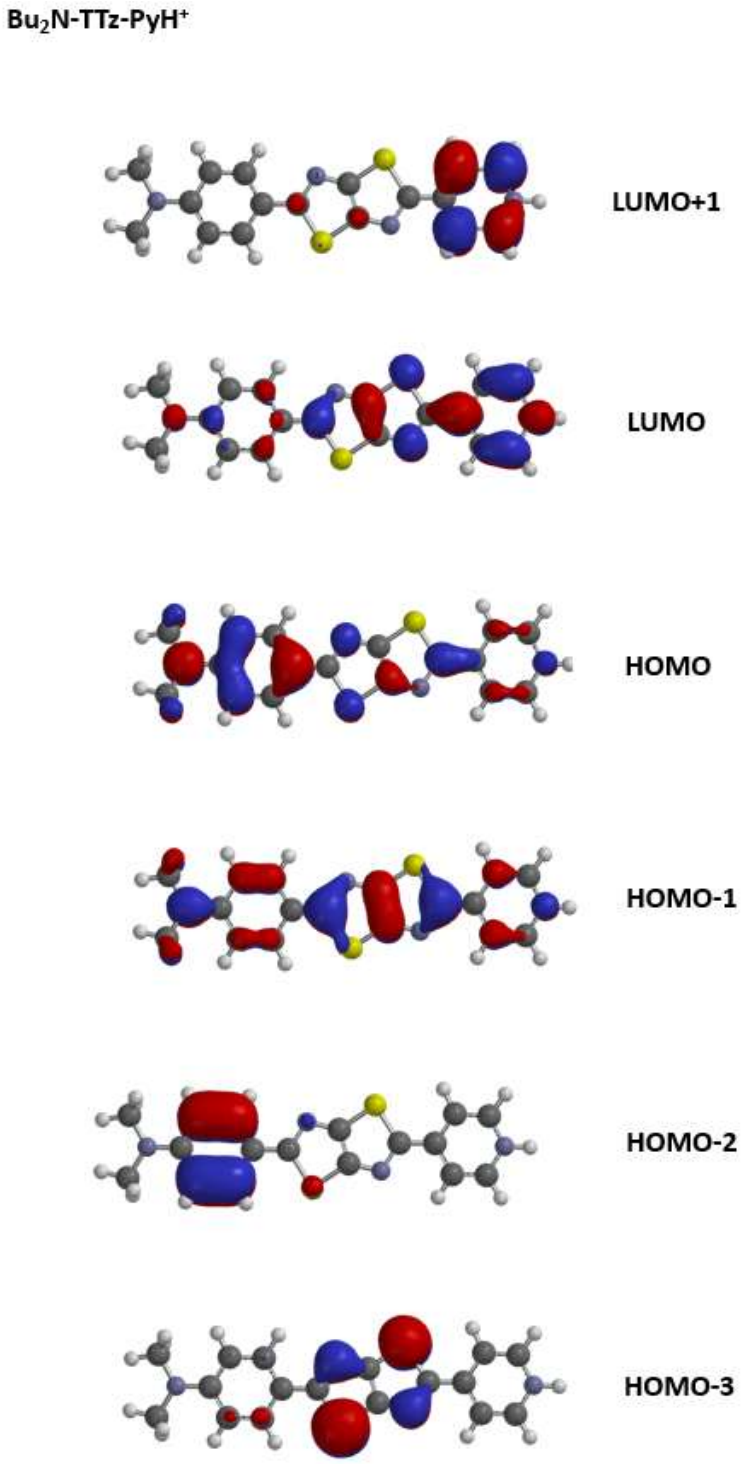

Figure F10. DFT (B3LYP density functional with 6-31G* basis set) calculations for Bu_2N-TTz-PyH^+

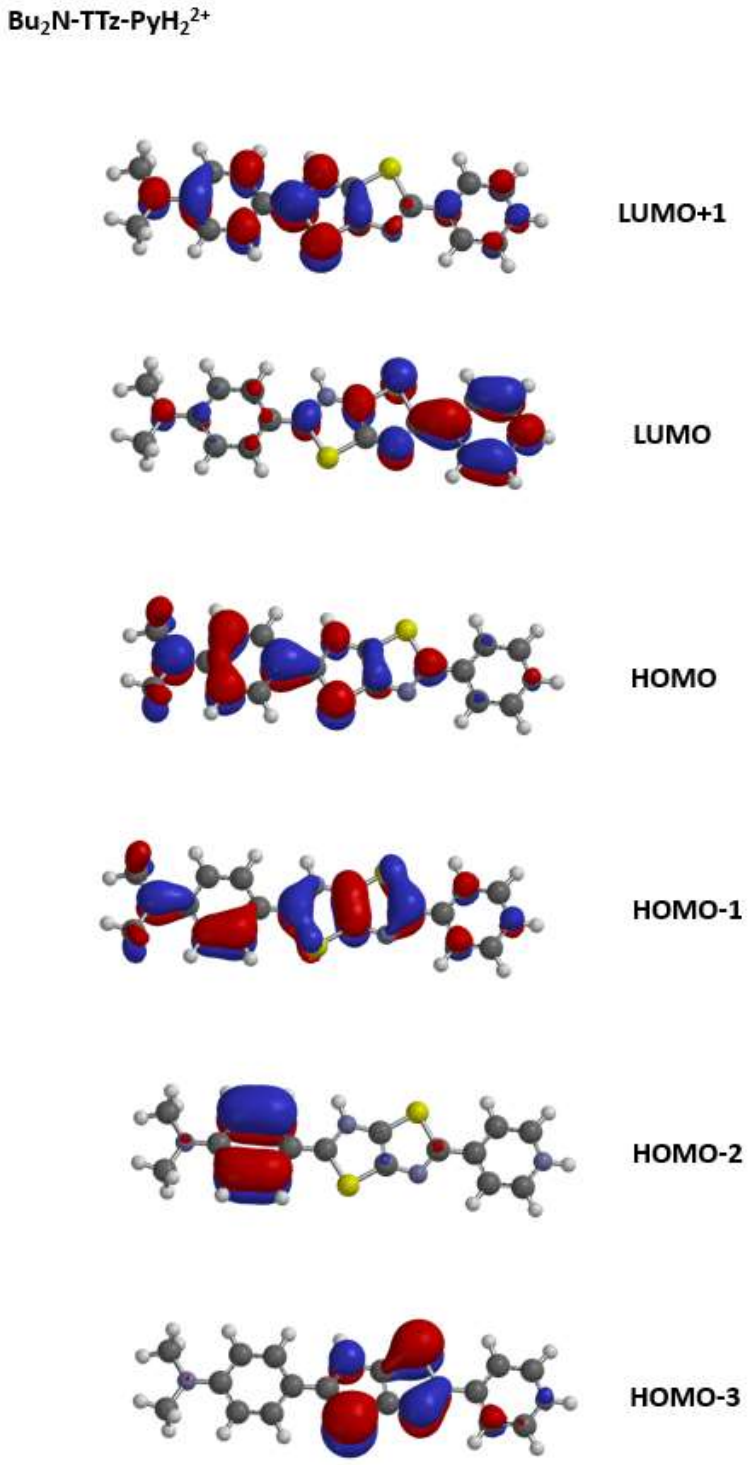

Figure F11. DFT (B3LYP density functional with 6-31G* basis set) calculations for Bu_2N-TTz-PyH_2^{2+}

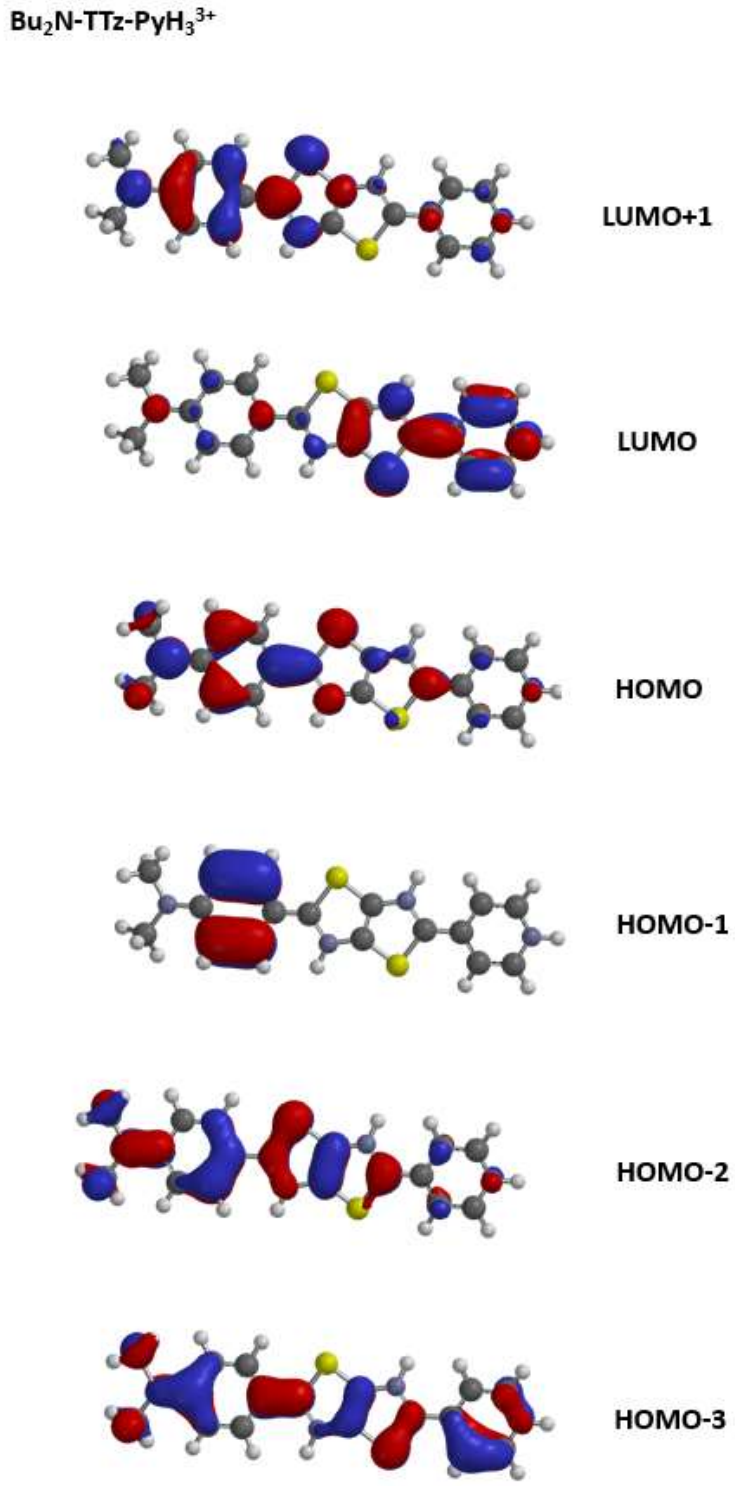

Figure F12. DFT (B3LYP density functional with 6-31G* basis set) calculations for Bu_2N-TTz-PyH_3^{3+}

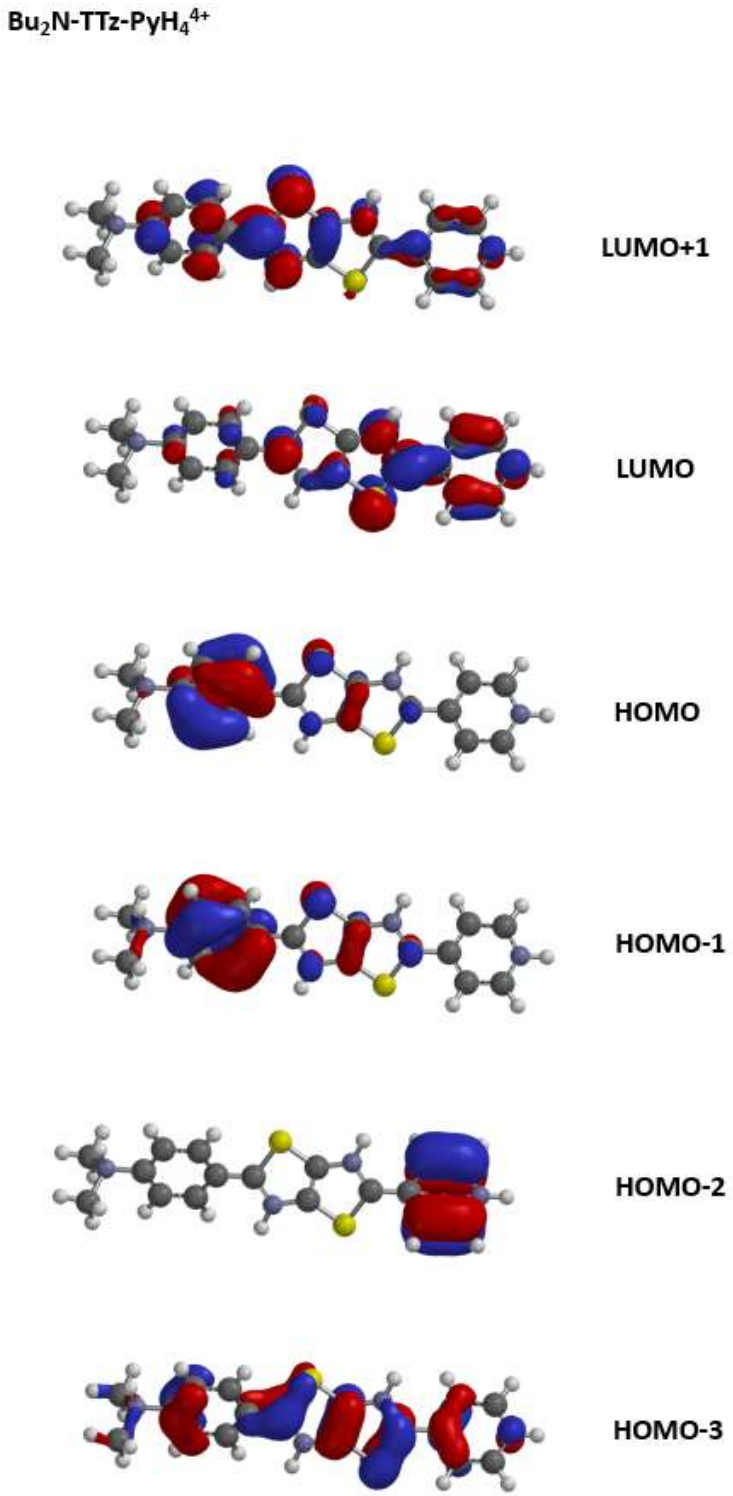

Figure F13. DFT (B3LYP density functional with 6-31G* basis set) calculations for Bu_2N-TTz-PyH_4^{4+}

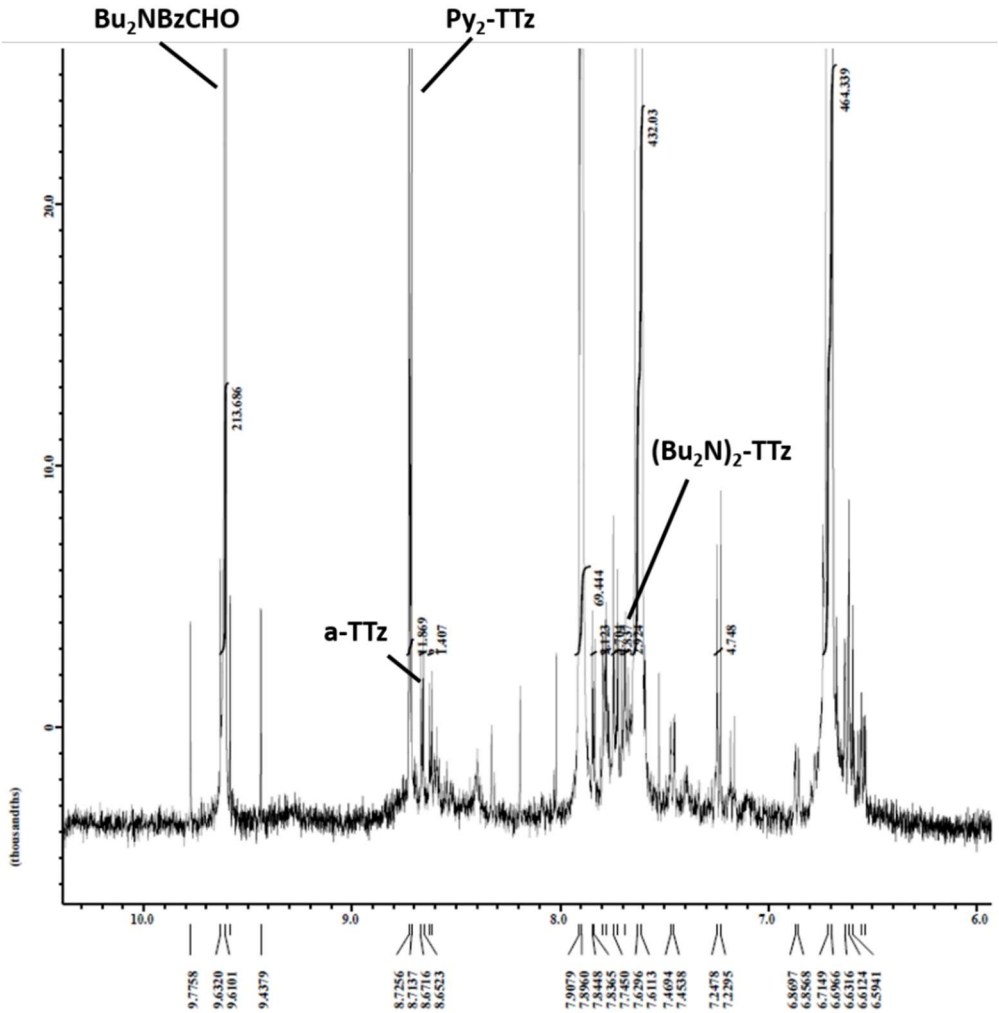

mole ratio starting materials (PyBzCHO, dithiooxamide, $Bu_2NBzCHO$)	1.25 : 1 : 5
N_2	No
Dithiooxamide added at temperature	No
DDQ	No
mole ratio in crude [Py_2-TTz, Bu_2N-TTz-Py, $(Bu_2N)_2$-TTz, $Bu_2NBzCHO$]	12 : 1 : 0.95 : 201
% mass a-TTz in crude	0.81 %

Figure F14. NMR of Bu_2N-TTz-Py with corresponding reaction conditions.

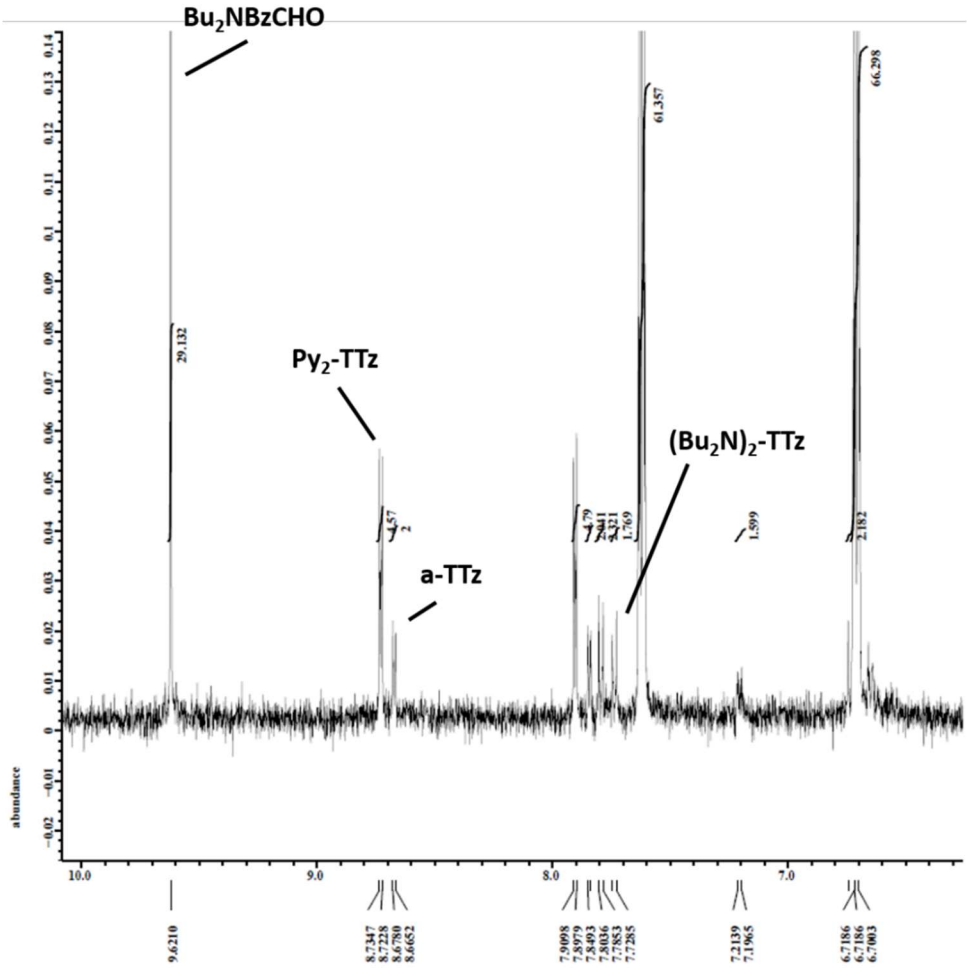

mole ratio starting materials (PyBzCHO, dithiooxamide, $Bu_2NBzCHO$)	1.25 : 1 : 5
N_2	4 h
Dithiooxamide added at temperature	Yes
DDQ	2 h
mole ratio in crude [Py_2-TTz, Bu_2N-TTz-Py, $(Bu_2N)_2$-TTz, $Bu_2NBzCHO$]	1.15 : 1 : 0.44 : 29
% mass a-TTz in crude	5.39 %

Figure F15. NMR of Bu_2N-TTz-Py with corresponding reaction conditions.

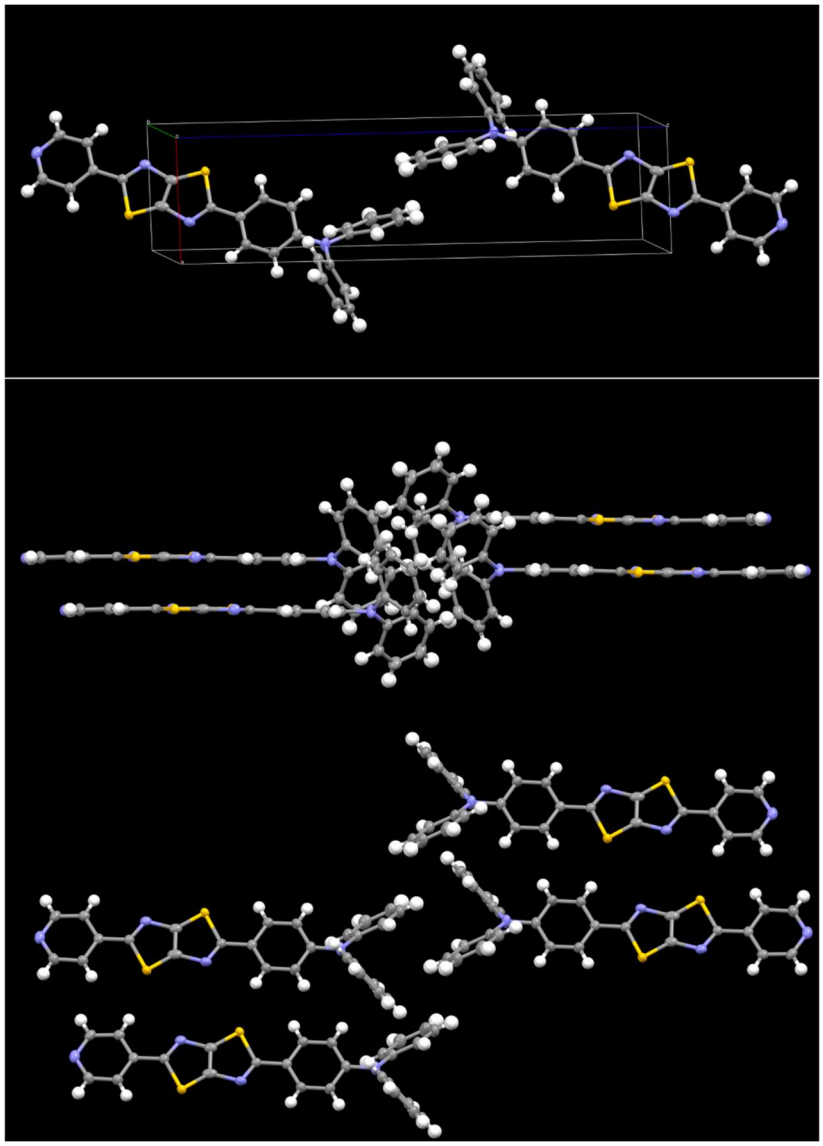

Figure F16. Crystal structure of Ph_2N-TTz-Py demonstrating planarity. The torsional angles across the 2,5 substituent positions was calculated to be 0.3°.